THE STUDY OF PHOTOPHYSICAL PROPERTIES OF ORGANIC-LANTHANIDE HYBRID MATERIALS AND THEIR APPLICATIONS

BY

Guochen Bao

Institute for Biomedical Materials & Devices

School of Mathematical and Physical Sciences, Faculty of Science

University of Technology Sydney

Supervisors:

Prof. Dayong Jin (UTS)
Dr. Shihui Wen (UTS)
Dr. Jiajia Zhou (UTS)
Prof. Ka-Leung Wong (HKBU)
Prof. Peter A. Tanner (HKBU)
Prof. Jean-Claude G. Bünzli (EPFL)

This thesis is presented for the degree of Doctor of Philosophy

March 2021

CERTIFICATE OF ORIGINAL AUTHORSHIP

I, Guochen Bao, declare that this thesis, is submitted in fulfilment of the requirements for the award of Doctor of Philosophy, in the School of Mathematical and Physical Sciences, Faculty of Science, at the University of Technology Sydney.

This thesis is wholly my own work unless otherwise reference or acknowledged. In addition, I certify that all information sources and literature used are indicated in the thesis.

I certify that the work in this thesis has not previously been submitted for a degree nor has it been submitted as part of the requirements for a degree at any other academic institution except as fully acknowledged within the text. This thesis is the result of a Collaborative Doctoral Research Degree program with Hong Kong Baptist University as part of a Collaborative Doctoral Research Training Program.

This research is supported by the Australian Government Research Training Program.

Production Note:
Signature: Signature removed prior to publication.

Date: 24 March 2021

ACKNOWLEDGEMENTS

As a cotutelle Ph.D student at the University of Technology Sydney (UTS) and Hong Kong Baptist University (HKBU), I have been assisted by many people during my Ph.D period. I deeply appreciate all of them.

Firstly, I would like to express my sincere gratitude to my principal supervisor at UTS, Prof. Dayong Jin, for his professional guidance and helpful encouragement during my research study. What I learned from him are not only academic research skills but also the philosophy of research. I learned a lot from his self-motivated and optimistic attitude to life and research. He provides me with excellent research facilities and technical support, which is important for me to complete my research work. He provides me with many opportunities to learn and improve my abilities including attending international conferences. This valuable experience broadens my horizon and benefits my life in both research and daily life.

I thank my principal supervisor at HKBU, Prof. Ka-Leung Wong, for his professional guidance and inspiration during my Ph.D study. I thank Prof. Peter A. Tanner (HKBU) and Prof. Jean-Claude G. Bünzli (Swiss Federal Institute of Technology Lausanne) for the knowledge they taught me in the field of photophysics and lanthanide chemistry and their help in my experiments and paper writing. I thank my co-supervisors Dr Shihui Wen (UTS) and Dr Jiajia Zhou (UTS) for their support in my experiments and daily life. All of them are my respected teachers and friends. Without their help and support, I cannot complete my research tasks. All the things they shared with me are precious gifts to me.

I thank all my dear friends and colleagues at both UTS and HKBU for their support and help during my research study. They are Dr Fan Wang, Dr Gungun Lin, Dr Qian Su, Dr Xiaoxue Xu, Dr Zhiguang Zhou, Dr Yinghui Chen, Dr Olga Shimoni, Dr Wei Ren, Dr Hao He, Dr Chao Mi, Dr Ming Guan, Dr Du Li, Dr Le Zhang, Dr Jiayan Liao, Dr Chaohao Chen, Mr Xuchen Shan, Mr Yongtao Liu, Mr Yuan Liu, Ms Huan Wu, Ms Xiangjun Di, Mr Dejiang Wang, Mr Baolei Liu, Mr Guocheng Fang, Mr Sheng Mei, and Mr Yunfei Shang, Mr Lei Ding, Mr Guan Huang from UTS, and Dr Zhenyu Liu, Dr

Hongguang Li, Dr Chi-Fai Chan, Dr Jingxiang Zhang, Dr Sheng Tong, Dr Jie Pan, Dr Lijun Jiang, Dr Yan Zhou, Dr Yonghong Zhang, Dr Joan Goetz, Dr Yuxia Luo, Dr Shuai Zha, Mr Chen Xie and Mr Ziyuan Meng, from HKBU. Besides, a special acknowledgement is also given to all the technicians from UTS and HKBU for their professional support and kind help in my experiments.

Lastly, I would like to express my gratefulness to my family, for their endless love and great care during my study. I hope they have a healthy and joyful life.

List of Publications

1. **GuochenBao**, ShihuiWen*, GungunLin, Jingli Yuan, Jun Lin, Ka-Leung Wong*, Jean-Claude G. Bünzli*, Dayong Jin*. Learning from lanthanide complexes: The development of dye-lanthanide nanoparticles and their biomedical applications. *Coordination Chemistry Reviews*, 2021, 429, 213642.
2. **Guochen Bao***. Lanthanide complexes for drug delivery and therapeutics. *Journal of Luminescence,* 2020, 228 , 117622
3. **Guochen Bao**, Dayong Jin*. Nanoparticles give mice infrared vision. *Nature Photonics* 2019, 13 (5), 304-305.
4. **Guochen Bao**, Zhenyu Liu, Yuxia Luo, Ka-Leung Wong*, Peter A Tanner*. Effects of europium spectral probe interchange in Ln-dyads with cyclen and phen moieties. *Dalton transactions* 2019, 48 (13), 4314-4323.
5. **Guochen Bao**, Ka-Leung Wong*, Peter A. Tanner*. A reversible rhodamine B based pH probe with large pseudo-Stokes Shift. *ChemPlusChem* 2019, 84 (7), 816-820.
6. **Guochen Bao**, Ka-Leung Wong*, Dayong Jin*, Peter A. Tanner*. A stoichiometric terbium-europium dyad molecular thermometer: energy transfer properties. *Light: Science & Applications* 2018, 7 (1), 96.
7. **Guochen Bao**, Shuai Zha, Zhenyu Liu, Yan-Ho Fung, Chi-Fai Chan, Hongguang Li, Pak-Ho Chu, Dayong Jin, Peter A. Tanner*, Ka-Leung Wong*. Reversible and sensitive Hg^{2+} detection by a cell-permeable ytterbium complex. *Inorganic chemistry* 2018, 57 (1), 120-128.
8. Yunfei Shang, **Guochen Bao**, Jiajia Zhou, Ka-Leung Wong, Chunhui Yang, Dayong Jin*. Lanthanide-doped upconversion luminescent materials for point of care diagnosis. *Journal of the Chinese Rare Earth Society* 2018, 26 (2), 129-146. (Co-first author)
9. Yuxia Luo, Zhenyu Liu, Sam Chun-Kit Hau, Yau Yuen Yeung, Ka-Leung Wong*, Kwok Keung Shiu, Xueyuan Chen, Haomiao Zhu, **Guochen Bao**, Peter A. Tanner*. Electronic spectra of $Cs_2NaYb(NO_2)_6$: is there quantum cutting? *The Journal of Physical Chemistry A* 2018, 122 (17), 4381-4388.
10. Hongguang Li, Rongfeng Lan, Chi-Fai Chan, **Guochen Bao**, Chen Xie, Pak-Ho Chu, William

C. S. Tai, Ka-Leung Wong*. A luminescent lanthanide approach towards direct visualization of primary cilia in living cells. *Chemical communications* 2017, 53 (52), 7084-7087.

TABLE OF CONTENTS

LIST OF ABBREVIATIONS

a.u.	arbitrary unit
$CDCl_3$	deuterated chloform
CD_3OD	deuterated methanol
d	doublet
DCM	dichloromethane
DCNP	downconversion nanoparticle
DET	Dexter energy transfer
DFT	density functional theory
DIPEA	N, N‟-diisopropylethylamine
DMSO	dimethylsulphoxide
DSNP	downshifting nanoparticle
EA	ethyl acetate
EtOH	ethanol
FRET	Förster resonance energy transfer
HOMO	highest occupied molecular orbital
HPLC	high performance liquid chromatography
Hz	hertz
ICG	indocyanine green
ISC	intersystem crossing
J	coupling constant
K	degree Kelvin
Ln	lanthanide
LOD	limit of detection
LUMO	lowest unoccupied molecular orbital
m	multiplet
M^+	molecular ion
MeCN	acetonitrile

MeOH	methanol
MOF	metal-organic framework
MS	mass spectroscopy
m/z	mass to charge ratio
MTT	3-(4,5-dimethyl-2-thiazolyl)-2,5-diphenyl -2-H-tetrazolium bromide
NIR	near infrared
NMR	nuclear magnetic resonance
ppm	parts per million
PDT	photodynamic therapy
PTT	photothermal therapy
r.t.	room temperature
s	singlet
t	triplet
TTA	triplet triplet annihilation
TEA	triethylamine
TFA	trifluoroacetic acid
THF	tetrahydrofuran
UCNP	upconversion nanoparticle
UV	ultraviolet
Vis	visible
δ	chemical shift (in ppm)
℃	degree Celsius
λ_{ex}	excitation wavelength (in nm)
λ_{em}	emission wavelength (in nm)

ABSTRACT

Significant progress has been made in recent years to produce a new generation of dye-lanthanide hybrid materials with physicochemical properties for various applications. The lanthanide complexes, where organic ligands are engineered to chelate individual lanthanide ions, are broadly used in analytical, biological, and clinical applications. However, the visible emission suffers from low penetration depth in biological tissues, the synthesis of hetero-dinuclear complexes remains challenging because lanthanide ions are chemically similar, and there is a lack of systems for comprehensive study of ligand-lanthanide energy transfer. To this end, the primary focus of my thesis is to develop near-infrared probes, hetero-dinuclear compounds and energy transfer platforms based on lanthanide complexes for energy transfer study and sensing applications (Chapter 2, 3, & 4). In Chapter 2, I design and synthesize an ytterbium complex-based sensor for the detection of Hg^{2+} ions. In Chapter 3, I report a pair of stoichiometric terbium-europium complexes as molecular thermometers and study their energy transfer properties. In Chapter 4, I investigate the spectral structure and intensity changes of a pair of dinuclear complexes.

Learning from lanthanide complexes, considerable progress has recently been made to exploit the hybrid structure of lanthanide-doped inorganic nanoparticles “coated” with organic dyes. This has resulted in hybrid materials that have many benefits, for example, large absorption cross-section, easy modification, tuneable spectral bands, long lifetimes, and large (anti)-Stokes shift. To improve the performance of upconversion process, near-infrared dyes with high quantum yields are required for efficient sensitisation of lanthanide nanoparticles, and diverse energy transfer systems are required for brighter upconversion emissions. Therefore, the parallel program of my thesis is to develop brighter dye-lanthanide nanoparticle upconversion systems, including dye-sensitised upconversion nanoparticles (Chapter 5) and ytterbium-mediated upconversion system (Chapter 6). In Chapter 5, I exploit a dye sensitised

upconversion nanoparticle with highly enhanced upconversion emission by developing a NIR dye (TPEO-IR783) with a quantum yield of 22.46% which is 3 times higher than that of reported UCNP sensitiser, IR806. In Chapter 6, I develop an ytterbium nanoparticle-mediated upconversion system and the design bypasses the specific requirement of traditional sensitisers in TTA system, providing a wide range of opportunities for deep light penetration applications.

Overall, this thesis has eight chapters, including the introduction of dye-lanthanide hybrid materials (Chapter 1), three lanthanide complex-based projects (Chapter 2, 3, & 4), two dye-lanthanide nanoparticle-based projects (Chapter 5 & 6), experimental details (Chapter 7) and conclusions and perspectives (Chapter 8).

Chapter 1 Introduction

1.1 Introduction of dye-lanthanide hybrid materials

Advances in the development of new-generation optical materials have brought great opportunities for emerging applications in bioimaging[1], display[2], anti-counterfeiting[3], data storage[4], lasing[5, 6], and life sciences[7, 8]. Among these materials, organic dyes[9, 10], transition metal complexes[11], lanthanide materials[12] and quantum dots (QDs)[13] have been the most explored. In particular, organic dyes have been widely utilised because of their ease for bio-conjugation, small size, and biocompatibility. They have large absorption cross-sections with broad absorption bands, making them as excellent photon harvesters. Apart from the downshifting emission process, lanthanide materials also have upconversion luminescence (anti-Stokes), which enables the conversion of lower-energy light in near-infrared (NIR) range into visible or ultraviolet light. They also possess unique advantages, including independent spectral positions, excellent photo-stability, sharp emission bands, and long luminescent lifetimes[14]. However, the Laporte forbidden 4f-4f transitions limit lanthanide materials to small absorption cross-section, which is more than three orders of magnitude smaller than that of organic dyes.[15] Therefore, high excitation power is typically required in order to populate the excited states of lanthanide materials.[16]

The bridging of organic dyes with lanthanide ions may bring the opportunity to improve the light harvest efficiency of lanthanide materials. For instance, the chelating of organic ligands creates asymmetry atmosphere to the lanthanide ions, which could improve the efficiency of 4f-4f forced electric dipole transitions. The organic ligands absorb energy and then transfer to lanthanide materials to increase

**A version of this chapter has been included in the published papers "Learning from lanthanide complexes: The development of dye-lanthanide nanoparticles and their biomedical applications. Coordination Chemistry Reviews, 2021, 429, 213642." "Lanthanide complexes for drug delivery and therapeutics. Journal of Luminescence, 2020, 228 , 117622".*

the emission intensity thereof. This is termed „antenna effect". Moreover, the combination of inorganic lanthanides and organic dyes could potentially enable the fine-tuning of absorption ranges and allow large separation between excitation and emission in spectral wavelengths.[17, 18] These benefits constantly drive the research in the design and characterisation of innovative dye-lanthanide materials with tailored properties and could potentially open up new avenues for a variety of applications.

This Chapter presents recent advances in dye-lanthanide hybrid materials as well as their biomedical applications (Figure 1.1). The energy level features and photophysical characteristics of organic dyes and lanthanides are firstly discussed. We then illustrate five types of hybrid materials, including lanthanide complex, dye-sensitised downshifting and downconversion nanoparticles (Dye-DSNPs and Dye-DCNPs), dye-sensitised upconversion nanoparticles (Dye-UCNPs), and nanoparticle-dye energy transfer system (UCNP-Dye). While illustrating their energy transfer processes, optical features, and widespread biomedical applications, we identify the challenges and prospective opportunities in material engineering for better performance of the hybrid system.

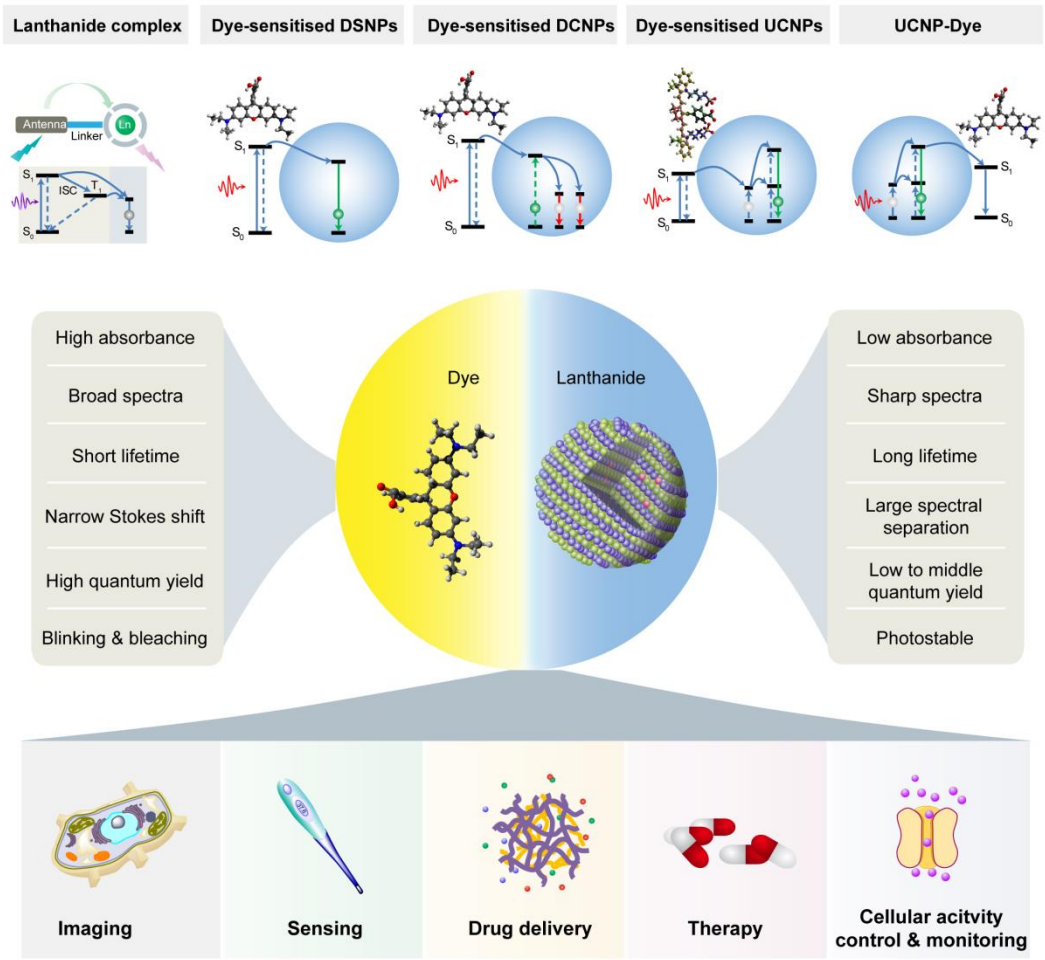

Figure 1.1. Illustration of dye-lanthanide hybrid materials and their biomedical applications. Five types of representative dye-lanthanide hybrid materials are displayed with their energy transfer diagrams, including lanthanide complex, Dye-DSNPs, Dye-DCNPs, Dye-UCNPs, and UCNP-Dye. The biomedical applications illustrated are imaging, sensing, drug delivery, therapy, and cellular activity control and monitoring.

1.2 Photophysical properties of organic dyes and lanthanide materials

1.2.1 Basis of energy levels of organic dyes

Organic dyes are a class of organic molecules which can absorb light and are usually perceived as being coloured as a result of receptors in human eyes. The absorption bands are generated when the electron transfers from a ground state to an excited state. An organic dye is capable to absorb light, which typically requires the dye molecules to possess a chromophore. The chromophore contains

a conjugated system whose structure consists of alternating multiple and single bonds.[19]

Molecular orbital

The chromophores‟ properties of light absorption and emission attribute to their π orbitals, which are formed with two adjacent p atomic orbitals (Figure 1.2a). In atomic orbital, the behaviour of an electron is described by a mathematical function. Each orbital can accommodate up to two electrons which can be identified by spin quantum numbers. The conjugated system of most organic dyes is constructed by constituent p orbitals. The two nearby p atomic orbitals overlap side by side, forming two new orbitals, namely, a bonding orbital π and an antibonding orbital π* (Figure 1.2a). These orbitals in conjugated systems ally together and build up the so-called „molecular orbitals‟ (MO). The highest occupied molecular orbital (HOMO) and the lowest unoccupied molecular orbital (LUMO) are two widely known molecular orbitals (Figure 1.2b).[20] The energy difference between HOMO and LUMO (HOMO-LUMO gap) is generally the lowest energy that the electronic excitation is possible in a molecule.

Singlet and triplet

Singlet and triplet states are well-known energy states of an organic dye. They are differentiated according to the spin states (s) of its electrons. Specifically, a dye is in its singlet state if 2S + 1 is equal to 1, here, the S is the vector sum of all the electron spins in its chromophore; it is in its triplet state if the value of 2S +1 is 3. The ground state is a singlet state. When a molecule with a singlet ground state is excited, either an excited singlet state or an excited triplet state forms. In excited singlet state, the spin of the excited electron is still paired with the ground state electron. In the triplet state, the spin the excited eletron is same with the ground state electron. The singlet state can transform to triplet state or vice versa. The process is known as intersystem crossing. Fluorescence and phosphorescence are used to describe the luminescence emitted from singlet and triplet states,

respectively. The emission from excited singlet to ground is called fluorescence. The singlet lifetime is typically in the nanosecond range.[21] Emission from a triplet state to the ground state is spin-forbidden. The triplet emission is called phosphorescence which has a longer lifetime, in the range extended from microsecond to second.[22-24] Ab initio calculations such as density functional theory (DFT) and Hartree–Fock (HF) methods can be used to obtain the enery levels.

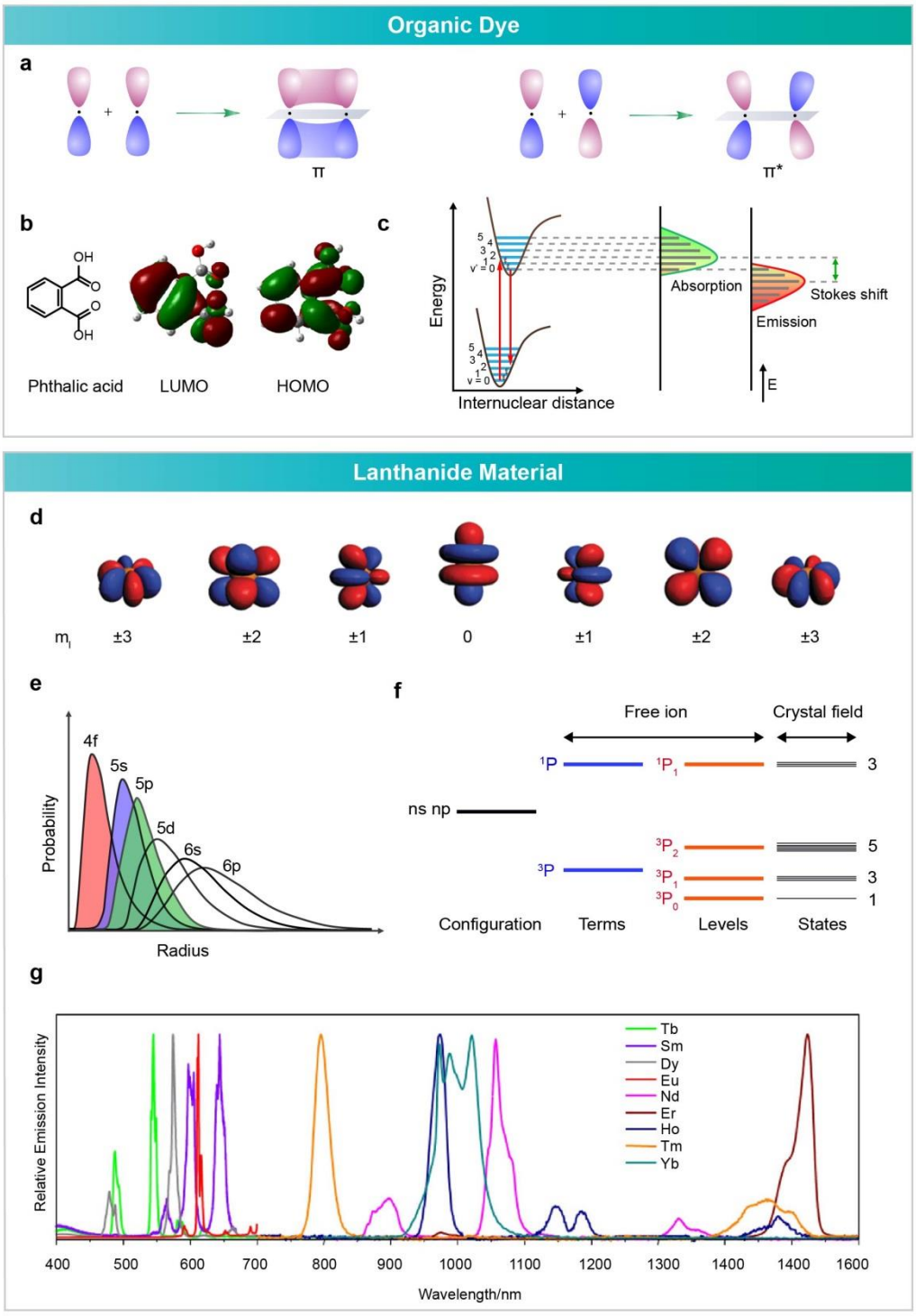

Figure 1.2. Energy level properties of organic dyes and lanthanide materials. (a) Two π molecular orbitals, including bonding orbital (π) and anti-bonding molecular (π) formed by two p orbitals via side-by-side interaction. (b) Structure of phthalic acid and its HOMO and LUMO orbitals. Adapted from Ref.* [25]*, Copyright (2015), with permission from Elsevier. (**c**) Schematic illustration of the broad absorption, emission spectra and Stokes shift of an organic dye. (d) Representation of 4f orbitals of the lanthanides. Adapted from Ref.* [26]*, Published by the PCCP Owner Societies. (e) Schematic illustration of the probability of 4f,*

5s, 5p, 5d, 6s and 6p orbitals as a function of the electron-nucleus distance. (f) Terminologies of energy levels of two-electron orbitals (ns np). (g) Typical emission spectra of lanthanide(III) complexes in solution. Reprinted from Ref.[27], Copyright (2017), with permission from Elsevier.

1.2.2 Basis of energy levels of lanthanide materials

Lanthanide materials and their electronic configurations

The lanthanide group consists of 15 metal elements with atomic numbers from 57 to 71. The lanthanide elements are typically shown at the bottom in the periodic table. The 15 lanthanide elements together with scandium and yttrium in group 3 in the periodic table are called the rare earth elements[28].

There are seven representations of lanthanide 4f orbitals (Figure 1.2d). The 4f orbitals from lanthanum to lutetium in the periodic table are gradually filled with electrons. The 4f orbitals influence the physical and chemical properties of lanthanides, making them different from other metallic elements. The lanthanide 4f orbitals are shielded by their 5s and 5p electrons in the outer orbitals. Therefore, the 4f orbitals are relatively isolated (Figure 1.2e), making them less likely to form covalent and less affected by the surrounding environment. As the seven 4f orbitals are partially filled, except for lanthanum and lutetium, the unpaired electrons render lanthanides with strong magnetic moments.

The configuration of lanthanides can be described as $[Xe]4f^x5d^y6s^2$. The lanthanide elements are generally on +3 oxidation state. In the Ln^{3+} ions, two 6s electrons and one 5d or 4f electron are lost, generating the configuration as $[Xe]4f^x$ (x = 0 – 14). There are some exceptions to the oxidation states. For instance, the Ce^{3+} ion could further lose one electron that results in a stable electronic configuration of $[Xe]4f^0$ as Ce^{4+}. Another example is europium, as Eu^{3+} can further obtain an electron, leading to a configuration of $[Xe]4f^7$ to form Eu^{2+} with a stable half-filled 4f orbital. In addition to Eu^{2+} and Ce^{4+}, Yb^{2+} and Tb^{4+} also exist. [29-31]

Basic terms of lanthanide energy levels

The lanthanide energy levels are described by several quantum numbers. They are principle quantum number (n), orbital angular momentum quantum number (l), magnetic quantum number (m_l), spin quantum number (s), spin magnetic quantum number (m_s) and total angular momentum quantum number (j). The principal quantum number depicts the atom‟s electron shells. The value of n can be ranging from 1 to the outermost shell‟s number. The subshell of orbitals is described by the orbital angular momentum quantum number, the value of l ranging from 0 to n-1, which is described by a letter including s, p, d, f, g, h, i, k, l, m, n, o, q, r, t, u, v, w, x, y for the values from 0 to 19. The magnetic quantum number (m_l) is used to depict the orientation of subshells in the space, the value of which ranges between −l to l (Figure 1.2d). The spin quantum number has a value of ½, while the spin magnetic quantum number describes the spin information of electrons, valued -½ or ½. In the lanthanide energy level terminology, the J-multiplet energy levels are described by an important parameter, the total angular momentum quantum number, with the value that equals to the vector addition of l and s. For the case of several electrons in the orbitals, the overall quantum numbers of the system can be deduced by vector addition of each value, for example, $\mathbf{S} = \Sigma\mathbf{s}$, $\mathbf{L} = \Sigma\mathbf{l}$. The term degeneracy can further depict the splitting of energy levels. For instance, J-multiplet degeneracy equals to $2\mathbf{J}+1$.

The energy levels of lanthanide 4f transitions can be written by $^{2S+1}L_J$, where the corresponding letter is used to represent the orbital angular momentum quantum number (L). Resulting from the degeneracy of spin quantum number, different terms are deduced from the orbital configuration. Taking the ns np two-electron system as an example (Figure 1.2f), the lanthanide energy level terminology is shown below. The orbital angular momentum L equals 1 because of s = 0, p = 1 and it is shown as P. There are two terms namely ^1P and ^3P and according to the values of 2S + 1 (it is 1 and 3). Each term divides into levels by the total angular momentum quantum numbers. The J values are the vector

addition of L and S. Therefore, the energy level of ^1P can be described as $^1P_1$. While for the case of ^3P, there are 3 J- multiplet, including 0, 1, 2. Thus, the levels of ^3P are depicted as $^3P_0$, $^3P_1$ and $^3P_2$, respectively. It should be noted that the $^{2S+1}L_J$ level usually contains multiple peaks in the emission spectra. This is because of the splitting of J levels via crystal-field interactions. Each J level has up to 2J +1 states. In all, each term contains as many as (2S + 1)(2L + 1) states[32] in the case of L ⩾ S, namely, nine states for ^3P level and three states for ^1P level.

1.2.3 Optical properties of organic dyes and lanthanide materials

Table 1.1. *Optical properties of organic molecules and inorganic lanthanide materials*

	Organic dye	Lanthanide
Absorption bandwidth	100 – 300 nm	< 100 nm
Emission bandwidth	100 – 300 nm	< 100 nm
Stokes‟ shift	Several tens nm	Very small
Molar absorption coefficient	10^3 to 10^5 M^{-1} cm^{-1}	<10 M^{-1} cm^{-1}
Quantum yield	High	Low to middle
Lifetime	ns	μs to ms
Photostability	Blinking & bleaching	Stable

Band characteristic and Stokes' shift

The optical properties of organic dyes and lanthanide materials are listed in Table 1.1. One of the most significant features of trivalent lanthanide ions is their fingerprint luminescence. The $[Xe]4f^n$ electronic configuration (n = 0–14, where n is the number of 4f electrons) of lanthanide ions generates numerous electronic levels, the number of which is given by 14!/n!(14 – n)!. For example, the total degeneracy of Eu^{3+} (which has six 4f electrons) is 3003.[32] The luminescence of trivalent lanthanide ions involves 4f-4f transitions except for Ce^{3+}.[33] The luminescence of Ce^{3+} involves 4f-5d transitions which is also the case for Ln^{2+} ions. Because of the shielding effect of 4f orbitals by $5s^2$ and $5p^6$ sub-shells, the energy levels of trivalent lanthanide are well confined, resulting in sharp emission bands with energies little dependent on the ion environment (Figure 1.2g).[27, 34]

Lanthanide ions have very small Stokes‟ shifts[35, 36] but when excited through the antenna effect, the resulting apparent Stokes‟ shifts become very large.

Organic dyes have broad absorption and emission bands (Figure 1.2c). The absorbed and emitted photons are mainly from the zero-phonon level, and vibrational progressions can often be observed on the absorption/emission bands due to the coupling of electronic wavefunctions with vibrational levels (vibronic transitions) (Figure 1.2c). As organic chromophores normally display relatively small Stokes‟ shifts (a few tens of nm), substantial overlap between absorption and emission bands is commonly observed.[37, 38]

Absorption efficiency, quantum yield and lifetime

Selection rules play an important role in lanthanide transitions. Because Laporte rules forbid the electric dipole 4f-4f transitions,[39] the molar absorptivity of 4f-4f transition has extremely low efficiency, usually <10 M^{-1} cm^{-1},[16] and low spontaneous emission probability. Thus, the lanthanide materials have long lifetimes, usually in the range of microsecond to the millisecond. On one hand, long luminescent lifetime increases the non-radiative process and reduces the quantum yield of lanthanide emission. On the other hand, a relatively long lifetime enables time-gated measurements, which uses a delay for luminescent signals from the irradiation pulse. By this technique, the unwanted fastly decayed emission and irradiation light can be removed from the long-lifetime luminescence. Therefore, this technique improves the signal-to-noise ratio. However, the lanthanides have small absorption cross section,[15] which hinders their further applications.[16]

The dye counterparts possess an absorption cross-section several orders of magnitude larger than those of lanthanides.[40] The organic dyes often have high quantum yields, for instance, rhodamine dye was reported having a quantum yield of 97%[41]. The fluorescence emission of organic dye is quite fast (several ns) after they are excited to the singlet excited states. On the other hand, the triplet emission of organic dye has a longer lifetime (μs to ms).[22-24] In most cases, the

triplets are not excited by direct photon absorption, but by intersystem crossing from excited singlet states. To improve the intersystem crossing, heavy atom effect is required by presenting heavy atoms such as Br, Cl, and transition metals.[42] The heavy atom effect for the promotion of intersystem is attributed to the increase of spin-oribit coupling because of the interaction between chromaphore and heavy atom perturber.[43]

Photostability

As discussed, organic dyes can populate its triplet states from the singlet states *via* intersystem crossing, and the molecules remain in excited states for a long period due to the long triplet lifetime. These excited states can stop further absorption of light, making the dyes photophysically dark. If the dark period recovers, this process is called blinking. If the dark period is unrecoverable due to the dye structure change in the light exciting process, the phenomenon is called bleaching.[44] The blinking of organic dyes is used in stochastic optical reconstruction microscopy super-resolution imaging.[45] On the other hand, the lanthanide emissions should also have an off-on pattern because of the long lifetimes. However, since the emission is from lanthanide ion, the structure cannot be destroyed in the light excitation process and the lanthanide emission is stable. For the nanoparticles doped with lanthanides, they have thousands of emitters in each nanoparticle and the off-on pattern is cancelled out. So they are not blinking and bleaching. The photostability makes lanthanide nanoparticles excellent for long-term biomedical applications.

1.2.3. Energy transfers mechanisms

The energy transfer processes in the lanthanide-dye hybrid materials include non-radiative (Förster, multipolar, or Dexter) and radiative mechanisms. All these mechanisms require overlap between the emission spectrum of the donor and the absorption spectrum of the acceptor. The non-radiative energy transfer is highly distance dependent.

The energy transfer in Förster (electric dipole-electric dipole, ed-ed) mechanism is through electrostatic interactions, in which the donor non-radiatively releases its excited state energy to the ground state and simultaneously the acceptor receives the energy and populates its excited state. The energy transfer rate (k_{ET}) for electric dipole-electric dipole energy transfer in Förster theory is inversely proportional to the sixth power of the distance between donor and acceptor:[46]

$$k_{ET} = \frac{\phi_D}{\tau_D}\frac{9(ln10)\kappa^2}{128\pi^5 N_A n^4}\frac{1}{R^6}J(\lambda) \quad (1-1)$$

where ϕ_D is the donor quantum yield in the absence of the acceptor; τ_D is the donor lifetime in the absence of the acceptor; κ^2 is the orientation factor of donor and acceptor with values between 0 to 4 and the average value of 2/3 for an isotropic medium; N_A is Avogadro‟ number (6.022. × 10^{23} mol^{-1}); n is the refractive index; R is the distance between donor and acceptor and $J(\lambda)$ is the spectral overlap integral given as:[46]

$$J(\lambda) = \int_0^{\infty} f_D(\lambda)\varepsilon_A(\lambda)\lambda^4 d\lambda \quad (1-2)$$

where λ is wavelength; $f_D(\lambda)$ is the shape function of the donor emission and $\varepsilon_A(\lambda)$ is the absorption coefficient of the acceptor.

The Förster distance (R_0) of energy transfer is the distance between donor and acceptor for which 50% energy of excited donor transferred to acceptor. At R_0, the energy transfer rate (k_{ET}) is equal to the donor decay rate in absence of acceptor (k_D). Since $k_D = 1/\tau_D$, thus $k_{ET} = 1/\tau_D$; R_0 is deduced from Eq. (1-1) as follows:

$$R_0^6 = \phi_D \frac{9(ln10)\kappa^2}{128\pi^5 N_A n^4}J(\lambda) \quad (1-3)$$

On the other hand, the Dexter (exchange, ex) mechanism features a double electron transfer during which an electron of the donor in the excited state is transferred to the acceptor, while simultaneously an electron of the acceptor in its ground state is transferred to the donor. This process requires donor-acceptor wavefunction overlap and a short D-A distance. The energy transfer rate by the

exchange mechanism depends as the inverse exponential of the D-A distance:[47]

$$k_{ET} = \frac{2\pi}{h} D \frac{1}{e^{2R/L}} \int_0^{\infty} f_D(\lambda)\varepsilon_A(\lambda)\lambda^4 d\lambda \quad (1-4)$$

where h is Planck constant; D is Dexter parameter, R is distance between donor and acceptor; L is sum of the Van der Waals radii of the donor and the acceptor. Along with the electron exchange process, spin function can be changed on both donor and acceptor simultaneously.[48]

Other mechanisms that are less discussed because more difficult to quantify are electric dipole - electric quadrupole (ed-eq) and electric quadrupole - electric quadrupole (eq-eq) mechanisms with distance dependences in R^{-8} and R^{-10}, respectively. In his seminal paper, Dexter estimates that the relative contributions of these mechanisms in a cubic inorganic matrix are ed-ed >> ed-eq ≈ ex >> eq-eq. However more recent models indicate that eq-eq mechanism can be quite effective up to R = 20 Å.[49]

In the radiative mechanism, photons emitted by the donor are absorbed directly by the acceptor. The absorption rate depends on R^{-2} instead of R^{-6}. The acceptor concentration, absorption coefficient, and length of light path determine the reabsorption efficiency by the acceptor.

The radiative and non-radiative mechanisms can be differentiated by the donor's lifetime change upon interaction with the acceptor. The donor lifetime in radiative reabsorption remains unchanged, while non-radiative pathways lead to reduced lifetime of the donor in presence of the acceptor. Experimentally, the non-radiative energy transfer efficiency (η_{ET}) can be simply determined from the donor's lifetimes in presence (τ_{DA}) and in absence (τ_D) of acceptor:

$$\eta_{ET} = 1 - \frac{\tau_{DA}}{\tau_D} \quad (1-5)$$

1.3 Dye-lanthanide hybrid materials

Lanthanide materials and organic dyes are different in photophysics. The combination of these two materials brings many advantageous properties, for

example, efficient light absorption, large stokes or anti-Stokes shifts, elongated lifetime, and good tuneability of excitation and emission ranges. These new optical features have made the dye-lanthanide hybrid materials attractive in various applications such as biological sensing,[50] thermometry,[51] imaging,[52, 53] drug delivery,[54] theranostics,[55] optogenetics[56] and solar cells[57]. Typical dye-lanthanide hybrid materials are lanthanide complex, Dye-DSNPs, Dye-DCNPs, Dye-UCNPs, and UCNP-Dye (Figure 1.1).

1.3.1 Lanthanide complex

A lanthanide complex typically has a lanthanide ion and a chromophore. The metal centre determines the emission property of a complex. The chromophore serves as a light harvester, which is more efficient than lanthanide ions. To coordinate the lanthanide ion, a chelator is usually needed to ensure efficient energy transfer between the chromophore and the lanthanide ion.

Lanthanide coordination chemistry

Although the lanthanide ions have almost no covalent properties, they form coordinative complexes with an organic ligand by electrostatic forces. In the complexes, lanthanide ions are hard Lewis acids and favour the coordination with hard bases in the order of O > N > S.[58] Because the lanthanide ions have almost the same size, the exchange of lanthanide ions has almost no effect on the coordinative structure of the complexes.

A lanthanide complex consists of a lanthanide ion that is coordinated by charged or neutral ligands which are attached by ion-dipole or ion-ion interactions. The ligands and lanthanide ion are bonded together by electrostatic forces, therefore, the coordination symmetry is determined by the ligands in the first coordination sphere. The inner coordination sphere has the molecules or ions that are directly connected to lanthanide ions, while the molecules or ions in other coordination sphere interact with the molecules or ions in the inner sphere. The steric effect of the molecules determines the coordination number by inter-ligand

repulsion in the first sphere. The coordination number of a lanthanide ion in lanthanide complexes are commonly 6, 8 or 9.[59] In a solvent medium, negatively charged ligands, especially oxygen ligands, can effectively attach to metal centre to form stable lanthanide complexes. If there are not enough atoms of in the inner coordination sphere, the anions or solvent molecules can bind to the lanthanide ions.[60, 61] The inner sphere makes more contribution to the symmetry properties of complexes than other spheres. The photophysical properties of lanthanide are influenced by the symmetry of complexes.

Though the change of lanthanide ions does not affect the coordination chemistry of the lanthanide complexes, the luminescent properties including emission wavelength, intensity, and lifetimes are influenced by the change of lanthanide ions. Eu^{3+}, Tb^{3+} and Yb^{3+} are the most commonly used lanthanide ions with red, green and near-IR emissions, respectively (Figure 1.3a).[60, 62, 63] While, Gd^{3+} and La^{3+} ions are always used to study the coordination atmosphere and the energy levels of the chromophore.[64, 65]

Antenna effect

As lanthanide ions have poor absorption, the brightness of lanthanide materials is low when excited *via* the forbidden 4f-4f transitions.[66] However, the brightness of lanthanide emission can be enhanced by an organic chromophore by transferring its absorbed energy to its nearby lanthanide ions. This process terms the antenna effect. The chromophore absorbs the energy and transfers to its triplet state ($S_1 \rightarrow T_1$) through the intersystem crossing. The triplet energy then is transferred from chromophore to the lanthanide ions ($T_1 \rightarrow Ln^{3+}$) (Figure 1.3b)[66]. When the chromophore triplet state and the lanthanide excited state are close, the energy transfer process can be more efficient. Also, an energy gap between the triplet and lanthanide is required to diminish the back energy transfer. For europium and terbium ions, the optimum gap is 2500 – 3500 cm^{-1}.[67] Apart from the dominant $S_1 \rightarrow T_1 \rightarrow Ln^{3+}$ energy transfer pathway, there are other forms of energy transfer

pathways in the lanthanide complex, such as direct singlet-lanthanide energy transfer[67, 68]. Many organic molecules are reported as chromophores for lanthanide complexes including phenanthroline[69], phenlyethynylpridine[70], azaxanthone[71], terypyridine[72], porphine[73], pyridinedicarboxylic acid[74] (Figure 1.3b). The chromophores not only harvest the light for the complexes, but they also determine the chemical and photophysical properties of the lanthanide complexes.

The chelator

To form stable complexes with lanthanides, the chromophores should have chelators or incorporate with chelating ligands to coordinate with metal ions (Figure 1.3c).[60, 69, 75-77] Chelating antennas can directly connect the chromophores to metal centres and shorten the donor-acceptor distance for more efficient energy transfer. The chelators in lanthanide complexes can help to break the symmetry[64] of lanthanide emitters. This induces the mix of the f and d-orbital and the 4f-4f transitions are somewhat allowed with the d-orbital trait. The chelators are designed with larger coordination numbers[75] or cage structure[76] to prevent lanthanide centre from quenching by the solvent coordination. Many organic ligands, for example, DOTAs,[60, 78, 79] β-diketones,[69] pyridines,[75, 80, 81] porphine,[73] and carboxylic acids,[77] are developed for lanthanide complexes with high luminescence and desired chemical and physical properties.

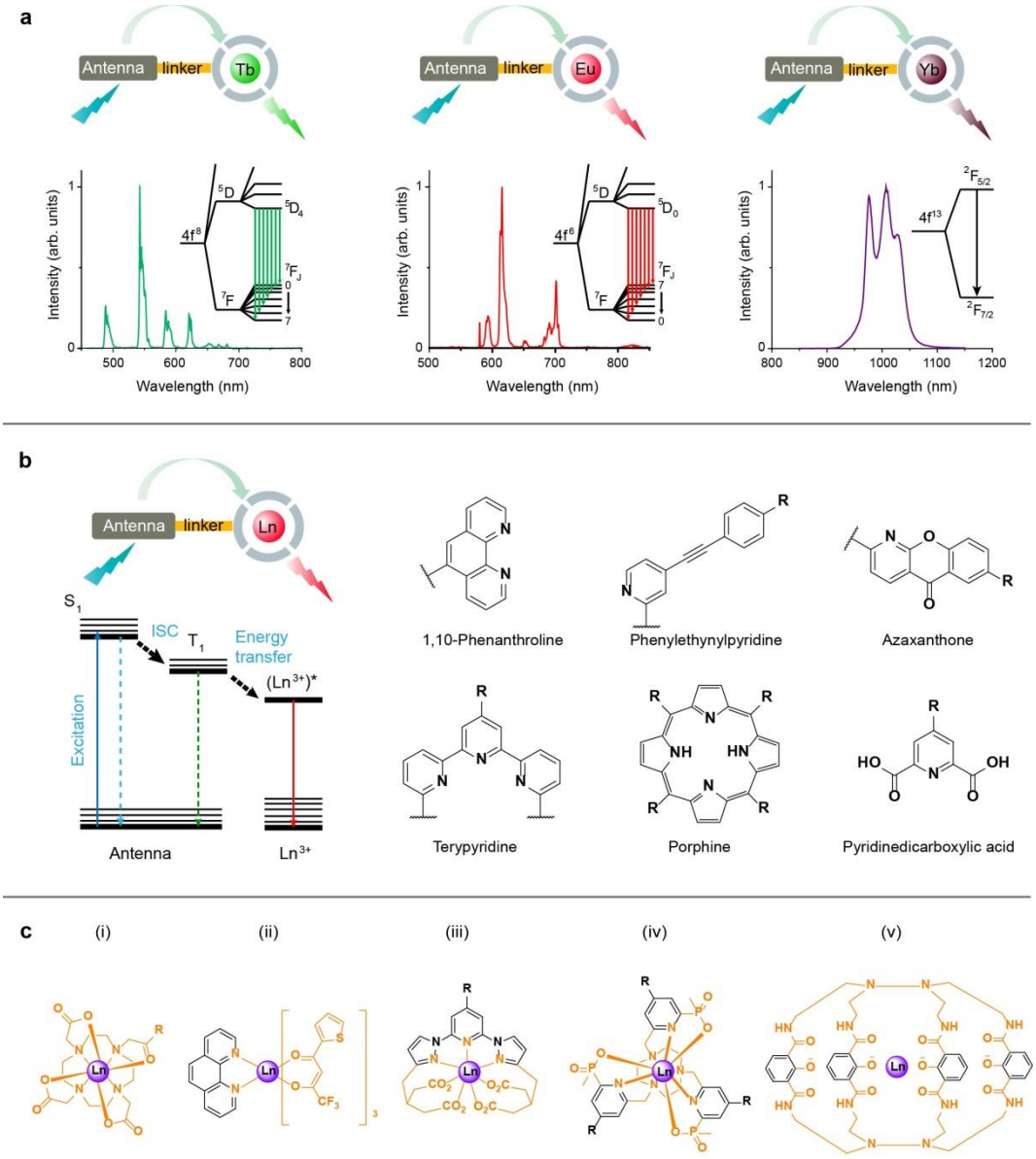

Figure 1.3. Metal centre, chromophore, and chelator of lanthanide complex. (a) Metal centres and typical luminescent spectra of Tb, Eu, Yb complexes. (b) Energy transfer diagram of antenna-lanthanide (Left) and example of the chromophores used in lanthanide complexes (Right)[69-74]*. (c) Typical chelators for lanthanide coordination, including cyclen (i) and chromophores themselves (ii-v) as chelating ligands.*[60, 69, 75-77]

1.3.2 Dye-sensitised downshifting and downconversion nanoparticles

Like lanthanide complexes, lanthanide downshifting nanoparticles (DSNPs) provides an energy shifts between excitation and emission. Doping lanthanide ions into inorganic nanocrystal hosts could protect them from energy deactivation by the solvents or chelating molecules. This protection leads to more efficient

energy utilisation. Moreover, different kinds of lanthanide ions could be co-doped in a nano-matrix to build highly efficient downconversion nanoparticles which can convert one higher energy photon into two or more photons.[82]

As discussed before, the absorption cross section is quite low for the 4f transition-based lanthanide materials. To address this challenge, the photosensitising by dyes is a highly useful strategy to enhance the absorption of lanthanide-doped nanocrystals. The antenna effect of DSNPs was firstly reported in 2007 by Zhang et al. They used tropolonate as sensitiser and coated them on the surface of Yb^{3+} or Nd^{3+} doped downshifting nanoparticles.[15] The resulting hybrid nanoparticles have similar bands in absorption spectra to the corresponding tropolonate lanthanide complexes. The excitation at 340 nm to chromophore in the hybrid nanoparticles generates characteristic Yb^{3+} or Nd^{3+} emissions. The lifetimes of hybrid nanoparticles are longer than those of the Nd^{3+} or Yb^{3+} complexes. This indicates that the tropolonate-caped DSNPs can reduce non-irradiative quenching. This strategy led to more than three orders of magnitude of emission intensity enhancement through the dye sensitisation of Ln^{3+} doped nanoparticles.[16] It should be noted that the formed dye-DSNPs contain multiple dye molecules on the nanoparticle surface, making them resistant from blinking and bleaching that happens in the single dye molecule.

For biomedical applications, deep tissue penetration is a critical requirement for using luminescent nanomaterials as in vivo probes. The optimal probes have both excitation and emission locating in biological windows (NIR region). To develop NIR probes, Prasad et al. utilised indocyanine green (ICG), a NIR dye, as an antenna to sensitise DSNPs with the emission at NIR-II region (Figure 1.4a,b).[83] In this research, active Nd shells were designed as a bridge for energy transfer from the ICG to Yb, Er, Ho, Tm, or Pr doped cores. By NIR irradiation to the ICG, NIR emissions ranging from 1000 to 1530 cm^{-1} were generated in the NIR-II windows. The luminescence signal could be detected within the tissue depth of 23 mm using the dye-DSNPs.

Recent advances of lanthanide-based hybrid materials brought dye-sensitised

lanthanide nanoparticle from the downshifting nanoparticles to down-conversion nanoparticles (DCNPs). Meijerink et al. have revealed the first dye-sensitised downconversion where the coumarin molecules were caped on the Pr^{3+}/Yb^{3+} co-doped $NaYF_4$ nanoparticles(Figure 1.4c-e).[17] Coumarin molecules attach to the surface of downconversion nanoparticles *via* the electrostatic attraction by its carboxylic group to lanthanide ions. The coumarin emission and Pr^{3+} excitation have good spectral overlap to ensure efficient energy transfer from the organic molecules to Pr^{3+} ions. The excited Pr^{3+} ions then convert its energy to the excited states of nearby Yb^{3+} ion, giving NIR downconverting emission. The hybrid materials showed a coumarin band in the excitation spectrum, (Figure 1.4d), which is direct evidence of the dye sensitisation. In the design, there was a 30 times enhancement of ytterbium emission by the coumarin-sensitisation.

In the design of Dye-DSNPs or Dye-DCNPs, the size of nanoparticles needs to be considered since the increase in the size of nanocrystals can reduce the environmental quenching effect but lead to a longer donor-acceptor distance for the energy transfer pairs. The energy transfer efficiency is largely dependent on the donor-acceptor distance for both Dexter-type and Förster-type mechanisms. It should be noted that the energy transfer in the dye-sensitised DSNPs or DCNPs has more than one dye donors and more than one lanthanide accepters. The competing effect, migration of energy, and concentration quenching should be taken into careful consideration when designing new highly efficient materials. Like lanthanide complexes, triplet states of the organic dye is important to match the energy level with the lanthanide excited states for efficient DET type energy transfer.[16]

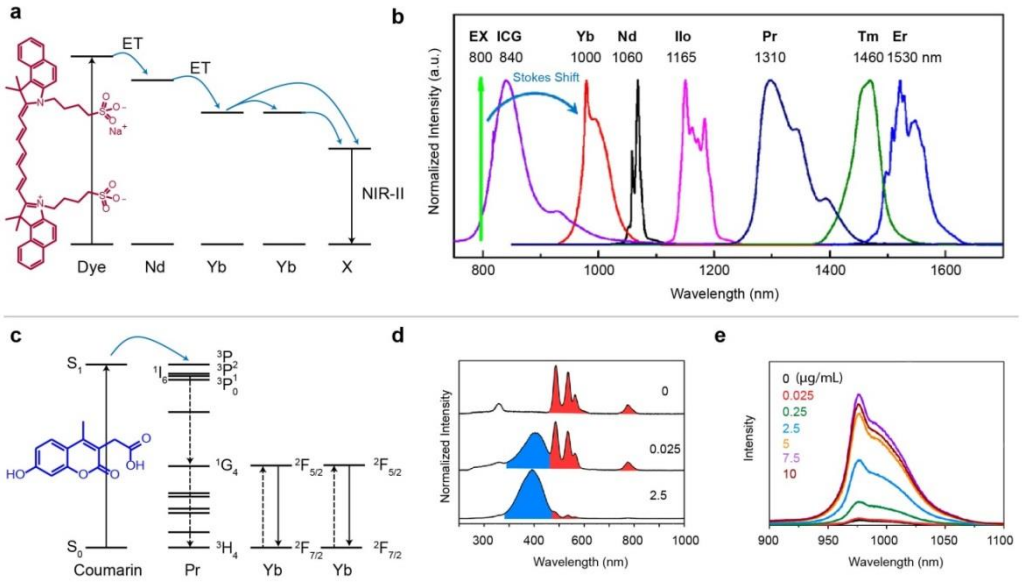

Figure 1.4. Dye-sensitised downshifting and downconversion nanoparticles. The energy transfer diagram (a) and NIR emission peaks (b) of ICG dyes and ICG sensitised downshifting nanoparticles with tuneable emissions in NIR-II biological window. Reprinted with permission from Ref. [83]*. Copyright (2016) American Chemical Society. (c-e) Coumarin sensitised lanthanide nanoparticles for quantum cutting. Energy transfer diagram (c), excitation spectra by monitoring* Yb^{3+} *emission with various coumarin concentrations (d) and* Yb^{3+} *Emission spectra with different concentration of coumarin (e). Figures (d) and (e) are adapted with permission from Ref.* [17]*. https://pubs.acs.org/doi/abs/10.1021/acs.jpclett.8b00516 Further permissions related to the material excerpted should be directed to the ACS.*

1.3.3 Dye-sensitised upconversion nanoparticles

Lanthanide upconversion nanoparticles are capable of covert the low energy photons into high energy photons. The anti-Stokes shift of the emission wavelength and the excitation wavelength of UCNPs is potential in background-free imaging and sensing applications. Sensitisers and activators are doped in the host materials in typical UCNPs. $NaGdF_4$ and $NaYF_4$ are common host nanocrystals. Yb ions or Nd ions are used as sensitisers, they have absorption in 980 nm and 808 nm, respectively. Er ions, Tm ions, or Ho ions are usually chosen as acceptor. When exciting the particles, the sensitisers harvest NIR light and transfer to acceptors, gradually populate the ladder-like energy levels in the acceptors to produce upconverting emissions.[84-87] By choosing the acceptor ions,

the upconversion emission ranges are tunable from UV to NIR light.[88, 89] The absorptions of UCNPs are usually weak and narrow because of the forbidden feature of 4f-4f transitions. Like lanthanide complexes, an organic antenna can be used to increase the absorption capacity of UCNPs. In 2012, Hummelen et al.[90] reported the first dye-sensitised UCNPs. In their report, the NIR dye IR808 was used to sensitise the Yb, Er-doped UCNPs. As a result of enhanced absorption by the NIR dye, the upconversion emission increases 3,300 times (Figure 1.5a). The enhancement is achieved by harvesting the energy firstly by NIR dyes, which can be funnelled to Yb^{3+} to activate the higher energy levels of the emitters via a multi-photon process.

Since there was an overlap of dye emission and Yb absorption, the energy transfer pathway was first proposed as FRET from IR806 singlet to Yb^{3+} ions.[90] But the spectral overlap is insufficient, while the energy transfer efficiency was determined to be as high as 50%.[90] This indicates that there should be other energy transfer pathways from IR806 to the lanthanide upconversion nanoparticles. Recently, Garfield et al. revealed that IR-806 triplet emission has an excellent overlap with the Yb^{3+} ion absorption spectrum in UCNPs (Figure 1.5b). The energy absorbed by IR806 can transfer to Yb^{3+} ions through triplet, which is similar to lanthanide complexes.[91] When doping Gd^{3+} in UCNPs, the upconversion emission increased 30 times. This is because the Gd^{3+} is heavier than the Y^{3+} ions in the host.[91] The heavier Gd^{3+} ions provide a heavy atom effect to populate the triplet of IR806 *via* intersystem crossing and transfer more energy from singlet to triplet. The triplet population of IR806 was examined by monitoring the singlet lifetime. The doping of Gd^{3+} in UCNPs reduced the singlet lifetime of the IR806 on the UCNP surface, indicating the enhanced energy transfer from dye singlet to dye triplet.[91]

To decrease to mismatch of between the singlet emission and Yb absorption, the core@active-shell structures were developed for improving the brightness of Dye-sensitised UCNPs (Figure 1.5c).[56, 92] Nd^{3+} and Yb^{3+} are common energy transporters. They are doped in the shells and to accept energy from dye and

transfer it to the upconverting core.[93, 94] In this system, Nd^{3+} and Yb^{3+} in the active shells absorb the light at 800 nm and 980 nm, respectively, which guarantees the broad energy harvest from NIR dyes. Also, the surface quenching could be suppressed by the active shells without emitters. This strategy of doping Nd^{3+} and Yb^{3+} at active shells provided high energy transfer efficiency (up to 98%) from NIR dye to upconversion nanoparticles.[18]

The absorption wavelength range of Dye-UCNPs could be further expanded by a combination of different kinds of NIR dyes (Figure 1.5d). In a typical example, Han et al. co-caped the IR783 and IR845 to the $NaYF_4$:20% Yb^{3+},2% Er^{3+} and formed the Dye-UCNPs with broad absorption wavelength from 730 nm to 890 nm[95]. Typical NIR dyes utilised for the sensitisation of UCNPs are summarized in Table 1.2, with the emission lying in the range suited for effective energy transfer to UCNPs. The lowest emission energy was revealed by IR1061, a NIR-II dye,[96] and it has emission in the same range of the Yb^{3+} absorption. This allows the energy transfer from IR1061 singlet to Yb^{3+} ions in UCNPs. Also, for the case to Tm^{3+} doped UCNPs, an upconverted emission locates at around 800 nm. The NIR-II dye can avoid the reabsorption of the Tm^{3+} emissions. Therefore, the IR1061 sensitised UCNPs doped with Tm^{3+} can have both the excitation and emission in the biological windows. In addition to the NIR ranges, the dye for sensitisation of UCNP and also be extended to the visible window via multi-dye strategy. The dyes in visible range have a large energy gap between the dye emission and Yb absorption. The gap can be bridged by an intermediate dye to cascade the transfer to UCNPs (Figure 1.5e). For instance, BODIPY-FL, Cy3.5, and IR806 were caped on the surface of UCNPs, allowing sequential inter-ligand energy transfers to the UCNPs. This strategy extends the absorption range of dye-sensitised UCNPs to the blue, green, and red ranges.[97]

The energy transfer from the dye sensitiser to UCNPs is complicated and multiple pathways contribute to the overall energy transfer process. For instance, the energy transfers not only from dyes to Yb^{3+} sensitisers but also to emitters.[98] When NIR irradiation of the dye, a fast population of Er^{3+} was observed,

indicating the direct energy transfer to Er^{3+} ions.[98] Because of the triplet energy levels of the cyanine dyes such as IR806 match well with Yb^{3+} energy level (Figure 1.5b) and the Yb^{3+} excited states have a long lifetime, the energy can also transfer from Yb^{3+} to dye triplet.[99] When more dye molecules are capped on the nanoparticle surface, there is more back energy transfer from nanoparticles to dyes. This was confirmed by a lifetime study where the increased dyes reduced the lifetimes of UCNPs. Since back energy transfer results in the quenching of dye-sensitised UCNPs, it should be diminished to improve the brightness of UCNPs. One possible strategy is to tune the triplet energy levels and allows a suitable separation between the dye triplet and Yb^{3+} energy level. An optimum energy gap between dye triplet and Yb absorption can allow efficient energy transfer from the dye to upconversion nanoparticles and effectively suppress the back energy transfer at a maximum.

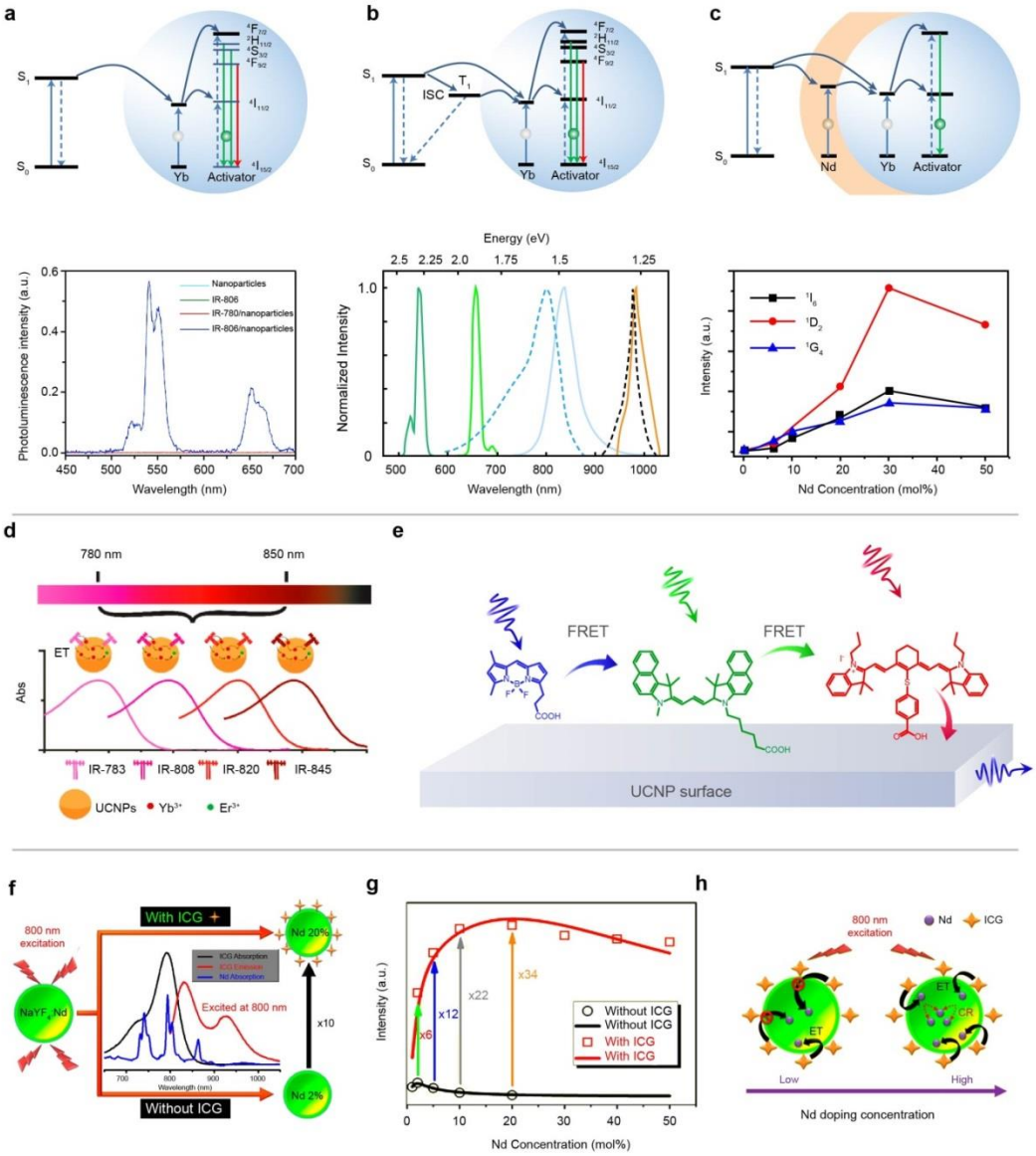

Figure 1.5. Dye-sensitised UCNPs. (a) Schematic illustration of dye-sensitised upconversion nanoparticles and energy transfer diagram from singlet states of dye to UCNPs (top), and the emission spectra of IR-806 sensitised Er^{3+} doped UCNPs, UCNPs with IR780, IR806 only, and UCNPs only (bottom). Reproduced by permission from Ref. [90]. Copyright 2012 Springer Nature. (b) Schematic illustration of the energy transfer from the dye to UCNPs via triplet states by intersystem crossing (top), and the spectra of dye-sensitised upconversion nanoparticles including the Er^{3+} emission (green and red curves), IR806 absorption (dashed blue curve), IR806 fluorescence (solid, light blue curve), UCNP absorption (dashed purple curve) and IR806 phosphorescence (yellow curve)(bottom). Reproduced by permission from Ref.[91] Copyright 2018 Springer Nature. (c) Schematic illustration of multidimensional energy transfer pathways of dye-sensitised core@active-shells upconversion nanoparticles (top), and the upconversion luminescence intensities from the $^1I_6$, $^1D_2$, and $^1G_4$ states as a function of the Nd^{3+} concentration in $NaYbF_4$:5%Tm^{3+}@$NaYF_4$:x%Nd^{3+} UCNPs

(bottom). Reprinted with permission.[93] Copyright 2015 American Chemical Society. (d) Schematic illustration of UCNPs with tunable excitation by different dyes. Republished with permission of the Royal Society of Chemistry, from Ref. [95]; permission conveyed through Copyright Clearance Center, Inc. (e) Schematic illustration of three-dye-sensitised upconversion nanoparticles. (f) Illustration of Nd optimal doping concentration with and without ICG, including the Nd absorption, ICG absorption and emission. (g) Integrated upconversion luminescence intensities with and without ICG as a function of Nd doping concentrations. (h) Illustration of the energy transfer mechanism from the dye to Nd-doped UCNPs, including the low and high concentrations. (f), (g) and (h) is adapted with permission.[100] Copyright 2016 American Chemical Society.

Table 1.2. *NIR dyes for the sensitisation of UCNPs.*

Structure	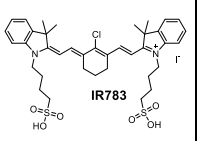	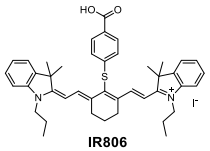	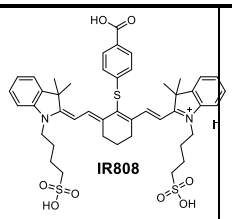	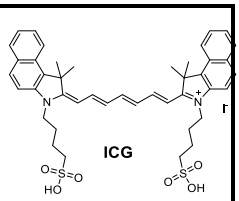
Emission range (nm)	750-1100[92, 95]	750-1000[56, 90, 91]	750-1100[93, 95, 101]	760-1060[18, 55, 100]
Structure	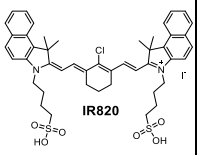	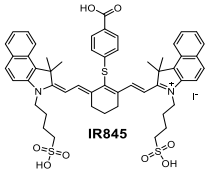	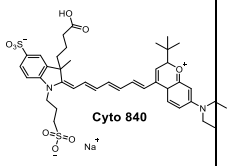	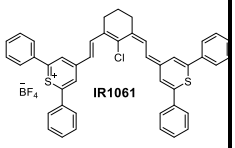
Emission range (nm)	760-1150[95]	770-1150[95]	800-1100[102]	900-1250[96]

The combination of UCNPs not only enhances the upconverted emission, but it could also overcome the concentration quenching of the UCNPs.[55, 100] The constraint of concentration quenching in lanthanide-doped UCNPs has been known for years, which limits the amount of the dopants and the brightness of UCNPs. Using NIR dye sensitisation, the optimal Nd^{3+} concentration in the Nd^{3+} doped $NaYF_4$ upconversion nanoparticles was increased from 2 to 20 mol%[100] (Figure 1.5f-h), with about ten times of enhancement of upconverted emission. For ICG sensitised UCNPs, the nanoparticles doped with 20 mol% Er^{3+} has shown around 32 times brighter than 2 mol% Er^{3+}-doped UCNPs.[55] However, these UCNPs reported for overcoming concentration quenching are limited to the

single doped UCNPs, whose upconversion efficiency is much lower than the sensitiser-emitter co-doped system.[55, 100] Since high power can overcome concentration quenching,[103] the dye on the UCNP surface can increase the light absorption and lower the power for overcoming concentration quenching of co-doped UCNPs.

1.3.4 UCNP-Dye system

UCNPs show great promise as the donor to transfer energy to surface dyes due to their advantageous optical properties including high optical stability, large anti-Stokes shift, multiple and narrow spectral bands. Therefore, UCNP-Dye donor-acceptor systems are frequently employed to study the energy transfer process in a hybrid material system. Both radiative and non-radiative pathways are vital for UCNPs-to-dye energy transfer. If the donor-acceptor distance is close enough, the non-radiative pathway is more efficient. Within the Förster distance, the energy transfer from donor to acceptor is with more than 50% efficiency. The non-radiative pathway is non-efficient at a longer distance and radiative reabsorption is a more important pathway since dye molecules possess large absorption cross-section. The non-radiative and radiative energy transfers together quench the UCNPs‟ emission. The two energy transfer pathways can be differentiated by donor lifetime measurement. The non-radiative pathway leads to a decreased lifetime of the donor which is independent in the radiative pathway.[104]

Since the FRET processes are sensitive to the distance of donor-acceptor pairs, the radius of UCNPs has a significant effect on the energy transfer efficiency (Figure 1.6a). UCNPs with large size have inefficient energy transfer from the emitters in the core to the surface dyes. Small-sized UCNPs have the short distance of donor-acceptor pairs for efficient energy transfer, while the larger surface-to-volume ratio leads to the surface deactivation[105]. To overcome these challenges, structure designs of UCNPs have been studied. For example, a core@shell structure with Yb sensitiser ions in core and Er^{3+} or Tm^{3+} emitter ions in the shell was designed. This core@shell structure shortens the average

donor-acceptor distance (Figure 1.6b). This strategy generated a significant enhancement of rhodamine emission in UCNP-rhodamine system in comparison with the conventional UCNP structures (Figure 1.6b).[105] In another example, an active shell is doped in the middle of the sandwich structure. This design diminishes the surface deactivation of emitters by the outer inert shell and reduces the average distance from the emitter to the dye (Figure 1.6c). The inert core with long-distance from surface dye does not participate in energy harvesting. The efficient energy transfer in the sandwich structure also enables efficient quenching of the donor's emission,[106] offering excellent sensitivity for sensing applications. In addition to the sandwich structure to shorten the average distance, the energy migrator was designed to drain the energy in the core to the nanoparticle surface. For example, The Gd^{3+} was used as energy migrator to overcome the spatial separation of emitters and dyes on the surface in the large UCNP-Dye system. (Figure 1.6d).[107] By doping Gd^{3+} ions in the host, energy harvested in the inner core can migrate to the surface and largely enhances the emission intensity of acceptor dyes.

UCNPs have multiple emission colours, which allows building single excitation-duplexed energy transfer system by capping different types of dye acceptors. This advantage allows simultaneous multiplexing by the same excitation wavelength.[108] In particular, higher information-carrying capacity could be achieved by the combination of dyes with core@shell UCNPs doped with multiple lanthanide emitters in each layer[109]. To further extend the capacity, a NIR dye can be used as a sensitiser to form the dye-UCNPs-dye system (Figure 1.6e,f).[102] One interesting thing in the UCNP-Dye system is when loading more dye acceptors to the system, the upconversion emission peak can be the quenched. These properties enable the dyes as excellent nano filters to the UCNPs and single emission UCNPs can be developed by cutting out the undesired peaks by capping high loading dyes on the surface of UCNPs.[110]

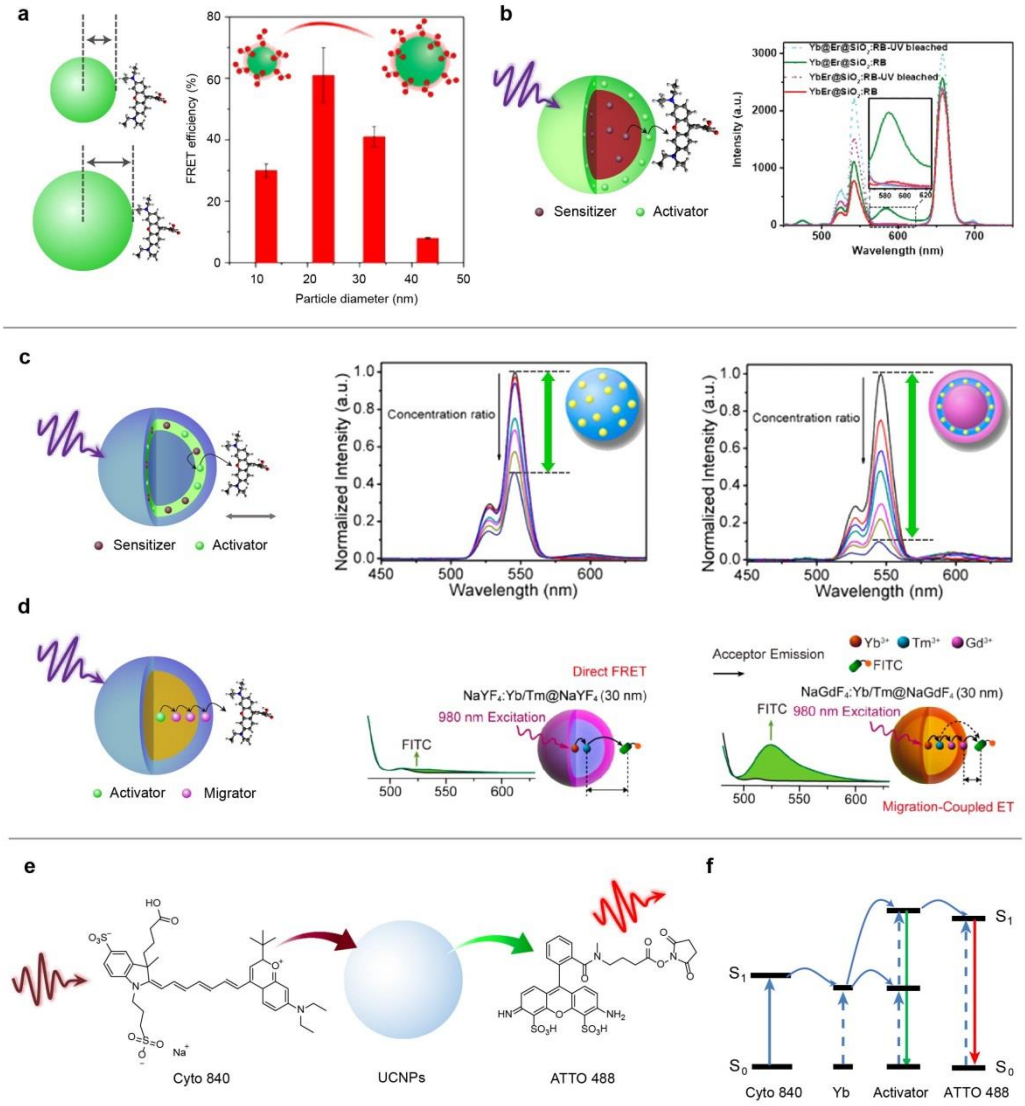

Figure 1.6. UCNP-Dye energy transfer system. (a) Schematic illustration showing the size of UCNPs results in different energy transfer distance from UCNPs to dye (left) and FRET efficiency of dye-capped upconversion nanoparticles as a function of particle size (right). Reprinted with permission.[104] *Copyright 2017 American Chemical Society. (b) Schematic illustration of sensitiser-core@active-shell structure (left), and the emission spectra of RB-coated UCNP@SiO_2 nanospheres with unbleached RB and UV-bleached RB excited at 980 nm. Republished with permission of Royal Society of Chemistry, from Ref.* [105]*; permission conveyed through Copyright Clearance Center, Inc. (c) Sandwich structure of inert-core@active-shell@inert-shell, and the emission spectra of UCNPs with a varying concentration ratio of dye and UCNPs. Reprinted with permission.*[106] *Copyright 2015 American Chemical Society. (d) Schematic illustration of energy migration by Gd^{3+} bridged energy transfer in large nanoparticle (left), and the emission with (dark green curve) and without (black curve) the dye (FITC) conjugated to the UCNPs (middle, $NaYF_4$ as host; right; $NaGdF_4$ as host). Reprinted with permission.*[107] *Copyright 2016 American*

Chemical Society. (e) Simultaneous excitation and emission sensitisation of upconversion nanoparticles by Cyto 840 and ATTO 488. (f) Energy transfer diagram showing that the energy harvested by Cyto 840 transfers to UCNPs and then to ATTO 488.

As a result of the long lifetime of UCNPs, the excited states of lanthanide ions are easily quenched by surface quencher and defects.[111] Organic dyes have several orders of magnitude faster luminescent decay than lanthanide emitters. The quantum yield can be enhanced by transferring the energy to organic dyes in the UCNP-Dye materials. For instance, in a UCNPs caped with ATTO 542 as dye acceptor, there is a ten-fold enhancement of overall upconverted emission for the 10.9 nm UCNPs.[111] In addition to luminescence enhancement, UCNP-Dye system also provides an easy way to tune the upconversion emission wavelength.[104, 111] Also, a delayed fluorescence of dye acceptors is expected[50] and the lifetime can be easily tuned by adjusting non-radiative energy transfer and quenching through changing the concentrations of donors and acceptors. However, in UCNP-dye system, the surface quenching and solvent deactivation quench the emission intensity as the energy in the UCNPs transfers to surface dyes. Therefore, it is challenging to obtain a huge quantum yield enhancement.

1.4 Applications of dye-lanthanide hybrid materials

Compared with the conventional biological tags such as organic dyes and quantum dots, dye-lanthanide hybrid nanomaterials have many advantages, including large Stokes or anti-Stokes shifts which separate the emission and excitation bands, long luminescent lifetimes for time-gated background-free bio-detections, and working in the NIR region (optical transparency window) for deep tissue applications. This makes them excellent candidates for biomedical applications. There are a large library of organic dyes and the dyes are easy to be modified. It is easy to build responsive dye-lanthanide hybrid materials with desired optical properties for sensing and diagnostic applications. The drug molecules can be loaded in the nanoparticle composite or attached on the

lanthanide complexes. This makes the hybrid materials excellent as drug carriers. Besides, many dye-lanthanide hybrid materials can be used as therapeutic agents themselves in chemotherapy, photothermal therapy (PTT) and photodynamic therapy (PDT). Also, the anti-Stokes properties make the upconverting materials useful tools for remote NIR control and monitoring cellular activities. Here we discuss the recent advances of dye-lanthanide hybrid materials for biomedical applications including bio-imaging, bio-sensing, drug delivery, therapy and cell activity controlling and monitoring.

1.4.1 Imaging

Bioimaging allows visualising biological phenomena and events and becomes a useful tool for exploring the biological process and disease diagnosis. Dye-lanthanide hybrid materials with good biocompatibility are excellent optical imaging probes and frequently used in the biomedical field. For example, lanthanide complexes are small and easy to modify to form the multifunctional probes. Lanthanide-doped nanoparticles could be surface modified with silica shell[112], organic dyes[113], or polymers[56] to render them desired multifunction. For instance, by intraperitoneal or intravenously administrating to nude mice, polyethyleneimine-capped nanoparticles exhibit quick redistribution to the liver and gastrointestinal system for *in vivo* organ imaging.[50]

For *in vivo* bioimaging, the tissue absorption and scattering largely limited light penetration depth in biological samples (Figure 1.7a,b).[114, 115] The scattering coefficient obeys a proportional relation to $(1/\lambda)^{w}$, where the exponent (w) varies for different tissues.[116, 117] Therefore, the ultraviolet and visible ranges suffer severe penetration problem. The suitable range of light for deep tissue applications lies in 650 – 1800 nm.[118, 119] This optical biological transparent window is divided into NIR-I (700 – 950 nm), NIR-II (1000 – 1350 nm) and NIR-III (1550 – 1870 nm) by the absorption of water existed in biosamples.[120] The water molecule contains one oxygen and two hydrogen atoms. The absorption properties of water molecule mainly come from three kinds of the vibration modes,

including symmetric stretch ($v_{s(s)}$), asymmetric stretch ($v_{s(as)}$) and bend (v_b) (Figure 1.7a). The water absorption at 980 nm between NIR-I and NIR-II is due to triple stretch vibrations ($3v_s$); the peak at 1470 nm is produced by two stretch vibrations ($2v_s$); while the intense absorption at 1900 nm is corresponding to one stretch and one bend vibrations ($v_s + v_b$) (Figure 1.7b).[121-123]

Many efforts have been devoted to developing NIR imaging nanoprobes for improved bioimaging in deep tissue. Ytterbium complexes are promising candidates as NIR imaging probes with the emission centred at 980 nm.[63, 124, 125] As shown in Figure 1.7c,d, a typical porphyrin-ytterbium complex Yb-3 was utilized for visualizing Hela cells by its NIR emission.[124] The NIR channel showed good colocalization with visible lysosome tracker (LysoTracker Green). Taking advantage of large absorption of chromophores, the excitation power for NIR imaging was as low as 4 μW cm^{-2}. Though Soret band (at around 408 nm) still lays in the low penetration range, the Q bands of porphyrin (red) allow relatively deep penetration capacity. Further efforts are still on demand to develop lanthanide complexes with both excitation and emission in NIR biological windows. An alternative strategy to shift the absorption to NIR range is the two-photon technique.[126] For instance, 860 nm two-photon excitation of porphyrin-ytterbium was demonstrated for mitochondria imaging.[63] It should be noted that the NIR dye-sensitised UCNPs and DSNPs, as well as UCNP-dye, typically possess NIR excitations, which could be good candidates for deep tissue imaging. For example, a water-dispersible Cy7-sensitised upconversion nanocomposite (CS: Nd-Cy7@PC) was demonstrated for lymphatic imaging with 808 nm excitation (Figure 1.7e,f).[92] Possessing both NIR excitation and emission, Cy7-sensitised $NaYbF_4$@$NaYF_4$: Nd DSNPs were successfully used for blood vessel imaging and imaging-guided peritumoral lymph node dissection.[52]

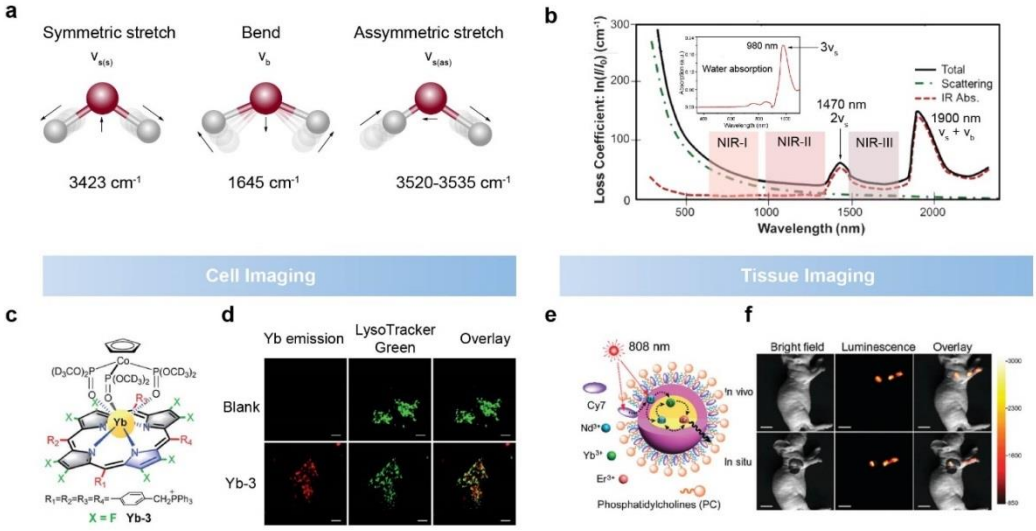

*Figure 1.7. The bioimaging applications of dye-lanthanide hybrid materials. (a) Vibration modes of a water molecule. (b) The loss coefficient of the human skin at a different wavelength and the marked biological windows for deep tissue imaging. Republished with permission of the Royal Society of Chemistry, from Ref. [120]; permission conveyed through Copyright Clearance Center, Inc. Inset: absorption spectrum of water peaked at 980 nm. Republished with permission of the Royal Society of Chemistry, from Ref. [123]; permission conveyed through Copyright Clearance Center, Inc. (c) Structure of complex **Yb-3**. (d) Confocal images of the Hela cells cultured with complex **Yb-3** and LysoTracker Green at different channels. (c) and (d) are adapted from Ref. [124] Published by The Royal Society of Chemistry. (e) Structure illustration of Cy7-sensitised UCNPs. (f) Upconverting images of Cy7-sensitised core@shell UCNPs by NIR excitation. (e) and (f) is republished with permission of the Royal Society of Chemistry, from Ref. [92]; permission conveyed through Copyright Clearance Center, Inc.*

The autofluorescence of tissues increases the background noise and reduces the image contrast, which limits the sensitivity of bioimaging. Lanthanide materials have emission lifetime in the microsecond to millisecond range, while the emission lifetimes of biological fluorophores are merely several nanoseconds. Therefore, the long lifetime of dye-lanthanide hybrid materials allows time-gated optical microscopy to get background free images, which significantly increase the detection sensitivity (Figure 1.8a).[127, 128] For example, with BHHCT-europium complex stained on the Giardia lamblia cyst, a background-free image can be obtained by time-gated imaging strategy (Figure 1.8b).[127] However, the millisecond excited lifetime of lanthanide materials causes low photon flux and

reduce the luminescence intensity. In this regard, the tunning of the fluorescence lifetime can be employed to improve the fluorescence intensity of lanthanide probes. It can be achieved by introducing acceptor dyes *via* luminescence resonance energy transfer (LRET) to increase the decay rate. LRET is an alternative to FRET where the donor is a luminophore instead of a fluorophore and the acceptor is still a fluorophore.[129] For example, by incorporating an LRET acceptor, the lifetime of complex Eu^{3+}/ATBTA greatly decreased, resulting in a huge increase of photon flux (Figure 1.8c-e). This strategy can increase the time-gated signal intensity by 170 folds, and the signal-to-noise ratios finally enhanced by 75 times in comparison with conventional time-gated imaging.[130]

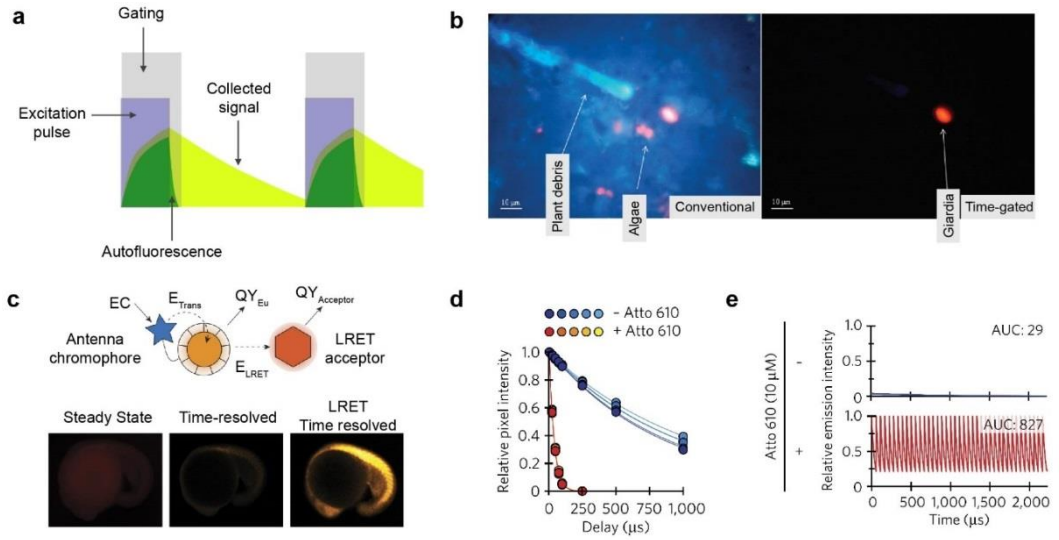

Figure 1.8. The ultrasensitive imaging enabled by time-resolved technique. (a) Schematic illustration of the principle of time-gated technique. (b) Conventional (left) and time-gated (right) images of the Giardia lamblia cyst labelled with BHHCT-europium complex. Adapted with permission.[127] Copyright 2011 American Chemical Society. (c) The energy cascades of Eu complex and its luminescence resonance energy transfer (LRET) emissions (top), and the zebrafish embryos images labelled with Eu^{3+}/DTBTA complex through steady-state, time-gated, and LRET time-gated methods (bottom). (d) Average intensities of time-resolved images of Eu^{3+}/ATBTA-functionalized beads in the presence and absence of LRET acceptor Atto 610, imaging mode includes conventional and LRET-enhanced time-resolved imaging. (e) Relative emission intensity in an identical time range with individual cycles including a 1-µs excitation pulse, 1-µs delay, and either a 2,000-µs (− Atto 610) or 50-µs (+ Atto 610) acquisition period. (c), (d) and (e) are adapted by permission from Ref.[130] Copyright 2018 Springer Nature.

Target-specific imaging allows scientists to visualise and distinguish precise locations of biological samples. For instance, a europium complex **HGEu001** (Figure 1.9a) was reported to exhibit specificity to primary cilia, and direct visualisation was achieved upon ultraviolet (one-photon) and NIR excitation (two-photon) (Figure 1.9b).[70] It is interesting to note that the chirality of a probe affects the sub-cellular uptake process. A europium complex EuL^2 was reported to selectively localise in the mitochondrial by its L-enantiomer and predominantly in the lysosomal region by its D-enantiomer (Figure 1.9c,d).[131] Many other dye-lanthanide hybrid materials also illustrate targeting capacity to specific cell types. A lanthanide-based metallacrown, $Ln^{3+}[12\text{-}MC_{Zn(II),pyzHA}\text{-}4]_2[24\text{-}MC_{Zn(II),pyzHA}\text{-}8]$, showed the ability to differentiate necrotic cells from HeLa cells.[132] By incorporation of folic acid on the surface, specific cancer cell targeting can be achieved by dye-lanthanide hybrid nanoparticles.[133]

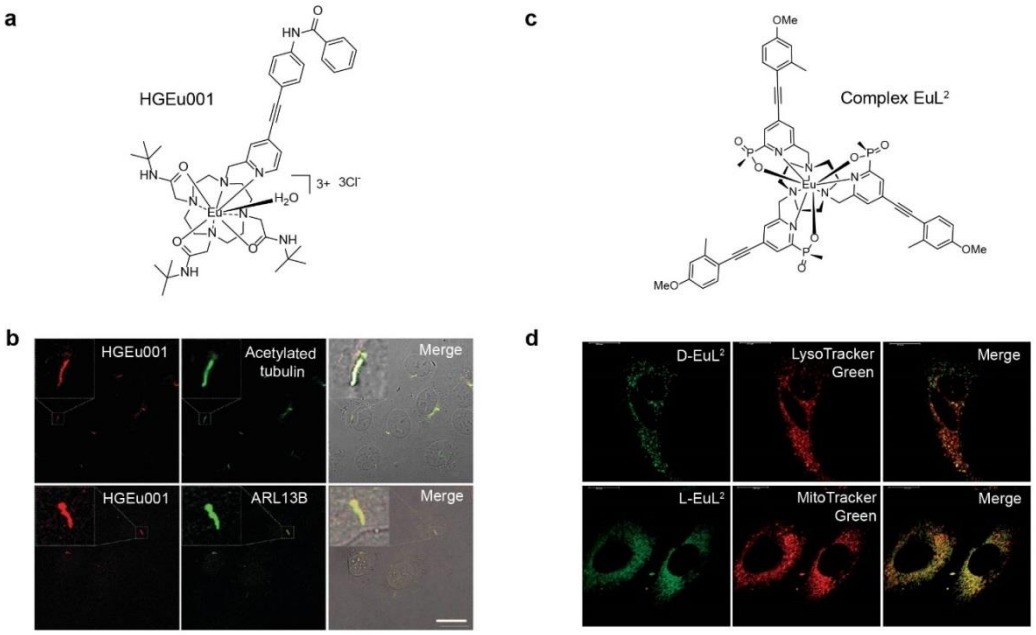

Figure 1.9. Organelle specific bioimaging. (a) Structure of complex HGEu001. (b) Confocal images of primary cilia (organelle) stained by HGEu001 (left) and primary cilium markers acetylated tubulin or ARL13B (middle), and their overlay (right). Republished with permission of the Royal Society of Chemistry, from Ref. [70]; permission conveyed through Copyright Clearance Center, Inc. (c) Structure of complex EuL^2. (d) Images of NIH-3T3 cells stained with complex D-EuL^2 and L-EuL^2 and LysoTracker Green or MitoTracker Green and their overlay is

indicating predominate lysosomal localisation by D-EuL^2 and selective mitochondrial localisation by L-EuL^2. Adapted from Ref.[131] Published by the Royal Society of Chemistry.

1.4.2 Sensing

There are many activities and events at the cellular or molecular levels in biology, which display *in vivo* physiological and pathological information. For instance, a single change on DNA sequence can cause a gene mutation that damages cells and organs, consequently resulting in serious diseases. The dyshomeostasis of metal ions in the human body, such as Zn^{2+} can lead to the disorder of proteins and enzymes.[134] The bio-accumulation of a heavy metal pollutant can cause nervous system damage and cognitive disorders.[38] The developments of materials science have been driven by the need for excellent probes to explore the process of biological activities and disease diagnostics. The non-invasive optical approach can probe the biological information while avoiding the patients‟ painfulness during the biopsy process. In this case, the dye-lanthanide hybrid materials serve as an excellent optical probe in the biomedical field. These hybrid materials enable the tunable optical properties through the combination of organic dyes and lanthanides. Also, the hybrid probes can response to various analytes including essential trace elements[134-138], toxic metal ions,[139] anions,[140-142] DNAs,[143, 144] biomarkers[145], and biology-related small molecules.[146]

The responsive signals can be produced by interfering the light absorption, energy transfer or emission processes by the presence of analysed substances (Fig.10). These interference events include changing the energy transfer rate by varying the distance of donor-acceptor pairs or separating the energy transfer pairs (Figure 1.10a,b). The energy transfer is highly sensitive to the distance of donor-acceptor pairs, for example, inverse sixth-power distance dependence in FRET. Therefore, distance manipulation of energy transfer pairs by the analyte can provide an effective way to obtain responsive signals. For instance, the antenna 4,7-diphenyl-1,10-phenanthroline-disulfonate (**BPS**) of complex **1**·**Eu**·**BPS** has a higher affinity to Fe^{2+} than that to Eu^{3+}, the presence of Fe^{2+} can

turn off Eu^{3+} emission *via* the replacement of coordinating ion (Figure 1.10a). The Fe^{2+} detection limit can reach to 10 pM using this Eu^{3+} complex probe.[136] A similar demonstration was utilised for Zn^{2+} sensing by sulfonated 8-hydroxyquinoline (**HQS**) sensitised ytterbium complex **2·Yb·8-HQS**. Upon the addition of Zn^{2+} to the **2·Yb·8-HQS** solution, the NIR emission of Yb^{3+} displayed a decrease while green light appeared from the new formed Zn^{2+} complex.[135] The strategy of analyte-induced bond cleavage is also adapted to manipulate the energy transfer distance of donor-acceptor pairs. For example, β-diketonate–Eu^{3+} complex on the surface of Tb^{3+} complex-encapsulated silica nanoparticles was quenched upon exposure to hypochlorous acid (HOCl), resulting in a significant colour change of the hybrid materials from red to green.[141] Another representative design is to use the steric barrier by analytes to change energy transfer distance as illustrated in Figure 1.10b. For example, the binding of Cu^{2+} to an aza-18-crown-6 moiety of complex **EuL1** makes the new formed Cu^{2+}-aza-18-crown-6 moiety more prone to compete with Eu^{3+}-DO3A arm for the attaching with the chromophore. And this process elongated energy transfer distance from antenna to Eu^{3+} emitter. Interestingly, the signal is reversible in the presence of S^{2-}, where S^{2-} can remove Cu^{2+} from the aza-18-crown-6 moiety.[147]

Besides the distance manipulation, the structure changes of organic dyes triggered by the analytes also provide opportunities to interfere with energy transfer pathways to give responsive signals. Structure changes rearrange the conjugated systems that alert energy levels, resulting in shifts of band positions (Figure 1.10c), or turn-on or turn-off of a transition (Figure 1.10d). The strategy of analyte-induced absorption band shifting can also be utilized in the UCNP-Dye system. For instance, a cyanine dye, hCy7, was modified on the surface of Er^{3+} and Tm^{3+} co-doped UCNPs (Figure 1.10c). The emission at 650 nm of Er^{3+} was quenched due to the absorption of hCy7 at the same wavelength. In the presence of liposoluble methylmercury, the absorption of hCy7 was shifted to around 800 nm, which is overlap with the emission from Tm^{3+}. Therefore, the emission at 800 nm of Tm^{3+} was quenched while the emission at 650 nm was recovered in the

hybrid system, providing a self-referenced sensing platform for deep tissue applications.[139]

The absorption efficiency change with analyte-induced molecules structure change attracted considerable efforts to develop hybrid materials as sensing probes. For example, the absorption efficiency of the rhodamine can be modulated through the control of opening and closing of its spiro-ring. A rhodamine derivative modified UCNPs were developed for Cu^{2+} detection (Figure 1.10d). Cu^{2+} ion triggered the ring-opening process, resulting in turning on the absorption in around 550 nm and quenching the green emission. Consequently, a responsive signal was obtained to indicate the concentration of Cu^{2+}.[138] Similar strategies were applied for sensing of Fe^{3+}, Hg^{2+}, HOCl and CN^-. [137, 142, 148, 149] The structure changes also influence energy transfer efficiency, which can be employed for biological sensing. For example, a Eu^{3+} complex **Eu.2** was utilized for the detection of sulfide in biological samples. The transformation of chromophore structure from the azide to amino by the reduction of sodium hydrosulfide can be reflected in the change of energy transfer from the antenna to europium emitter. A 20-fold enhancement of europium fluorescence intensity was observed in the presence of sulfide.[140]

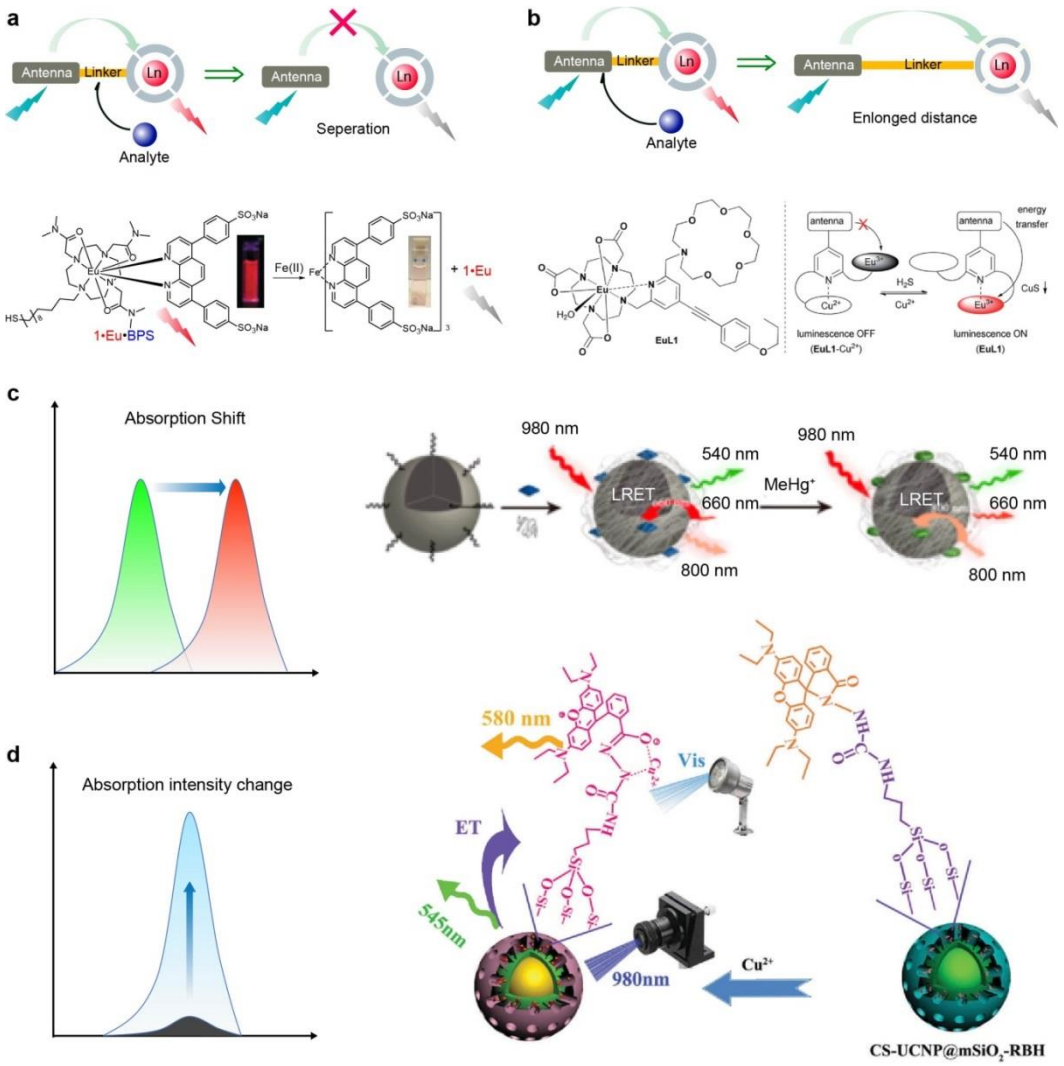

*Figure 1.10. The sensing applications of dye-lanthanide hybrid materials. (a) Schematic illustration of the separation of the chromophore and lanthanide emitting centre (top), and Fe^{2+} sensing by **1·Eu·BPS** complex via Fe^{2+} induced separation of the chromophore and emitting centre (bottom). Republished with permission of Royal Society of Chemistry, from Ref. [136]; permission conveyed through Copyright Clearance Center, Inc. (b) Schematic illustration of the distance changing between the chromophore and lanthanide emitting centre of lanthanide complex (top), and the structure of **EuL1** and sensing mechanism of europium complex for Cu^{2+} and S^{2-} (bottom). Adapted from Ref. [147] Published by The Royal Society of Chemistry. (c) Schematic illustration showing the absorption shift of the dye as a response to the stimuli (top), and $MeHg^{+}$ sensing enabled by hCy7 absorption band shift of hCy7-UCNPs (bottom). Adapted with permission.[139] Copyright 2013 American Chemical Society. (d) Schematic illustration showing the absorption intensity change of the dye as a response to the stimuli (top), and the sensing mechanism that enabled by a turn-on of the absorption of the energy transfer acceptor (bottom). Republished with permission of the Royal Society of Chemistry, from [138]; permission conveyed through Copyright Clearance Center, Inc.*

In addition to the sensing of biology-relative substances, the dye-lanthanide hybrid materials were also employed to monitoring the biological conditions in the physiological or pathological process such as drug hepatotoxicity,[50] local pH[150-152] and temperature.[51, 153] Drug-induced organ injury is a common concern for the usage of the medicine. However, direct monitoring of drug toxicity is still challenging. Peng et al. demonstrated real-time hepatotoxicity monitoring of a typical anti-fever drug, paracetamol, in living animals using the UCNPs modified with cyanine dye. An overdose of the paracetamol causes the generation of reactive nitrogen species ($NOOO^-$), which can lead to cell death and serve as a direct indicator of hepatotoxicity. $NOOO^-$-responsive chromophore Cy7 was coated on the surface of Tm-doped UCNPs and acted as energy acceptor to absorb the upconverted emission of UCNPs at 800 nm. The nanosensor gives a suppressed emission at 800 nm because of the energy transfer process to Cy7 from UCNPs in the absence of $NOOO^-$. While the $NOOO^-$ breaks the bond of Cy7 and leads to the recovery of 800 nm emission due to disabling the absorption of Cy7 at this wavelength. It should be noted that this nanoprobe could monitor the hepatotoxicity in living mice owing to its NIR excitation and emission in the biological window.[50]

pH and temperature are two critical biological parameters for cells and organs. The pH imbalance is commonly found in cellular dysfunctions such as cancer and cell proliferation. To monitor acidity in living cell, a pH-sensitive pHrodo™ Red-succinimidyl ester was coated on the surface of Yb^{3+}/Er^{3+} co-doped UCNPs (Figure 1.11). Upon 980 nm excitation, a pH-responsive signal can be obtained through the energy transfer between pHrodo™ Red-succinimidyl ester and UCNPs. This system could be used as an effective pH sensor with a working range from pH 7.2 to 2.5.[150] In vivo temperature mapping by a non-contact optical method is useful to reveal the biological process with minimum influence on living biosystem. To realize in vivo temperature sensing, a triplet-triplet annihilation (TTA) dyad-based nanothermometer, TTA-Nd-NPs, was explored to monitor body temperature in a physiological temperature range. The

chromophores of PtTPBP and BDM serve as TTA sensitiser and annihilator, respectively. The diffusion of TTA is thermo-elevated and highly sensitive to slight temperature changes. The incorporated Nd-doped NPs is relatively inner to temperature change and serve as an internal calibration reference.[51]

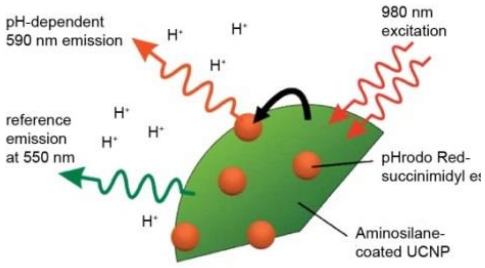

Figure 1.11. The illustration of pH sensing by UCNP-pHrodo™ Red-based pH sensor. Republished with permission of the Royal Society of Chemistry, from Ref. [150]; permission conveyed through Copyright Clearance Center, Inc.

1.4.3 Drug delivery

Efficient control of drug release is crucial to improve the effectiveness of a drug and minimise its side effects. The ideal drug carrier should take the preloaded drug to target lesions and release the needed drug in a specified time range. The drug release can be induced by many stimuli such as pH, temperature, redox state, specific enzyme, light and ultrasound.[133, 154] Among all these stimuli, light, as a remote trigger, stands out as an excellent candidate. Optical materials such as dye-lanthanide hybrids are exciting candidates as the nanocarrier for controlled drug release. Light control of drug release is mainly realised by photoresponsive molecules, which change their chemical or physical structures by the exposure to light. There are typically three types of photoresponsive mechanisms, including the photodissociation of metal-organic bond, the photocleavage of the covalent bond and the photo stirred by light-triggered isomerization conversion (Figure 1.12). By incorporating of photo-responsive molecules to lanthanide materials, numerous photo-controlled drug delivery systems have been exploited.

Many transition metal-organic complexes experience the dissociation when exposed to the light with a certain wavelength (Figure 1.12a). This phenomenon

can be used to remote control of drug release. For instance, a europium complex **EuL** was designed as a drug carrier for the delivery of Pt and Ru anti-cancer drugs (Figure 1.12a).[60, 155] **EuL** was coordinated with the transition metal drug to form lanthanide-transition metal prodrug complex. When exposed to ultraviolet or visible light, the prodrug underwent dissociation, releasing both antitumor drug and **EuL** complex. The fluorescence of **EuL** is simultaneously activated, which serves as the indicator of the releasing process. Two-photon absorption triggered drug release was used to overcome the tissue penetration problem. The lanthanide centre in this delivery system can also be changed with the ions with multiple modalities for drug release monitoring such as Gd^{3+} for MRI.[156] When modifying the lanthanide-transition metal prodrug on the surface of UCNPs, the predrug molecule can be activated by ultraviolet emission upon NIR light triggering.[157] Another notable example of drug release is realised by ruthenium complexes. The ruthenium complexes serve as photoactive valves (Figure 1.12a). Mesoporous silica was loaded with anticancer drug, doxorubicin, and capped by photoactive ruthenium complexes. Upon exposure of NIR irradiation, the upconverted ultraviolet emission from UCNPs triggers the photodissociation of ruthenium complex, thereby opening nanogates for the release of drug molecules.[158]

A library of organic species undergoes photocleavage in specific covalent bonds of their structures. These structures follow a typical fashion: a carbon connected with one heteroatom (N, or O) on one side and a conjugated structure (typically phenyl group) on the other side.[159-166] When exposing with the ultraviolet light, the C-O or C-N bond is broken and the carbon transforms to the carboxylic group, releasing the attached fragment. When incorporating drug to these photoresponsive molecules on UCNPs, the photocleavage can be triggered by ultraviolet emission of UCNPs *via* NIR excitation. By adopting this approach, a well-known anti-cancer drug 5-fluorouracil was connected to a photolabile o-nitrobenzyl tether, which is anchored on the surface of UCNPs (Figure 1.12b). The ultraviolet emission generated by UCNPs upon 980 nm excitation triggered the cleavage of bonds, which link the 5-fluorouracil and UCNPs, releasing drugs

within 14 min.[164] In addition to the surface function of UCNPs, micelle and nanocage are more capable of loading of drugs and photoresponsive molecules. As shown in Fig.12b, the NIR light was employed to induce the dissociation of the copolymer micelles for the release of co-loaded molecules (Figure 1.12b).[167] Yolk–shell structured nanocages were also developed for this purpose. The large pore volume of mesoporous silica endows huge loading capacity of the drug molecules. More importantly, the mesoporous silica nanocage can avoid premature release of the drug by preventing the contact of prodrug molecule with the enzymes in a living system. When loading UCNPs and photoresponsive molecule-conjugated anticancer drug into the nanocage, effective chlorambucil was released by NIR irradiation for *in vivo* tumour treatment.[166] Using NIR induced bond cleavage strategy, various drugs and cell regulators have been successfully delivered to the bio-system for therapy and bio-regulation through remote NIR control. For instance, remote control of stem cell differentiation was achieved by intracellular chondro-inductive kartogenin delivery and real-time regulation of calcium levels through an upconversion nanocarrier.[168] By surface coating of UCNPs, photocleavage of the covalent bond was utilised for siRNA delivery cross cellular membranes where siRNA alone cannot.[169]

Photostirrer is actualised by photoisomerizable molecules that experience physical change by light irradiation (Figure 1.12c). Azobenzene is a typical structure that has been employed as molecular photo stirred for controlled drug delivery. The exposure of ultraviolet light triggers the transform from trans-isomer to cis-isomer, while the visible light converted it back to transform. A representative example is the light-controlled release of anticancer drug doxorubicin (Dox). Dox and azobenzene groups (azo) were loaded to mesoporous silica-coated UCNPs. The simultaneous UV emission and visible emission from UCNPs upon 980 nm excitation are immediately absorbed by the azo group and produced back and forth wagging motion due to the isomerization. This molecular impeller propelled Dox release *via* NIR light excitation.[170] In another example, the amphiphilic molecule containing azobenzene moiety was modified on the surface

of UCNPs and used for the drug release with 980 nm excitation (Figure 1.12c).[171] Except for azobenzene derivatives, other light-responsive isomers such as spiropyran and diarylethene are also promising candidates as the photostirrer for controlled drug release.[172, 173] For instance, the spiropyran modified on the polymer was demonstrated as the photostirrer for the DOX release (Figure 1.12c). The co-modified folic acid provided the nanocarrier with high tumour-specificity.[172]

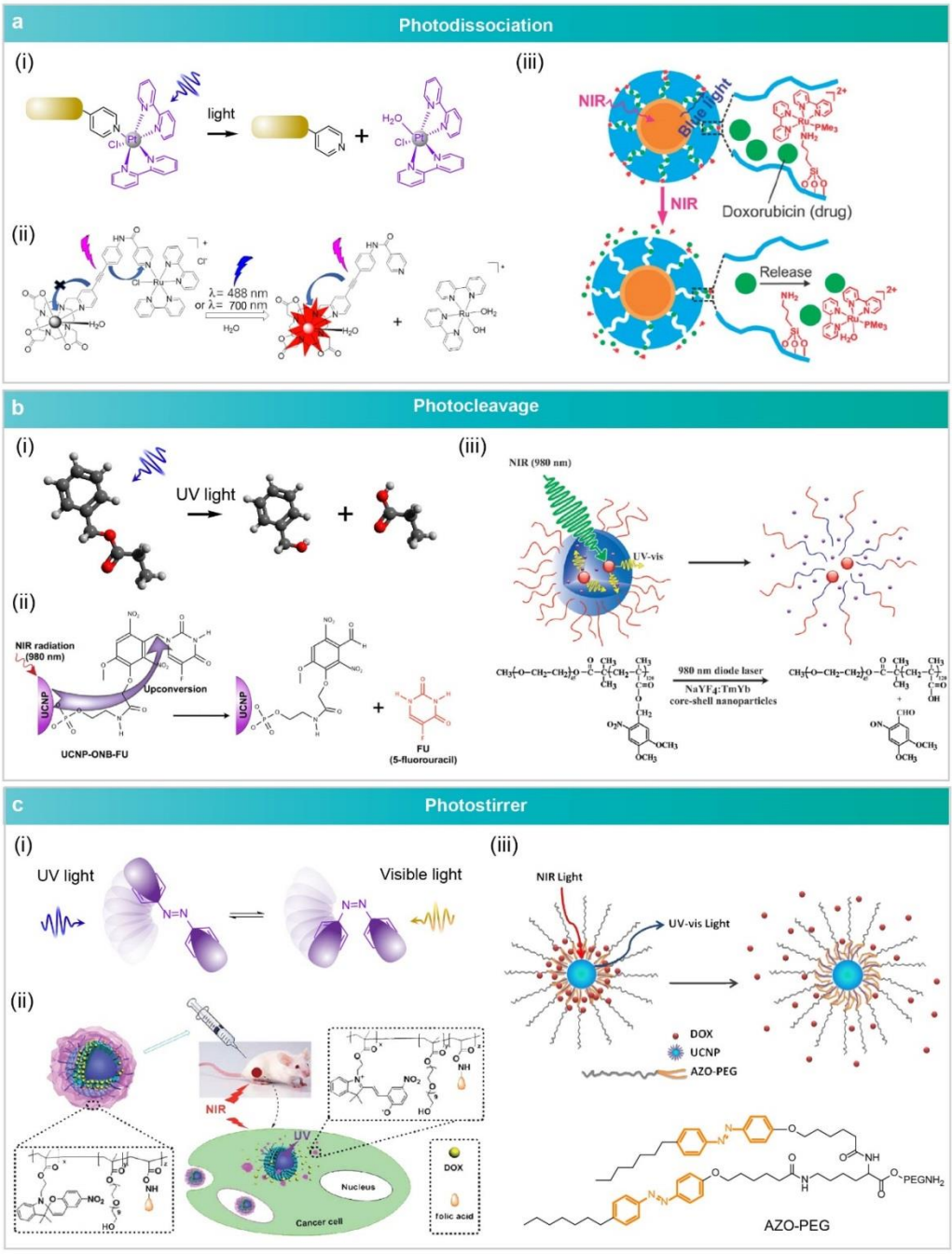

Figure 1.12. Drug delivery by dye-lanthanide hybrid materials. (a)

Photodissociation. (i) Schematic illustration of photodissociation of metal-organic bonds. (ii) Controllable anticancer drug release and monitoring by europium-ruthenium complex via one or two photo excitation. Adapted from Ref. [60] *Published by The Royal Society of Chemistry. (iii) Ru-complex photogate on silica-coated UCNPs for NIR triggered doxorubicin delivery. Reproduced from Ref.* [158] *(b) Photocleavage. (i) Schematic illustration of the photocleavage of the covalent bond. (ii) Anticancer drug 5-fluorouracil delivery by UCNPs emission induced covalent bond cleavage. Reprinted with permission.* [164] *Copyright 2014 American Chemical Society. (iii) Illustration of NIR light-triggered drug release enabled by the photocleavage of the surface polymer. Reprinted with permission.*[167] *Copyright 2011 American Chemical Society. (c) Photostirrer. (i) Schematic illustration of the photostirrer by light triggered isomerisation conversion. (ii) Spiropyran and folic acid modified UCNPs for targeted and photo-controlled drug delivery. Republished with permission of Royal Society of Chemistry, from Ref.* [172]*; permission conveyed through Copyright Clearance Center, Inc. (iii) Illustration of NIR controlled drug release by UCNPs composite modified with azo containing polymer. Adapted from Ref.* [171]*. Copyright (2018), with permission from Elsevier.*

1.4.4 Therapy

Dye-lanthanide hybrid materials are not only effective drug carriers but also the excellent therapeutic agents themselves (Figure 1.13). The FDA approved commercial lanthanide medicine such as lanthanum carbonate (Fosrenol) for disease treatment, which proves safety and feasibility of the lanthanide materials for clinical applications.[174] The FDA approval encourages the researchers from both academic and industry fields to explore novel therapeutic lanthanide-based hybrid agents. There are currently several types of therapeutic methods using dye-lanthanide hybrid materials, including chemotherapy, photothermal therapy, and photodynamic therapy.

Chemotherapy

Many lanthanide materials could be used as a chemotherapeutic agent. Though possessing different coordination properties with transition metals, the use of lanthanide complexes as therapeutic agents has attracted considerable attention since the first success of Platinum anti-cancer drug. For example, an ytterbium(III) octaethylporphyrin complex (**Yb-OEP**) (Figure 1.13a) was reported to have

anti-cancer activity with sub-micromolar IC_{50} value. The complex undergoes anti-cancer process through endoplasmic reticulum stress pathway-associated apoptosis.[175] A series of dihalo-8-quinolinoline lanthanide complexes (Figure 1.13b) displayed higher cytotoxicity against cancer than the free quinolinoline ligand. The anti-cancer process occurs through the binding of complex to DNA molecules.[176, 177] By incorporating platinum to lanthanide complex, the newly formed hybrid complex possesses strong DNA binding capacity and serves as simultaneous imaging and therapeutic agents. For example, the complex [*cis*-$Pt_2Eu(L)(H_2O)$] (Figure 1.13c) displayed anti-cancer properties by possessing two therapeutic platinum centres. In this hybrid complex, nuclear localization could be revealed by the emission of the europium.[178] In addition to these, other therapeutic mechanisms are presented for the usage of the lanthanide complex. For example, Motexafin gadolinium (MGd) (Figure 1.13d) can kill cancer through the targeted inhibition of thioredoxin reductase and ribonucleotide reductase[179, 180].

Photothermal therapy

PTT uses the heating effect of light, especially NIR light, to treat various diseases. Nanomaterials as heat probes can significantly scale down the treatment area, improve the therapeutic accuracy and reduce the damage of the healthy cells.[181] Lanthanide nanoparticles are useful photothermal therapeutic materials due to their NIR excitations and the capability of imaging-guided therapy.[182] The NIR dye can further improve the absorption efficiency and reduce the tissue damage by lower the excitation power. For example, it is reported that ICG-UCNPs exhibited better heating effect than pure ICG and pure nanoparticles at identical conditions in the PTT process. Under irradiation (0.67 W cm^{-2}) at 808 nm for 5min, ICG-UCNPs produced a 50% drop of cellular viability, while no change on cellular viability was found in the absence of NIR irradiation.[55] Target-specific PTT can improve the therapeutic accuracy by co-loading of specific targeting molecules on the nanoparticle surface. A core-shell UCNPs

($NaYF_4$:Yb,Er@$NaYF_4$:Yb@$NaYF_4$:Yb,Nd) modified with folate acid can facilitate cell endocytosis, making it a potential tumour-targeted drug for PTT (Figure 1.13e). The photothermal effect upon 793 nm irradiation can be enhanced by increasing the dye number on the surface of lanthanide nanoparticles (Figure 1.13f,g).[112]

Photodynamic therapy

Different from the heating effect of PTT by light irradiation, the PDT treats the lesions by the generation of reactive singlet oxygen ($^1O_2$). Upon a certain wavelength of light excitation, the photosensitiser can be populated to their triplet states from the excited singlet states through intersystem crossing process. The newly generated triplet states of photosensitisers then react with the ambient oxygen molecule to produce singlet oxygen.[183] The singlet oxygen is highly reactive oxidant which kills the tumour cells around it. The first FDA-approved PDT drug, Photofrin, is a porphyrin-based singlet oxygen generator for the treatment of oesophagal cancer.[184] Dye-lanthanide hybrid materials can be used as the PDT agents since the lanthanide can enhance intersystem crossing by heavy atom effect. In particular, lanthanide complexes are good candidates because most of the lanthanide complexes involve triplet states in the energy transfer process. A series of therapeutic agents, [Ln(dpq)$_3$(tfnb)$_3$] (Ln = Tb or Eu), were reported to strongly bind to DNA and bovine serum albumin, displaying the cytosolic and nuclear localisation. The anti-cancer efficacy is *via* the cleavage of DNA under the exposure of ultraviolet light. Both of Tb and Eu agents show photocytotoxicity toward the cancer cell line after ultraviolet light irradiation.[185] Inspired by the first approved PDT drug, the porphyrin-based lanthanide complexes attracted considerable attention as PDT agents. For instance, the porphyrin-based complex **Gd-N** was developed as tumour-specific photosensitiser (Figure 1.13h). It was revealed that **Gd-N** could recognize tumour cells through anionic phosphatidylserine membrane by its cation. It showed a 51% quantum yield of singlet oxygen generation and the solid tumour was suppressed by treatment in a

short period. Interestingly, its Yb counterpart showed no singlet generating capacity.[186] To further enable specific tumour recognition, targeting peptides can be employed to the photosensitiser to achieve more precise therapy.[73]

To facilitate tissue penetration, the organic photosensitisers are usually modified on the surface of UCNPs, which convert NIR irradiation to ultraviolet and visible light for the generation of cytotoxic singlet oxygen. Examples of such organic photosensitisers include chlorine, porphyrin and rhodamine derivatives such as Ce6,[187] ZnPc,[188] and Rose Bengal[189]. Employing this strategy, a Ce6 coated $NaYF_4$: Yb, Er@$NaGdF_4$ core@shell UCNPs was developed for the PDT applications. Upon 980 nm excitation, UCNPs displayed the visible and UV emissions to trigger Ce6 for the generation of singlet oxygen.[187] Nd^{3+} doped active shell[113] and NIR dye (Figure 1.13i)[113] were usually incorporated to sensitise UCNPs to reduce the heating effect of 980 nm irradiation and enhance the absorption efficiency. To ensure the therapeutic efficacy, Ac-FKC(StBu)AC(SH)-CBT, a tumor-specific cathepsin protease, was modified on the surface of UCNPs (Figure 1.13j). When exposure to enzyme overexpressed cancer cells, the cleavage of peptides triggered the crosslinking between the neighbouring UCNPs, then resulting in the aggregation of PDT molecule-bearing UCNPs at tumor site. This accumulation largely enhances the PDT process. Obvious tumor suppression was observed in tumour-bearing mice after the treatment with Ce6-modified UCNPs (Figure 1.13k).[190]

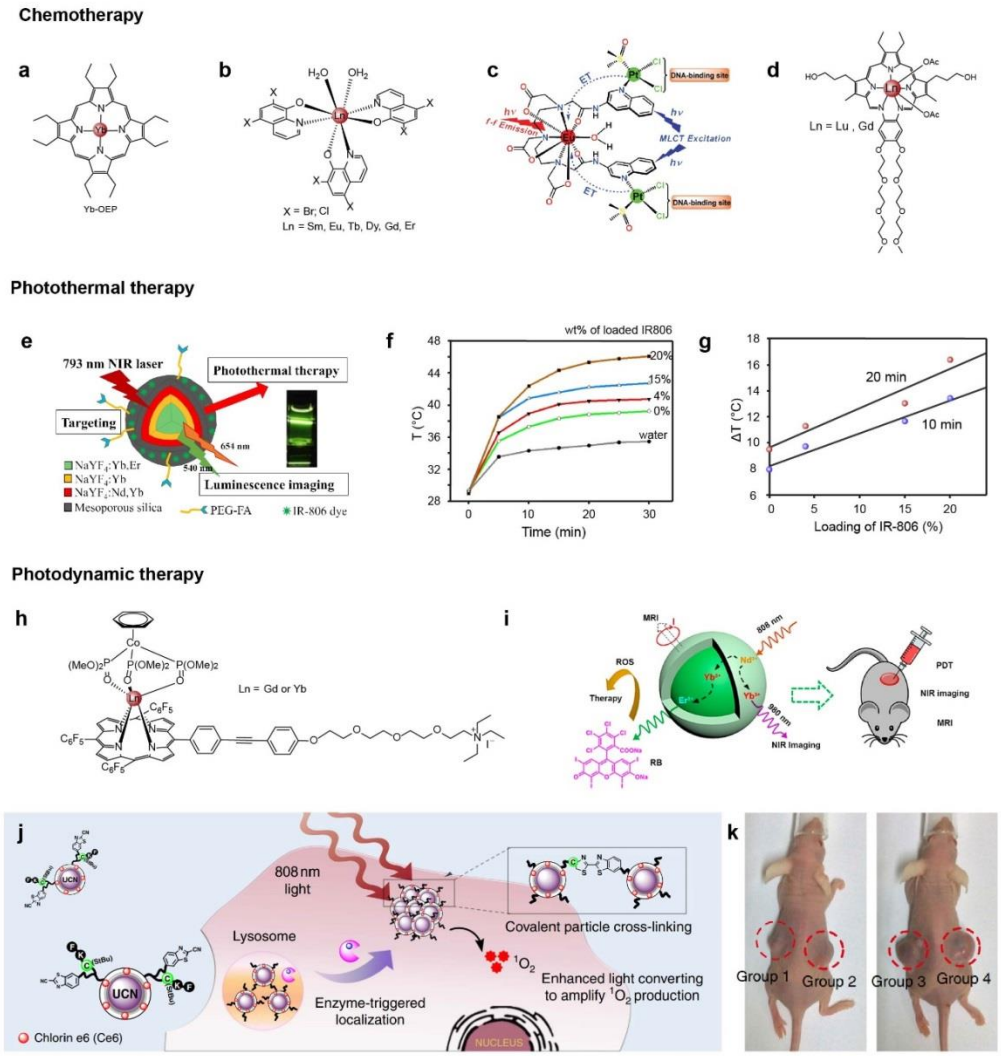

Figure 1.13. Dye-lanthanide hybrid materials for therapeutical applications. Structure of (a) Yb-OEP,[175] *(b) quinolone derivative complexes,*[176, 177] *(c) complex [cis-Pt_2Eu(L)(H_2O)],*[178] *and (d) MGd and MLu.*[191] *(c) is reproduced from Ref.* [178] *Published by The Royal Society of Chemistry. (e) Schematic illustration of PTT and luminescence imaging by UCNPs incorporated with IR806 photothermal sensitisers. (f) Temperature changes with radiation time for UCNPs with various IR806 loading (wt%). (g) Temperature changes as a function of IR-806 loading after 10 min and 20 min of 793 nm laser irradiation. (e), (f) and (g) are adapted from Ref.* [112] *(h) Structure of PDT complexes* ***Gd-N*** *and* ***Yb-N****.*[186] *(i) Schematic graph of UCNP-RB material as PDT, MRI and luminescence imaging agent. Reprinted with permission.*[113] *Copyright 2016 American Chemical Society. (j) Illustration of enzyme-responsive cross-linking of UCNPs for selective tumour accumulation and photodynamic tumour treatment. (k) Images of tumour-bearing mice after treatment with Ce6-modified UCNP (group 1), control UCNP (group 2), Ce6-modified UCNP without NIR light exposure (group 3) and saline (group 4).* ***(j)*** *and****(k)*** *are adapted from Ref.* [190]

1.4.5 Control and monitoring cellular activities

Optical control and monitoring of the events and activities at cellular or subcellular levels is an exciting approach in the biomedical field. Most light-controlled cell activities need the UV or visible light, which limited their further applications. The emission of UCNPs can provide triggering signals in deep tissue by remote NIR excitation. For instance, a representative cellular activity manipulation is the optogenetic neuron control by NIR light (Figure 1.14a). By employing IR806-UCNPs, the optogenetic neuron excitation window was successfully shifted to NIR range. The power densities of 800 nm excitation for triggering of the act of potential firing was only 1.5 W/mm^2, quite lower than the corresponding two-photon neuron cell activation. This strategy allows precise spatial and temporal control of neuron cell activities.[56]

In addition to the control of cell activities, dye-lanthanide hybrid materials are also used for profiling the states and interactions of different proteins. As shown in Figure 1.14b, simultaneous profiling of hosphorylation and ubiquitination of proteins was addressed by dual emission sensitisation of UCNPs.[108] Hosphorylation and ubiquitination are critical post-translational modifications and important in many physiological processes. The UCNPs were modified with the aptamer, which can selectively bind the HER2 protein. The fluorescent molecular probe was labelled with a green dye Cy3 to form the recognizer of the phosphorylation of HER2 and **Cy3-pTag**; while the Ub antibodies with ubiquitination recognition were labelled with dye Cy5.5 to form **Cy5.5-UbA**. Upon 980 nm irradiation, the green and red emissions from the UCNPs can be used to monitor the phosphorylation and ubiquitination process by duplexed energy transfer to labelled dyes. This allows simultaneous profiling of post-translational modifications of targeted proteins by a single excitation wavelength.[108] Similarly, by labelling different dyes to the monosaccharides, aptamer modified UCNP was successfully employed for the profiling terminal monosaccharide pattern *via* duplexed resonance energy transfers to the

corresponding dyes.[192] Moreover, the energy transfer between UCNPs and dye molecules was utilized for the investigation of protein-protein interactions. Drees et al. investigated the interaction of two kinds of proteins, Tom20 and Tom7, in a living cell by energy transfer between UCNPs and tetramethylrhodamine (TMR). The Tom7 protein was labeled with an energy donor UCNPs, while the Tom20 was labeled with an energy acceptor TMR. Therefore, the emission intensity of the acceptor TMR under 980 nm excitation could indicate the distance between Tom7-UCNPs and Tom20-TMR, reporting of protein-protein interactions.[193] Except for the demonstrated emerging applications, far more capacities can be realised by the rapid development in dye-lanthanide hybrid materials.

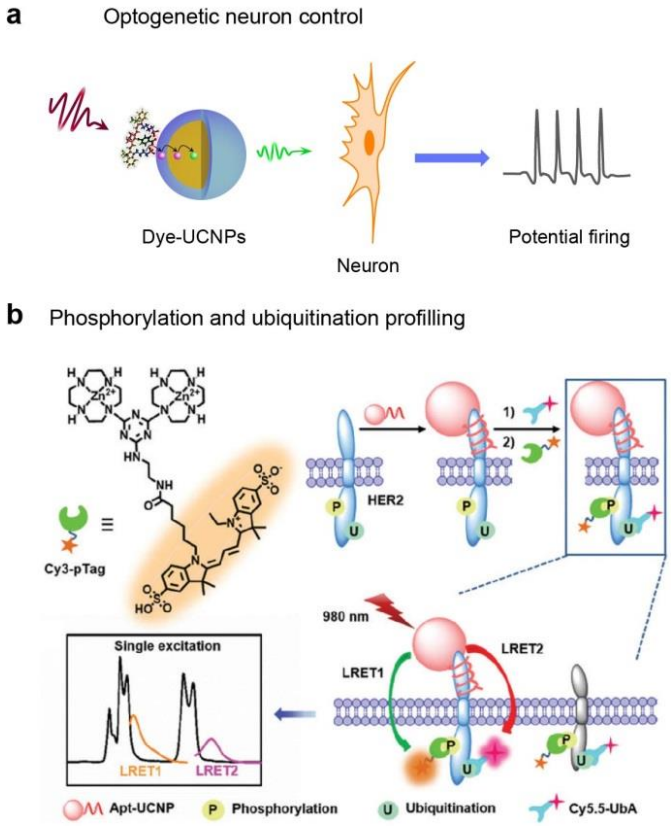

Figure 1.14. Dye-lanthanide hybrid materials for cellular activities control and monitoring. (a) Dye-UCNPs enabled optogenetic control of the neuron under NIR excitation. (b) The single excitation-duplexed imaging strategy for the simultaneous profiling of phosphorylation and ubiquitination. Republished with permission of the Royal Society of Chemistry, from Ref. [108]; permission conveyed through Copyright Clearance Center, Inc.

1.5 Thesis outline

This thesis focuses on the development of organic-lanthanide hybridisation chemistry, spectroscopy and energy transfer properties. The scope of my research work is to develop dye-lanthanide hybrid materials, study their photophysical properties and their applications. There are eight chapters in this thesis.

In Chapter 1, I introduce the background of dye-lanthanide materials by reviewing the recent advances in the field of dye-lanthanide hybrid materials, centring on investigating their photophysical and photochemical properties. Five representative dye-lanthanide hybrid material systems including lanthanide complex, dye-sensitised downshifting (DSNPs), dye-sensitised downconversion nanoparticles (DCNPs), dye-sensitised upconversion nanoparticles (UCNPs), and UCNPs-dye energy transfer systems have been thoroughly discussed in this chapter, with special focus on their energy transfer processes, optical properties and design principles. We highlight the key applications of dye-lanthanide hybrid materials in bioimaging, sensing, drug delivery, therapy, and cellular activity studies.

In Chapter 2, I design and synthesize an ytterbium complex-based Hg^{2+} sensor. I investigate the photophysical properties of the cell-permeable ytterbium complex. The titration, sensitivity, selectivity and reversibility were surveyed. The probe shows reversible binding with Hg^{2+} in aqueous solution and in vitro by off−on visible and NIR emission. The fast response and 150 nM sensitivity of Hg^{2+} detection are based upon FRET and the lanthanide antenna effect. The binding mechanism is suggested by NMR employing the motif structure in a La complex and by DFT calculations.

In Chapter 3, I report a pair of stoichiometric terbium-europium dyads as molecular thermometers and study their energy transfer properties. A strategy for synthesizing hetero-dinuclear complexes that comprise chemically similar lanthanides is introduced in which a pair of thermosensitive dinuclear complexes, **cycTb-phEu** and **cycEu-phTb,** was synthesized. We then investigated the singlet

and triplet states, low-temperature emission. The sensitive temperature-dependent luminescent intensity ratios of europium and terbium emission over a wide temperature range (50 - 298 K and 10 - 200 K, respectively) and their temporal dimension responses were surveyed. The energy transfer from Tb^{3+} to Eu^{3+} and the energy transfer from ligand to lanthanide ions are investigated. The thermal sensing properties of the probes are also studied.

In Chapter 4, I investigate the spectral structure and intensity changes of a pair of dinuclear complexes with a europium ion on cyclen site and a lanthanum ion on phen site or vice verses (**cycEu-phLa** and **cycLa-phEu)**. We also study the singlet and triplet, and intersystem crossing by their corresponding La complexes. We determined the singlet-triplet intersystem crossing rate with values as ~10^8 s^{-1}. Though the two europium complexes have the same components and the same energy levels, they present different photophysical properties due to the different coordination environment. The band positions are different in the emission spectra. The emission of **cycEu-phLa** showed a stronger relative intensity of $^5D_0 \rightarrow {}^7F_2$ transition whereas the relative intensity of $^5D_0 \rightarrow {}^7F_4$ transition was weaker in comparison with **cycLa-phEu**. We found the **cycEu-phLa** have higher internal quantum efficiency while the **cycEu-phLa** have higher sensitising efficiency, though they have similar external quantum yield.

In Chapter 5, I report a dye sensitised upconversion nanoparticle with highly enhanced upconversion emission. I design and synthesized a new dye by connecting tetraphenylethene (TPE) with the cyanide NIR dye (IR783). The absorption, emission and quantum yield of the resulting compound (TPEO-IR783) ware measured and compared with the reported NIR dyes. The TPEO-IR783 is used as a sensitiser to form dye sensitised UCNPs, showing more than 200-fold upconversion emission than the reported IR806 sensitised UCNPs under the same condition.

In Chapter 6, I report an ytterbium nanoparticle-mediated upconversion system. The system enables the singlet energy of sensitiser transfer to the acceptor triplet states with no requirement of intersystem crossing (ISC). I demonstrate the

upconversion method with IR808 and rubrene acid. By introducing an intermediate ytterbium energy level in $NaGdF_4$:Yb nanoparticles, the upconversion can be activated while the donor-acceptor only mixture does not show any upconversion emission. The strategy does not require specific modification of sensitiser for intersystem crossing.

Chapter 7 is the experiment sections where details of experiments in each chapter have been shown.

Conclusions and perspectives are given in Chapter 8, which summarizes the key achievement presented in this thesis. I also identify the challenges and prospective opportunities in material engineering for better performance of the new hybrid systems.

1.6 References

1. X. Rao, T. Song, J. Gao, Y. Cui, Y. Yang, C. Wu, B. Chen and G. Qian, *J. Am. Chem. Soc.*, 2013, **135**, 15559-15564.
2. R. Deng, F. Qin, R. Chen, W. Huang, M. Hong and X. Liu, *Nat. Nanotechnol.*, 2015, **10**, 237.
3. Y. Lu, J. Zhao, R. Zhang, Y. Liu, D. Liu, E. M. Goldys, X. Yang, P. Xi, A. Sunna, J. Lu, Y. Shi, R. C. Leif, Y. Huo, J. Shen, J. A. Piper, J. P. Robinson and D. Jin, *Nat. Photon.*, 2013, **8**, 32-36.
4. F. D. Natterer, K. Yang, W. Paul, P. Willke, T. Choi, T. Greber, A. J. Heinrich and C. P. Lutz, *Nature*, 2017, **543**, 226-228.
5. L. Sánchez-García, M. O. Ramírez, R. M. Solé, J. J. Carvajal, F. Díaz and L. E. Bausá, *Light Sci. Appl.*, 2019, **8**, 14.
6. G. Lin and D. Jin, *Nat. Nanotechnol.*, 2018, **13**, 534-536.
7. Y. Liu, P. Bhattarai, Z. Dai and X. Chen, *Chem. Soc. Rev.*, 2019, **48**, 2053-2108.
8. J. A. Broussard, B. Rappaz, D. J. Webb and C. M. Brown, *Nat. Protoc.*, 2013, **8**, 265-281.
9. L. Kortekaas and W. R. Browne, *Chem. Soc. Rev.*, 2019, **48**, 3406-3424.
10. D. Li, W. Qin, B. Xu, J. Qian and B. Z. Tang, *Adv. Mater.*, 2017, **29**, 1703643.
11. R. Kuriki, H. Matsunaga, T. Nakashima, K. Wada, A. Yamakata, O. Ishitani and K. Maeda, *J. Am. Chem. Soc.*, 2016, **138**, 5159-5170.
12. Y. Liu, Y. Lu, X. Yang, X. Zheng, S. Wen, F. Wang, X. Vidal, J. Zhao, D. Liu, Z. Zhou, C. Ma, J. Zhou, J. A. Piper, P. Xi and D. Jin, *Nature*, 2017, **543**, 229-233.

13. C. Galland, Y. Ghosh, A. Steinbruck, M. Sykora, J. A. Hollingsworth, V. I. Klimov and H. Htoon, *Nature*, 2011, **479**, 203-207.
14. J. Zhou, J. L. Leano, Jr., Z. Liu, D. Jin, K. L. Wong, R. S. Liu and J. G. Bunzli, *Small*, 2018, **14**, e1801882.
15. J. Zhang, C. M. Shade, D. A. Chengelis and S. Petoud, *J. Am. Chem. Soc.*, 2007, **129**, 14834-14835.
16. P. Agbo, T. Xu, M. Sturzbecher-Hoehne and R. J. Abergel, *ACS Photonics*, 2016, **3**, 547-552.
17. Z. Wang and A. Meijerink, *J. Phys. Chem. Lett.*, 2018, **9**, 1522-1526.
18. G. Chen, W. Shao, R. R. Valiev, T. Y. Ohulchanskyy, G. S. He, H. Ågren and P. N. Prasad, *Adv. Opt. Mater.*, 2016, **4**, 1760-1766.
19. S.-K. Ko, Y.-K. Yang, J. Tae and I. Shin, *J. Am. Chem. Soc.*, 2006, **128**, 14150.
20. A. Minsky, A. Y. Meyer and M. Rabinovitz, *Tetrahedron*, 1985, **41**, 785-791.
21. G. Bao, K.-L. Wong and P. A. Tanner, *ChemPlusChem*, 2019, **84**, 816-820.
22. Z. Yu, Y. Wu, Q. Peng, C. Sun, J. Chen, J. Yao and H. Fu, *Chem. Eur. J.*, 2016, **22**, 4717-4722.
23. Z. An, C. Zheng, Y. Tao, R. Chen, H. Shi, T. Chen, Z. Wang, H. Li, R. Deng, X. Liu and W. Huang, *Nat. Mater.*, 2015, **14**, 685.
24. G. Bao, Z. Liu, Y. Luo, K.-L. Wong and P. A. Tanner, *Dalton Trans.*, 2019, **48**, 4314-4323.
25. S. R. Pilli, T. Banerjee and K. Mohanty, *J. Mol. Liq.*, 2015, **207**, 112-124.
26. H. Ramanantoanina, M. Sahnoun, A. Barbiero, M. Ferbinteanu and F. Cimpoesu, *Phys. Chem. Chem. Phys.*, 2015, **17**, 18547-18557.
27. I. Martinić, S. V. Eliseeva and S. Petoud, *J. Lumines.*, 2017, **189**, 19-43.
28. A. Jordens, Y. P. Cheng and K. E. Waters, *Miner. Eng.*, 2013, **41**, 97-114.
29. M. Shang, S. Liang, H. Lian and J. Lin, *Inorg. Chem.*, 2017, **56**, 6131-6140.
30. Y. Pan, W. Wang, Y. Zhu, H. Xu, L. Zhou, X. Liu and L. Li, *J. Alloys Compd.*, 2018, **769**, 932-939.
31. M. Suta and C. Wickleder, *Adv. Funct. Mater.*, 2017, **27**, 1602783.
32. K. Binnemans, *Coord. Chem. Rev.*, 2015, **295**, 1-45.
33. C.-K. Duan, P. A. Tanner, V. Makhov and N. Khaidukov, *J. Phys. Chem. A*, 2011, **115**, 8870-8876.
34. H. Uh and S. Petoud, *C. R. Chim.*, 2010, **13**, 668-680.
35. P. P. Ferreira da Rosa, Y. Kitagawa and Y. Hasegawa, *Coord. Chem. Rev.*, 2020, **406**, 213153.
36. A. Baz, H. El Hamzaoui, I. Fsaifes, G. Bouwmans, M. Bouazaoui and L. Bigot, *Laser Phys. Lett.*, 2013, **10**, 055106.
37. D. Pfeifer, A. Russegger, I. Klimant and S. M. Borisov, *Sens. Actuator B-Chem.*, 2020, **304**, 127312.
38. G. Bao, S. Zha, Z. Liu, Y. H. Fung, C. F. Chan, H. Li, P. H. Chu, D. Jin, P. A. Tanner and K. L. Wong, *Inorg. Chem.*, 2018, **57**, 120-128.

39. M. D. Wisser, S. Fischer, P. C. Maurer, N. D. Bronstein, S. Chu, A. P. Alivisatos, A. Salleo and J. A. Dionne, *ACS Photonics*, 2016, **3**, 1523-1530.
40. T. Liang, Q. Wang, Z. Li, P. Wang, J. Wu, M. Zuo and Z. Liu, *Adv. Funct. Mater.*, 2020, **30**, 1910765.
41. R. F. Kubin and A. N. Fletcher, *J. Lumin.*, 1982, **27**, 455-462.
42. M. E. Alberto, B. C. De Simone, G. Mazzone, E. Sicilia and N. Russo, *Phys. Chem. Chem. Phys.*, 2015, **17**, 23595-23601.
43. A. López de Guereñu, P. Bastian, P. Wessig, L. John and M. U. Kumke, *Biosensors*, 2019, **9**, 9.
44. T. Ha and P. Tinnefeld, *Annu. Rev. Phys. Chem.*, 2012, **63**, 595-617.
45. Z. Zhang, S. J. Kenny, M. Hauser, W. Li and K. Xu, *Nat. Methods*, 2015, **12**, 935-938.
46. P. A. Tanner, L. Zhou, C. Duan and K.-L. Wong, *Chem. Soc. Rev.*, 2018, **47**, 5234-5265.
47. X. Wang, R. R. Valiev, T. Y. Ohulchanskyy, H. Ågren, C. Yang and G. Chen, *Chem. Soc. Rev.*, 2017, **46**, 4150-4167.
48. D. L. Dexter, *J. Chem. Phys.*, 1953, **21**, 836-850.
49. A. N. Carneiro Neto, R. T. Moura and O. L. Malta, *J. Lumines.*, 2019, **210**, 342-347.
50. J. Peng, A. Samanta, X. Zeng, S. Han, L. Wang, D. Su, D. T. Loong, N. Y. Kang, S. J. Park, A. H. All, W. Jiang, L. Yuan, X. Liu and Y. T. Chang, *Angew. Chem. Int. Ed.*, 2017, **56**, 4165.
51. M. Xu, X. Zou, Q. Su, W. Yuan, C. Cao, Q. Wang, X. Zhu, W. Feng and F. Li, *Nat. Commun.*, 2018, **9**, 2698.
52. Q. Liu, X. Zou, Y. Shi, B. Shen, C. Cao, S. Cheng, W. Feng and F. Li, *Nanoscale*, 2018, **10**, 12573-12581.
53. J. Xu, P. Yang, M. Sun, H. Bi, B. Liu, D. Yang, S. Gai, F. He and J. Lin, *ACS Nano*, 2017, **11**, 4133-4144.
54. T. Zhao, P. Wang, Q. Li, A. A. Al-Khalaf, W. N. Hozzein, F. Zhang, X. Li and D. Zhao, *Angew. Chem. Int. Ed. Engl.*, 2018, **57**, 2611-2615.
55. D. Wang, D. Wang, A. Kuzmin, A. Pliss, W. Shao, J. Xia, J. Qu and P. N. Prasad, *Adv. Opt. Mater.*, 2018, **6**, 1701142.
56. X. Wu, Y. Zhang, K. Takle, O. Bilsel, Z. Li, H. Lee, Z. Zhang, D. Li, W. Fan, C. Duan, E. M. Chan, C. Lois, Y. Xiang and G. Han, *ACS Nano*, 2016, **10**, 1060-1066.
57. S. Hao, Y. Shang, D. Li, H. Ågren, C. Yang and G. Chen, *Nanoscale*, 2017, **9**, 6711-6715.
58. F. S. Richardson, *Chem. Rev.*, 1982, **82**, 541-552.
59. M. L. Aulsebrook, B. Graham, M. R. Grace and K. L. Tuck, *Coord. Chem. Rev.*, 2018, **375**, 191-220.
60. H. Li, C. Xie, R. Lan, S. Zha, C. F. Chan, W. Y. Wong, K. L. Ho, B. D. Chan, Y. Luo, J. X. Zhang, G. L. Law, W. C. S. Tai, J. G. Bunzli and K. L. Wong, *J. Med. Chem.*, 2017, **60**, 8923-8932.

61. A. Nonat, C. F. Chan, T. Liu, C. Platas-Iglesias, Z. Liu, W. T. Wong, W. K. Wong, K. L. Wong and L. J. Charbonniere, *Nat. Commun.*, 2016, **7**, 11978.
62. D. Liu, Y.-N. Zhou, J. Zhao, Y. Xu, J. Shen and M. Wu, *J. Mater. Chem. C*, 2017, **5**, 11620-11630.
63. T. Zhang, X. Zhu, C. C. Cheng, W. M. Kwok, H. L. Tam, J. Hao, D. W. Kwong, W. K. Wong and K. L. Wong, *J. Am. Chem. Soc.*, 2011, **133**, 20120-20122.
64. N. M. Shavaleev, S. V. Eliseeva, R. Scopelliti and J. C. Bunzli, *Inorg. Chem.*, 2015, **54**, 9166-9173.
65. A. D. Kovalenko, I. S. Bushmarinov, A. S. Burlov, L. S. Lepnev, E. G. Ilina and V. V. Utochnikova, *Dalton Trans.*, 2018, **47**, 4524-4533.
66. J.-C. G. Bünzli, *Coord. Chem. Rev.*, 2015, **293-294**, 19-47.
67. S. V. Eliseeva and J. C. Bunzli, *Chem. Soc. Rev.*, 2010, **39**, 189-227.
68. M. C. Heffern, L. M. Matosziuk and T. J. Meade, *Chem. Rev.*, 2014, **114**, 4496-4539.
69. M. A. Shipman, K. J. Ramhit and B. A. Blight, *J. Mater. Chem. B*, 2016, **4**, 3043-3045.
70. H. Li, R. Lan, C.-F. Chan, G. Bao, C. Xie, P.-H. Chu, W. C. S. Tai, S. Zha, J.-X. Zhang and K.-L. Wong, *Chem. Commun.*, 2017, **53**, 7084-7087.
71. D. G. Smith, R. Pal and D. Parker, *Chem. Eur. J.*, 2012, **18**, 11604-11613.
72. K. Gupta and A. K. Patra, *Eur. J. Inorg. Chem.*, 2018, **2018**, 1882-1890.
73. Y. Zhou, C.-F. Chan, D. W. J. Kwong, G.-L. Law, S. Cobb, W.-K. Wong and K.-L. Wong, *Chem. Commun.*, 2017, **53**, 557-560.
74. J. Andres, R. D. Hersch, J.-E. Moser and A.-S. Chauvin, *Adv. Funct. Mater.*, 2014, **24**, 5029-5036.
75. J. W. Walton, A. Bourdolle, S. J. Butler, M. Soulie, M. Delbianco, B. K. McMahon, R. Pal, H. Puschmann, J. M. Zwier, L. Lamarque, O. Maury, C. Andraud and D. Parker, *Chem. Commun.*, 2013, **49**, 1600-1602.
76. J. Xu, T. M. Corneillie, E. G. Moore, G. L. Law, N. G. Butlin and K. N. Raymond, *J. Am. Chem. Soc.*, 2011, **133**, 19900-19910.
77. J. Yuan, G. Wang, K. Majima and K. Matsumoto, *Anal. Chem.*, 2001, **73**, 1869-1876.
78. H. Li, F. L. Chadbourne, R. Lan, C. F. Chan, W. L. Chan, G. L. Law, C. S. Lee, S. L. Cobb and K. L. Wong, *Dalton Trans.*, 2013, **42**, 13495-13501.
79. A. Takacs, R. Napolitano, M. Purgel, A. C. Benyei, L. Zekany, E. Brucher, I. Toth, Z. Baranyai and S. Aime, *Inorg. Chem.*, 2014, **53**, 2858-2872.
80. M. Bortoluzzi, E. Bianchin, S. Roppa, V. Bertolasi and F. Enrichi, *Dalton Trans.*, 2014, **43**, 10120-10131.
81. Z. Pan, G. Jia, C.-K. Duan, W.-Y. Wong, W.-T. Wong and P. A. Tanner, *Eur. J. Inorg. Chem.*, 2011, **2011**, 637-646.
82. B. M. van der Ende, L. Aarts and A. Meijerink, *Adv. Mater.*, 2009, **21**, 3073-3077.
83. W. Shao, G. Chen, A. Kuzmin, H. L. Kutscher, A. Pliss, T. Y. Ohulchanskyy and P. N. Prasad, *J. Am. Chem. Soc.*, 2016, **138**,

16192-16195.
84. F. Wang, S. Wen, H. He, B. Wang, Z. Zhou, O. Shimoni and D. Jin, *Light Sci. Appl.*, 2018, **7**, 18007.
85. F. Wang, R. Deng and X. Liu, *Nat. Protoc.*, 2014, **9**, 1634-1644.
86. Z. Zhang, Y. Liu, Y. Fang, B. Cao, J. Huang, K. Liu and B. Dong, *Adv. Sci.*, 2018, **5**, 1800748.
87. G. Bao and D. Jin, *Nat. Photonics*, 2019, **13**, 304-305.
88. J. Zhou, S. Wen, J. Liao, C. Clarke, S. A. Tawfik, W. Ren, C. Mi, F. Wang and D. Jin, *Nat. Photon.*, 2018, **12**, 154-158.
89. L. Wang, H. Dong, Y. Li, C. Xue, L.-D. Sun, C.-H. Yan and Q. Li, *J. Am. Chem. Soc.*, 2014, **136**, 4480-4483.
90. W. Zou, C. Visser, J. A. Maduro, M. S. Pshenichnikov and J. C. Hummelen, *Nat. Photon.*, 2012, **6**, 560-564.
91. D. J. Garfield, N. J. Borys, S. M. Hamed, N. A. Torquato, C. A. Tajon, B. Tian, B. Shevitski, E. S. Barnard, Y. D. Suh, S. Aloni, J. B. Neaton, E. M. Chan, B. E. Cohen and P. J. Schuck, *Nat. Photon.*, 2018, **12**, 402–407.
92. X. Zou, M. Xu, W. Yuan, Q. Wang, Y. Shi, W. Feng and F. Li, *Chem. Commun.*, 2016, **52**, 13389-13392.
93. G. Chen, J. Damasco, H. Qiu, W. Shao, T. Y. Ohulchanskyy, R. R. Valiev, X. Wu, G. Han, Y. Wang, C. Yang, H. Agren and P. N. Prasad, *Nano Lett.*, 2015, **15**, 7400-7407.
94. F. Zhao, D. Yin, C. Wu, B. Liu, T. Chen, M. Guo, K. Huang, Z. Chen and Y. Zhang, *Dalton Trans.*, 2017, **46**, 16180-16189.
95. X. Wu, H. Lee, O. Bilsel, Y. Zhang, Z. Li, T. Chen, Y. Liu, C. Duan, J. Shen, A. Punjabi and G. Han, *Nanoscale*, 2015, **7**, 18424-18428.
96. C. Hazra, S. Ullah, Y. Serge, L. G. Caetano and S. J. L. Ribeiro, *J. Mater. Chem. C*, 2018, **6**, 4777-4785.
97. J. Lee, B. Yoo, H. Lee, G. D. Cha, H.-S. Lee, Y. Cho, S. Y. Kim, H. Seo, W. Lee, D. Son, M. Kang, H. M. Kim, Y. I. Park, T. Hyeon and D.-H. Kim, *Adv. Mater.*, 2017, **29**, 1603169.
98. S. Alyatkin, E. Ureña-Horno, B. Chen, O. L. Muskens, A. G. Kanaras and P. G. Lagoudakis, *J. Phys. Chem. C*, 2018, **122**, 18177-18184.
99. B. Xue, D. Wang, L. Tu, D. Sun, P. Jing, Y. Chang, Y. Zhang, X. Liu, J. Zuo, J. Song, J. Qu, E. J. Meijer, H. Zhang and X. Kong, *J. Phys. Chem. Lett.*, 2018, **9**, 4625-4631.
100. W. Wei, G. Chen, A. Baev, G. S. He, W. Shao, J. Damasco and P. N. Prasad, *J. Am. Chem. Soc.*, 2016, **138**, 15130-15133.
101. J. Xu, M. Sun, Y. Kuang, H. Bi, B. Liu, D. Yang, R. Lv, S. Gai, F. He and P. Yang, *Dalton Trans.*, 2017, **46**, 1495-1501.
102. C. D. LaBoda and C. L. Dwyer, *Adv. Funct. Mater.*, 2016, **26**, 2866-2874.
103. J. Zhao, D. Jin, E. P. Schartner, Y. Lu, Y. Liu, A. V. Zvyagin, L. Zhang, J. M. Dawes, P. Xi, J. A. Piper, E. M. Goldys and T. M. Monro, *Nat. Nanotechnol.*, 2013, **8**, 729-734.
104. V. Muhr, C. Wurth, M. Kraft, M. Buchner, A. J. Baeumner, U.

Resch-Genger and T. Hirsch, *Anal. Chem.*, 2017, **89**, 4868-4874.
105. K. Huang, H. Liu, M. Kraft, S. Shikha, X. Zheng, H. Agren, C. Wurth, U. Resch-Genger and Y. Zhang, *Nanoscale*, 2018, **10**, 250-259.
106. Z. Li, S. Lv, Y. Wang, S. Chen and Z. Liu, *J. Am. Chem. Soc.*, 2015, **137**, 3421-3427.
107. R. Deng, J. Wang, R. Chen, W. Huang and X. Liu, *J. Am. Chem. Soc.*, 2016, **138**, 15972-15979.
108. F. Ma, L. Zhang, B. J. C. Wong and J. Lei, *Chem. Commun.*, 2018, **54**, 3648-3651.
109. H. Wen, H. Zhu, X. Chen, T. F. Hung, B. Wang, G. Zhu, S. F. Yu and F. Wang, *Angew. Chem. Int. Ed. Engl.*, 2013, **52**, 13419-13423.
110. L. Zhou, R. Wang, C. Yao, X. Li, C. Wang, X. Zhang, C. Xu, A. Zeng, D. Zhao and F. Zhang, *Nat. Commun.*, 2015, **6**, 6938.
111. M. D. Wisser, S. Fischer, C. Siefe, A. P. Alivisatos, A. Salleo and J. A. Dionne, *Nano Lett.*, 2018, **18**, 2689–2695.
112. S. L. Lin, Z. R. Chen and C. A. Chang, *Nanotheranostics*, 2018, **2**, 243-257.
113. Y. Li, J. Tang, D. X. Pan, L. D. Sun, C. Chen, Y. Liu, Y. F. Wang, S. Shi and C. H. Yan, *ACS Nano*, 2016, **10**, 2766-2773.
114. R. Weissleder, *Nat. Biotechnol.*, 2001, **19**, 316.
115. S. A. Filatova, I. A. Shcherbakov and V. B. Tsvetkov, *J. Biomed. Opt.*, 2017, **22**, 35009.
116. J. Zhao, D. Zhong and S. Zhou, *J. Mater. Chem. B*, 2018, **6**, 349-365.
117. A. N. Bashkatov, E. A. Genina, V. I. Kochubey and V. V. Tuchin, *J. Phys. D: Appl. Phys.*, 2005, **38**, 2543.
118. L. Prodi, E. Rampazzo, F. Rastrelli, A. Speghini and N. Zaccheroni, *Chem. Soc. Rev.*, 2015, **44**, 4922-4952.
119. Y. Gu, Z. Guo, W. Yuan, M. Kong, Y. Liu, Y. Liu, Y. Gao, W. Feng, F. Wang, J. Zhou, D. Jin and F. Li, *Nat. Photonics*, 2019, **13**, 525-531.
120. E. Hemmer, A. Benayas, F. Légaré and F. Vetrone, *Nanoscale Horiz.*, 2016, **1**, 168-184.
121. G. E. Walrafen and E. Pugh, *J. Solution Chem.*, 2004, **33**, 81-97.
122. E. Hemmer, N. Venkatachalam, H. Hyodo, A. Hattori, Y. Ebina, H. Kishimoto and K. Soga, *Nanoscale*, 2013, **5**, 11339-11361.
123. B. Li, Y. Zhang, R. Zou, Q. Wang, B. Zhang, L. An, F. Yin, Y. Hua and J. Hu, *Dalton Trans.*, 2014, **43**, 6244-6250.
124. Y. Ning, J. Tang, Y.-W. Liu, J. Jing, Y. Sun and J.-L. Zhang, *Chem. Sci.*, 2018, **9**, 3742-3753.
125. T. Zhang, C. F. Chan, R. Lan, H. Li, N. K. Mak, W. K. Wong and K. L. Wong, *Chem. Commun.*, 2013, **49**, 7252-7254.
126. Y. Chen, R. Guan, C. Zhang, J. Huang, L. Ji and H. Chao, *Coord. Chem. Rev.*, 2016, **310**, 16-40.
127. D. Jin and J. A. Piper, *Anal. Chem.*, 2011, **83**, 2294-2300.
128. M. Rajendran and L. W. Miller, *Biophys J.*, 2015, **109**, 240-248.

129. K. Bhattacharya, L. Bernasconi and D. Picard, *Sci. Rep.*, 2018, **8**, 2801.
130. U. Cho, D. P. Riordan, P. Ciepla, K. S. Kocherlakota, J. K. Chen and P. B. Harbury, *Nat. Chem. Biol.*, 2018, **14**, 15-21.
131. A. T. Frawley, Holly V. Linford, M. Starck, R. Pal and D. Parker, *Chem. Sci.*, 2018, **9**, 1042-1049.
132. I. Martinic, S. V. Eliseeva, T. N. Nguyen, V. L. Pecoraro and S. Petoud, *J. Am. Chem. Soc.*, 2017, **139**, 8388-8391.
133. C. Wang, L. Cheng and Z. Liu, *Biomaterials*, 2011, **32**, 1110-1120.
134. K. A. McCall, C.-c. Huang and C. A. Fierke, *J. Nutr.*, 2000, **130**, 1437S-1446S.
135. S. Comby, S. A. Tuck, L. K. Truman, O. Kotova and T. Gunnlaugsson, *Inorg. Chem.*, 2012, **51**, 10158-10168.
136. O. Kotova, S. Comby and T. Gunnlaugsson, *Chem. Commun.*, 2011, **47**, 6810-6812.
137. R. Wei, Z. Wei, L. Sun, J. Z. Zhang, J. Liu, X. Ge and L. Shi, *ACS Appl. Mater. Interfaces*, 2016, **8**, 400-410.
138. Y. Xu, H. Li, X. Meng, J. Liu, L. Sun, X. Fan and L. Shi, *New J. Chem.*, 2016, **40**, 3543-3551.
139. Y. Liu, M. Chen, T. Cao, Y. Sun, C. Li, Q. Liu, T. Yang, L. Yao, W. Feng and F. Li, *J. Am. Chem. Soc.*, 2013, **135**, 9869-9876.
140. M. Tropiano and S. Faulkner, *Chem. Commun.*, 2014, **50**, 4696-4698.
141. H. Ma, B. Song, Y. Wang, D. Cong, Y. Jiang and J. Yuan, *Chem. Sci.*, 2017, **8**, 150-159.
142. J. Liu, Y. Liu, Q. Liu, C. Li, L. Sun and F. Li, *J. Am. Chem. Soc.*, 2011, **133**, 15276-15279.
143. L. Ancel, C. Gateau, C. Lebrun and P. Delangle, *Inorg. Chem.*, 2013, **52**, 552-554.
144. A. M. Nonat, S. J. Quinn and T. Gunnlaugsson, *Inorg. Chem.*, 2009, **48**, 4646-4648.
145. M. D. Yilmaz and H. A. Oktem, *Anal. Chem.*, 2018, **90**, 4221-4225.
146. E. Pershagen, J. Nordholm and K. E. Borbas, *J. Am. Chem. Soc.*, 2012, **134**, 9832-9835.
147. Z. Liang, T.-H. Tsoi, C.-F. Chan, L. Dai, Y. Wu, G. Du, L. Zhu, C.-S. Lee, W.-T. Wong, G.-L. Law and K.-L. Wong, *Chem. Sci.*, 2016, **7**, 2151-2156.
148. Y. Zhou, W. Pei, C. Wang, J. Zhu, J. Wu, Q. Yan, L. Huang, W. Huang, C. Yao, J. S. Loo and Q. Zhang, *Small*, 2014, **10**, 3560-3567.
149. X. Ge, L. Sun, B. Ma, D. Jin, L. Dong, L. Shi, N. Li, H. Chen and W. Huang, *Nanoscale*, 2015, **7**, 13877-13887.
150. R. Arppe, T. Nareoja, S. Nylund, L. Mattsson, S. Koho, J. M. Rosenholm, T. Soukka and M. Schaferling, *Nanoscale*, 2014, **6**, 6837-6843.
151. F. Li, Y. Du, J. Liu, H. Sun, J. Wang, R. Li, D. Kim, T. Hyeon and D. Ling, *Adv. Mater.*, 2018, **30**, e1802808.
152. T. Gunnlaugsson, J. P. Leonard, K. Sénéchal and A. J. Harte, *J. Am. Chem. Soc.*, 2003, **125**, 12062-12063.

153. G. Bao, K.-L. Wong, D. Jin and P. A. Tanner, *Light Sci. Appl.*, 2018, **7**, 96.
154. S. Mura, J. Nicolas and P. Couvreur, *Nat. Mater.*, 2013, **12**, 991.
155. H. Li, R. Lan, C.-F. Chan, L. Jiang, L. Dai, D. W. J. Kwong, M. H.-W. Lam and K.-L. Wong, *Chem. Commun.*, 2015, **51**, 14022-14025.
156. H. Li, B. I. Harriss, A. Phinikaridou, S. Lacerda, G. Ramniceanu, B. T. Doan, K. L. Ho, C. F. Chan, W. S. Lo, R. M. Botnar, R. Lan, C. Richard, G. L. Law, N. J. Long and K. L. Wong, *Nanotheranostics*, 2017, **1**, 186-195.
157. Y. Min, J. Li, F. Liu, E. K. Yeow and B. Xing, *Angew. Chem. Int. Ed. Engl.*, 2014, **53**, 1012-1016.
158. S. He, K. Krippes, S. Ritz, Z. Chen, A. Best, H.-J. Butt, V. Mailänder and S. Wu, *Chem. Commun.*, 2015, **51**, 431-434.
159. C. J. Carling, F. Nourmohammadian, J. C. Boyer and N. R. Branda, *Angew. Chem. Int. Ed. Engl.*, 2010, **49**, 3782-3785.
160. J. V. Garcia, J. Yang, D. Shen, C. Yao, X. Li, R. Wang, G. D. Stucky, D. Zhao, P. C. Ford and F. Zhang, *Small*, 2012, **8**, 3800-3805.
161. S. Sortino, *J. Mater. Chem.*, 2012, **22**, 301-318.
162. P. T. Burks, J. V. Garcia, R. GonzalezIrias, J. T. Tillman, M. Niu, A. A. Mikhailovsky, J. Zhang, F. Zhang and P. C. Ford, *J. Am. Chem. Soc.*, 2013, **135**, 18145-18152.
163. Y. Yang, B. Velmurugan, X. Liu and B. Xing, *Small*, 2013, **9**, 2937-2944.
164. L. L. Fedoryshin, A. J. Tavares, E. Petryayeva, S. Doughan and U. J. Krull, *ACS Appl. Mater. Interfaces*, 2014, **6**, 13600-13606.
165. W. Li, J. Wang, J. Ren and X. Qu, *J. Am. Chem. Soc.*, 2014, **136**, 2248-2251.
166. L. Zhao, J. Peng, Q. Huang, C. Li, M. Chen, Y. Sun, Q. Lin, L. Zhu and F. Li, *Adv. Funct. Mater.*, 2014, **24**, 363-371.
167. B. Yan, J. C. Boyer, N. R. Branda and Y. Zhao, *J. Am. Chem. Soc.*, 2011, **133**, 19714-19717.
168. H. Kang, K. Zhang, Q. Pan, S. Lin, D. S. H. Wong, J. Li, W. Y.-W. Lee, B. Yang, F. Han, G. Li, B. Li and L. Bian, *Adv. Funct. Mater.*, 2018, **28**, 1802642.
169. Y. Yang, F. Liu, X. Liu and B. Xing, *Nanoscale*, 2013, **5**, 231-238.
170. J. Liu, W. Bu, L. Pan and J. Shi, *Angew. Chem. Int. Ed. Engl.*, 2013, **52**, 4375-4379.
171. X. Li, D. Liu, Y. Wang, S. Xu and H. Liu, *Colloids Surf., A*, 2018, **555**, 55-62.
172. Q. Xing, N. Li, Y. Jiao, D. Chen, J. Xu, Q. Xu and J. Lu, *RSC Adv.*, 2015, **5**, 5269-5276.
173. E. Hatano, M. Morimoto, T. Imai, K. Hyodo, A. Fujimoto, R. Nishimura, A. Sekine, N. Yasuda, S. Yokojima, S. Nakamura and K. Uchida, *Angew. Chem. Int. Ed. Engl.*, 2017, **56**, 12576-12580.
174. M. T. Kaczmarek, M. Zabiszak, M. Nowak and R. Jastrzab, *Coord. Chem. Rev.*, 2018, **370**, 42-54.
175. W.-L. Kwong, R. Wai-Yin Sun, C.-N. Lok, F.-M. Siu, S.-Y. Wong, K.-H.

Low and C.-M. Che, *Chem. Sci.*, 2013, **4**, 747-754.
176. Z.-F. Chen, X.-Y. Song, Y. Peng, X. Hong, Y.-C. Liu and H. Liang, *Dalton Trans.*, 2011, **40**, 1684-1692.
177. Y. C. Liu, Z. F. Chen, X. Y. Song, Y. Peng, Q. P. Qin and H. Liang, *Eur. J. Med. Chem.*, 2013, **59**, 168-175.
178. A. Chandra, K. Singh, S. Singh, S. Sivakumar and A. K. Patra, *Dalton Trans.*, 2016, **45**, 494-497.
179. S. I. Hashemy, J. S. Ungerstedt, F. Zahedi Avval and A. Holmgren, *J. Biol. Chem.*, 2006, **281**, 10691-10697.
180. F. Zahedi Avval, C. Berndt, A. Pramanik and A. Holmgren, *Biochem. Biophys. Res. Commun.*, 2009, **379**, 775-779.
181. X. Zhu, W. Feng, J. Chang, Y. W. Tan, J. Li, M. Chen, Y. Sun and F. Li, *Nat. Commun.*, 2016, **7**, 10437.
182. Y. Dai, D. Yang, D. Yu, C. Cao, Q. Wang, S. Xie, L. Shen, W. Feng and F. Li, *ACS Appl. Mater. Interfaces*, 2017, **9**, 26674-26683.
183. J.-X. Zhang, W.-L. Chan, C. Xie, Y. Zhou, H.-F. Chau, P. Maity, G. T. Harrison, A. Amassian, O. F. Mohammed, P. A. Tanner, W.-K. Wong and K.-L. Wong, *Light Sci. Appl.*, 2019, **8**, 46.
184. D. Wu, L. Fan, C. Xu, Z. Liu, Y. Zhang, L. Liu, Q. Wang and L. Tao, *J. Biophotonics*, 2015, **8**, 764-774.
185. S. Dasari, S. Singh, S. Sivakumar and A. K. Patra, *Chem. Eur. J.*, 2016, **22**, 17387-17396.
186. T. Zhang, R. Lan, C. F. Chan, G. L. Law, W. K. Wong and K. L. Wong, *Proc. Natl. Acad. Sci. U. S. A.*, 2014, **111**, E5492-5497.
187. Y. I. Park, H. M. Kim, J. H. Kim, K. C. Moon, B. Yoo, K. T. Lee, N. Lee, Y. Choi, W. Park, D. Ling, K. Na, W. K. Moon, S. H. Choi, H. S. Park, S. Y. Yoon, Y. D. Suh, S. H. Lee and T. Hyeon, *Adv. Mater.*, 2012, **24**, 5755-5761.
188. S. Cui, D. Yin, Y. Chen, Y. Di, H. Chen, Y. Ma, S. Achilefu and Y. Gu, *ACS Nano*, 2013, **7**, 676-688.
189. X. Li, Z. Guo, T. Zhao, Y. Lu, L. Zhou, D. Zhao and F. Zhang, *Angew. Chem. Int. Ed. Engl.*, 2016, **55**, 2464-2469.
190. X. Ai, C. J. Ho, J. Aw, A. B. Attia, J. Mu, Y. Wang, X. Wang, Y. Wang, X. Liu, H. Chen, M. Gao, X. Chen, E. K. Yeow, G. Liu, M. Olivo and B. Xing, *Nat. Commun.*, 2016, **7**, 10432.
191. C. Berndt, T. Kurz, S. Bannenberg, R. Jacob, A. Holmgren and U. T. Brunk, *Cancer Lett.*, 2011, **307**, 119-123.
192. N. Wu, L. Bao, L. Ding and H. Ju, *Angew. Chem. Int. Ed. Engl.*, 2016, **55**, 5220-5224.
193. C. Drees, A. N. Raj, R. Kurre, K. B. Busch, M. Haase and J. Piehler, *Angew. Chem. Int. Ed. Engl.*, 2016, **55**, 11668-11672.

Chapter 2 Reversible and sensitive Hg^{2+} detection by visible and NIR emission from ytterbium complex

2.1 Introduction

Heavy metal pollution has gained increased concern as careless and rapid industrial development.[1] Among the heavy metal pollutants, the mercury ion is one of the most severe threats because the mercury ion has an intense affinity to the thiol groups which are rich in peptides and proteins. The binding to these proteins cause the dysfunction of most enzymes and functional proteins.[2] The mercury has poor biodegradability and can bio-aggregate through the food chains. The pollutant causes many diseases including cognitive disorder, kidney failure, and brain and nervous system damage.[3-7] Therefore, the concerns over the hazards of mercury have driven scientists to develop mercury sensors for applications in biological and environmental fields.

Fluorescent probes are able to detect heavy metal ion quantitatively and are useful for sensing the mercury pollutions. Many works have been made to develop various fluorescent sensors with the structures including semisquaraines[3], rosamine,[8] porphyrins[9] and rhodamine.[4, 10-14] The rhodamine based mercury sensor is attractive because of its ring-opening feature. The mercury ions can trigger the ring-opening process which provides distinguished photophysical advantages such as high sensitivity, reversibility, selectivity and fast response.[4, 11] However, the organic dye-based fluorescent sensors have considerable challenges that need to be overcome. Many organic sensors have a poor solubility in aqueous solution and require a mixture of organic solvent and water.[6, 9-11, 15] The organic dye has narrow Stokes shift which usually poses an interference to the signal by the excitation light.[6, 11] Fluorescence

**A version of this chapter has been included in the published paper "Reversible and Sensitive Hg^{2+} Detection by a Cell-PermeableYtterbium Complex. Inorg. Chem. 2018, 57, 120−128".*

Resonance Energy Transfer (FRET) is a tool to overcome the narrow Stokes shift by transferring the energy to an acceptor to give an energy gap between emission and excitation.[16,17] On the other hand, lanthanide complexes are good candidates as luminescent sensors which offer a large separation between emission and excitation spectral bands. Except, the lanthanide complexes have characteristic emission peaks and long lifetimes.[18, 19] Our previously reported ytterbium-based mercury sensor, YbPor-L, demonstrates some of these properties and has the reasonable sensitivity.[9] Importantly, the mercury probe has the emission band in the near-infrared range which locates in the biological window. However, the probe has poor aqueous solubility, making it impossible to be used in bio-detections. The limit of detection is not sensitive enough, with a value of 10 μM in a mixed solution of buffer and organic solvent.[9] Moreover, the visible responsive signal has a very narrow separation between signal and excitation. These drawbacks drive us to develop a more sensitive and biocompatible sensor for the use of mercury ion detection.

Herein, we report our new design of the dual responsive mercury sensor, **GBYb001**. The **GBYb001** integrates an ytterbium complex with a rhodamine B detecting moiety (Figure 2.1). We introduced a cyclen with amide chains to coordinate with the ytterbium ion, making the complex positively-charged, which provides water solubility to the overall complex. We put a carbodithioate unit which can catch the mercury ion since the sulfur has a strong affinity with the element of mercury. This provides the sensor with selectivity towards mercury ion. The rhodamine is the sensing unit. The **GBYb001** is in ring-closed form. The mercury ion induces the ring-opening of the rhodamine sensing unit and gives the responsiveness. The construction of the complex is achieved by connecting these units to the 4-(phenylethynyl)pyridine (**py**) unit which is a chromophore to absorb excitation light and transfer the energy to both rhodamine unit and the ytterbium ion. The sensor gave both turn-on visible and near-infrared signals upon the presence of mercury ion. Both emission bands have large separations between emission signals and the excitation light. We synthesized **GBYb002** without rhodamine unit as a control which showed

no responsiveness to mercury ion (Figure 2.1). The sensor exhibits a low limit of detection, fast response, good reversibility and biological compatibility.

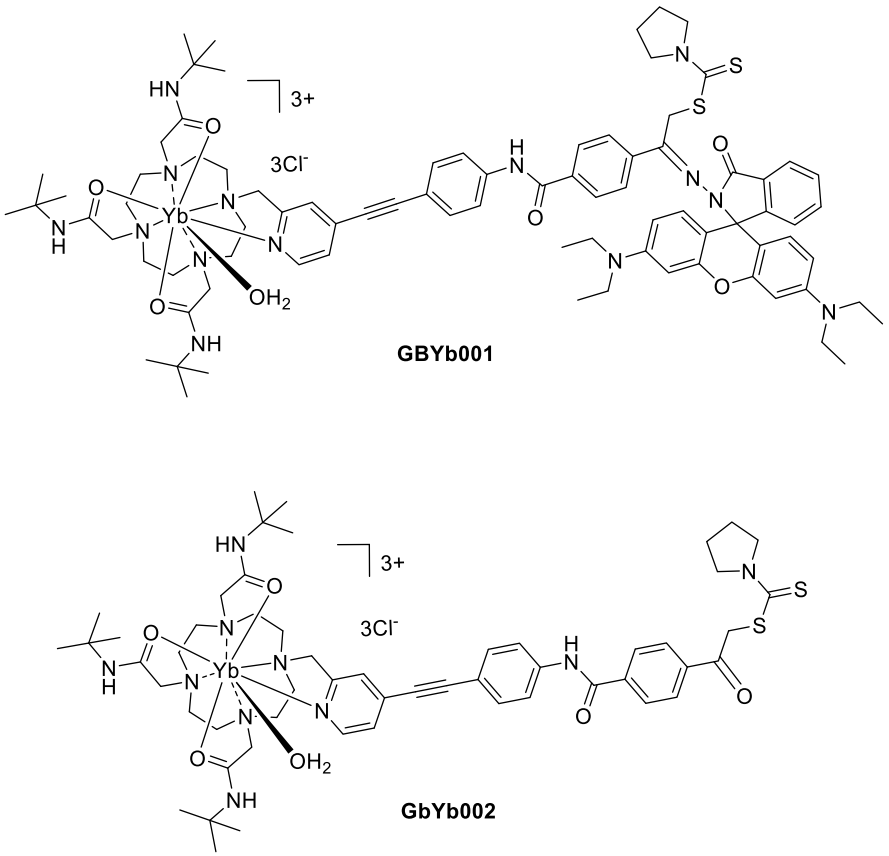

*Figure 2.1. Structure of complex **GBYb001** and its control **GBYb002**.*

2.2 Results and discussion

2.2.1 Synthesis of GBYb001, GBLa001 and GBYb002

GBYb001 was synthesized by coordinating Yb(III) with cyclen moiety of ligand **GB001**, which was prepared by the connecting chromophore, cyclen, thiol fragment and rhodamine B through a series of steps (Schemes 2.1, 2.2, 2.3). Compound **2-3** was synthesized from methyl 4-acetylbenzoate via bromination, substitution by ammonium pyrrolidine-1-carbodithioate, and demethylation (Scheme 2.1). Compound **2-5** was synthesized from 2-methylpropan-2-amine by two step-substitution (Scheme 2.2). Compound **2-10** was synthesized from (4-bromopyridin-2-yl)methanol through coupling with ethynyltrimethylsilane, removal of TMS, coupling with tert-butyl (4-iodophenyl)carbamate, substitution with **2-5**, and de-protection of Boc group.

Ligand **2-13** was then obtained by coupling **2-10** with **2-3**, substitution with hydrazine hydrate and then the rhodamine B unit (Scheme 2.3). The control compound, **GBYb002**, was synthesized by coordinating an ytterbium ion with the intermediate **2-11** (Scheme 2.4). The intermediates and final complexes were characterized by various spectroscopic techniques.

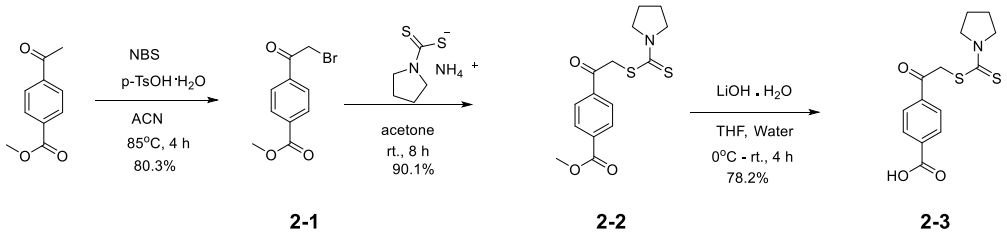

*Scheme 2.1. Synthesis of **2-3.***

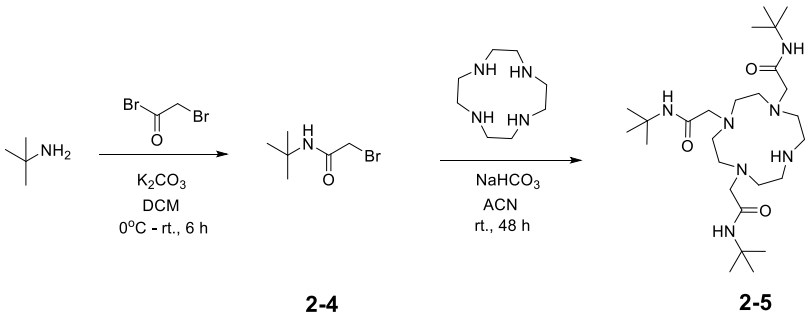

*Scheme 2.2. Synthesis of the trisubstituted macrocyclic **2-5.***

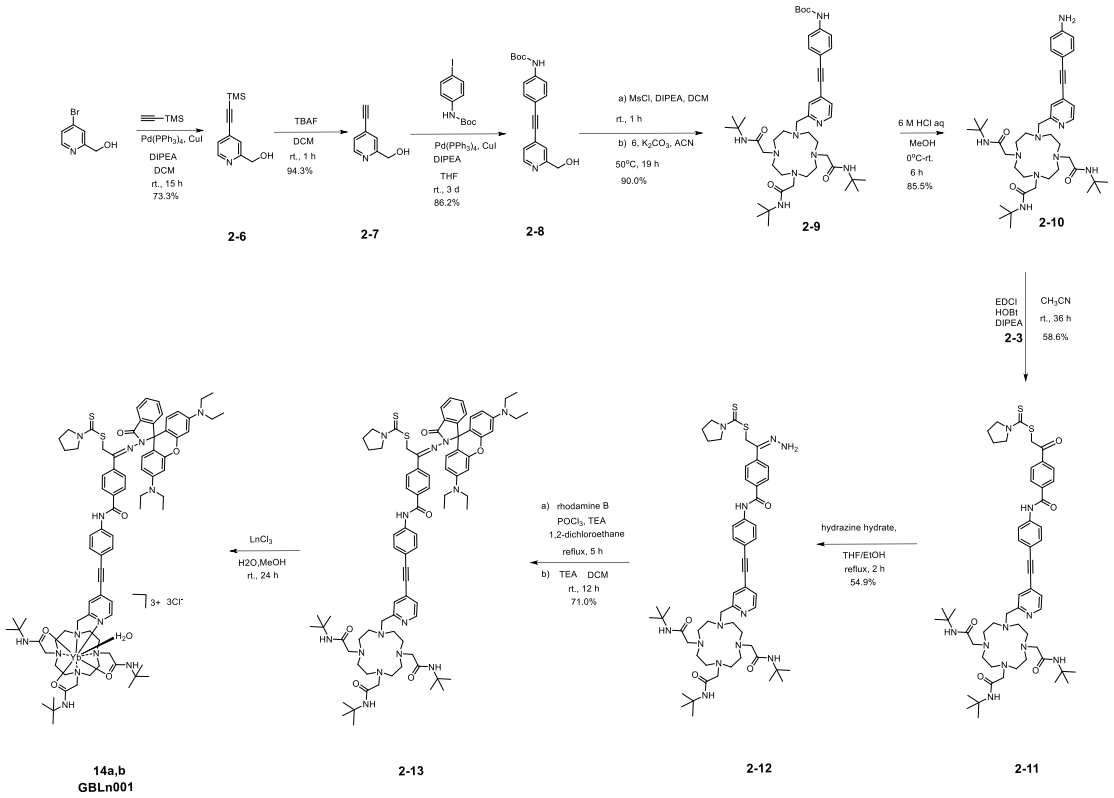

Scheme 2.3. Synthesis of ***GBLn001.***

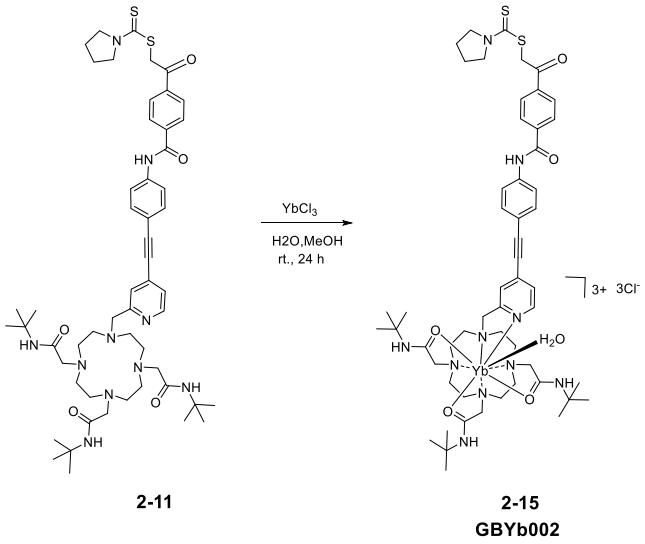

Scheme 2.4. Synthesis of control ***GbYb002****.*

2.2.2 Photophysical properties

GBYb001 shows a strong **py** absorption band in HEPES buffer. The absorption peaked at 325 nm with absorption efficiency ε = 26180 M^{-1} cm^{-1}. The sensor exhibits

a weak rhodamine B absorption band peaked at 565 nm (Figure 2.2). The complex showed a weak red emission band at 591 nm when excited the **py** chromophore. This emission band belongs to $\pi \rightarrow \pi^*$ transition of the rhodamine unit. The **py** showed no emission band due to quenching of the rhodamine by the energy transfer process (Figure 2.3). This is demonstrated that in the excitation spectrum of rhodamine B emission, where not only rhodamine B absorption but also the substituted pyridine absorption are present (Figure 2.4). The FRET energy transfer enables the good separation between the excitation light and the rhodamine emission. The **py** emission (taken from intermediate **2-11)** and rhodamine excitation have sufficient spectral overlap to ensure the FRET process (Figure 2.5). The emission of compound **2-11** at room temperature is considered to be from a singlet excited state, and it is quenched by the ytterbium ion in **GBYb001**.

We observed a weak ytterbium emission at around 980 nm when we excited the complex at 355 nm in CH_3CN solvent. This emission is from the $^2F_{5/2} \rightarrow {}^2F_{7/2}$ transition of ytterbium ion (Figure 2.6). The ytterbium ion has no absorption band at 355 nm, and the emission is because of the energy transfer to ytterbium acceptor from **py** chromophore or the rhodamine unit. Direct excitation on the rhodamine at 570 nm does not produce ytterbium emission, so we conclude that the energy transfer is from the **py** chromophore. The donor nonradiative transition of the **py** donor is electric dipole allowed, and the acceptor transition is forced electric dipole and electric quadrupole allowed.

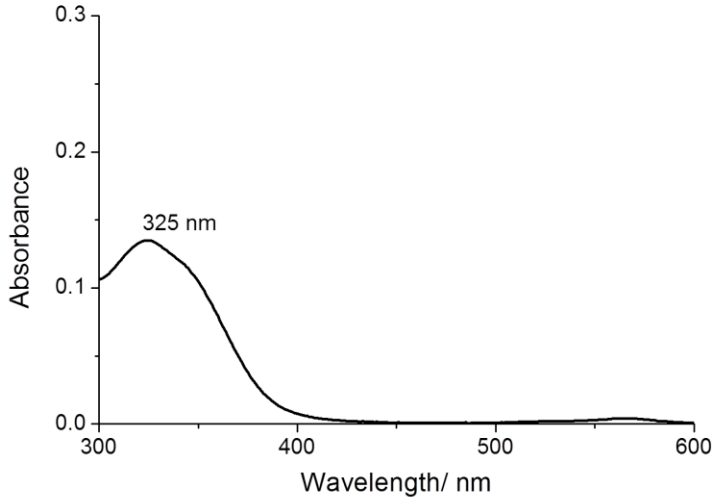

*Figure 2.2. UV-vis spectrum of **GBYb001** (5μM) in HEPES buffer.*

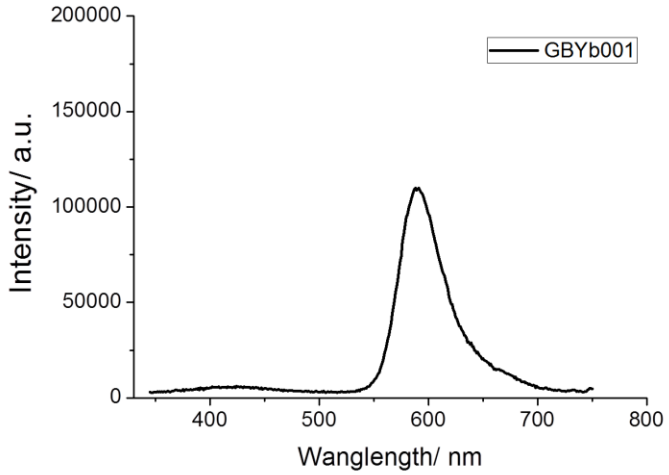

*Figure 2.3. Emission spectra of **GBYb001** (5 μM) in HEPES buffer (λ_{em} = 300 nm).*

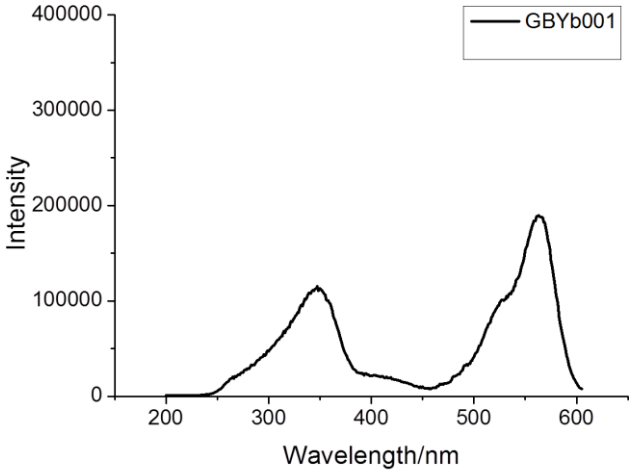

Figure 2.4. Excitation spectra of GBYb001 (5 μM) in HEPES buffer (λ_{em} = 615 nm).

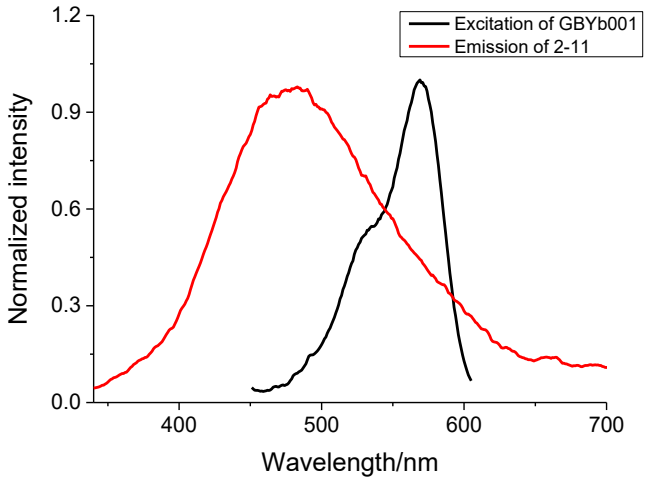

*Figure 2.5. Overlap of the emission spectrum of intermediate **2-11** (red) (5 μM) and excitation spectrum of ring-opened **GBYb001** (5 μM) triggered by Hg^{2+} (50 μM) in HEPES buffer solution.*

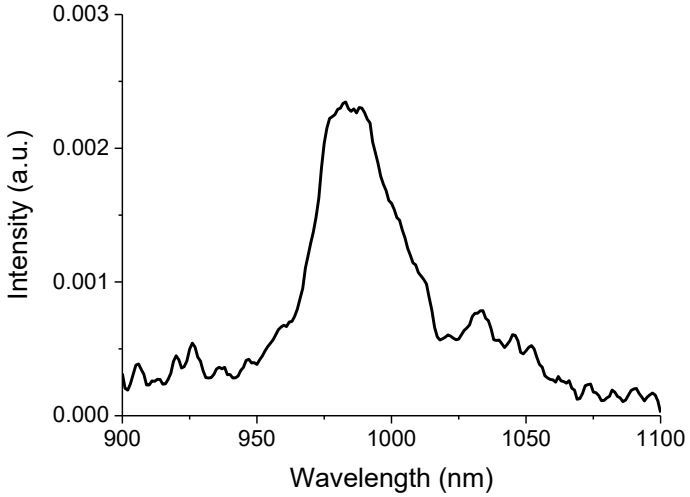

*Figure 2.6. Emission spectrum (λ_{ex} = 355 nm) of **GBYb001** (10 μM) in MeCN.*

2.2.3 Titration with Hg^{2+}

When added the mercury ion into **GBYb001** in the HEPES buffer solution, the transparent solution changed to red immediately. We observed a 22-time enhancement of the absorption intensity, and the absorption peak of rhodamine showed a 10 nm redshift (Figure 2.7). Meanwhile, the absorption band at 325 nm showed a slight decrease. This is not because of the dilution but suggests a change of the complex structure. On the other hand, when adding the mercury ion, there was no obvious absorption change of the solution of control **GBYb002** which has a similar structure but without the rhodamine part (Figure 2.). This indicates that the response towards the mercury ion is because of the rhodamine unit. The mercury ion induced the ring-opening of the spirocyclic ring at rhodamine unit. This occurs rapidly at room temperature in the buffer solution. The binding stoichiometry of mercury ion and **GBYb001** is 1:1 according to the Job's plot of the absorption bands of rhodamine unit, where the absorbance showed a maximum with 50% mole fraction (Figure 2.7, inset). We estimated the binding constant by nonlinear least-squares analysis[20] of the rhodamine absorption intensity at 575 nm (Figure 2.9). The value K_b is 2.05 ± 0.3 × 10^5 M^{-1}.

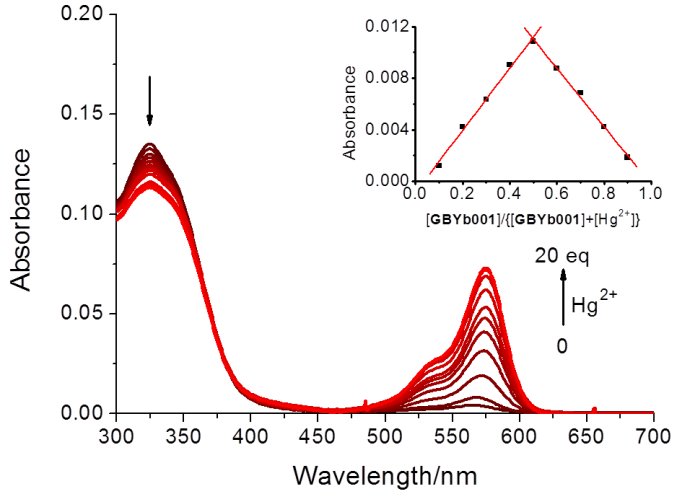

*Figure 2.7. Changes in the absorption spectrum of **GBYb001** (5 μM) in HEPES buffer solution upon titration with Hg^{2+} (0→20 equiv.). Inset: Job's plot at 575 nm, [**GBYb001**] + [Hg^{2+}] = 5 μM.*

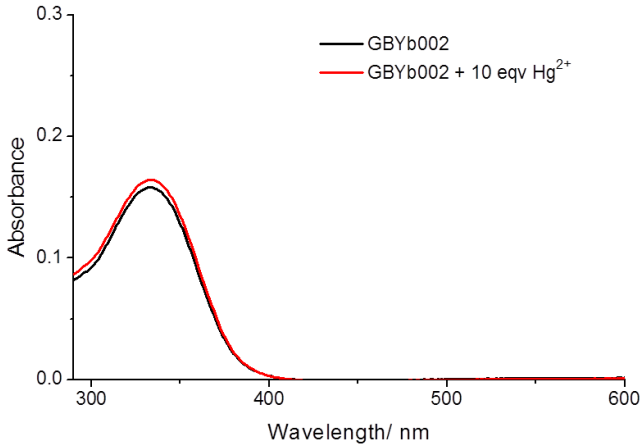

*Figure 2.8. The absorption spectra of **GBYb002** (5 μM) in HEPES buffer solution with and without Hg^{2+}.*

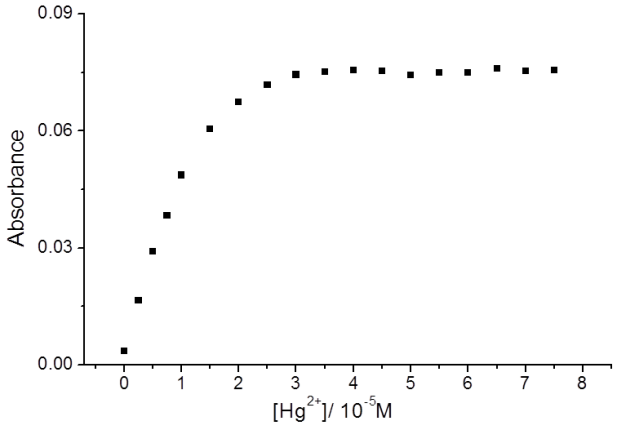

Figure 2.9. The absorption intensity enhancement of the visible light at 575 nm versus concentration of Hg^{2+}

The changes in the sensor fluorescence intensity were carried out in a HEPES buffer solution or acetonitrile solution. When adding the mercury ion to the solution, both the visible and NIR regions showed the turn-on emission upon the irradiation to the **py** chromophore (Figure 2.8). We rationalize that the enhancement of visible emission was due to the enhanced rhodamine absorption which increased the overlap with **py** emission. Therefore, the energy transfer from **py** unit to rhodamine unit is more efficient. The **py** emission is neglectable in comparison with the rhodamine emission upon exciation on the **py** unit (Figure 2.11). In the excitation spectra, both **py** unit and rhodamine moiety showed enhanced excitation bands by monitoring the rhodamine emission with the addition of mercury ions (Figure 2.10). The relative enhancement of the excitation band of **py** unit in the normalized excitation spectrum is larger than that of rhodamine excitation band upon the addition mercury ion (Figure 2.11). Hence the energy transfer from **py** to rhodamine is more efficient in ring-opened rhodamine. The emission enhancement is linearly proportional to the mercury concentration when it is less than 20 μM (Figure 2.8). The detection limit is (LOD) determined to be 150 nM (Figure 2.12) which is lower than that of our previous work, YbPor-**L**.[9] On the other hand, ytterbium emission enhancement is because of the absorption band shift of the py unit in acetonitrile (Figure 2.13). The ligand-ytterbium energy transfer provides a large separation between the absorption and emission bands. However, there was no ytterbium emission when we excited the

rhodamine unit, indicating that no energy is transferred from the rhodamine unit to ytterbium ion. The ytterbium emission after the addition of mercury ion showed a lifetime of 2.31 μs (Figure 2.14) and the quantum yield valued 0.012%. The lifetime differentiates the ytterbium emission from the shorter lifetime species. The detection limit from ytterbium emission was evaluated to be 5.0 μM (Figure 2.15), showing two times lower than our previous work.[9] The ytterbium emission locates in the biological window, where the light has deeper tissue penetration.[21]

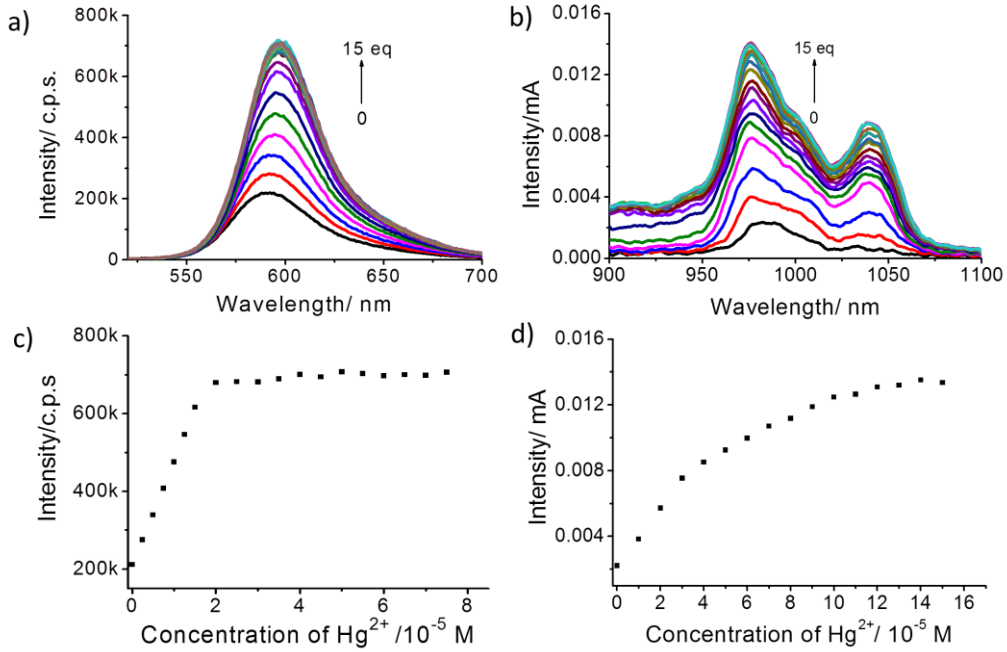

*Figure 2.8. a) Visible fluorescence response (λ_{ex} = 346 nm) of **GBYb001** (5 μM) upon addition of Hg^{2+} in HEPES buffer. b) The near-IR emission (λ_{ex} = 355 nm) of **GBYb001** (10 μM) in CH_3CN upon addition of Hg^{2+}. c), d) Plots of the enhancement at 596 nm and 980 nm, respectively.*

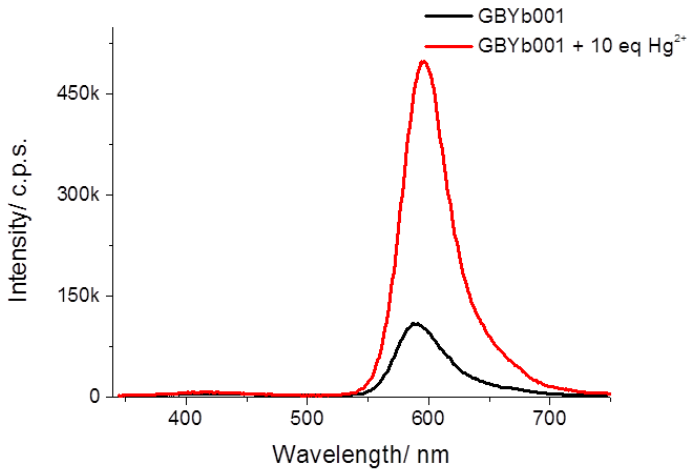

*Figure 2.9. Emission spectra (λ_{ex} = 300 nm) of **GBYb001** (5 μM) with and without Hg^{2+} (50 μM) in HEPES buffer.*

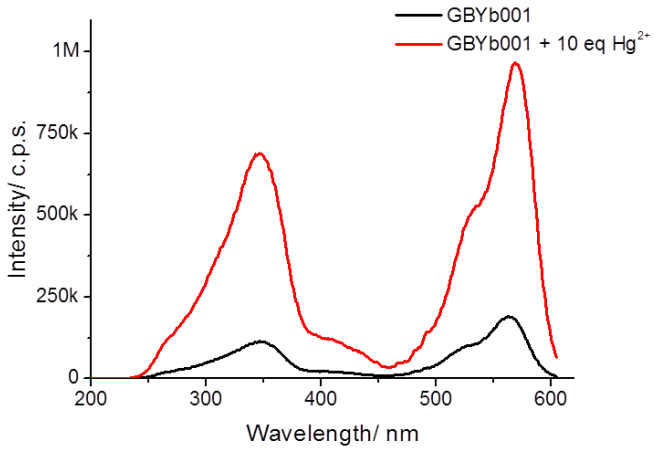

Figure 2.10. Excitation spectra of GBYb001 (5 μM) with and without Hg^{2+} (50 μM) in HEPES buffer (λ_{em} = 615 nm).

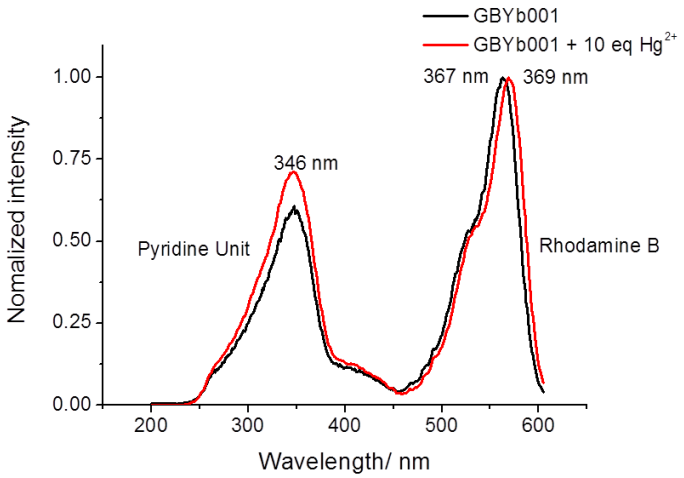

Figure 2.11. Normalized excitation spectra of ***GBYb001*** *(5 μM) with and without* Hg^{2+} *(50 μM) in HEPES buffer (*λ_{em} *= 615 nm).*

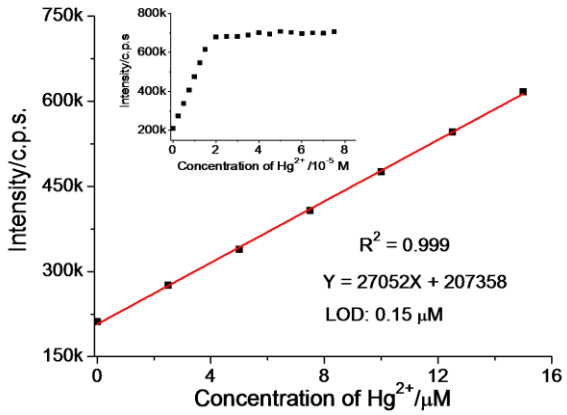

Figure 2.12. The linear intensity enhancement at 596 nm of ***GBYb001*** *(5 μM) in HEPES buffer (*λ_{ex} *= 355 nm) versus the concentration of* Hg^{2+} *added. The detection limit was estimated as 0.15 μM according to LOD = 3σ/S, where σ is the standard deviation of eleven blank signals and S is the slope of the calibration curve. Inset: The overall intensity enhancement of at 596 nm.*

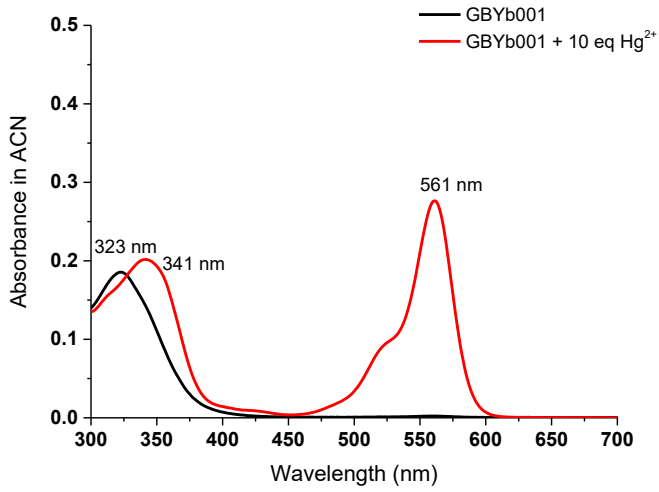

*Figure 2.13. The absorption spectra of **GBYb001** in CH_3CN (5 μM) with and without the addition of Hg^{2+}.*

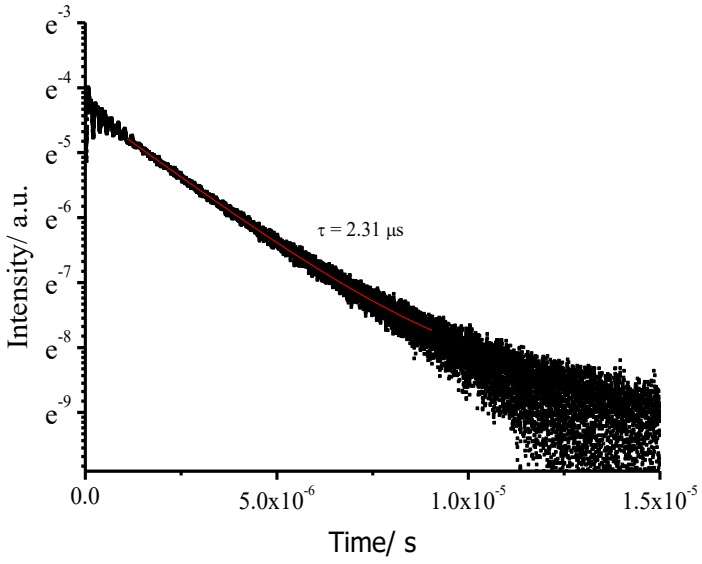

Figure 2.14. The decay of NIR emission (980 nm) of GBYb001 with Hg^{2+} in MeCN, excited at 355 nm.

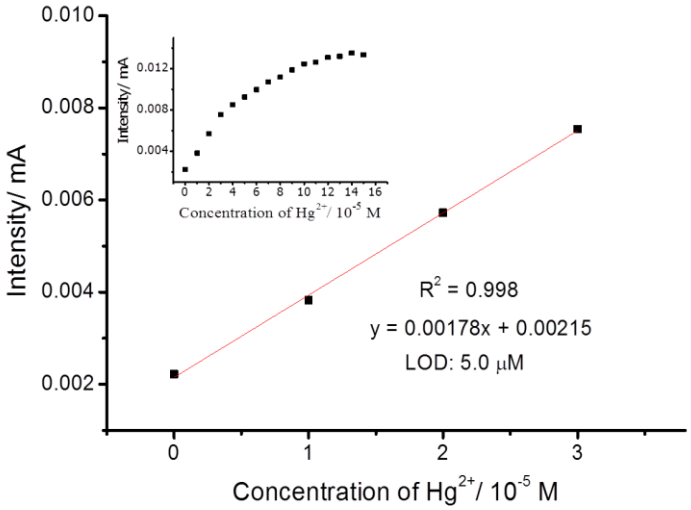

Figure 2.15. The linear intensity enhancement at 980 nm of ***GBYb001*** *(10 μM) in CH_3CN (λ_{ex} = 355 nm) versus concentration of Hg^{2+} added. The detection limit was estimated as 5.0 μM according to LOD = 3σ/S, where σ is the standard deviation of eleven blank signals and S is the slope of the calibration curve. Inset: The overall intensity enhancement of at 980 nm.*

2.2.4 Selectivity

To examine the selectivity of the mercury probe, both emission signals in visible and near-infrared ranges were investigated with adding various biologically and environmentally essential metal ions. The measurement conditions were the same as that for the mercury ion. The common metal ions in living organisms such as Ca^{2+}, K^{+} Mg^{2+}, Na^{+} had insignificant changes in both emission channels (Figure 2.16). The sensor also showed selectivity to mercury ion over a wide library of other transition metal ions, heavy metal ions, alkali-earth-metal ions and alkali-metal ions. The selectivity towards these ions indicates that the sensor can be potential for applications in the biological samples.

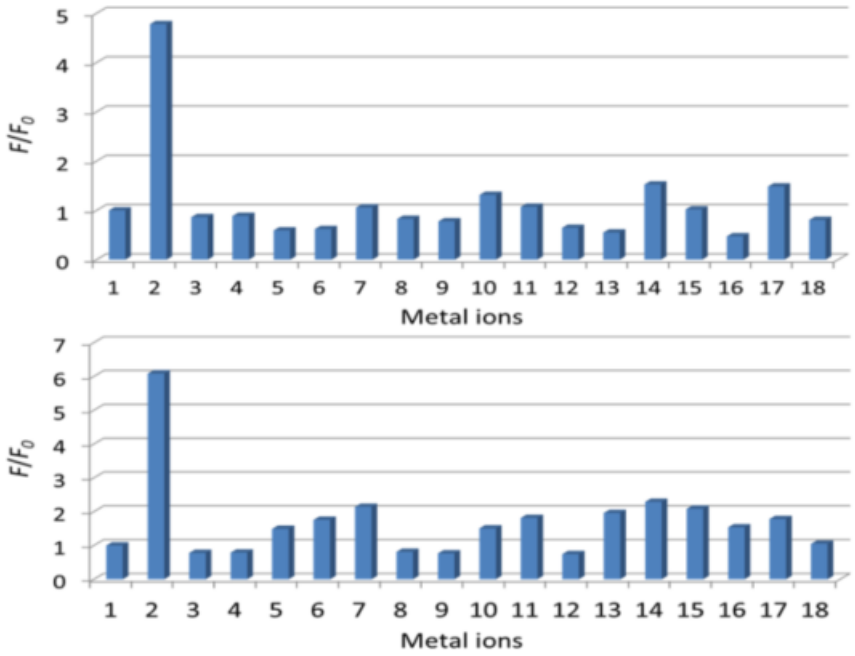

Figure 2.16. a). Visible fluorescence ratio of ***GBYb001*** *(5 μM, λ_{ex} = 525 nm) in HEPES buffer at 596 nm and b) NIR fluorescence ratio of* ***GBYb001*** *(10 μM, λ_{ex} = 355 nm) in CH_3CN at 980 nm. Metal ions: 1, blank (normalized as F_0); 2, Hg^{2+}; 3, Cu^{2+}; 4, Cu^{+}; 5, Co^{2+}; 6, Cd^{2+}; 7, Ca^{2+}; 8, K^{+}; 9, Li^{+}; 10, Fe^{3+}; 11, Fe^{2+}; 12, Cs^{+}; 13, Mg^{2+}; 14, Pb^{2+}; 15, Sn^{2+}; 16, Ni^{2+}; 17, Al^{3+}; 18, Na^{+}.*

2.2.5 Reversibility

We next examined the reversibility of the mercury probe. Cellular thiol-containing compounds, for instance, glutathione, cysteine, and peptides and proteins that contain thiol groups can detoxify the mercury. Since these compounds have high binding affinity to the mercury ions, we assume that the thiol group can remove the mercury ion on the mercury-**GBYb001** complex. This will recover the mercury-free sensor molecules. We chose the sodium sulphide as the thiol source because it has good dissociation capacity in the buffer solution. The addition of S^{2-} anions resulted in an immediate decrease in emission of the sensor to its original intensity. When adding the mercury ions again to the solution, the enhancement of emission could be recovered (Figure 2.17). We recorded three cycles of the turn-on and recovery of the sensor. This phenomenon suggested that the sensor can monitor not only the cellular mercury level but also the cellular thiol species, which removes the mercury in the cells.

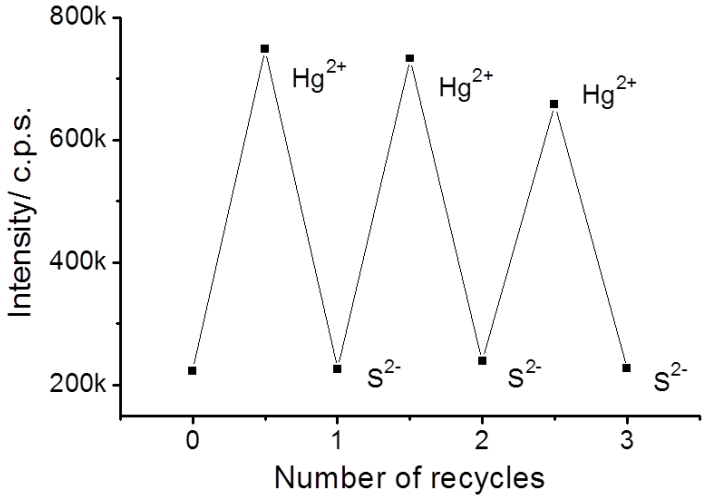

Figure 2.17. Luminescence intensity at 596 nm of GBYb001 (5μM) in HEPES buffer (λ_{ex} = 346 nm) on alternate addition of Hg^{2+} and S^{2-}.

2.2.6 Mechanism study

We use a La motif structure of the complex, **GBLa001**, to examine the ring-opening and closing mechanism by ^{1}H NMR. The measurements were carried out in DMSO-d_6 solvent with the addition of mercury ion and sulphide ion (Figure 2.18). The peak at 10.52 ppm, ascribed to the proton on the amide between the two aromatic rings, undertook a slight shift to 10.55 ppm when adding the mercury ion. The peak at 7.39 ppm disappeared and there was a new signal at 8.28 ppm appeared. The peak at 7.39 ppm belongs to the aromatic hydrogen adjacent to the spiro carbon. The peak appeared at 8.28 ppm belongs to the aromatic hydrogen adjacent to the carbonyl group on the spiro ring. Slight downfield shifts were also observed for other hydrogens on the same aromatic ring. The signals of hydrogens on the other two aromatic groups showed a similar trend. One the other hand, the tricyclic ring on the rhodamine moiety (6.32 – 6.52 ppm) and pyridine ring (8.38 ppm, 7.20 ppm) showed no change of the hydrogen peak positions. The reversibility of the sensor was also observed in the NMR spectrum. With the addition of sulphide in the measuring solution, the peaks recovered to their original positions because the sulphide ions removed the mercury ions from the sensor molecules and the spiro-ring recovered to

the ring-closed form. This correlated the emission changes of the probe in the presence of mercury and sulphide ions.

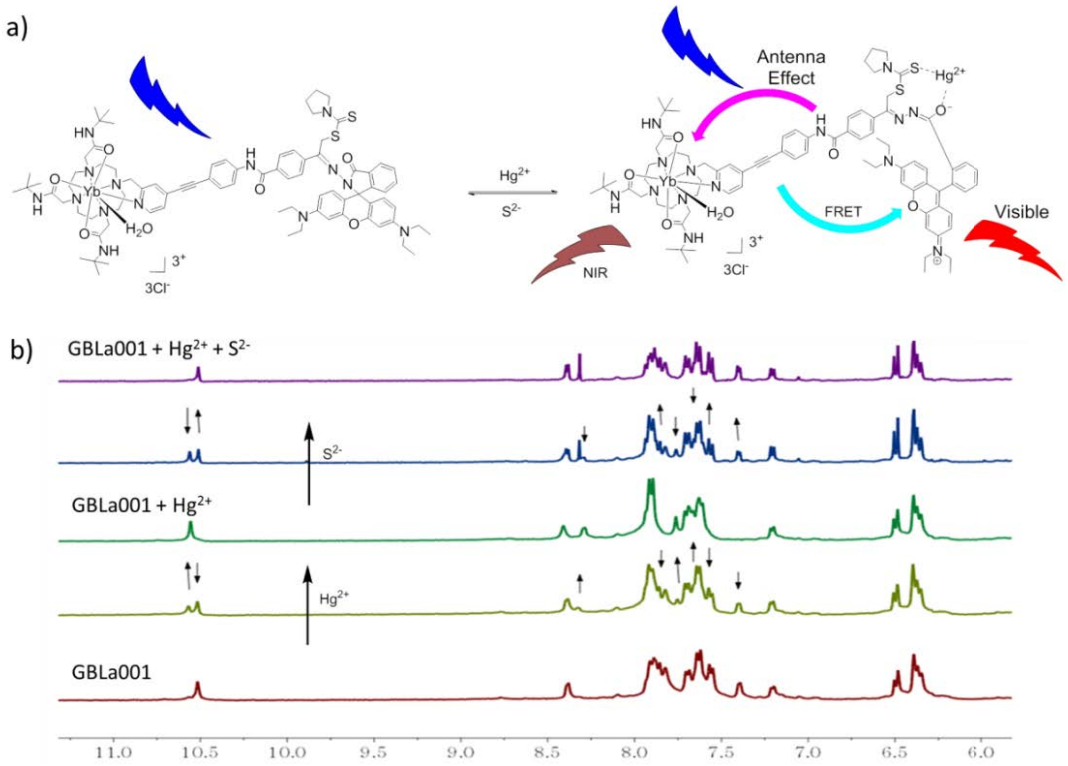

*Figure 2.18. a) Proposed mechanism of the spiro-ring opening and closing process triggered by Hg^{2+} and S^{2-}. b) ^1H NMR spectra of **GBLa001** in d-DMSO upon addition of Hg^{2+} and then S^{2-}.*

The energy transfer mechanism of the ring-opened form was studied by DFT calculations with molecular fragments of the sensor. The relative geometry of the **py** and rhodamine parts is shown in Figure 2.19a. The LUMO and HOMO of the **py** unit are displayed in Figure 2.19b and the lowest singlet transition is almost polarized along the axis of the triple bond. The closed-ring and open-ring units are shown in Figure 2.19c,d. The lowest singlet transition is more intense for the ring-opened form and the respective $S_0 \rightarrow S_1$ transitions are almost polarized orthogonally. Notably, there exists the electron delocalization across the three rings in the-opened form while it is broken in the ring-closed form.

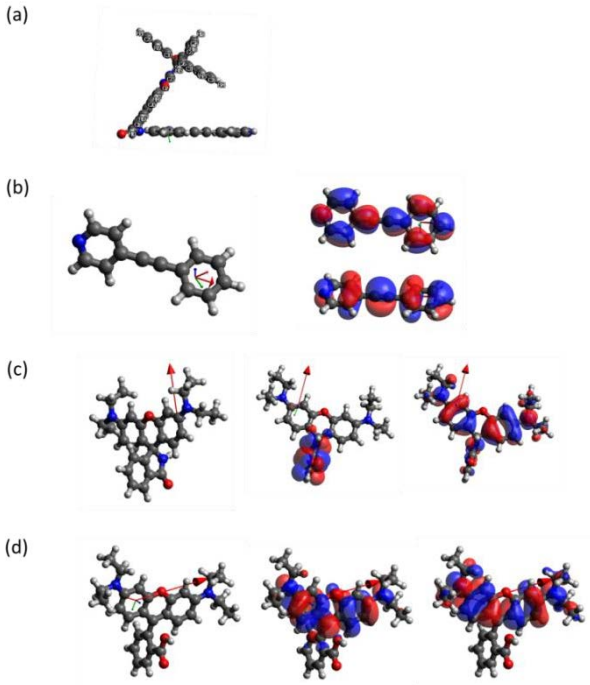

*Figure 2.19. The orientation of **py** and rhodamine parts; (b) **py** fragment with LUMO (top) and HOMO (bottom); (c) ring closed fragment with LUMO (left) and HOMO (right); (d) ring-opened fragment with LUMO (left) and HOMO (right). The dipole moments are indicated by red arrows.*

2.2.7 Confocal microscopic images, MTT and cellular uptake

We demonstrated the practical application of our sensor in fluorescence imaging of mercury ion in living MRC-5 cells by confocal imaging microscopy. The cells treated with **GBYb001** (5 μM) showed a weak luminescence. We observed a gradual increase of luminescence when the cells were treated with gradually increased concentration of mercury ions (Figure 2.20a-d). We then examined the reversibility of the sensor in the living cells by incubating the cells (that were treated with 10 μM of mercury ions) with 1 mM of sulphide ions for 1 h at 37 °C. The increased fluorescence intensity decreased to its initial levels (Figure 2.20e). This observation is consistent with the results in the buffer solution. Cytotoxicity and cellular uptake efficiency are critical features for biological sensors. The MTT result showed low cytotoxicity of **GBYb001** on the MRC-5 cells and the IC_{50} value is 88.5 μM (Figure 2.21). The cellular uptake was evaluated by incubating the sensor with MRC-5 cells for various time durations. The sensor showed good uptake by the MRC-5 cells, and the uptake reached the maximum in 30 min (Figure 2.24). The cellular experimental results suggested that

our sensor is suitable to visualize the cellular mercury concentration and to monitor the cellular detoxification of the mercury.

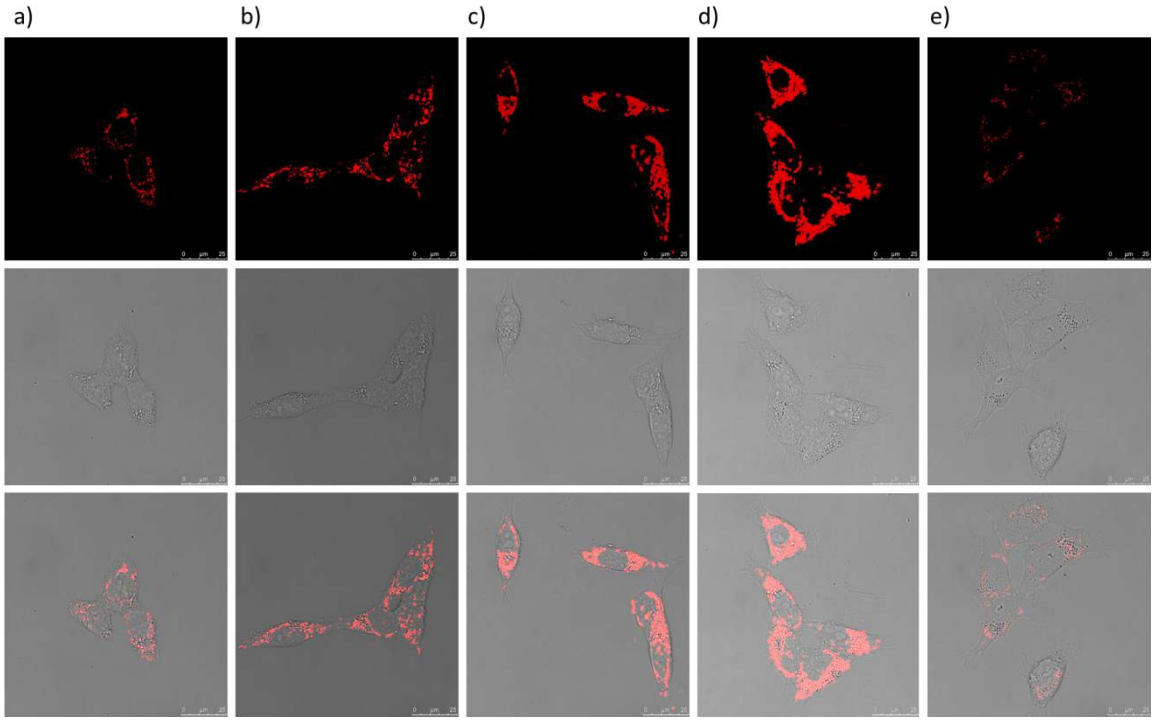

Figure 2.20. Confocal microscopic images of MRC-5 cells pretreated with 5 μM of ***GBYb001*** *for 1h and then treated with a) 0 μM, b) 2.5 μM, c) 5 μM, d) 10 μM* Hg^{2+} *for 0.5 h. e) Fluorescence image of same cells of d) further treated with 1 mM of* S^{2-} *and incubated for 1 h. top: fluorescence images; middle: bright field; bottom: overlay.*

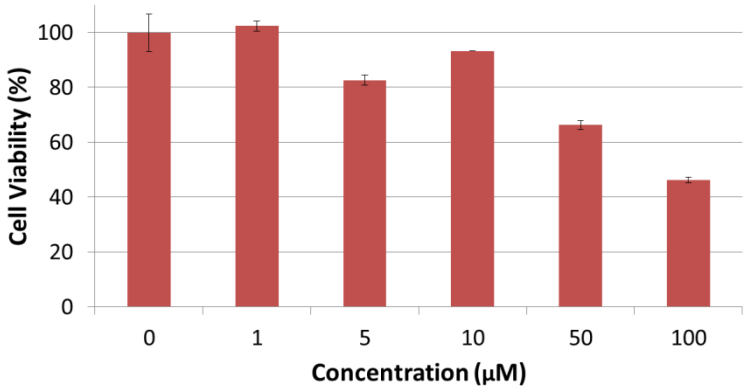

Figure 2.21. Cell Viability of ***GBYb001*** *towards MRC-5 cells (*IC_{50} *= 88.5 μM). The cells were incubated with gradient concentration (0 μM, 1 μM, 5 μM, 10 μM, 50 μM, 100 μM) of* ***GBYb001*** *for 24 h in the dark.*

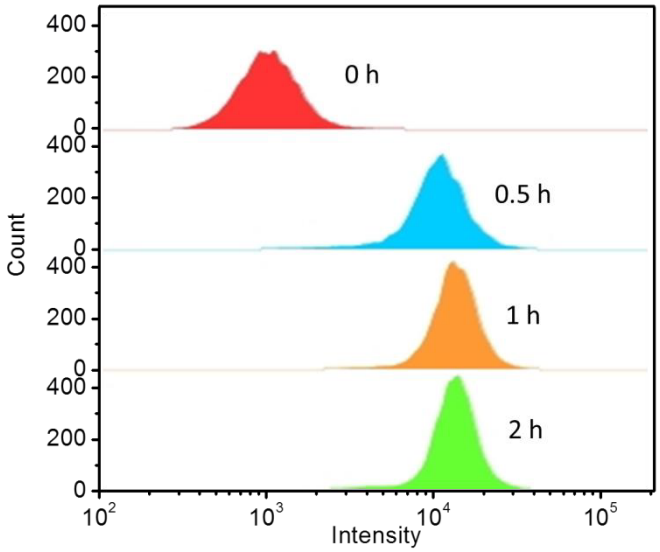

*Figure 2.22. Flow cytometric analysis of the cellular uptake by monitoring the emission of **GBYb001** in FL-2 channel (wavelength > 585 nm) in the MRC-5 cells. The cells were incubated with 5 μM of **GBYb001** for 0 h (control), 0.5 h, 1 h and 2 h in dark, and then treated with 50 μM of Hg^{2+} for 0.5 h.*

2.3 Conclusions

To conclude, we developed an ytterbium complex, **GBYb001**, as mercury sensor. The design was based on an ytterbium complex with connection of a rhodamine unit. The sensor is selective, sensitive and fastly responsive to the mercury ion. It has both visible and near-infrared responsive turn-on signals. The mechanism of ring-opening and recovery process was studied by NMR spectra using the La motif structure. With the large separation of excitation and emission in both emission channels, the biological compatible probe was successfully demonstrated for visualizing the concentration changes of mercury ion in living cells.

2.4 References

1. Q. Sun, B. Aguila, J. Perman, L. D. Earl, C. W. Abney, Y. Cheng, H. Wei, N. Nguyen, L. Wojtas and S. Ma, *J. Am. Chem. Soc.*, 2017, **139**, 2786-2793.
2. Z. Yan, H. Xue, K. Berning, Y. W. Lam and C. S. Lee, *ACS Appl. Mater. Interfaces*, 2014, **6**, 22761-22768.
3. Y. Li, S. He, Y. Lu and X. Zeng, *Org. Biomol. Chem.*, 2011, **9**, 2606-2609.
4. S.-K. Ko, Y.-K. Yang, J. Tae and I. Shin, *J. Am. Chem. Soc.*, 2006, **128**, 14150.
5. N. Huang, L. Zhai, H. Xu and D. Jiang, *J. Am. Chem. Soc.*, 2017, **139**,

2428-2434.
6. W. Duan, Y. Han, Q. Liu, J. Cui, S. Gong, Y. Ma, C. Zhang and Z. Sun, *Tetrahedron Lett.*, 2017, **58**, 271-278.
7. B. Liu, *Biosens. Bioelectron.*, 2008, **24**, 762-766.
8. M. Taki, K. Akaoka, S. Iyoshi and Y. Yamamoto, *Inorg. Chem.*, 2012, **51**, 13075-13077.
9. T. Zhang, C. F. Chan, R. Lan, W. K. Wong and K. L. Wong, *Chem.-Eur. J.*, 2014, **20**, 970-973.
10. S. K. Kim, K. M. K. Swamy, S.-Y. Chung, H. N. Kim, M. J. Kim, Y. Jeong and J. Yoon, *Tetrahedron Lett.*, 2010, **51**, 3286-3289.
11. Y.-K. Yang, K.-J. Yook and J. Tae, *J. Am. Chem. Soc.*, 2005, **127**, 16760-16761.
12. S. K. Patil and D. Das, *Spectrochim. Acta A Mol. Biomol. Spectrosc.*, 2019, **210**, 44-51.
13. H. N. Kim, M. H. Lee, H. J. Kim, J. S. Kim and J. Yoon, *Chem. Soc. Rev.*, 2008, **37**, 1465-1472.
14. Y. Yang, C.-Y. Gao, J. Liu and D. Dong, *Anal. Methods*, 2016, **8**, 2863-2871.
15. T. Zhang, B. Wu, Z. Zou, Y. Wu, J. Zheng, W.-K. Wong and K.-L. Wong, *J. Lumines.*, 2016, **170**, 187-193.
16. B. N. Ahamed and P. Ghosh, *Inorganica Chim. Acta*, 2011, **372**, 100-107.
17. J. A. Broussard, B. Rappaz, D. J. Webb and C. M. Brown, *Nat. Protoc.*, 2013, **8**, 265-281.
18. M. C. Heffern, L. M. Matosziuk and T. J. Meade, *Chem. Rev.*, 2014, **114**, 4496-4539.
19. N. Hildebrandt, C. M. Spillmann, W. R. Algar, T. Pons, M. H. Stewart, E. Oh, K. Susumu, S. A. Diaz, J. B. Delehanty and I. L. Medintz, *Chem. Rev.*, 2017, **117**, 536-711.
20. J. Bourson, J. Pouget and B. Valeur, *J. Phys. Chem*, 1993, **97**, 4552-4557.
21. A. M. Smith, M. C. Mancini and S. Nie, *Nat. Nanotechnol.*, 2009, **4**, 710-711.

Chapter 3 A Stoichiometric Terbium-Europium Dyad Molecular Thermometer: Energy Transfer Properties

3.1 Introduction

Luminescent materials for temperature sensing have attracted many attentions in environmental engineering, aeronautical engineering, and industrial processes[1-4]. They have excellent advantages over traditional thermometers including fast response, high sensitivity, and tolerance to extreme atmospheres[5-7]. Particularly, there is no additional requirement of emission intensity calibration for the self-referencing optical thermometers which are more accurate because of its noninvasive operation[8, 9].

Materials that contain two types of lanthanide ions are of great attraction for the design of a self-referencing thermal probes[10]. Lanthanide materials have properties including sharp emission bands[11, 12] and a large energy separation between the excitation and emission bands,[13] which makes them better than organic dyes or quantum dots[14]. Besides, lanthanide emissions have long lifetimes which is an important property for enhancing the signal-to-noise by time-gated techniques [15]. The temperature-dependent quenching and energy transfer between the dopant ions or between the host and lanthanide ion allow luminescent responses for different lanthanide ions with a change in temperature. Many lanthanide materials are used for temperature sensings, such as lanthanide nanocrystals[16], lanthanide metal-organic frameworks (MOFs)[5, 17], lanthanide-organic polymers[1], and lanthanide-doped complexes[18-20].

However, the doped materials are difficult to be synthesized with the same qualities and identical concentrations by different preparation batches; the donor-acceptor distances are random and need to estimate by statistics treatment. In

**A version of this chapter has been included in the published paper "A stoichiometric terbium-europium dyad molecular thermometer: energy transfer properties. Light: Science and Applications, 2018, 7, 96".*

the mixed doping system, it also has donor-donor or acceptor-acceptor migrations. This makes the energy transfer kinetics more complicated. Hence, the hetero-dinuclear lanthanide complex is potential as a self-calibrated thermometer because it has a fixed donor-acceptor distance (e.g. Figure 3.1),[12] definite structure and stoichiometric donor-acceptor ratio. The donor-acceptor distance in the dinuclear complex is fixed so that the energy transfer rates study does not need statistical treatment. With different lanthanide ions at each binding site, there are less donor-donor and acceptor-acceptor energy migrations. The chromophore of lanthanide complexes has large absorption cross-section and largely increase the light-harvesting ability for the lanthanide ions. However, the synthesis of hetero-dinuclear complexes is challenging and only a few literatures report[18,21] the energy transfer study by hetero-dinuclear lanthanide complexes, but with homo-dinuclear complex as an impurity in the hetero-materials. Even though researchers put many efforts on developing strategies to synthesize pure hetero-polynuclear complexes[22, 23] with different lanthanide ions which are chemically similar, there remains challenging to synthesize hetero-dinuclear complexes by a simple strategy. This challenge is severe for lanthanide chemists.

Herein, we develop two hetero-dinuclear lanthanide complexes, **cycEu-phTb** and **cycTb-phEu**, as luminescent temperature probes. These two types of lanthanide ions are coordinated on two different coordination sites by two separated steps to avoid forming the homo-dinuclear complexes. These dinuclear complexes with clear validation of the metal ratio and the fixed donor-acceptor distance outweigh other doping materials in terms of the understanding energy transfer and temperature monitoring performance. The 1,10-phenanthroline (**phen**) moiety together with pyrrolidine dithiocarbamate was used as ligand to coordinated with a series of lanthanide ions.[24] The cyclen was widely used as ligand to coordinate with lanthanide ions and it has been connected with phen to form lanthanide complexes. In our dinuclear complexes, the cyclen and phen are used as binding site. The 1,10-phenanthroline moiety is used as a chromophore to harvest light and transfer the energy to terbium and europium. The emission ratio of europium over terbium

increases as the temperature rises. The temperature increase causes the europium and terbium emissions to decrease, but with different rates. This is because of processes of different energy transfer from chromophore to terbium and europium as well as the energy transfer from terbium to europium ion. Complexes **cycEu-phTb** and **cycTb-phEu** (Figure 3.1) exhibit distinct photophysics because of the unique binding site for each ion. The energy transfer processes have been investigated in detail.

3.2 Results and discussion

3.2.1 Structure

We modelled the 166-atom structure of the complex **cycTb-phEu** by MOPAC[25, 26] using the semi-empirical software RM1 in the programme LUMPAC.[27, 28] Both europium and terbium are 8-coordinated. Terbium ion is coordinated to four oxygen atoms and four nitrogen atoms while the europium ion is coordinated to six sulphur atoms and two nitrogen atoms. A simplified 100-atom structure was used to optimize the structure with the aliphatic rings replaced by CH_2 groups in ORCA[24-27] (Figure 3.1). The bond distance comparison in the two different optimizations is detailed in Table 3.1.

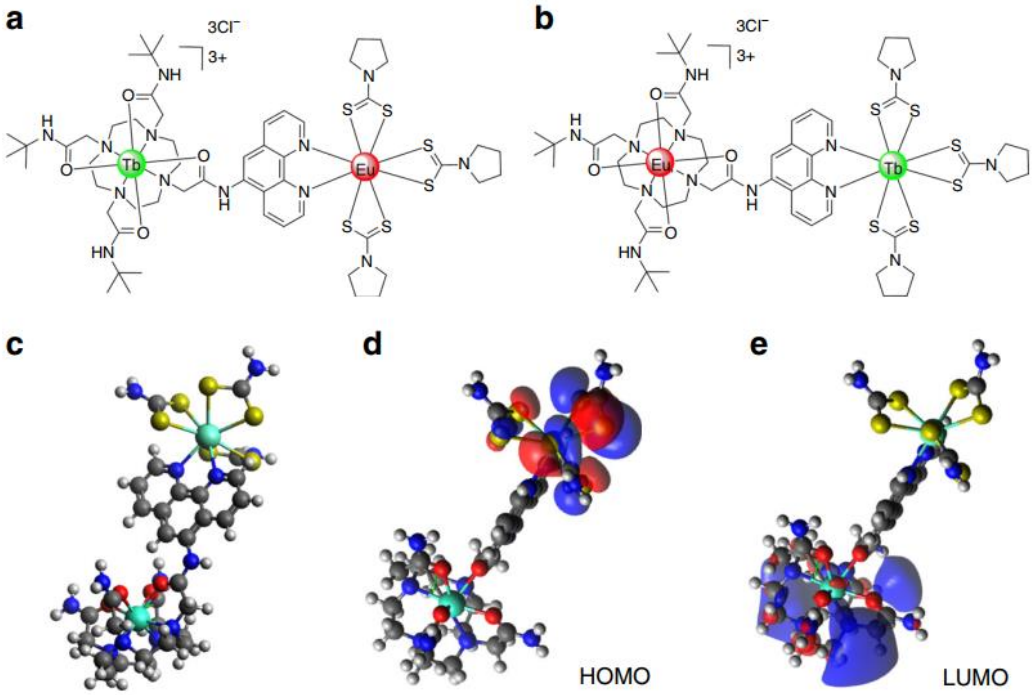

Figure 3.1. The structures of complexes (a) ***cycTb-phEu*** *and (b)* ***cycEu-phTb*** *and (c) optimized geometry of the simplified 100-atom structure of* ***cycTb-phEu*** *as determined using the PBeh-3c functional[29] with basis def2-SVP[30] and effective core potentials for Tb and Eu[31] in ORCA[32]. The charge-transfer nature of the (d) HOMO and (e) LUMO are shown.*

Table 3.1. Comparison of bond distances (in Å) from optimizations of (a) 166-atom optimization using RM1 in MOPAC; (b) 100-atom optimization of simplified structure using PBeh-3c in ORCA.

Bond distance	MOPAC[a]	PBeh-3c[b]
Eu-S	2.85±0.06	2.92±0.01
Eu-N	2.51±0.09	2.56±0.00
Tb-O	2.30±0.05	2.30±0.04
Tb-N	2.40±0.11	2.41±0.07
Tb-Eu	10.46	10.69

3.2.2 Synthesis

The synthetic scheme of complexes and ligands is shown in Scheme 3.1. Compound **3-1** was synthesized by substituting the 2-bromoacetyl bromide with 1,10-phenanthrolin-5-amine. Ligand **3-2** was synthesized by substituting the compound **3-1** with a tri-armed cyclen derivative. Complexes **3-3** were synthesized by coordinating one equivalent lanthanide ion with ligand **3-2** in MeOH and H_2O mixed

solution. The pyrrolidine dithiocarbamate is chosen as ligands to coordinate on the second binding sites because pyrrolidine dithiocarbamate has less interference with the energy transfer process. The complexes **3-4** (**cycLn^1-phLn^2**) were synthesized by coordinating three equivalents of ammonium pyrrolidine-1-carbodithioate and one equivalent lanthanide ion to the complex **3-3**. The La motif complex showed that three pyrrolidine dithiocarbamates were successfully coordinated to the complex in the ^{1}H NMR data, which agrees with a previous report[24]. This synthetic methodology provides a simple way to synthesize hetero-dinuclear complexes that contain different lanthanide ions.

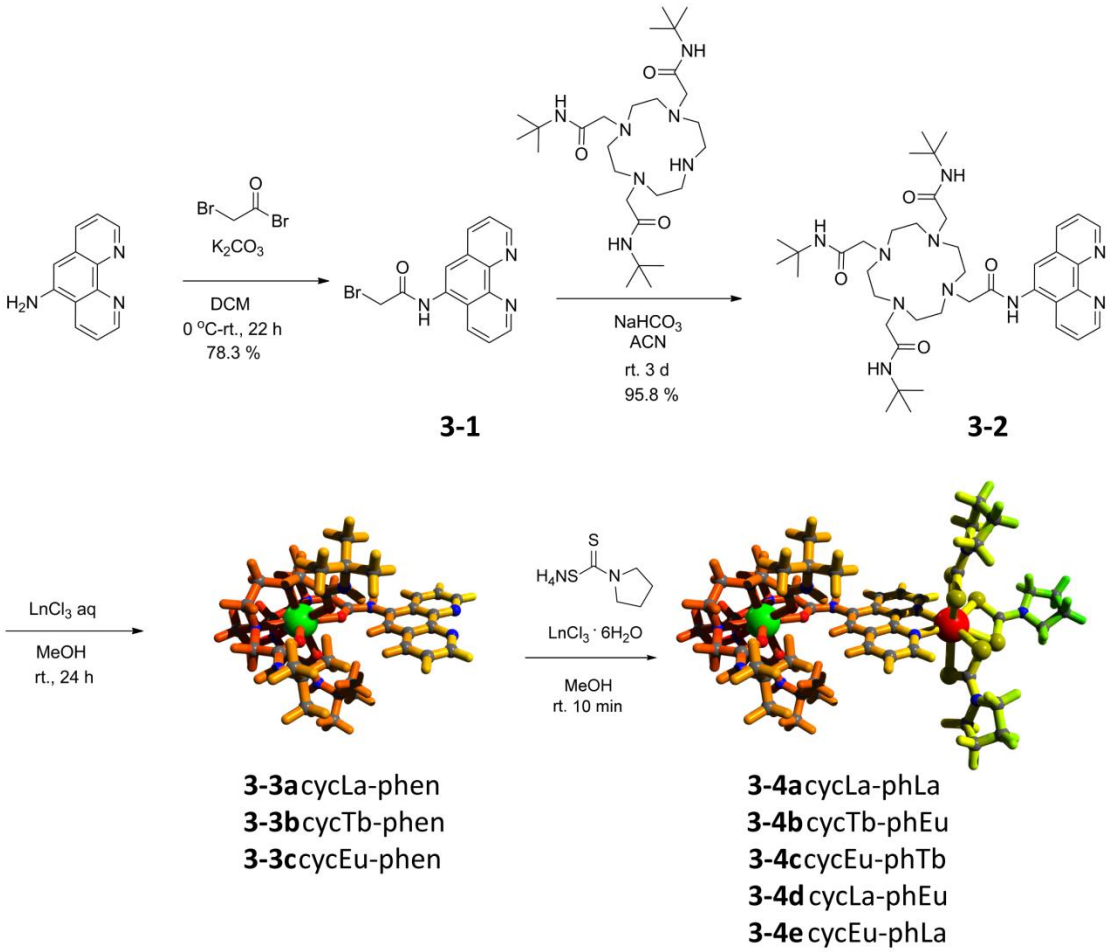

Scheme 3.1. Synthesis of ligands and complexes.

3.2.3 Singlet and triplet states

We investigate the singlet and triplet levels of the chromophore by its La motif

complex because La ions have no 4f-4f energy levels and it produces a heavy atom effect to the ligand for the generation of triplet emission via the intersystem crossing. We measured the singlet emission by the **cycLa-phLa** complex at room temperature and recorded the triplet emission at 77 K (Figure 3.2). The **cycLa-phLa** complex showed an emission band peaked at 398 nm with energy of 25121 cm^{-1} by room temperature excitation at 273 nm (Figure 3.2b), the emission band is attributed to the singlet transition of the chromophore. At 77 K, the singlet emission intensity relatively decreases, the emission band redshifts. We observed the triplet emission dominant in the green light range (Figure 3.2a). The $T_1 \rightarrow S_0$ transition at 497 nm (20124 cm^{-1}) is determined by the zero phonon line, and we found a progression to lower energy of the symmetric ring C=N mode with 1471±6 cm^{-1}. The excitation spectrum of the triplet state shows the population of T_1 by a singlet level at around 400 nm (Figure 3.3a). A further singlet state at 273 nm was demonstrated in the excitation spectrum of the singlet emission (Figure 3.3b). At this range, we observed that all the **cycLn-phLn** complexes in solution have a strong band, for example, **cycLa-phEu** absorption in Figure 3.2c. Actually, the excitation spectra of **cycEu-phLa** and **cycLa-phEu** at room temperature show that other singlet states participate in the energy transfer from ligand to lanthanide ion (Figure 3.4 and Figure 3.5). We measured the singlet lifetime at room temperature with a value of 1.6 ns and the triplet lifetime at 77 K with a value of 0.26 s.

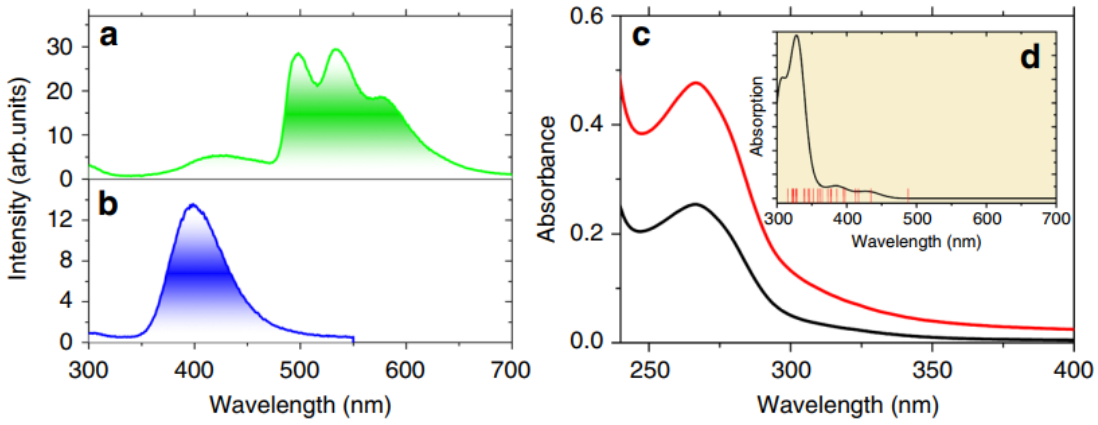

*Figure 3.2. Optical spectra. The 77 K phosphorescence (a) and 298 K fluorescence (b) of **cycLa-phLa** (λ_{exc} = 273 nm) in the solid state. (c) Room temperature absorption spectrum of **cycLa-phEu** in buffer solution at pH 7.4 at two concentrations: black, 5*

μM; red, 10 μM. The insert (d) shows the simulated absorption spectrum in the gas phase between 300 and 700 nm as determined from LUMPAC[27] with the triplet levels marked by vertical lines. The singlet transitions were broadened with widths of 2000 cm^{-1}.

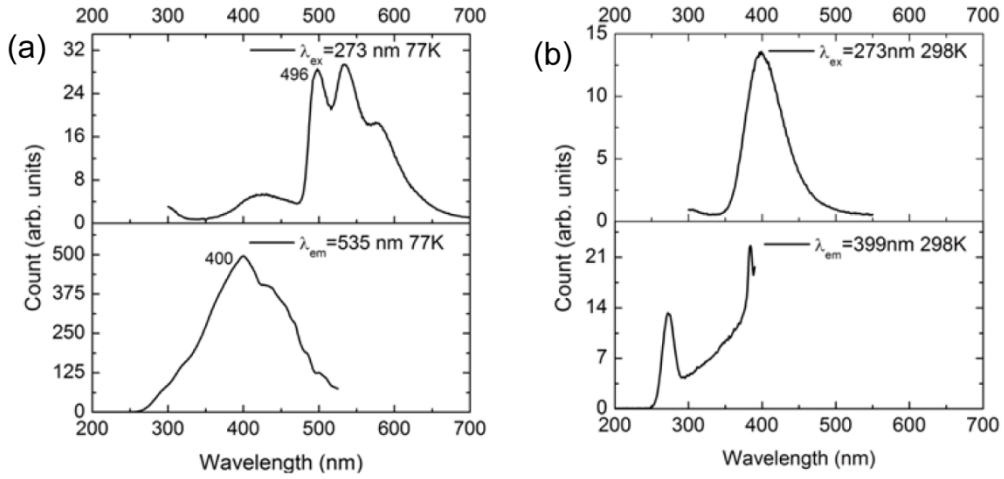

*Figure 3.3. (a) Triplet emission and excitation spectra of **cycLa-phLa** in the solid-state at 77 K. (b) Singlet emission and excitation spectrum of **cycLa-phLa** at 298 K in the solid-state.*

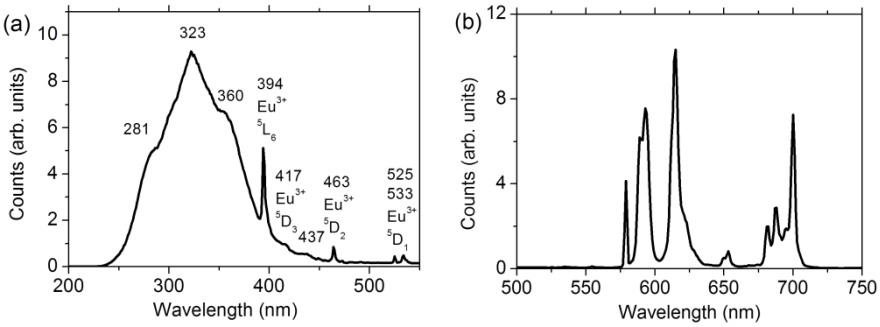

*Figure 3.4. Excitation (λ_{em} 615 nm) and emission (λ_{exc} 321 nm) of **cycEu-phLa** in the solid phase at room temperature. Note the weak $^5D_1$ emission in this system.*

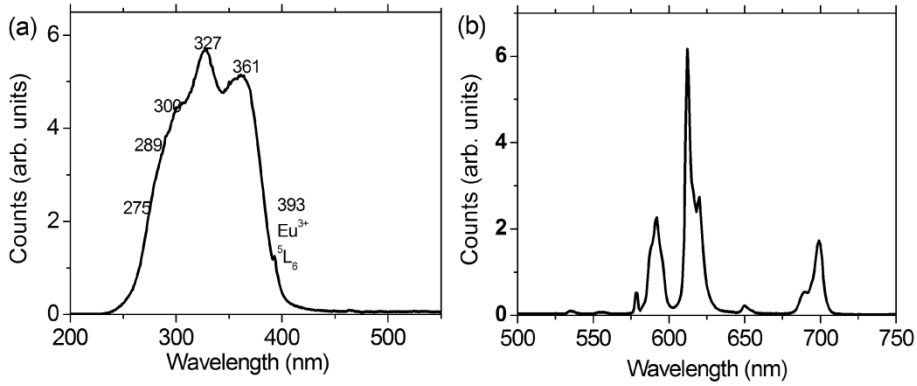

*Figure 3.5. Excitation and emission of **cycLa-phEu** in the solid phase at room*

temperature. Note the weak $^5D_1$ emission in this system. $^5D_1 \rightarrow {}^7F_0$ is at 525 nm (19048 cm^{-1}) and bands are observed at 534.6, 552.8 and 558.4 nm (i.e., 342, 948 and 1140 cm^{-1} to lower energy).

3.2.4 Lanthanide luminescence at low temperature

We measured the low-temperature emission spectra of the complexes **cycTb-phEu** and **cycEu-phTb** at 10 K at 355 nm excitation (Figure 3.6). The emission spectra show the characteristic emission bands: $^5D_0 \rightarrow {}^7F_J$ (J = 0-6) for europium and $^5D_4 \rightarrow {}^7F_J$ (J = 6-4) for terbium, respectively. In both cases, the europium emission dominates. The forced electric dipole transitions ($^5D_0 \rightarrow {}^7F_2$ and $^5D_0 \rightarrow {}^7F_4$) are stronger than the magnetic dipole-allowed transition ($^5D_0 \rightarrow {}^7F_1$). The $^5D_0 \rightarrow {}^7F_0$ transition which can be found in the C_n, C_{nv}, and C_s symmetry, showed a sharp band in both complexes, implying that only one type of binding mode is in each complex. Table 3.3 and Table 3.4 show the spectral details with the derived europium and terbium energy level. For the europium emission, the main difference between the two complexes is that $^5D_0 \rightarrow {}^7F_4$ transition of **cycEu-phTb** is stronger and has more resolved bands. Interestingly, when the lanthanide ions in the cyclen sites, their emission peaks are shaper for both europium and terbium because the cyclen site is more rigid than the phen site.

The $^5D_0 \rightarrow {}^7F_2$ transition is hypersensitive and more affected by the coordinative atmosphere than other forced electric dipole transitions. This makes the $^5D_0 \rightarrow {}^7F_2$ peak good indicator of the symmetry of the binding site.[33] The area ratio of the $^5D_0 \rightarrow {}^7F_2$ is 3.93 times of $^5D_0 \rightarrow {}^7F_1$ for **cycTb-phEu** and 2.33 times for **cycEu-phTb.** The $^5D_0 \rightarrow {}^7F_6$, which is forced electric dipole transition, shows a very week emission peak in both **cycTb-phEu** and **cycEu-phTb**.

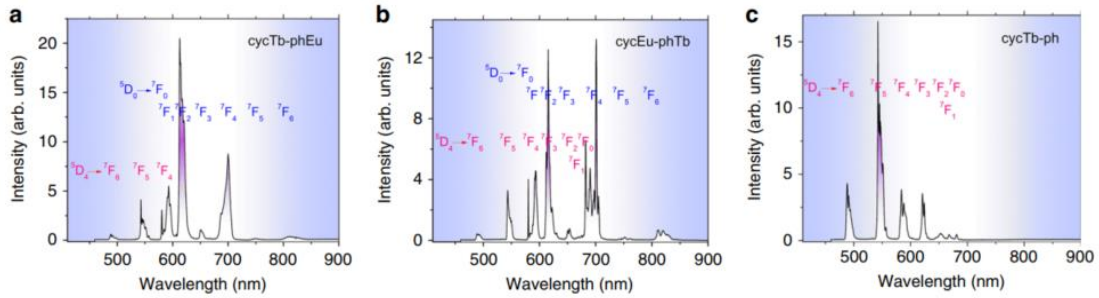

*Figure 3.6. The emission spectra (λ_{exc} = 355 nm) of complexes **cycTb-phEu** (a), **cycEu-phTb** (b) and **cycTb-phen** (c) at 10 K in the solid state. The Tb^{3+} transitions are marked in red, and those of Eu^{3+} are marked in blue.*

Figure 3.6c shows the **cycTb-phen** emission spectrum at 10 K. The Tb^{3+} surrounding environment is the same as the dinuclear complex **cycTb-phEu** (Figure 3.6a) though the $(pdtc)_3Eu$ part is not present. The terbium-europium distance in the complex **cycTb-phEu** is 10.6±0.1 Å. The crystal field levels of terbium ion of **cycTb-phen** and **cycTb-phEu** are the same within experimental error as shown in Figure 3.6a and c and deduced in Table 3.3. For instance, the splittings of the emission peaks $^7F_5$ and $^7F_6$ are 407±5 cm^{-1} and 494 cm^{-1}, respectively, in both complexes. This gives the „spectroscopic vision" of terbium ion and shows the atomic core-like nature of 4f orbitals so that the crystal field for the terbium ion is effectively the same for both terbium complexes.

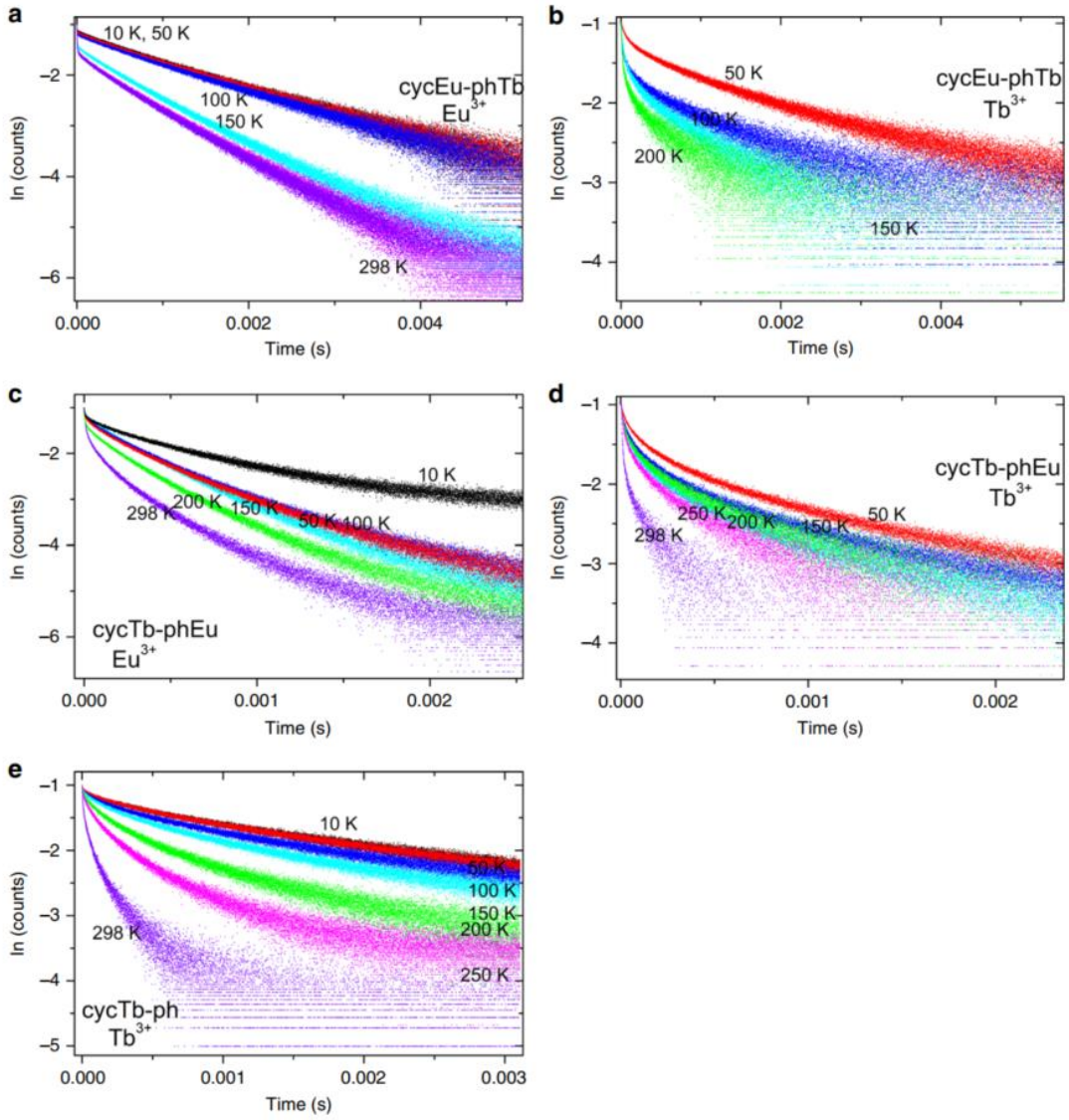

Figure 3.7. $^5D_0 \rightarrow {}^7F_4$ *Eu^{3+} and* $^5D_4 \rightarrow {}^7F_5$ *Tb^{3+} emission decays (λ_{exc} = 355 nm) at different temperatures:* ***cycEu-phTb*** *(a) Eu^{3+} and (b) Tb^{3+};* ***cycTb-phEu*** *(c) Eu^{3+} and (d) Tb^{3+};* ***cycTb-phen*** *(e) Tb^{3+}. Black, 10 K; red, 50 K; blue, 100 K; cyan, 150 K; green, 200 K; magenta, 250 K; and violet, 298 K.*

3.2.5 Emission decay lifetimes of Tb^{3+} and Eu^{3+} and temperature dependence

The emission decay for the $^5D_0$ (europium) and $^5D_4$ (terbium) was measured by the peaks of $^5D_0 \rightarrow {}^7F_4$ transition of europium and $^5D_4 \rightarrow {}^7F_5$ transition of terbium because these peaks are well separated from other emission peaks. When excitated on the phen chromophore at 355 nm, the energy transfers from chromophore to europium and terbium ions. A further Tb-Eu energy transfer is well-documented in the literature[34-40]; however, only a very weak emission is observed when excited at 490

nm because of the week absorption of the terbium ion. Thus, we were unable to *directly* investigate the Tb-Eu energy transfer by 490 nm ($^5D_4 \rightarrow {}^7F_6$) excitation. Figure 3.7a–d displays the europium $^5D_0$ and terbium $^5D_4$ emission decays of both complexes **cycEu-phTb** and **cycTb-phEu** at different temperatures, Figure 3.7e illustrates the terbium decay of complex **cycTb-phen**. We analysed the decay data using mono- and bi-exponential functions as well as the integration of the decay curves.

Generally, the emission decays are not mono-exponential because of the initial faster decay, and the mono-exponential behaviour increase with time, as it shows mono-exponential behaviour after ~0.2 ms. The europium decay in complex **cycEu-phTb** (Figure 3.7a) comes closest to the mono-exponential decay behaviour. When we take the values measured after ~0.2 ms of the excitation pulse, the $^5D_0$ excited state lifetimes decrease from 0.34 ms to 0.25 ms in **cycTb-phEu** and from 0.64 to 0.58 ms in **cycEu-phTb** as the temperature increases from 10 K to room temperature. This may be because of the back-transfer to $^5D_1$ as well as multiphonon relaxation. The enhanced non-radiative decay caused by increasing the temperature can be another possible reason for the decrease of lifetimes. The $^5D_4$ lifetimes of terbium have greater changes, for instance, in complex **cycTb-phEu**, the lifetime changes from 0.42 ms to 0.11 ms from 10 K to 298 K and the lifetime of **cycEu-phTb** changes from 0.65 ms to 0.13 ms when the temperature increases from 10 K to 200 K. The "steady-state" lifetime, τ_{ST}, have the same trend but are different in magnitude. Additional energy transfer processes are thus involved, such as terbium-europium energy transfer.

3.2.6 Energy transfer from Tb^{3+} to Eu^{3+}

Ideally, this energy transfer can be assessed by a comparison of lifetimes of **cycTb-phEu** and its La or Gd motif structure; however, we considered the decays of **cycTb-phEu** and **cycTb-phen** as an alternative estimation since we did not synthesize the **cycTb-phLa**. The likely pathways[34-40] of energy transfer are from terbium $^5D_4$ (20482 cm^{-1}) to europium $^5D_1$ and $^5D_0$ with 1434 cm^{-1} and 3249 cm^{-1} energy differences. The europium $^5D_1$ has the lowest crystal field level at 19048 cm^{-1}

as we can see in Figure 3.5, the literature reported a value of ~19100 cm^{-1} [41]. The europium $^5D_0$ has energy level at 17233 cm^{-1} as shown in Table 3.3. The participation of europium $^5D_1$ in Figure 3.3a and b is not observed, particularly when compared with the **cycLa-phEu** spectrum (Figure 3.5), supporting the direct energy transfer from terbium to europium $^5D_0$, not to $^5D_1$. From first order selection rules[42], the $^5D_4$ – $^7F_6$, $^7F_5$ pathways involve an electric quadrupole and/or forced electric dipole transition. It is dipole and quadrupole forbidden to first order in the $^7F_0$ – $^5D_0$ transition, although it is both electric quadrupole and forced electric dipole allowed for the thermally-assisted $^7F_1$ – $^5D_0$ transition. Both $^7F_0$ – $^5D_0$ and $^5D_4$ – $^7F_6$ are forbidden by the exchange[43] selection rule, $|J - J'| = 0, 1$ with $J = 0 \leftrightarrow J' = 0$ forbidden. The Eu^{2+}-Tb^{4+} charge transfer state was not considered.

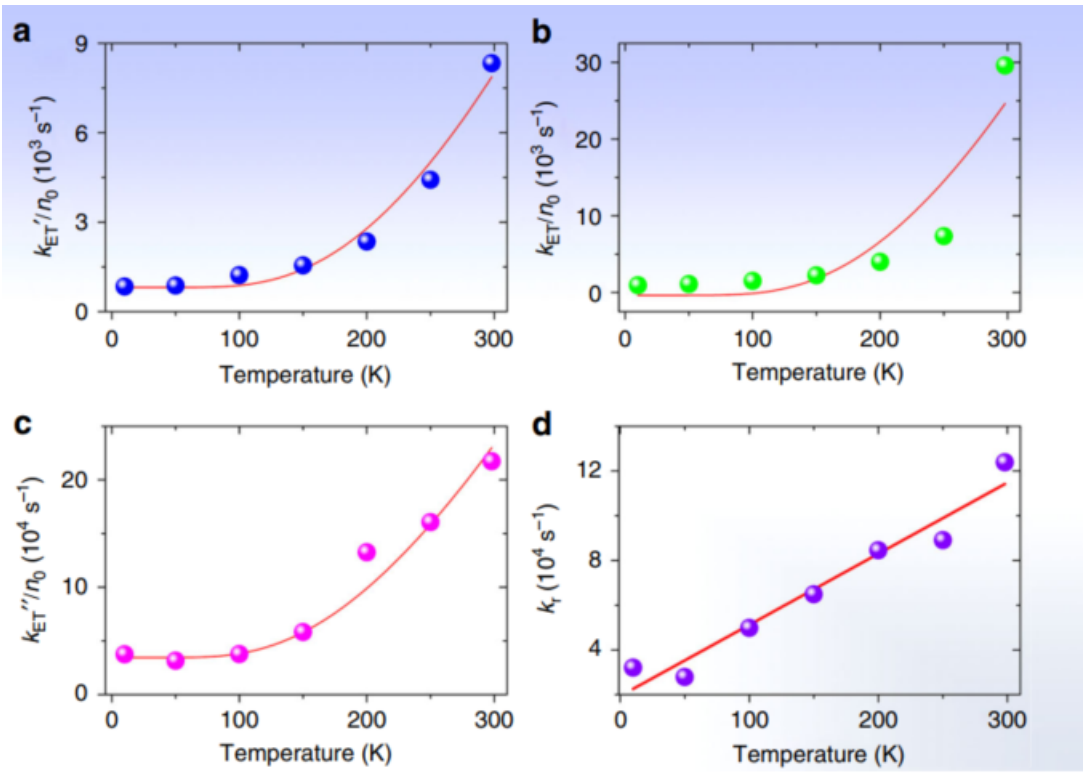

Figure 3.8. Simulation of experimental values for the Tb^{3+} – Eu^{3+} energy transfer rate versus temperature using Eq. 2: (a) k_{ET}' with values of a = 46.9 K^{-1} s^{-1} and b = 809 s^{-1}; (b) k_{ET} with values of a = 166 K^{-1} s^{-1} and b = -369 s^{-1}. (c) k_{ET}'' with values of a = 2793 K^{-1} s^{-1} and b = 34500 s^{-1}. (d) Linear plot of rise time of subtracted decay curves (Table 3.2) against temperature with a fitting of y = (1.93±0.58) + (318±32)x, R_{adj}^2 = 0.941.

*Table 3.2. Temperature variation of long-term decay constants, k_{TbEu} and k_{Tb}, for $^5D_4$ Tb^{3+} emission in **cycTb-phEu** and **cycTb-phen**. Temperature variation of Tb – Eu energy transfer rates deduced from the long-term lifetimes (k_{TbEu} - k_{Tb} = k_{ET}'), direct*

*subtraction of decay curves ($1/\tau_1 = k_{ET}$), and steady-state lifetimes ($1/\tau_{ST}$(**cycTb-phEu**) – $1/\tau_{ST}$(**cycTb-phen**) = k_{ET}", with τ_{ST}). The steady-state lifetime is determined by integration of the decay curves:* $\tau_{ST} = \int_0^\infty \frac{I(t)}{I(0)} dt$,. *The fitted parameter $k_r = 1/\tau_2$.*

Temp (K)	Rate constant (s^{-1})					
	k_{TbEu}	k_{Tb}	k_{ET}"	k_{ET}	k_{ET}""	k_r
10	2398	1555	843	943	35507	32062
50	2421	1545	876	1103	29165	27863
100	2740	1523	1217	1493	34131	49826
150	3086	1583	1503	2118	51931	64851
200	3751	1563	2188	3494	117128	84531
250	5618	1687	3931	5858	132653	89047
298	8811	1714	7096	21678	159544	123854

*Table 3.3. 10 K emission spectrum of **cycTb-phEu and cycTb-phen.***

cycTb-phEu						**cycTb-phen**			
Wavelength (nm)	Energy (cm^{-1})	Tb^{3+} Transition	Tb^{3+} CF level (cm^{-1})	Eu^{3+} Transition	Eu^{3+} CF level (cm^{-1})	Wavelength (nm)	Energy (cm^{-1})	Tb^{3+} Transition	Tb^{3+} CF level (cm^{-1})
						488.23	20482	$^5D_4 \rightarrow {}^7F_6$	20482/0
485.63 sh	20592	$^5D_4 \rightarrow {}^7F_6$	20592			490.87	20372		110
488.24	20482		20482/0			491.77	20335		147
491.03	20365		117			493.73	20254		228
492.48	20305		177			495.85	20167		315
498.09	20077		405			498.26	20070		412
541.61 sh	18463	$^5D_4 \rightarrow {}^7F_5$	2019			541.68 sh	18461	$^5D_4 \rightarrow {}^7F_5$	2021
542.68	18427		2055			542.47	18434		2048
545.35	18337		2145			545.18	18343		2139
547.03	18281		2201			546.65	18293		2189
548.41	18235		2247			548.3 sh	18238		2244
550.88 b	18153		2329			551.47 b	18133		2329
556.51	17969		2513			556.59	17967		2515
580.28	17233			$^5D_0 \rightarrow {}^7F_0$	17233/0	581.64 sh	17193	$^5D_4 \rightarrow {}^7F_4$	3289
584.33	17114	$^5D_4 \rightarrow {}^7F_4$	3368			583.78	17130		3352
590.58	16933			$^5D_0 \rightarrow {}^7F_1$	300	587.97	17008		3474
592.79	16869				364	592.62	16874		3608
595.54	16791				442	603.36	16574		3908
612.80	16319			$^5D_0 \rightarrow {}^7F_2$	914	620.78	16109	$^5D_4 \rightarrow {}^7F_3$	4373
614.33	16278				955	624.00	16026		4456
617.41	16197				1036	627.63	15933		4549
620.49	16116				1117	631.25	15842		4640
650.84	15365			$^5D_0 \rightarrow {}^7F_3$	1868	644.98	15504		4978
687.08	14554			$^5D_0 \rightarrow {}^7F_4$	2679	652.30	15330	$^5D_4 \rightarrow {}^7F_2$	5152
694.30	14403				2830	656.12	15241		5241

700.36	14278		2955	662.35	15098		5384
743.45	13451	$^5D_0 \rightarrow {}^7F_5$	3782	667.72	14976	$^5D_4 \rightarrow {}^7F_1$	5506
747.25	13382		3851	674.32	14830		5652
751.24	13311		3922	680.92	14686		5796
806.54	12399	$^5D_0 \rightarrow {}^7F_6$	4834	688.16	14532	$^5D_4 \rightarrow {}^7F_0$	5950
811.7	12320		4913				
817.36	12235		4998				

*Table 3.4. 10 K emission spectrum of **cycEu-phTb**. It is not possible to assign some emission bands to Eu^{3+} or Tb^{3+} so that both alternatives are listed in those cases.*

Wavelength	Energy (cm^{-1})	Tb^{3+} transition	Tb^{3+} CF level (cm^{-1})	Eu^{3+} transition	Eu^{3+} CF level (cm^{-1})
488.83	20457	$^5D_4 \rightarrow {}^7F_6$	20457/0		
493.62 b	20258		199		
542.17 sh	18444	$^5D_4 \rightarrow {}^7F_5$	2013		
543.08	18413		2044		
543.91	18385		2072		
544.78	18356		2101		
545.74 sh	18324		2133		
547.56 b	18263		2194		
549.81	18188		2269		
580.17	17236				17236/0
583.36	17142	$^5D_4 \rightarrow {}^7F_4$	3315		94
587.74	17014		3443	$^5D_0 \rightarrow {}^7F_1$	222
589.5 sh	16964		3493		272
591.52	16906		3551		331
592.71	16872		3585		365
593.91	16838		3619		399
595.6 sh	16790		3667		446
611.98	16340		4117	$^5D_0 \rightarrow {}^7F_2$	896
613.77	16293		4164		944
615.21	16255		4202		982
616.24	16227		4230		1009
618.68	16163		4294		1073
622.31	16069	$^5D_4 \rightarrow {}^7F_3$	4388		1167
624.3 sh	16018		4439		1218
628.67	15907		4550		1330
630.55	15859		4598		1377
646.41	15470		4987		1766
649.84	15388		5069	$^5D_0 \rightarrow {}^7F_3$	1848
650.73	15367		5090		1869
653.60	15300	$^5D_4 \rightarrow {}^7F_2$	5157		1936
665.94	15016		5441		2220
668.91	14950	$^5D_4 \rightarrow {}^7F_1$	5507		2287

674.61	14823		5634		2413
677.70	14756		5701		2481
681.27 sh	14678		5779		2558
682.10	14661		5796		2576
685.32	14592		5865	$^5D_0 \rightarrow {}^7F_4$	2645
688.29	14529	$^5D_4 \rightarrow {}^7F_0$	5928		2708
690.07	14491				2745
691.47 b	14462				2774
695.95 b	14369				2597
697.40	14339				2897
701.00	14265				2971
704.96	14185				3051
706.58	14153				3084
741.36	13489			$^5D_0 \rightarrow {}^7F_5$	3748
751.59	13305				3931
759.03	13175				4062
762.07	13122				4114
810.59	12337			$^5D_0 \rightarrow {}^7F_6$	4900
812.61	12306				4930
819.66	12200				5036
829.5 b	12055				5181
843.50	11855				5381

To examine the Tb-Eu energy transfer trend, different evaluation analyses were employed, including Tb-Eu energy transfer rates deduced from the direct subtraction of decay curves (k_{ET}), the long-term lifetimes (k_{ET}‘‘), and the steady-state lifetimes (k_{ET}‘‘‘). The constants of long-term luminescence decay (>0.2 ms) of **cycTb-phen** (k_{Tb}) and **cycTb-phEu** (k_{TbEu}) are listed in Table 3.2 together with the difference in k_{TbEu} - k_{Tb} = k_{ET}¨, taken to indicate the terbium-europium energy transfer rate. The energy transfer rate by employing k_{ET} and k_{ET}‘‘‘ are also detailed in the table. The magnitude of k_{Tb} does not change significantly with temperature, it changed by 10% from 10 K to 298 K. On the other hand, k_{TbEu} markedly enhances by 270% with the increase of temperature, and k_{ET}¨ can be depicted by an exponential growth model as shown in Figure 3.9. This indicated the temperature influence for the energy transfer process, which attributes to the involvement of $^7F_1$ and thermal population. Considering only the *J*-multiplets of europium $^7F_0$ and $^7F_1$, with the mean energy of the latter equal to 369 cm^{-1} (Table 3.3), and following the description in literature[44], the energy transfer

rate can be described as:

$k_{ET}(Tb \rightarrow Eu) = aN(^7F_1) \times T + bN(^7F_0)$ (1)

$k_{ET}(Tb \rightarrow Eu)/N(^7F_0) = a \times 3\exp(-369/kT) \times T + b$ (2)

where the partition function is shown by $[1+3\exp(-369/kT)] = P$, the k is the Boltzmann constant; a and b are constants; the value of 369 cm^{-1} is the average $^7F_1$ energy; and the $^7F_0$ and $^7F_1$ populations are $N(^7F_0) = n_0 = 1/P$ and $N(^7F_1) = n_1 = 3\exp(-369/kT)/P$, respectively. A fit of the k_{ET}‟ values from 10 K to 298 K in Table 3.2 is shown in Figure 3.8a by Eq. 2.

The low-temperature energy transfer pathway involves phonon(s) emission and $^7F_0$:

$^5D_4$ Tb^{3+} (20482) + $^7F_0$ Eu^{3+} (0) → $^7F_5$ Tb^{3+} (2019-2513) + Eu^{3+} $^5D_0$ (17233) + phonon (736-1230)

and/or

$^5D_4$ Tb^{3+} (20482) + $^7F_0$ Eu^{3+} (0) → $^7F_6$ Tb^{3+} (0-405) + Eu^{3+} $^5D_1$ (19048) + phonon (1029-1434)

where representative ranges of energies are shown in parentheses (in cm^{-1}); or it involves the participation of terbium $^7F_4$ with a low energy phonon absorption. The higher energy transfer rate at room temperature is because the forced electric dipole transition, $^7F_1 \rightarrow {}^5D_0$, is involved:

$^5D_4$ Tb^{3+} (20482) + $^7F_1$ Eu^{3+} (300-442) → $^7F_4$ Tb^{3+} (3289-3908) + Eu^{3+} $^5D_0$ (17233) ± phonon

Alternatively, the decay curves of complexes **cycTb-phen** and **cycTb-phEu** were directly subtracted as shown in Figure 3.10 and we fitted the resulting plots well with a bi-exponential function. The lifetime τ_1 represents the reciprocal of the terbium-europium energy transfer rate, k_{ET} as shown in Table 3.2. The values are comparable with those for k_{ET}‟, except that the value at room temperature is higher. The plot of the experimental k_{ET} values against inverse temperature is shown in Figure 3.8b and the fit using Eq. 2 shows a similar result as in Figure 3.8a. Figure

3.10 displays the fits of the subtracted curves which produce a rise time, τ_2, in all cases, which equals the reciprocal of the rate constant, k_r. These rate constants produce a linear plot as a function of temperature (Figure 3.8d). This is expected for a one phonon process. Finally, the plot in Figure 3.8c shows another alternative description for the energy transfer rate, k_{ET}'', which was calculated by steady-state decay lifetimes. Though the numerical values are different, the three fittings serve to confirm the importance of $^7F_1$ participation in the room temperature energy transfer process.

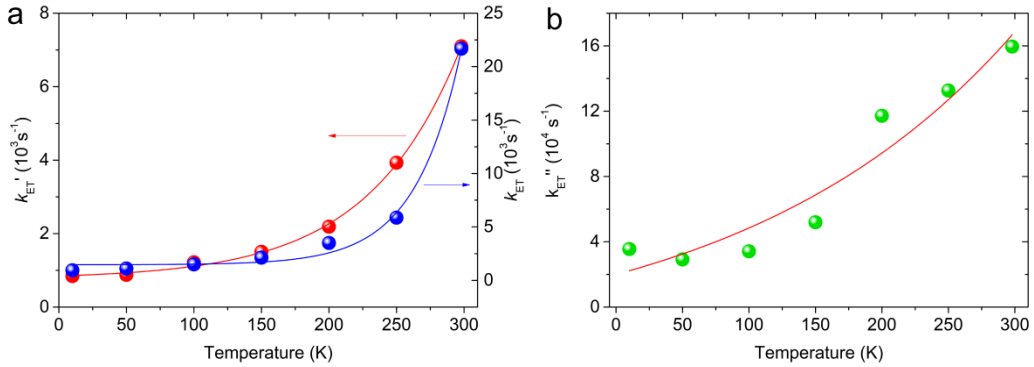

Figure 3.9. (a) Exponential growth models for Tb^{3+} → Eu^{3+} energy transfer rates deduced from long-term lifetimes (k_{ET}': black datapoints, red fitted curve) and subtracted decay curves (k_{ET}: blue data points, blue fitted curve). The fitting equations are: $k_{ET}' = (768\pm58) + (79\pm13)\exp[(68\pm2)/T]$, $R_{adj}^2 = 0.9989$. $k_{ET} = (1456\pm330) + (3.1\pm2.7)\exp[(34\pm3)/T]$, $R_{adj}^2 = 0.9925$. (b) Exponential growth model for Tb^{3+} → Eu^{3+} energy transfer rates deduced from steady-state lifetimes with the fitting equation: $k_{ET}'' = (-2.6\pm7.8)x10^4 + (4.6\pm6.6)x10^4\exp[(-208\pm156)/T]$, $R_{adj}^2 = 0.8936$.

The Tb-Eu energy transfer efficiency ($\eta_{ET} = 1 - k_{Tb}/k_{TbEu}$) has different values when calculated by the three different sets of rate constants. The value is above 0.9 and is reasonably independent as the temperature changes when the steady-state lifetime values are used.

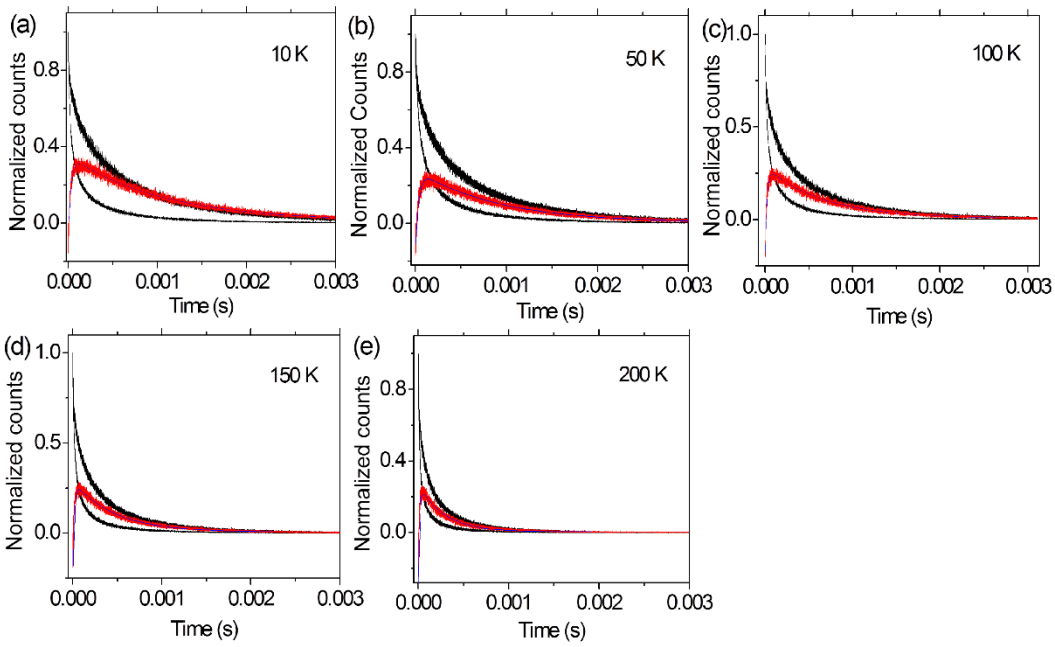

*Figure 3.10. Subtraction of decay curves of **cycTb-phen** and **cycTb-phEu**. The subtracted curves are in red and the fitting in blue.*

3.2.7 Energy transfer from antenna to Eu^{3+} ion

The triplet state of energy of ligand was measured with the complex **cycLa-phLa** (Figure 3.2), the value of 20124 cm^{-1} is below the terbium $^5D_4$ energy (20482 cm^{-1}) in the complex **cycTb-phEu**. While upon excitation of the ligand singlet, we observed strong terbium emission in the complex **cycTb-phen** at room temperature (Figure 3.11), which means that the excitation of ligand populates the terbium $^5D_4$ energy level. The europium $^5D_0$ level (17233 cm^{-1}) locates below the triplet state (~3300 cm^{-1}) with sufficient energy gap to avoid back transfer from europium to triplet. Except for the triplet–lanthanide transfer, there are also chances of energy transfer from higher ligand levels to the lanthanide ions by the 355 nm irradiation.

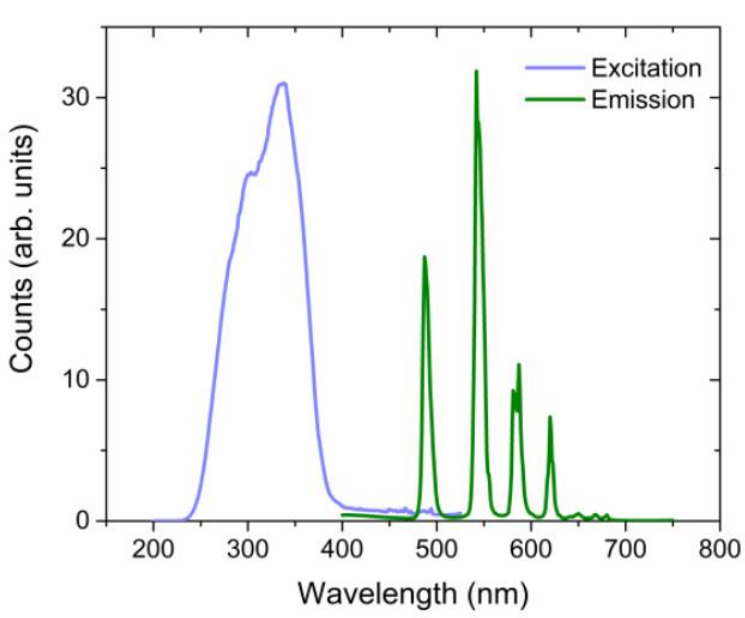

Figure 3.11. 298 K Emission and excitation spectra of ***cycTb-phen****.*

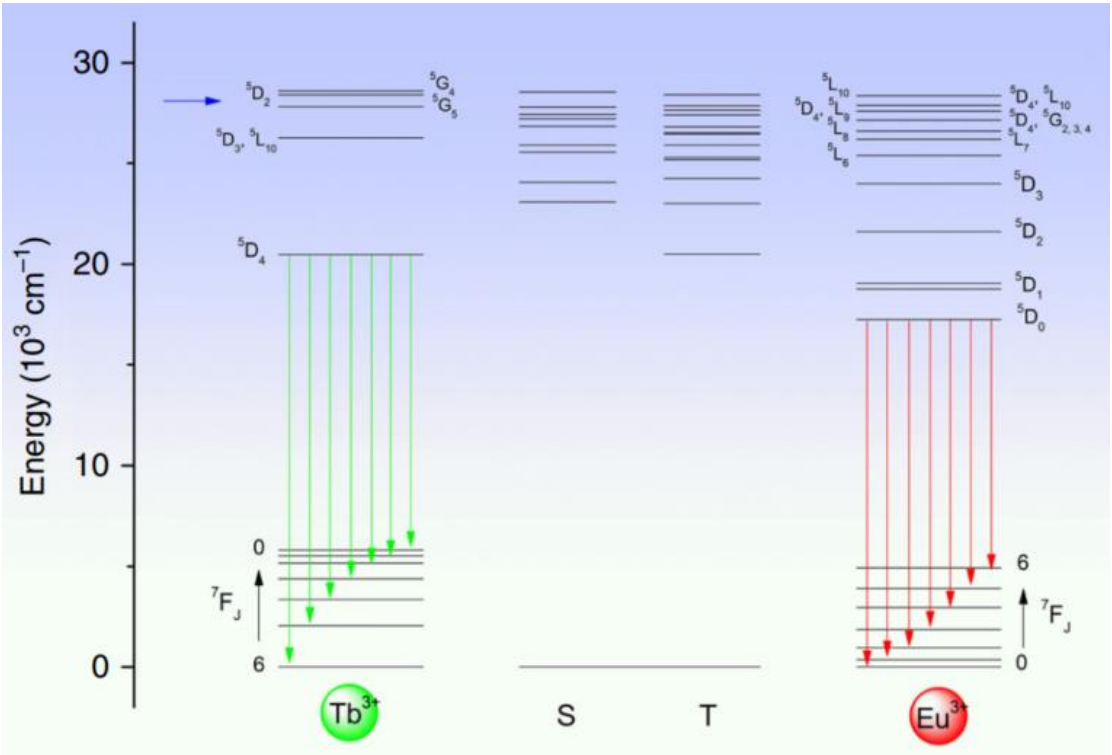

Figure 3. 12. Simplified energy level diagram for Tb^{3+} - Eu^{3+} dyads of singlets (S) and triplets (T) of ligand, and lower levels of Tb^{3+} and Eu^{3+} ions. The J-multiplet energy levels given for Tb^{3+} and Eu^{3+} may not be exact (and are split by the crystal field) but are illustrative of relative energies. The green and red vertical arrows mark emission from Tb^{3+} and Eu^{3+}, respectively. The blue horizontal arrow denotes the 355 nm excitation energy.

We calculated singlet and triplet levels by first optimizing the **cycTb-phEu** structure by the Sparkle/RM1 method in MOPAC[25]. Then, the optimized structure was used in LUMPAC under standard settings to calculate the excited energy levels using Zerner's intermediate neglect of differential overlap (ZINDO/S) semi-empirical method[27]. When the number of states changed in the calculation, different triplet state energies can be obtained. The 25 states calculation results are shown in Figure 3.2d, where 20501 cm^{-1} (487.8 nm) was the lowest triplet state. There are 25 triplet levels and 19 singlet levels in this calculation with the wavelengths longer than 315 nm. The lowest singlet energy levels were calculated to be at 433, 416 and 391 nm. Figure 3. *12* shows the relative energy levels of terbium, europium and ligand in the complex **cycTb-phEu**. The ligand energy levels are from the above calculation while the europium and terbium energy levels are from the experiment data or other systems.

The 355 nm irradiation into the complex can populate the ligand at ~360 nm (Figure 3.4), which we assume to be the level we calculated at 28550 cm^{-1} (Figure 3. *12*). There is a one phonon (~770 cm^{-1}) gap below this singlet level so that the internal conversion can be fast. Actually, all the singlet-singlet energy gaps down to the S_0 (calculated value of 433 nm) are with one phonon energy difference. The singlet level of the ligand is identified at 437 nm with the weak band (Figure 3.4). For these two singlets, the ligand-lanthanide energy transfer rates are faster than the internal conversion rate. In addition to these two energy levels, we use the LUMPAC programme to investigate the energy transfer rate to the europium ion from all of the potential states that were populated by 355 nm irradiation. The results by three different structure optimizations and calculations are listed in Table 7.2 and Table 7.3. The energies calculated are those from vertical Franck-Condon transitions to unrelaxed excited states.

Though the LUMPAC programme neglects internal conversion processes and intra-ligand intersystem crossing, it is currently the most informative analysis of ligand-lanthanide energy transfer processes. Table 7.2 and Table 7.3 show that the major ligand-europium energy transfer pathways involve upper europium *J*-multiplets, which is followed by internal nonradiative relaxation to europium $^5D_0$.

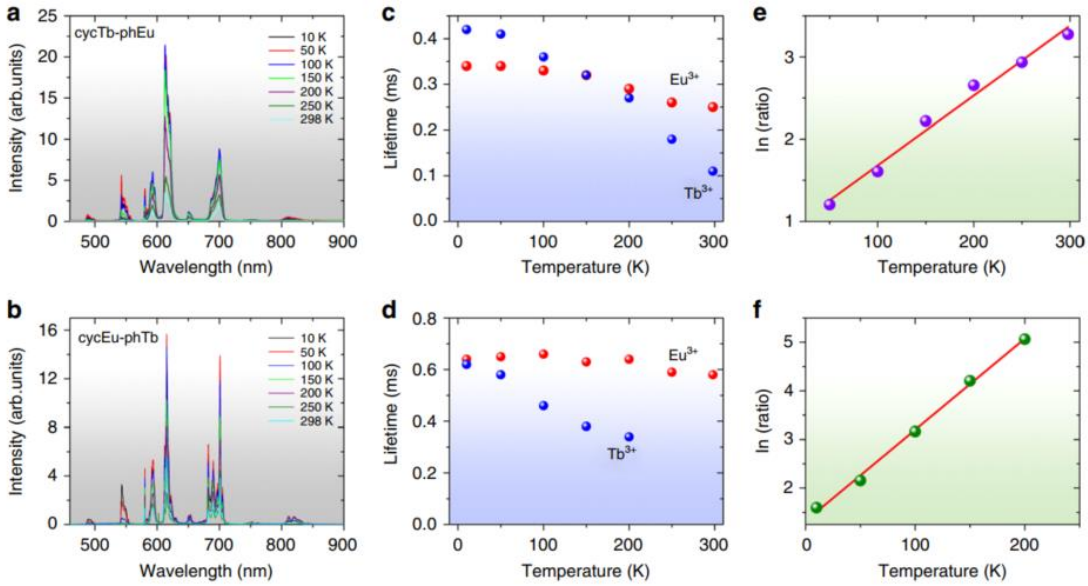

Figure 3.13. Emission spectra (λ_{exc} = 355 nm) and thermometric properties of complexes. ***cycTb-phEu*** *(a) and* ***cycEu-phTb*** *(b) recorded at 10 K, 50 K, 100 K, 150 K, 200 K, 250 K and 298 K. Temperature-dependent long-term lifetimes of $^5D_0$ (Eu^{3+}) and $^5D_4$ (Tb^{3+}) for* ***cycTb-phEu*** *(c) and* ***cycEu-phTb*** *(d). Natural logarithm of the emission count ratio $^5D_0 \rightarrow {}^7F_4$ (Eu^{3+}): $^5D_4 \rightarrow {}^7F_5$ (Tb^{3+}) plotted against temperature for (e)* ***cycTb-phEu*** *with fitting equation y = (0.83±0.10) + (0.0085±0.0005)x, R_{adj}^2 = 0.9823 and (f)* ***cycEu-phTb*** *with fitting equation: y = (1.32±0.07) ± (0.0188±0.0006)x, R_{adj}^2 = 0.9960.*

3.2.8 Thermometric properties

To examine their potential application as luminescent thermal probes, we investigated temperature-dependent luminescence intensity and lifetimes of both complexes **cycTb-phEu** and **cycEu-phTb** with the temperature between 10 K and 298 K (Figure 3.13). Moreover, the intensity changes of the terbium $^5D_4 \rightarrow {}^7F_5$ and europium $^5D_0 \rightarrow {}^7F_4$ transitions show the trends upon the temperature changes. In the complex **cycTb-phEu**, the major decrease in terbium occurs above ~50 K while the europium intensity decrease when the temperature is above ~100 K (Figure 3.14a). In the complex **cycEu-phTb**, the decreases occur at lower temperatures as shown in Figure 3.14b). The long-term lifetime changes of the terbium $^5D_4$ and europium $^5D_0$ states for these complexes **cycTb-phEu** and **cycEu-phTb** are shown in Figure 3.13c and d. These terbium changes are greater than for those of europium.

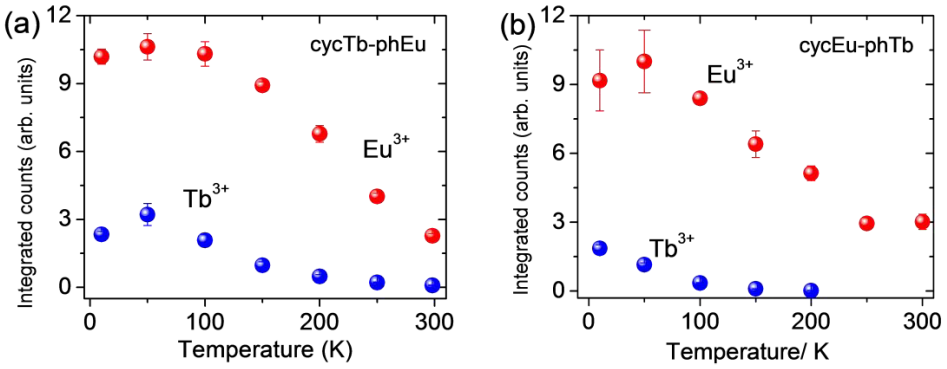

*Figure 3.14. The temperature-dependent integrated area of the $^5D_0 \rightarrow {}^7F_4$ (Eu^{3+}) and $^5D_4 \rightarrow {}^7F_5$ (Tb^{3+}) transitions for **cycTb-phEu** (a) and **cycEu-phTb** (b).*

The $^5D_4 \rightarrow {}^7F_5$ terbium transition and the $^5D_0 \rightarrow {}^7F_4$ europium transition have different temperature-responsive luminescent emission, indicating that both dinuclear complexes can be used as self-referencing thermometers. They are free of any cumbersome calibration of the fluorescent intensity, making them more reliable as luminescent thermal probes. The $^5D_4 \rightarrow {}^7F_5$ and the $^5D_0 \rightarrow {}^7F_4$ locate separately from other peaks, so the peaks are less affected.

The emission intensity ratio, R, presents an exponential growth curve as a function of temperature (Figure 3.15), and the natural logarithm of the intensity ratio is plotted in Figure 3.13e and f. The complex **cycEu-phTb** has a better fit. The relative sensitivity is described as $S = (dR/dT)/R$, i.e., the change of ratio with temperature divided by the ratio value. Since, from Figure 3.15b:

$R = A \times \exp(B \times T)$, where $A = 3.96$ and $B = 0.01857\ K^{-1}$, (2)

$S = B$, (3)

and the relative sensitivity is $1.86\%\ K^{-1}$. The temperature resolution, dT, is described by:

$dT = (1/S) \times (D/R)$

where D is the error (standard deviation) in R value at temperature T and is <1 °C at $T >$ 200 K (Figure 3.15c).

The dyad **cycEu-phTb** is therefore more suitable to be used as a luminescent self-referencing thermometer with both luminescent intensity ratio and lifetimes.

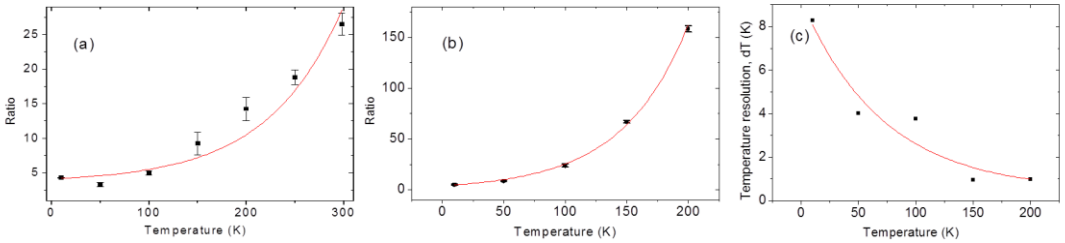

Figure 3.15. Intensity ratio of $^5D_0 \rightarrow {}^7F_4$: $^5D_4 \rightarrow {}^7F_5$ *for (a)* ***cycTb-phEu*** *at different temperatures fitted by the exponential growth curve : y = -(3.7±0.6) + (0.49±0.49)exp(x/(76±20)),* $R_{adj}^2 = 0.8962$. *(b)* ***cycEu-phTb*** *at different temperatures fitted by the exponential growth curve: y = (3.96±0.47)exp(x/(53.8±2.0)),* $R_{adj}^2 = 0.9960$. *(c) Temperature resolution, dT, of* ***cycEu-phTb*** *plotted against temperature. The first order exponential decay fit is a guide to the eye.*

3.3 Conclusion

We have developed a strategy for the synthesis of hetero-dinuclear complexes that contain two types of chemically similar lanthanides. By this strategy, we synthesized the **cycTb-phEu** and **cycEu-phTb** complexes. The triplet-lanthanide gaps for europium and terbium are different, resulting in different energy transfer performance for each lanthanide ions. Together with the energy transfer pathway from terbium to europium ion, the lanthanide complexes have a temperature-dependent luminescent ratio which increases with the rise of temperature. Both **cycTb-phEu** and **cycEu-phTb** complexes have excellent temperature sensitivity over a wide range of temperatures.

3.4 References

1. K. Miyata, Y. Konno, T. Nakanishi, A. Kobayashi, M. Kato, K. Fushimi and Y. Hasegawa, *Angew. Chem. Int. Ed.*, 2013, **52**, 6413-6416.
2. M. Hatanaka, Y. Hirai, Y. Kitagawa, T. Nakanishi, Y. Hasegawa and K. Morokuma, *Chem. Sci., 2017, **8**, 423-429*
3. M. Nakano, Y. Arai, I. Kotera, K. Okabe, Y. Kamei and T. Nagai, *PLoS One*, 2017, **12**, e0172344.
4. X. D. Wang, O. S. Wolfbeis and R. J. Meier, *Chem. Soc. Rev.*, 2013, **42**, 7834-7869.
5. Y. Cui, H. Xu, Y. Yue, Z. Guo, J. Yu, Z. Chen, J. Gao, Y. Yang, G. Qian and B. Chen, *J. Am. Chem. Soc.*, 2012, **134**, 3979-3982.
6. L. Marciniak, K. Prorok, L. Frances-Soriano, J. Perez-Prieto and A.

Bednarkiewicz, *Nanoscale*, 2016, **8**, 5037-5042.
7. I. N'Dala-Louika, D. Ananias, C. Latouche, R. Dessapt, L. D. Carlos and H. Serier-Brault, *J. Mater. Chem. C*, 2017, **5**, 10933-10937.
8. H. Lu, R. Meng, H. Hao, Y. Bai, Y. Gao, Y. Song, Y. Wang and X. Zhang, *RSC Adv.*, 2016, **6**, 57667-57671.
9. H. Wang, D. Zhao, Y. Cui, Y. Yang and G. Qian, *J. Solid State Chem.*, 2017, **246**, 341-345.
10. J. Zhou, Z. Xia, M. Bettinelli and Q. Liu, *RSC Adv.*, 2016, **6**, 2046-2054.
11. G. Morrison, A. M. Latshaw, N. R. Spagnuolo and H. C. Zur Loye, *J. Am. Chem. Soc.*, 2017, **139**, 14743-14748.
12. K. A. Romanova, A. Y. Freidzon, A. A. Bagaturyants and Y. G. Galyametdinov, *J. Phys. Chem. A*, 2014, **118**, 11244-11252.
13. G. Bao, S. Zha, Z. Liu, Y. H. Fung, C. F. Chan, H. Li, P. H. Chu, D. Jin, P. A. Tanner and K. L. Wong, *Inorg. Chem.*, 2018, **57**, 120-128.
14. Y. Yu, X. Guan, P. Luo, X. Li, F. Yan and W. Zhang, *J. Alloys Compd.*, 2018, **730**, 12-16.
15. Z. Dai, L. Tian, B. Song, Z. Ye, X. Liu and J. Yuan, *Anal. Chem.*, 2014, **86**, 11883-11889.
16. J. Yang, C. Zhang, C. Li, Y. Yu and J. Lin, *Inorg. Chem.*, 2008, **47**, 7262-7270.
17. X. Rao, T. Song, J. Gao, Y. Cui, Y. Yang, C. Wu, B. Chen and G. Qian, *J. Am. Chem. Soc.*, 2013, **135**, 15559-15564.
18. F. Tanaka and T. Ishibashi, *J. Chem. Soc., Faraday Trans.*, 1996, **92**, 1105.
19. Q. Zhong, H. Wang, G. Qian, Z. Wang, J. Zhang, J. Qiu and M. Wang, *Inorg. Chem.*, 2006, **45**, 4537-4543.
20. X. Liu, J. Zhu, H. Ni, B. Ma and L. Liu, *J. Macromol. Sci. B.*, 2015, **55**, 20-32.
21. A. Nonat, T. Liu, O. Jeannin, F. Camerel and L. J. Charbonniere, *Chem.-Eur. J.*, 2018, **24**, 3784-3792.
22. E. Debroye, M. Ceulemans, L. Vander Elst, S. Laurent, R. N. Muller and T. N. Parac-Vogt, *Inorg. Chem.*, 2014, **53**, 1257-1259.
23. L. S. Natrajan, A. J. Villaraza, A. M. Kenwright and S. Faulkner, *Chem. Commun.*, 2009, 6020-6022.
24. P. Pitchaimani, K. M. Lo and K. P. Elango, *J. Coord. Chem.*, 2015, **68**, 2167-2180.
25. J. J. P. Stewart, *J. Phys. Chem. Ref. Data*, 2004, **33**, 713-724.
26. R. G. B., F. R. O., S. A. M. and S. J. J. P., *J. Comput. Chem.*, 2006, **27**, 1101-1111.
27. J. D. Dutra, T. D. Bispo and R. O. Freire, *J. Comput. Chem.*, 2014, **35**, 772-775.
28. O. L. Malta, *J. Non. Cryst. Solids*, 2008, **354**, 4770-4776.
29. S. Grimme, J. G. Brandenburg, C. Bannwarth and A. Hansen, *J. Chem. Phys.*, 2015, **143**, 054107.
30. F. Weigend and R. Ahlrichs, *Phys. Chem. Chem. Phys.*, 2005, **7**, 3297-3305.
31. M. Dolg, H. Stoll and H. Preuss, *J. Chem. Phys.*, 1989, **90**, 1730-1734.
32. F. Neese, *Wiley Interdiscip. Rev. Comput. Mol. Sci.*, 2012, **2**, 73-78.

33. S. V. Eliseeva and J. C. Bunzli, *Chem. Soc. Rev.*, 2010, **39**, 189-227.
34. S. Sato, A. Ishii, C. Yamada, J. Kim, C. Song, A. Fujiwara, M. Takata and M. Hasegawa, *Polym. J., 2015, **47**, 195–200*.
35. I. G. Fomina, Z. V. Dobrokhotova, G. G. Aleksandrov, V. I. Zhilov, I. P. Malkerova, A. S. Alikhanyan, D. M. Zhigunov, A. S. Bogomyakov, V. I. Gerasimova, V. M. Novotortsev and I. L. Eremenko, *Polyhedron*, 2013, **50**, 297-305.
36. M. Irfanullah and K. Iftikhar, *Inorganica Chim. Acta*, 2013, **394**, 373-384.
37. T. Kim Anh, T. Ngoc, P. Thu Nga, V. T. Bitch, P. Long and W. Strk, *J. Lumines.*, 1988, **39**, 215-221.
38. I. Carrasco, F. Piccinelli and M. Bettinelli, *J. Lumines.*, 2017, **189**, 71-77.
39. Z. Hou, Z. Cheng, G. Li, W. Wang, C. Peng, C. Li, P. a. Ma, D. Yang, X. Kang and J. Lin, *Nanoscale*, 2011, **3**, 1568-1574.
40. D. M. Moran, P. Stanley May and F. S. Richardson, *Chem. Phys.*, 1994, **186**, 77-103.
41. K. Binnemans, *Coord. Chem. Rev.*, 2015, **295**, 1-45.
42. P. Tanner and C.-K. Duan, *Coord. Chem. Rev.*, 2010, **254**, 3026-3029.
43. D. L. Dexter, *J. Chem. Phys.*, 1953, **21**, 836-850.
44. I. Laulicht, S. Meirman and B. Ehrenberg, *J. Lumines.*, 1984, **31-32**, 814-816.

Chapter 4 Effects of Europium Spectral Probe Interchange in Ln-dyads with Cyclen and Phen Moieties

4.1 Introduction

Multinuclear lanthanide complexes are potential in many applications including bioassay[1], sensing[2], thermometry[3, 4] and white light sources[5]. In some of these complexes, the lanthanide ion is coordinated to a cyclen binding site[6, 7] and phenanthroline-based receptors are famous for metal ion sensing and recognition.[8] The construction of heterometallic lanthanide complexes[9-11] requires ingenuity in order to avoid formation of homodinuclear complexes[10, 12, 13] The lanthanide ions are attractive because they show sharp spectral bands with excellent colour purity, long lifetimes and the capacity to be effectively excited by an organic antenna[14, 15] which enable emission wavelengths far separated from the excitation wavelength.[16, 17] Europium ion is a well-known lanthanide probe reporter ion because its spectrum is simple and usually involves one excitation state, the $^5D_0$ state, for the population, and the spectra give the coordination and symmetry information of the binding sites.[18, 19]

The europium ion can efficiently convert the absorbed lights into emitted light, but it has a poor absorption capacity of the incident light. The organic chromophore of europium complex can absorb light efficiently by singlet – singlet transition which is spin-allowed. The energy on the excited singlet state (S_n) then transfer the energy to europium ion, and/or the singlet excited state can transfer to triplet states T_n, (usually T_1) *via* internal conversion and intersystem crossing, which followed by energy transfer to europium ion. This process is called the antenna effect. Since the early studies of ligand-lanthanide systems,[20, 21] significant interests have been drawn towards the understanding of the energy transfer [22, 23] and its optimization.[24-26]

**A version of this chapter has been included in the published paper "Effects of europium spectral probe interchange in Ln-dyads with cyclen and phen moieties. Dalton Trans., 2019, 48, 4314".*

However, there is no ligand-lanthanide system that has exact components to keep both the energy levels of ligand and lanthanide the same for the comparative study of the influence of the binding sites towards the spectra and energy transfer processes. To fill the gap, we use a binuclear complex with one probe lanthanide ion and on silent lanthanide ion in each binding site and exchange their position to study the influence of the binding sites. We choose the popular 1,4,7,10-tetraazacyclododecane (cyclen).[27-31] and 1,10-phenanthroline (phen)[9, 32-38] as chemically-distinct ligands for the dinuclear complexes. Since the ligands are exactly same, the energy levels of singlet and triplet of the complex are relatively insensitive to the interchange of the lanthanide ions.

We synthesized the lanthanide complexes **cycEu-phLa** and **cycLa-phEu** using our previous strategy in Chapter 3 (Figure 4.1).[4] The phen site is supplemented by the supporting chelators pyrrolidine-1-carbodithioate (pdtc). We use lanthanum ion to bind to the second coordinative site because lanthanum ion has no 4f electrons and can not accept energy from chromophore. The coordination number of lanthanide ion in the cyclen binding centre is 8 or 9, with 3 or 4 oxygen atoms and 4 nitrogen atoms surrounded,[27-29, 39-43] and in some case there is a water molecule coordinated.[30, 44-49] This showcase system provides a potential insight to better understand the ligand and metal ion energy transfer dynamics of a lanthanide complex.

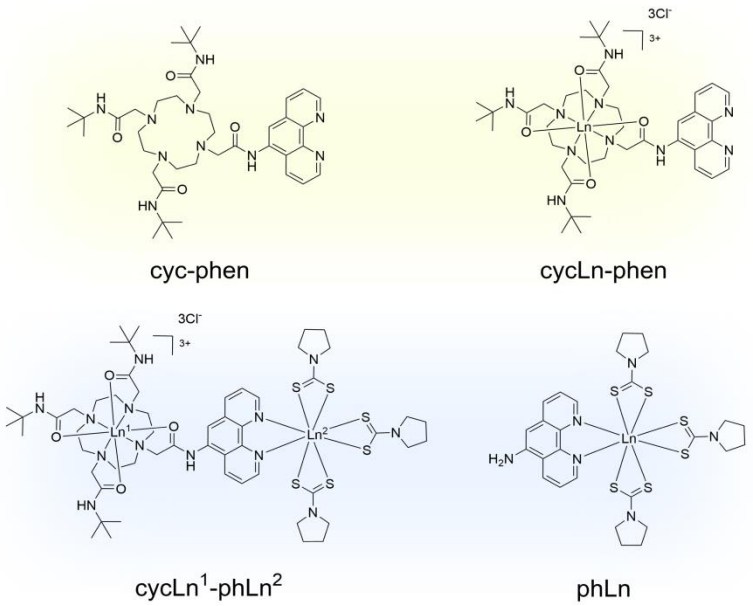

Figure 4.1. Structures and naming of some of the compounds employed in this work:

cyc-phen, cycLn^{1}-phLn^{2}, cycLn-phen and phLn where Ln represents a lanthanide element La or Eu.

4.2 Results and discussion

4.2.1 Synthesis

The dinuclear complexes **cycEu-phLa**, **cycLa-phEu** and **cycLa-phLa** were synthesized by coordinating lanthanide ion to three equivalents of ammonium pyrrolidine-1-carbodithioate and one equivalent of **cycEu-phen** or **cycLa-phen** (Scheme 4.1).[4] The complexes **phEu** and **phLa** were obtained with the same method by coordinating lanthanide ion to three equivalents of ammonium pyrrolidine-1-carbodithioate and one equivalent of 1,10-phenanthroline.[50] The NMR spectra (Figure 4.2) showed that there are three pyrrolidine dithiocarbamates coordinated in the complex, which is consistent with the previous report.[50] The coordinating of a second lanthanum ion to the binding site of **cycLa-phen**, led to the new peaks in NMR spectrum at δ 3.64 ppm (triplet, 12 hydrogens) and a at δ 1.82 ppm (quintuplet, 12 hydrogens). These peaks are from the pyrrolidine unit of the pyrrolidine dithiocarbamates. When the Van Vleck paramagnetic Eu^{3+} coordinates on different binding centre, the NMR spectra are different (Figure 4.3). The europium ion in the cyclen site of the **cycEu-phLa** shows an obvious shift between -19 and +29 ppm due to the short distance between the europium hydrogens in the cyclen coordination sites. The Eu^{3+} in the complex **cycLa-phEu** is coordinated with separated chelate, thus the **cycLa-phEu** has NMR peaks in range from 0 to 10 ppm. These complexes were also analysed by FT-IR spectroscopy.

Scheme 4.1. Synthesis of lanthanide complexes.

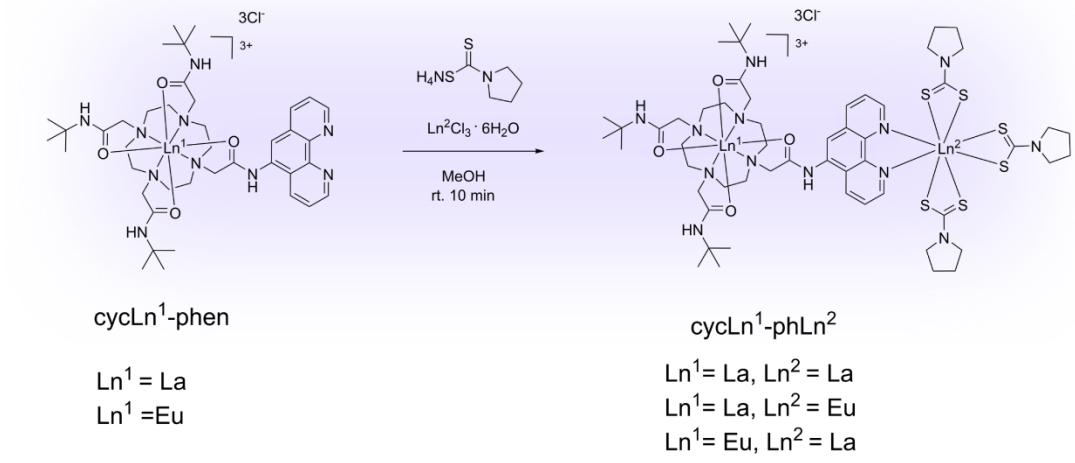

cycLn^1-phen

Ln^1 = La
Ln^1 =Eu

cycLn^1-phLn^2

Ln^1= La, Ln^2 = La
Ln^1= La, Ln^2 = Eu
Ln^1= Eu, Ln^2 = La

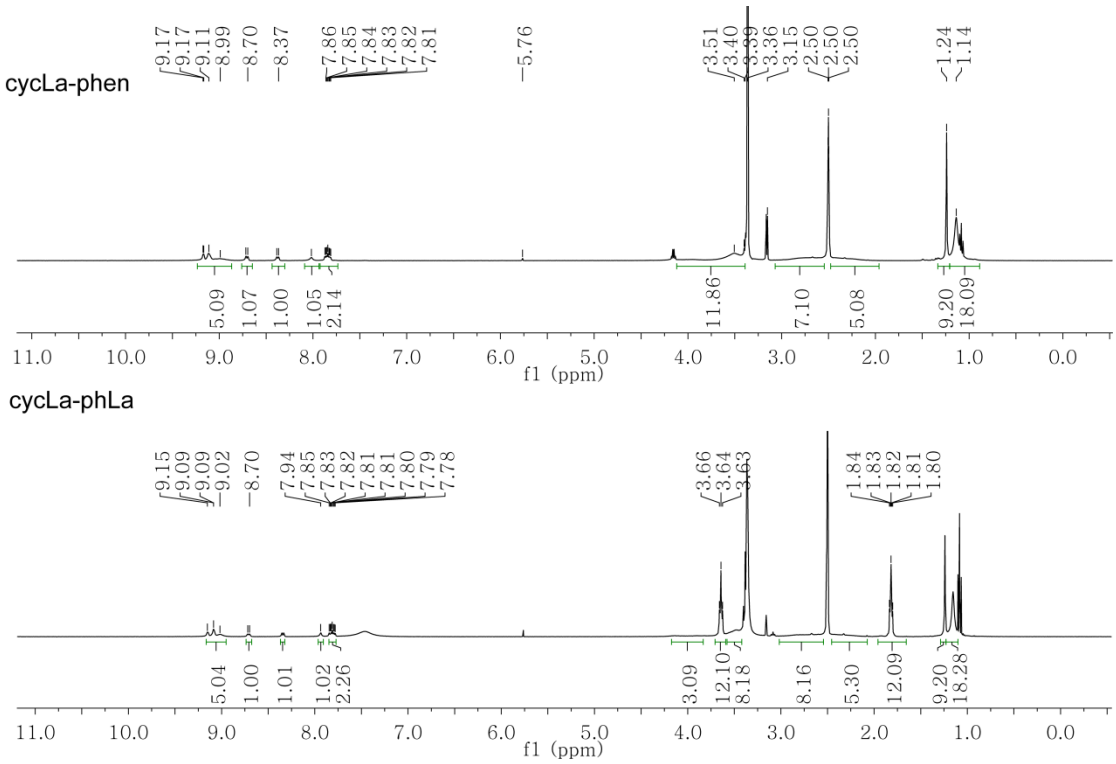

*Figure 4.2. ^{1}H NMR spectra of **cycLa-phen** and **cycLa-phLa**.*

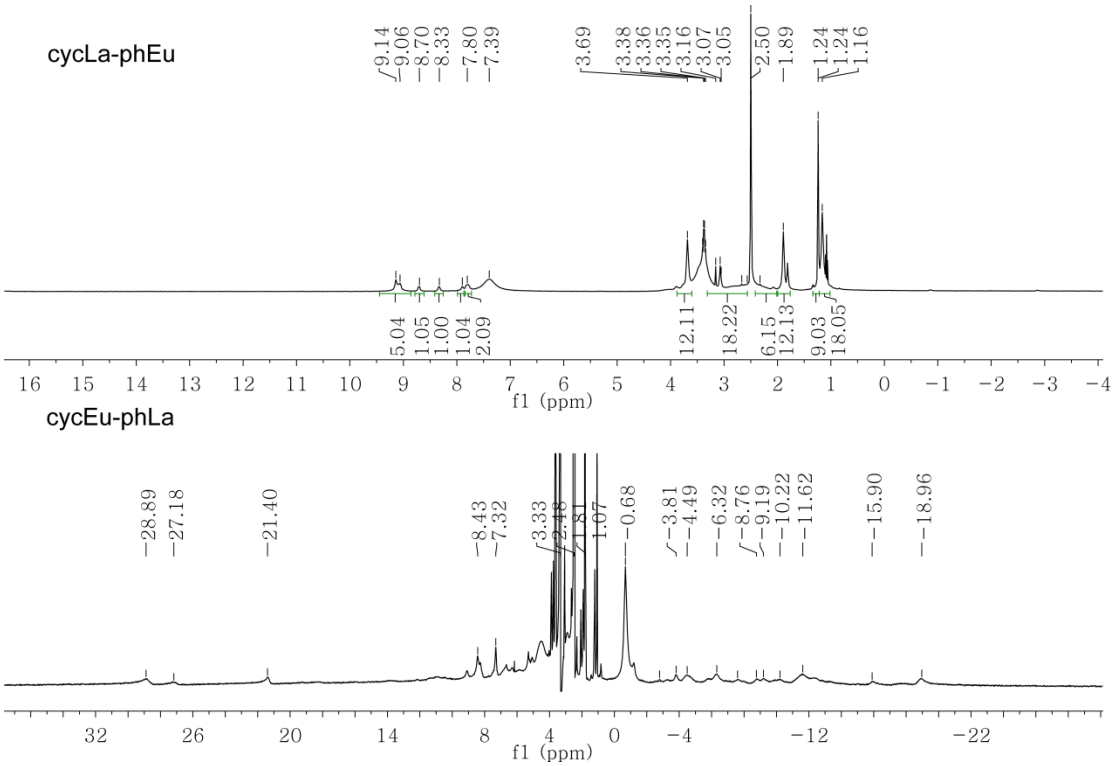

*Figure 4.3. ^{1}H NMR spectra of **cycLa-phEu** and **cycEu-phLa**.*

4.2.2 Singlet and triplet properties: intersystem crossing

In this part, we investigate the ligand excitation and emission spectra and the decay kinetics. The **cyc-phen** has no phosphorescent since there is insignificant intersystem crossing from singlet state to the triplet state. The decay comparison of **cycLa-phen** and **cycLa-phLa** with that of **cyc-phen** allows us to calculate the intersystem crossing rates.

As discussed before, the organic ligand in lanthanide complexes can considerably increase the absorption cross section and enhance the emission brightness of lanthanide ions. The typical energy transfer pathway is from chromophore singlet to triplet *via* intersystem crossing, and then to the lanthanide ions. Other energy transfer pathways also occur such as direct singlet-lanthanide energy transfer. Our previous study showed a direct singlet – Eu^{3+} energy transfer with a rate of ~10^{8} s^{-1} in terbium-europium dinuclear complexes.

The properties of singlet and triplet states are important in the lanthanide complexes. We investigated the chromophore energy levels using a lanthanum motif

because lanthanum ion does not have 4f-4f transitions. First, the peak maximum in the absorption spectra represents the transition to the unrelaxed singlet vibronic levels from the singlet S_0 level. There are two bands at 305 - 325 nm and 275 nm and a weak band at 357 nm in the absorption in a solid state of the ligand, phen (Figure 4.4). The band at 310 - 340 nm in the vapour state absorption spectrum belongs to the first singlet level with an oscillator strength value of 0.0031,[51] which is consistent with our DFT calculations. The absorption spectra simulations show a similar three-band pattern of the NH_2-phen and phen because of the transition overlapping of multiple excited singlet states (Figure 4.4). The cyclen ligand does not have absorption in the visible range (Figure 4.5).

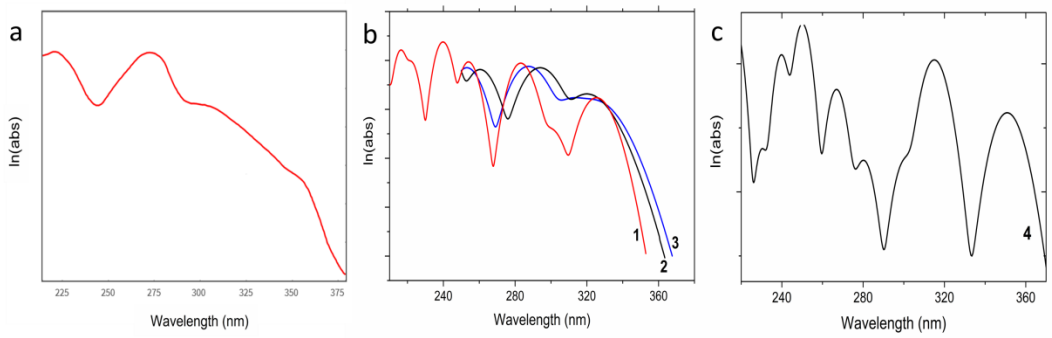

Figure 4.4. Electronic absorption spectrum of 1,10-phenanthroline (phen) (https://webbook.nist.gov/cgi/cbook.cgi?ID=C66717&Mask=400) (a) and calculated spectra of phen (b) and phenNH_2 (c). Note the logarithmic scale to show the very weak singlet absorption bands in the region ~360 nm. 1 Calculation using Firefly[S2] with B3LYP functional; 2, 3, 4 ORCA[S3] calculations using b B3LYP functional with with the basis def2-TZVP and the auxiliary basis def2/J, and 3 the hybrid GGA functional B3LYP/G and the Ahlrichs def2 basis set SV(P). 4 phenNH_2 using the B3LYP functional with the def2-TZVP basis set and the RIJCOSX approximation.

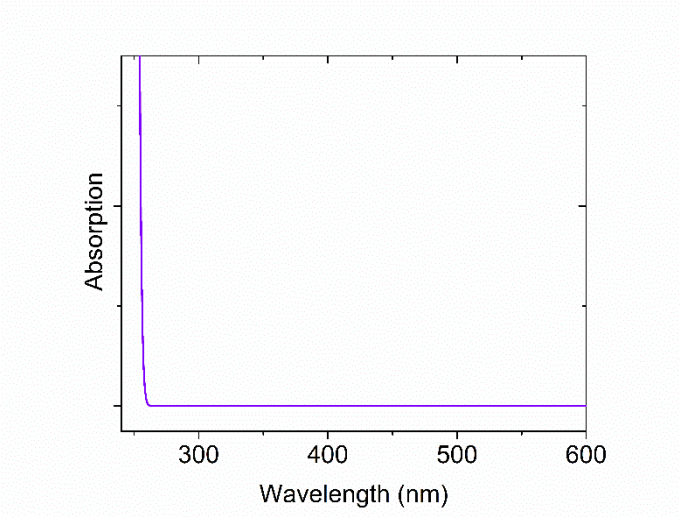

Figure 4.5. Calculated electronic absorption spectrum of cyclen by ORCA using the B3LYP functional with the basis def2-TZVP and the auxiliary basis def2/J using the RIJCOSX approximation.

Figure 4.6 shows the emission spectra of complexes **cycLa-phLa**, **cycLa-phen**, **phLa**, and ligand **cyc-phen** at 77 K and 298 K. The compounds **cycLa-phLa**, **cycLa-phen**, and ligand **cyc-phen** show a broad singlet band at around 400 nm at room temperature with vibronic structure of **cyc-phen** partially resolved. The phen singlet emission of vapour phase has a band peaked at ~370 nm.[51] The **cycLa-phLa** spectrum at room temperature shows another weak band at longer wavelength (Figure 4.6b), which locates in the region of **phLa** emission band **(**Figure 4.6d), because of the dithiocarbamate ligands. The absorption and emission spectra of **phLn** complexes with various ligands have been reported previously.[50, 52, 53] The **phLa** emission at 77 K shows both phosphorescence and fluorescence (Figure 4.6g). The ligand **cyc-phen** still showed fluorescence even at 77 K with the vibrational progression of C=N bond with a frequency of ~ 1340 cm^{-1} and the zero phonon line was more clearly exhibited. We observed no corresponding phosphorescence of **cyc-phen** at 77 K. The heavy atom effect in the complex **cycLa-phen** leads to intense phosphorescence emission at 77 K and more for the complex **cycLa-phLa** which has one more lanthanum ion in the complex.

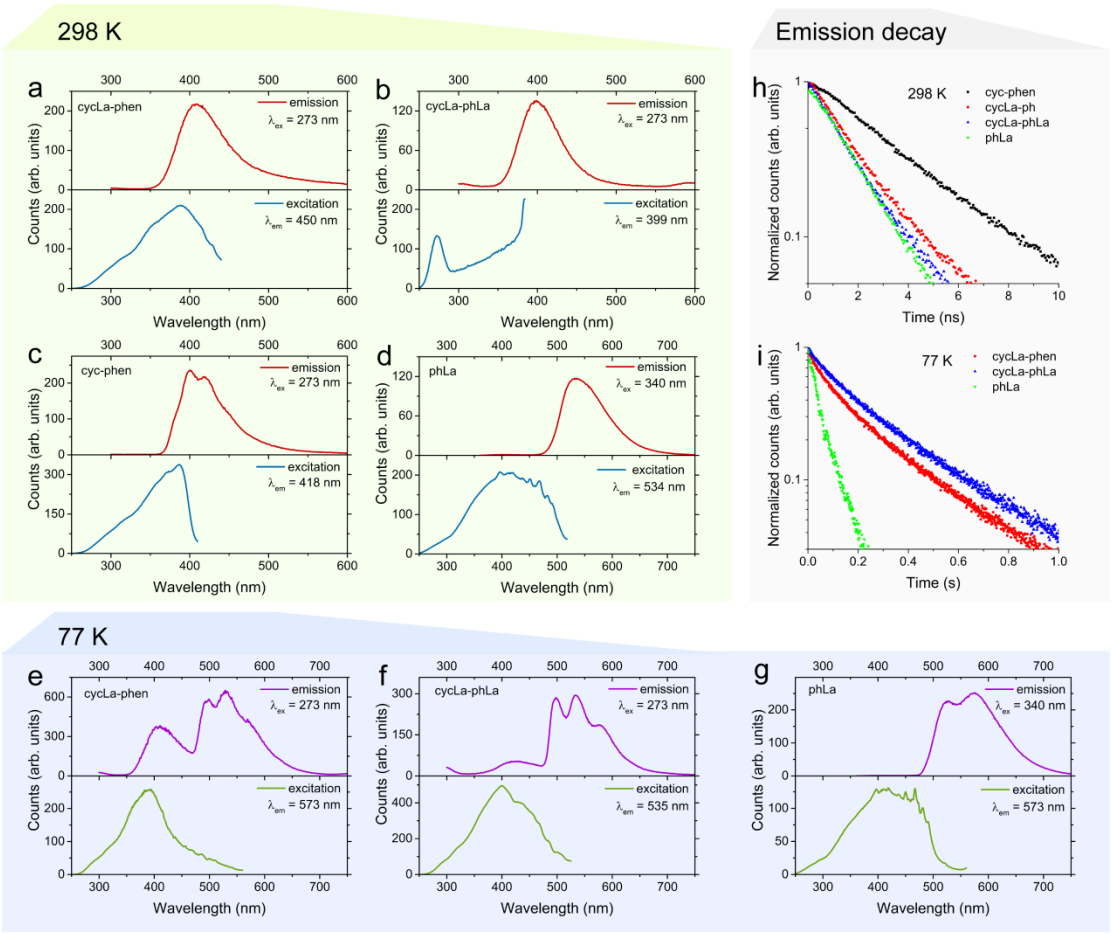

Figure 4.6. Room temperature solid-state emission (top) and excitation (bottom) spectra of lanthanum complexes and ligands: (a) ***cycLa-phen****; (b)* ***cycLa-phLa****; (c)* ***cyc-phen****; (d)* ***phLa****. 77 K solid-state emission (top) and excitation (bottom) spectra of lanthanum complexes and ligands: (e)* ***cycLa-phen****; (f)* ***cycLa-phLa****; (g)* ***phLa****. Superimposed structure between 400-500 nm in (d) and (g) is due to the xenon lamp. 298 K fluorescence decay (h) (λ_{exc} = 365 nm; λ_{em} = 450 nm) of* ***cyc-phen****,* ***cycLa-phen,*** ***cycLa-phLa*** *and (λ_{ex} = 365 nm; λ_{em} = 550 nm) of* ***phLa****; 77 K phosphorescence decay (i) (λ_{ex} = 355 nm; λ_{em} = 550 nm) of* ***cycLa-phen, cycLa-phLa*** *and (λ_{ex} = 355 nm; λ_{em} = 650 nm) of* ***phLa*** *in the solid state.*

The excitation spectrum of **cycLa-phen** singlet emission shows a structured band peaked at 389 nm with two sholders at around 300 nm and 350 nm (Figure 4.6a). The ligand **cyc-phen** exhibits a similar excitation band (Figure 4.6c). The **cycLa-phLa** excitation spectrum at 298 K was different since there is additional population by a singlet state at 283 nm (Figure 4.6b). The **phLa** excitation spectrum at 298 K exhibited a broad band peaked at around 400 nm (Figure 4.6d). The triplet excitation spectra of **cycLa-phen** (Figure 4.6e) **and cycLa-phenLa** (Figure 4.6f) at 77 K show a singlet absorption band at around 400 nm which similar to the **cyc-phen**

singlet emission (Figure 4.6c). The singlet and triplet emission were identified by the measurement of the monoexponential emission decay at 298 K and 77 K. The triplet lifetimes in solid state (40 ms - 180 ms, Table 4.1) are shorter than the phen lifetime (1.1 s) at 77 K in dichloromethane solution.[36] The lifetimes are longer than those of gadolinium cyclen complexes (~0.1 μs at 77 K in glassy medium[45] and gadolinium acylpyrazolone complexes (0.8-30 μs).[54] Without the magnetic spin-exchange interaction in gadolinium-ligand, the lifetimes of ligand triplet states are markably longer in the lanthanum complexes, with the longest value of 75 ms in complex $La(DPM)_3$.[55]

Table 4.1. Singlet (298 K) and triplet (77 K) lifetimes of ***cyc-phen****,* ***cycLa-phen cycLa-phLa and phLa.***

Compound	Singlet lifetime (ns)	k_{S-T} (298 K) (10^8 s^{-1})	Triplet lifetime (s)
cyc-phen	2.34	-	-
cycLa-phen	1.28	3.5	0.14
cycLa-phLa	1.15	4.4	0.18
phLa	1.17	4.3	0.04

The singlet decay of phen emission was monoexponential with a lifetime value of 7 ns in water solution and with a faster decay in cyclohexane (<1 ns).[56] The singlet decays in solid states are monoexponential in our study in Figure 4.6h,i. The singlet lifetime values are in ns range as shown in Table 4.1. Decreased singlet lifetimes were observed as the number of lanthanum ion increased. The decrease is because of the increased singlet deactivation for the intersystem crossing to populate the triplet states, k_{S-T}:

$$I_s(t) = I_s(0)\exp(-t/\tau)\exp(-k_{S-T}t)$$

where I_s is the singlet emission intensity and τ is the initial lifetime without intersystem crossing. Putting k_{S-T} for **cyc-phen** as 0 since no emission of triplet states was observed at 77 K, the values of k_{S-T} for the other complexes are displayed in Table 4.1. The intersystem crossing rate (k_{S-T}) is > 10^8 s^{-1} and it increases as the number of lanthanum ion presented in the complexes increases, because of enhanced spin-orbit coupling.

4.2.3 Excitation spectra of Eu^{3+} complexes

In this section, we compare the excitation spectra of the europium complexes. The excitation localized on the phen unit instead of the entire complexes. The excitation spectra of **cycEu-phLa**, **cycEu-phen, cycLa-phEu**, and **phEu** in Figure 4.7 were measured at room temperature. The europium absorption is weaker in **cycLa-phEu** than the phen ligand when the europium ion is located on the phen site. The europium absorption is relatively stronger in **cycEu-phLa** when the europium ion is located on the cyclen site. The results indicate a more efficient energy transfer from phen to europium with a closer phen-europium distance in the **cycLa-phEu**. The intensity change of $^7F_0 \rightarrow {}^5L_6$ transition is not because of the overlap with a LMCT band, as reported in another case,[57] because the relative intensity ratio of $^7F_0 \rightarrow {}^5L_6$ transition with other europium transitions does not change remarkably.

The three band structure that was observed in the excitation spectra of the ligands is also observed in the complexes (Figure 4.7). We subtracted out the europium absorption in Figure 4.7 and show the resulted spectra in Figure 4.8. The excitation spectra can be fitted with three Gaussian peaks at similar wavelengths, at 363 nm, 331 nm, and 284 nm. The peaks correspond to the singlet absorption transitions of the ligand because they have similar wavelength of maxima with the absorption of phen ligand (Figure 4.4), and are blueshifted from those in La complexes (Figure 4.6). Typically, the electron withdrawal groups in the phen such as protonation,[36] NO_2,[58] can induce a redshift in the excitation spectrum of phen. This has been observed previously, for instance, $[Eu(dpm)_2(NO_3)(tppo)_2]$ was reported to redshift relatively to the corresponding terbium system.[57]

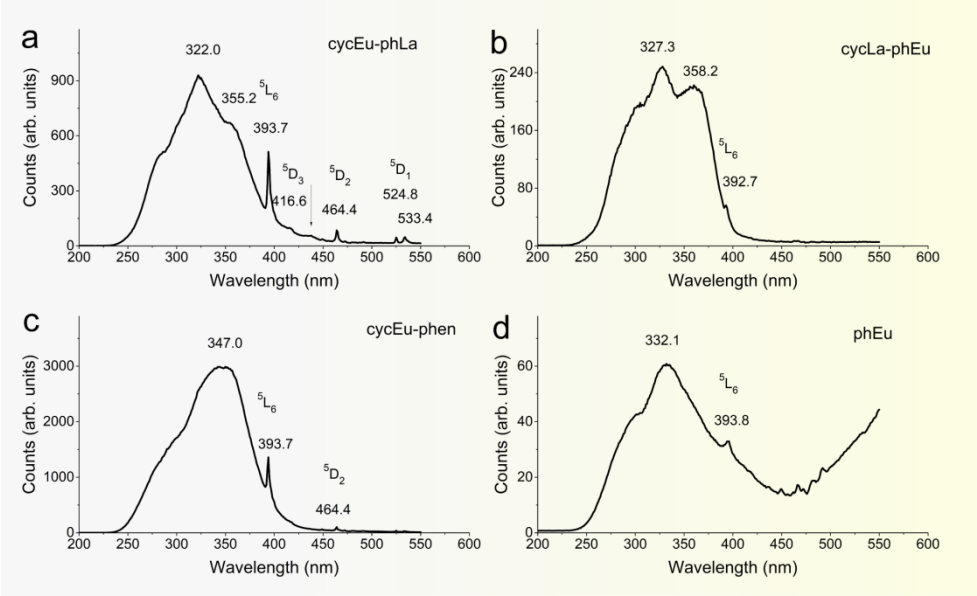

*Figure 4.7. Room temperature excitation spectra (monitored at the peak wavelength of the $^5D_0 \rightarrow {}^7F_2$ transition) of **cycEu-phLa**, **cycLa-phEu**, **cycEu-phen** and **phEu** in the solid state.*

Weaker bands in the excitation **cycEu-phLa** spectrum, with the strongest one at 437 nm marked by an arrow in Figure 4.7, do not correspond to the pure europium electronic transitions. Similar bands have also been reported previously but not been assigned in the europium complex with phen ligand.[38, 59] These bands are assigned to the vibronic structure of the $^7F_0 \rightarrow {}^5D_2$ hypersensitive transition.

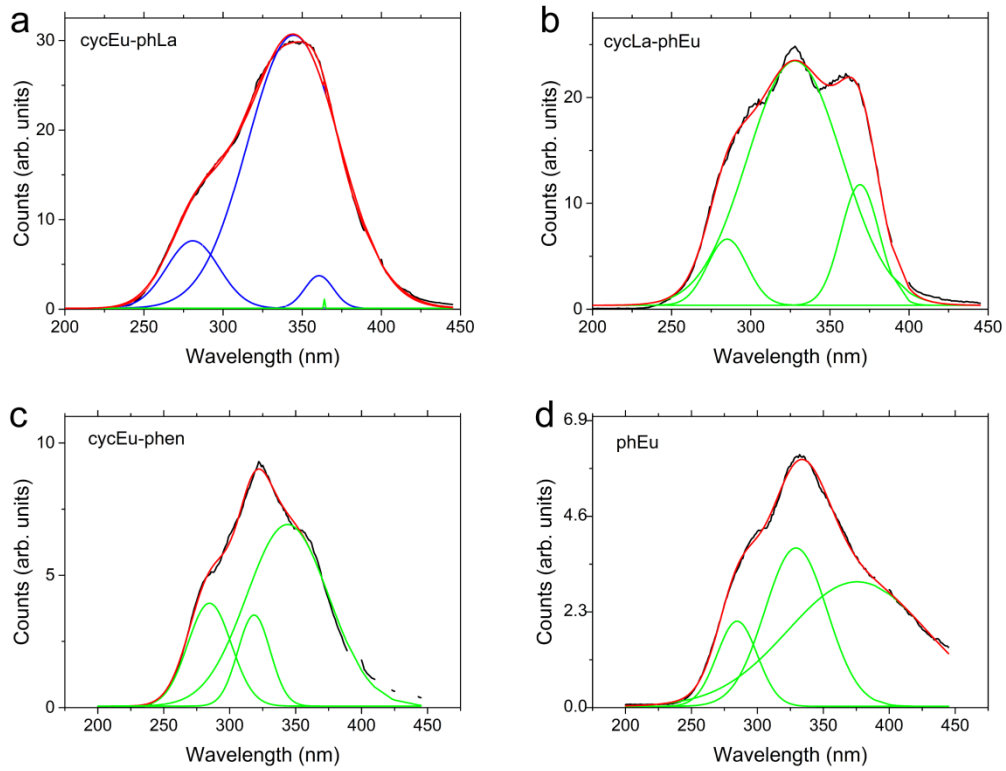

*Figure 4.8. The excitation spectra (monitored at the peak wavelength of the $^5D_0 \rightarrow {}^7F_2$ transition) of **cycEu-phLa**, **cycLa-phEu**, **cycEu-phen** and **phEu** in solid state with the $4f^6 - 4f^6$ transitions of Eu^{3+} removed and fitted by three Gaussians at 284 nm, 331 ± 13 nm and 363 ± 15 nm.*

4.2.4 Room temperature emission spectra of Eu^{3+} complexes.

The europium emission spectra of the complexes provide the symmetry information of the europium ion and enable the determination of radiative lifetimes and the calculation of Judd-Ofelt parameters (Ω). The decay determination enables the calculation of sensitisation efficiencies from the ligand to europium ion and internal quantum efficiencies. The interchange of europium and lanthanum ions also allows us to compare the spectra and decay of the europium luminescence of the two binding sites.

Figure 4.9 displays the normalized emission spectra at 298 K. Spectra of europium bonded to the four nitrogen and four oxygen atoms in cyclen ligand showed a characteristic emission band of the transition $^5D_0 \rightarrow {}^7F_4$ where there are two peaks at shortest wavelength.[45] Table 4.2 shows the relative intensities of $^5D_0 \rightarrow {}^7F_J$ where

the area of $^5D_0 \rightarrow {}^7F_1$ transition was set as 1. The high transition intensity ratio of $^5D_0 \rightarrow {}^7F_2$: $^5D_0 \rightarrow {}^7F_1$ generally indicates high "asymmetry" in the europium ion environment. When the europium inversion centre is lost, this increased ratio is expected, but other considerations were also discussed in the literature.[18] The $^5D_0 \rightarrow {}^7F_2$: $^5D_0 \rightarrow {}^7F_1$ ratio is sensitive to the coordination ligand or its substituent polarizabilities,[60] so the high ratio of the europium binding site with soft dithiocarbamate ligands in the complex **cycLa-phEu** may be expected while the complex **phEu** is less asymmetrical. The emission intensity followed an order of **phEu** (1) **< cycLa-phEu (**63) **< cycEu-phLa** (199) < **cycEu-phen** (4626), and the pyrrolidine dithiocarbamates are acting as quenching ligands. It has been reported that the quenching of the europium emission is because of the strong dithiocarbamate's electron-donating ability and the ease of Eu^{3+} to Eu^{2+} reduction promoting an efficient LMCT process.[61] To conclude, the comparison of **cycLa-phEu** and **cycEu-phLa** emissions showed the uniqueness of their spectra upon the interchange of the europium ion, they not only have different emission intensity, but also band structure (Figure 4.9).

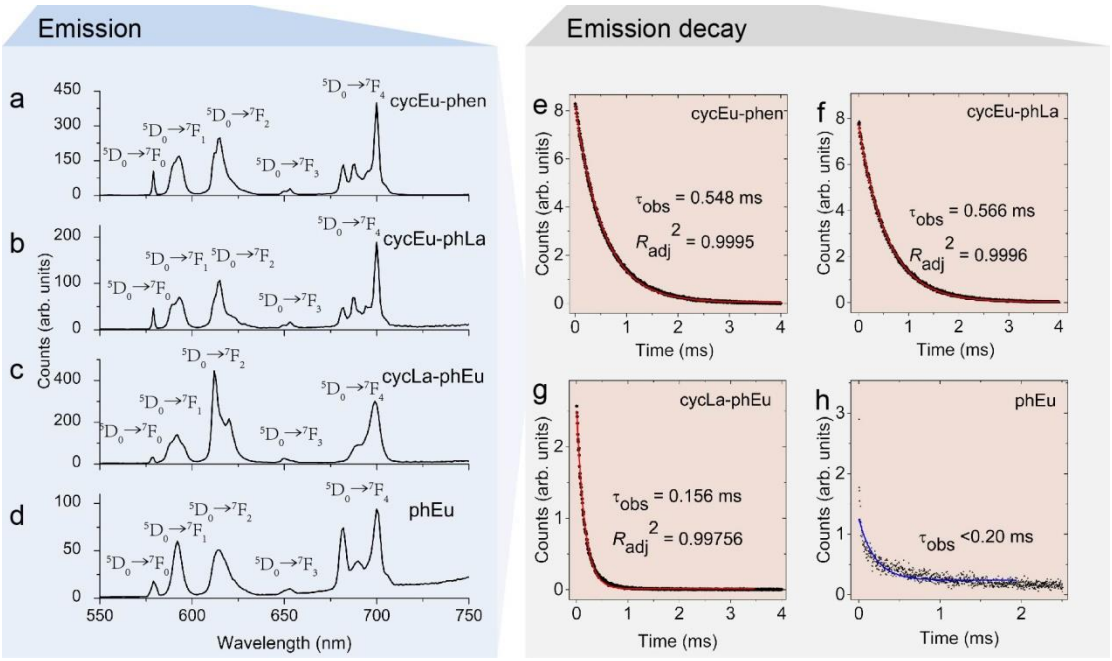

Figure 4.9. The room temperature emission spectra of (a-d) ***cycEu-phen***, ***cycEu-phLa***, ***cycLa-phEu***, *and* ***phEu*** *(λ_{ex} = 273 nm) in the solid state. Room temperature $^5D_0$ luminescence decays (e-h) of the studied Eu^{3+} systems (λ_{ex} = 355 nm).*

The radiative lifetimes and the deduced parameters Ω_2 and Ω_4 (Table 4.3) were determined by Judd-Ofelt analysis of the complex spectral intensities (details are described in the experimental section in chapter 7). Binnemans[16] has pointed out the hypersensitive transition $^5D_0 \rightarrow {}^7F_2$ is directly proportional to the parameter Ω_2. Indeed, the Ω_2 values (Table 4.3) follow this trend, with the **phEu** having the smallest magnitude and **cycLa-phEu** the largest one.

The relatively high $^5D_0 \rightarrow {}^7F_4$ intensity which accompanied with a high magnitude Ω_4 parameter has been attributed to a europium ion coordination polyhedron close to D_{4d} symmetry,[59] but it is not the case in complex **phEu**. Recently, Moura et al.[62] introduced the overlap polarizability concept, indicating a change of the formulation of the dynamic coupling mechanism. The ligands attached to the europium ion produce an induced dipole composing the original term associated with the effective core polarizability of the atoms that connected to europium, but supplemented by the overlap polarizability term. The relative contribution in the intensity parameters of the dynamic coupling mechanism is $\Omega_4 < \Omega_2$, but the overlap polarizability contribution exhibits the reverse trend. Thus, the Ω_4 values (Table 4.3) implies a high degree of Eu – S bonding covalency. The **phEu** has the Ω_4 value which is comparable to the value of the complex $Eu(NO_3)_3(phen)_2$.[62]

Figure 4.9 also shows the emission decay and their monoexponential fitting of the four complexes. When the europium locates in the cyclen binding site, the lifetimes do not change greatly, with values in 0.56 ± 0.01 ms, and they have internal quantum efficiencies with values of 17.3 ± 0.03% for the complexes **cycEu-phen** and **cycEu-phLa**(Table 4.3). On the other hand, the external quantum efficiency decreases for the complexes **cycEu-phLa, cycLa-phEu** and **phLa** in comparison with **cycEu-phen** due to the quenching of CS_2 group. The chromophore in these complexes is phen, and the sensitising efficiency (Φ_{sens}) is a parameter determined by both the sensitisation and quenching.

Table 4.2. Relative intensities of $^5D_0 \rightarrow {}^7F_J$ transitions of the studied Eu^{3+} systems normalized to that of $^5D_0 \rightarrow {}^7F_1$.

Complex	Relative intensity

	$^5D_0 \rightarrow {}^7F_0$	$^5D_0 \rightarrow {}^7F_1$	$^5D_0 \rightarrow {}^7F_2$	$^5D_0 \rightarrow {}^7F_3$	$^5D_0 \rightarrow {}^7F_4$
cycEu-phen	0.122	1	1.696	0.140	2.496
cycEu-phLa	0.123	1	1.603	0.150	2.536
cycLa-phEu	0.062	1	2.857	0.125	2.254
phEu	0.155	1	1.501	0.094	2.734

Table 4.3. Photophysical data for the Eu^{3+} complexes. $\Phi_{int} = \tau_{obs}/\tau_{rad}$; $\Phi_{sens} = \Phi_{ext}/\Phi_{int}$.

	cycEu-phen	**cycEu-phLa**	**cycLa-phEu**	**phEu**
τ_R (ms)	3.21	3.24	2.73	3.18
τ_{obs} (ms)	0.55	0.57	0.16	<0.20
Φ_{int} (%)	17.0	17.6	5.9	<6
Φ_{ext} (%)	4.4	0.40	0.38	<0.1
Φ_{sens} (%)	25.9	2.3	6.4	-
Ω_2 (10^{-20} cm^2)	2.77	2.61	4.59	2.44
Ω_4 (10^{-20} cm^2)	8.35	8.48	7.51	9.15

4.2.5 Low-temperature emission of the Eu^{3+} complexes.

The well-resolved emission spectra measured at the low temperature offer a sensitive probe of the europium ion local environment. Figure 4.10 shows the emission spectral of the complexes measured at 10 K covering the emission range from 560 nm and 880 nm. Then band details are shown in Table 4.4. The emission peak intensities obey the selection rule in which if $J = 0$ or $J' = 0$, the $|\Delta J| = 2,4,6$.[18] The number of electronic transitions for each $^5D_0 \rightarrow {}^7F_J$ transition for the europium ion located C_1 site symmetry are up to $2J+1$. Additional emission peaks should be caused by the impurities or electron-phonon couplings. Our present case is not caused by the first reason since the $^5D_0 \rightarrow {}^7F_0$ transition only presented one sharp band in each emission spectrum (Figure 4.10). As usual in 4f – 4f spectra, vibronic bands are assumed to be weaker than pure electronic transitions. Hence in Table 4.4 the bands at similar energy are highlighted for these two systems and then the number of bands for each transition to the terminal J-multiplet is equal to, or smaller than, 2J+1. The strongest vibronic bands are expected to correspond to totally-symmetric vibrational modes based upon the strongest forced electric dipole transitions. The latter are clearly the intense $^5D_0 \rightarrow {}^7F_2$ pure electronic transitions for these two systems at 615 nm. Very weak bands

to longer wavelength of 675 nm can be assigned to vibronic structure based upon this transition involving totally symmetric vibrational modes of 1435, 1502 cm^{-1}.

The $^5D_0 \rightarrow {}^7F_4$ transition of **cycEu-phLa** is more intense than **cycEu-phen**, which is also indicated by the slightly larger value of Ω_4. The derived crystal field energies of the complexes **cycEu-phLa** and **cycEu-phen** are almost the same. This is because the europium ion environment is actually unchanged with the incorporation of the lanthanum ion. That is to say, the „spectroscopy vision" of europium ion is unchanged.

As we mentioned above, when the europium ion in the cyclen binding site, there are two emission bands with similar intensity at the shorter wavelength range. The one with longer wavelength band further resolved into three peaks (Figure 4.10a,b).

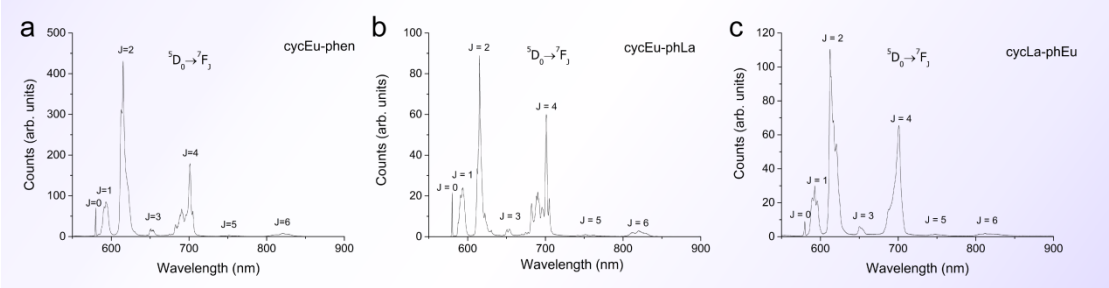

Figure 4.10. 10 K emission spectra of (a) ***cycEu-phen****, (b)* ***cycEu-phLa****, (c)* ***cycLa-phEu*** *(λ_{ex} = 355 nm) in the solid state.*

Table 4.4. Band energies in the nominal 10 K emission spectra of the Eu^{3+} complexes. The sample phEu has undergone decomposition.

	cycEu-phen		**cycEu-phLa**		**cycLa-phEu**		**phEu**	
$^7F_0$	17244w	0	17239w	0	17243w	0	17213s	0
$^7F_1$	17138vw	106	17142vw	97		--	17047vw	166
	17020sh	224	17010vvw	229		--		--
	16932m	312	16921m	318	16965m	278	16913vw	300
	16865m	379	16871m	368	16870m	373	16900sh	313
		--	16838m	401		--	16857sh	356
	16801bsh	443	16798sh	441	16772m	471	16840vw	373
							16762vw	451
$^7F_2$	16322s	922	16336ms	903	16327s	916	16315vw	898
		--	16292ms	947	16282s	961	16304vw	909
	16254vs	990	16255vs	984		--	16283vs	930
							16268s	945
		--	16215sh	1024	16206ms	1037	16214w	999
							16196w	1017
							16187sh	1026

	16142sh	1102	16173vbsh	1066		--	16159w	1054
							16133mw	1080
	16077sh	1167	16071w	1168	16105bm	1138	16087bvw	1126
		--	16007vbsh	1232	16004vbsh	1239	15958vw	1255
	15861vw	1383	15861vw	1378		--	15828vw	1385
$^7F_3$	15475vw	1769	15470vw	1769		--	15397vwsh	1816
		--	15388w	1851/ 867		--	15377vw	1836
	15367w	1877	15367w	1872	15379w	1864	15366sh	1847
							(15330vw)	1883
							(15313vw)	1900
	15289w	1955/ 1033	15297w	1942/ 958	15304w	1939	15292vw	1921
		--	15222vw	2017/ 1033	15250sh	1993	15253vw	1960
		--	15109vw	2130/ 1227		--		--
		--	15021vw	2218/ 1234		--		--
	14819vw	2425/ 1435	14823vw	2416/ 1432		--		--
	14752vw	2492/ 1502	14753vw	2486/ 1502		--		--
$^7F_4$	14647w	2597	14660w	2579		--		--
	14527w	2717	14527w	2712	14548m	2695	14585w	2628
	14486w	2758	14488w	2751		--	14477w	2736
		--	14467sh	2772		--		--
	14442w	2802	14445sh	2794		--	14410w	2803
	14369w	2875	14375w	2864		--	14384sh	2829
	14328sh	2916	14340vw	2899		--	14342w	2871
	14262m	2982	14261m	2978	14265ms	2978	14284w	2929
	14185mw	3059	14185mw	3054		--	14176w	3037
		--	14155sh	3084		--		--
		--	14112vw	3127		--		--
$^7F_5$	13477vw	3767	13489vw	3750	13478vw	3765	13491vw	3722
							13452vw	3761
							(13422vw)	3791
	13306vw	3938	13307vw	3932	13385vw	3858	13365vw	3848
							13262vw	3951
							13239vw	3974
	13117vw	4127	13121vw	4118	13222vbvw	4021		--
								--
								--
$^7F_6$	12331vw	4913	12332vw	4907	12413vbvw	4830	12413vw	4800

						12394sh	4819
	--	12300vw	4939	12322vw	4921	12288vw	4925
						12223vw	4990
12189vw	5055	12200vw	5039		--	12197vw	5016
12050vw	5194	12053sh	5186	12082vbvw	5161		
		11859vw	5380				

4.2.6 Room temperature solution spectra of the Eu^{3+} complexes.

We then compare the spectra in solution with those in solid states. The emission and excitation spectra at room temperature in solution are showed in Figure 4.11, Figure 4.12 and Figure 4.14. The luminescent spectra are different from the solid-state spectra, which implies a change of the europium coordination nature. It is indicated by (modified) Horrock's equation[49, 63, 64] that water molecules are coordinating to the cyclen binding sites in solution, while it is not apparent in solid states.[27, 29] The lowest energy transition of phenNH_2 is from an n → π* transition.

In the solid state (Figure 4.7), the lowest energy transition of phenNH_2 corresponds to an n → π* transition, corresponding to the HOMO-1 → LUMO transition (Figure 4.13). The (π,π*)and (n,π*) states of phen lie close and the solvent or pH changes can lead to spectral changes of both emission and excitation.[56, 65, 66] The **cycEu-phLa** has different emission spectra in water and deuterium water solutions in terms of spectral location and the relative intensities, indicating different coordination. On the other hand, when the europium ion is on the phen sites, the **cycLa-phEu** has a weaker emission in solutions such as deuterium water and deuterium methanol.

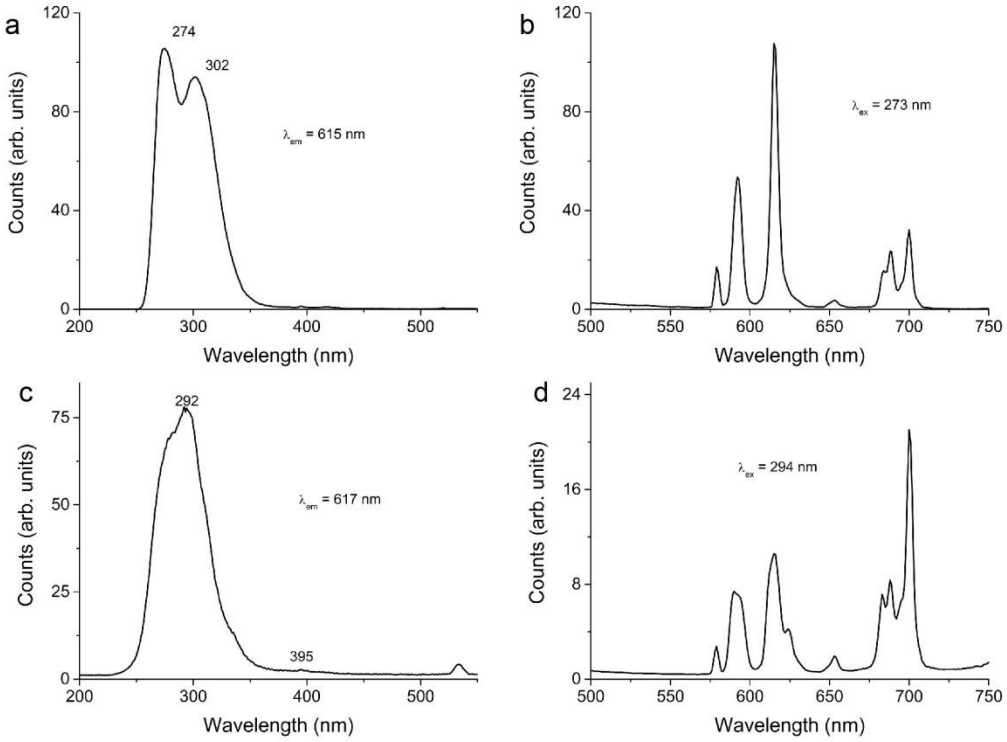

*Figure 4.11. Excitation and emission spectra of **cycEu-phen** in solution: (a) (b) 2 μM in DMSO; (c) (d) 2 μM in D_2O.*

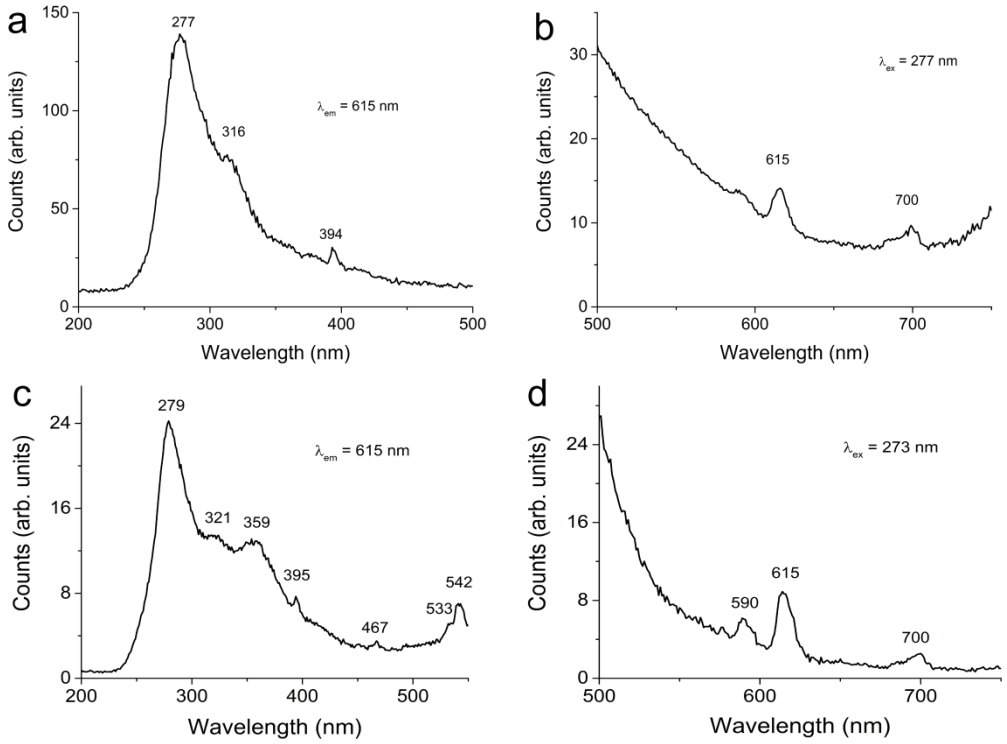

Figure 4.12. Excitation and emission spectra of **cycLa-phEu** in solution: (a) (b) 2 μM in D_2O; (c) (d) 2 μM in CD_3OD.

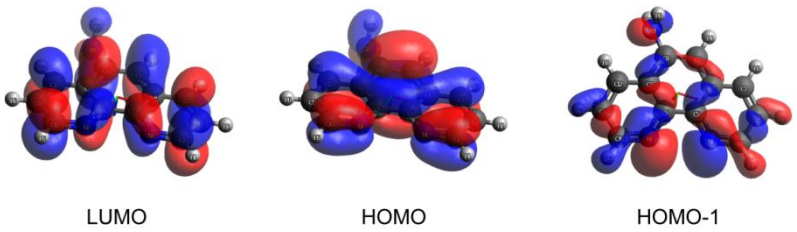

Figure 4.13. LUMO, HOMO and HOMO-1 of gaseous phase phenNH_2 from ORCA calculation. The lowest energy transition $S_0 \rightarrow S_1$ is calculated at 28733 cm^{-1} (348 nm) and corresponds mainly to HOMO-1 → LUMO transition.

The excitation spectra in solution were also different from the solid-state excitation spectra of the phen complexes.[33] Especially, the strong band at the longer wavelength in the solid state spectra are not present in the spectra measured in solution. Yang et al.[59] have reported the similar bands in the solid excitation spectrum of singlet states, so that the emission bands are not because of the ligand-metal charge transfer, but of the internal singlet-singlet transitions in the phen. These excitation bands contribute to energy transfer from ligand to europium ion in solid states, but they do not happen in solutions. The quenching of the europium emission when europium locates in the phen site is because of the inability of phen ligand to form complex with europium ion in the solution, this has been recognized previously.[67] To conclude, going from solid to solution, the spectral changes occur, because of the changes of the coordination environment of the europium ion.

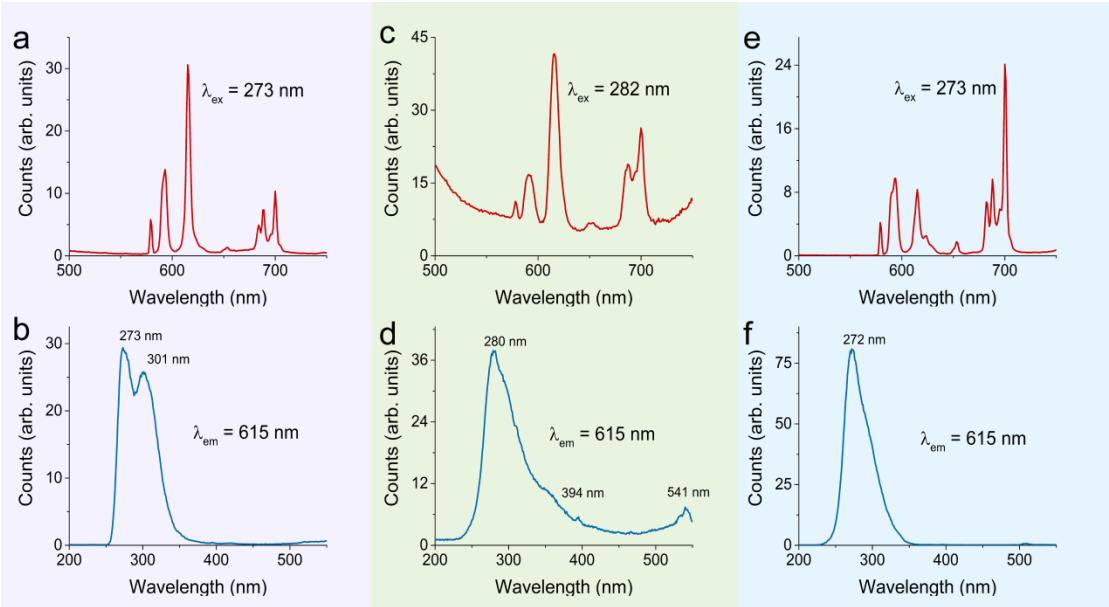

*Figure 4.14. Excitation and emission spectra of **cycEu-phLa** at 2 μM concentration in*

solution in: (a, b) DMSO; (c, d) CD_3OD; (e, f) H_2O.

4.3 Conclusion

To conclude, we have synthesized a pair of dinuclear complexes (**cycEu-phLa** and **cycLa-phEu)** with a europium ion on cyclen site and a lanthanum ion on phen site or vice verses. Though they have the same components and the same energy levels, they present different photophysical properties due to the different coordination environment. The band positions are different in the emission spectra. The emission of **cycEu-phLa** showed a stronger relative intensity of $^5D_0 \rightarrow {}^7F_2$ transition whereas the relative intensity of $^5D_0 \rightarrow {}^7F_4$ was weaker in comparison with **cycLa-phEu**. We found that the **cycEu-phLa** have a higher internal quantum efficiency while the **cycEu-phLa** have higher a sensitising efficiency, though they have similar external quantum yield. We determined the singlet-triplet intersystem crossing rate with values as $\sim 10^8$ s^{-1}. This study allows us a better understanding of the energy transfer from ligand to lanthanide ions, especially, in terms the binding sites.

4.4 References

1. S. Faulkner and S. J. A. Pope, *J. Am. Chem. Soc.*, 2003, **125**, 10526-10527.
2. J. C. Bunzli, A. S. Chauvin, C. D. Vandevyver, S. Bo and S. Comby, *Ann. N. Y. Acad. Sci.*, 2008, **1130**, 97-105.
3. M. S. Tremblay and D. Sames, *Chem. Commun.*, 2006, 4116-4118.
4. G. Bao, K.-L. Wong, D. Jin and P. A. Tanner, *Light Sci. Appl.*, 2018, **7**, 96.
5. T. J. Sorensen, M. Tropiano, O. A. Blackburn, J. A. Tilney, A. M. Kenwright and S. Faulkner, *Chem. Commun.*, 2013, **49**, 783-785.
6. K. Sénéchal-David, S. J. A. Pope, S. Quinn, S. Faulkner and T. Gunnlaugsson, *Inorg. Chem.*, 2006, **45**, 10040-10042.
7. K. A. Romanova, A. Y. Freidzon, A. A. Bagaturyants and Y. G. Galyametdinov, *J. Phys. Chem. A*, 2014, **118**, 11244-11252.
8. A. Bencini and V. Lippolis, *Coord. Chem. Rev.*, 2010, **254**, 2096-2180.
9. I. G. Fomina, Z. V. Dobrokhotova, G. G. Aleksandrov, V. I. Zhilov, I. P. Malkerova, A. S. Alikhanyan, D. M. Zhigunov, A. S. Bogomyakov, V. I. Gerasimova, V. M. Novotortsev and I. L. Eremenko, *Polyhedron*, 2013, **50**, 297-305.
10. S. Swavey, J. A. Krause, D. Collins, D. D'Cunha and A. Fratini, *Polyhedron*,

2008, **27**, 1061-1069.
11. T. J. Sørensen, A. M. Kenwright and S. Faulkner, *Chem. Sci.*, 2015, **6**, 2054-2059.
12. A. R. Ramya, M. L. Reddy, A. H. Cowley and K. V. Vasudevan, *Inorg. Chem.*, 2010, **49**, 2407-2415.
13. T. Morita, M. Damjanovic, K. Katoh, Y. Kitagawa, N. Yasuda, Y. Lan, W. Wernsdorfer, B. K. Breedlove, M. Enders and M. Yamashita, *J. Am. Chem. Soc.*, 2018, **140**, 2995-3007.
14. B. Alpha, R. Ballardini, V. Balzani, J.-M. Lehn, S. Perathoner and N. Sabbatini, *Photochem. Photobiol.*, 1990, **52**, 299-306.
15. A. V. M. de Andrade, R. L. Longo, A. M. Simas and G. F. de Sá, *J. Chem. Soc., Faraday Trans.*, 1996, **92**, 1835-1839.
16. K. Binnemans, *Coord. Chem. Rev.*, 2015, **295**, 1-45.
17. J.-C. G. Bünzli, *Chem. Rev.*, 2010, **110**, 2729-2755.
18. P. A. Tanner, *Chem. Soc. Rev.*, 2013, **42**, 5090-5101.
19. J. C. Bunzli and C. Piguet, *Chem. Soc. Rev.*, 2005, **34**, 1048-1077.
20. M. Latva, H. Takalo, V.-M. Mukkala, C. Matachescu, J. C. Rodríguez-Ubis and J. Kankare, *J. Lumines.*, 1997, **75**, 149-169.
21. S. Susumu and W. Masanobu, *Bull. Chem. Soc. Jpn.*, 1970, **43**, 1955-1962.
22. O. L. Malta, *J. Non. Cryst. Solids*, 2008, **354**, 4770-4776.
23. P. A. Tanner, L. Zhou, C. Duan and K.-L. Wong, *Chem. Soc. Rev.*, 2018.
24. S. Omagari, T. Nakanishi, Y. Kitagawa, T. Seki, K. Fushimi, H. Ito, A. Meijerink and Y. Hasegawa, *Sci. Rep.*, 2016, **6**, 37008.
25. R. C. Leif, L. M. Vallarino, M. C. Becker and S. Yang, *Cytometry A*, 2006, **69**, 767-778.
26. J. F. Lemonnier, L. Guenee, C. Beuchat, T. A. Wesolowski, P. Mukherjee, D. H. Waldeck, K. A. Gogick, S. Petoud and C. Piguet, *J. Am. Chem. Soc.*, 2011, **133**, 16219-16234.
27. T. J. Sørensen, L. R. Hill and S. Faulkner, *ChemistryOpen*, 2015, **4**, 509-515.
28. E. M. Surender, S. Comby, S. Martyn, B. Cavanagh, T. C. Lee, D. F. Brougham and T. Gunnlaugsson, *Chem. Commun.*, 2016, **52**, 10858-10861.
29. A. K. Junker, M. Tropiano, S. Faulkner and T. J. Sorensen, *Inorg. Chem.*, 2016, **55**, 12299-12308.
30. Y. O. Fung, W. Wu, C. T. Yeung, H. K. Kong, K. K. Wong, W. S. Lo, G. L. Law, K. L. Wong, C. K. Lau, C. S. Lee and W. T. Wong, *Inorg. Chem.*, 2011, **50**, 5517-5525.
31. G.-L. Law, K.-L. Wong, K.-K. Lau, H.-L. Tam, K.-W. Cheah and W.-T. Wong, *Eur. J. Inorg. Chem.*, 2007, **2007**, 5419-5425.
32. C. T. Li, Y. F. Zhao, H. M. Hu, H. Zhao, X. Wang and G. Xue, *Dalton Trans.*, 2016, **45**, 15436-15444.
33. E. Moretti, A. Talon, L. Storaro, A. Le Donne, S. Binetti, A. Benedetti and S. Polizzi, *J. Lumines.*, 2014, **146**, 178-185.
34. V. I. Tsaryuk, K. P. Zhuravlev, A. V. Vologzhanina, V. A. Kudryashova and V. F. Zolin, *Journal of Photochem. Photobiol. A: Chemistry*, 2010, **211**, 7-19.

35. J. Lhoste, N. Henry, T. Loiseau and F. Abraham, *Polyhedron*, 2011, **30**, 1289-1294.
36. N. Armaroli, L. De Cola, V. Balzani, J.-P. Sauvage, C. O. Dietrich-Buchecker and J.-M. Kern, *J. Chem. Soc., Faraday Trans.*, 1992, **88**, 553-556.
37. M. F. Belian, H. J. Batista, A. G. S. Bezerra, W. E. Silva, G. F. de Sá and S. Alves, *Chem. Phys.*, 2011, **381**, 29-34.
38. Z. Pan, G. Jia, C.-K. Duan, W.-Y. Wong, W.-T. Wong and P. A. Tanner, *Eur. J. Inorg. Chem.*, 2011, **2011**, 637-646.
39. L. A. Ekanger, D. R. Mills, M. M. Ali, L. A. Polin, Y. Shen, E. M. Haacke and M. J. Allen, *Inorg. Chem.*, 2016, **55**, 9981-9988.
40. A. M. Nonat, A. J. Harte, K. Senechal-David, J. P. Leonard and T. Gunnlaugsson, *Dalton Trans.*, 2009, 4703-4711.
41. H. Yang, L. Ding, L. An, Z. Xiang, M. Chen, J. Zhou, F. Li, D. Wu and S. Yang, *Biomaterials*, 2012, **33**, 8591-8599.
42. J. Vaněk, F. Smrčka, P. Lubal, I. Třísková and L. Trnková, *Monatsh. Chem.*, 2016, **147**, 925-934.
43. S. Quici, A. Casoni, F. Foschi, L. Armelao, G. Bottaro, R. Seraglia, C. Bolzati, N. Salvarese, D. Carpanese and A. Rosato, *J. Med. Chem.*, 2015, **58**, 2003-2014.
44. T. Gunnlaugsson, J. P. Leonard, K. Sénéchal and A. J. Harte, *J. Am. Chem. Soc.*, 2003, **125**, 12062-12063.
45. Z. Liang, C.-F. Chan, Y. Liu, W.-T. Wong, C.-S. Lee, G.-L. Law and K.-L. Wong, *RSC Adv.*, 2015, **5**, 13347-13356.
46. S. N. A. Jenie, Z. Du, S. J. P. McInnes, P. Ung, B. Graham, S. E. Plush and N. H. Voelcker, *J. Mat. Chem. B*, 2014, **2**, 7694-7703.
47. Z. Liang, T.-H. Tsoi, C.-F. Chan, L. Dai, Y. Wu, G. Du, L. Zhu, C.-S. Lee, W.-T. Wong, G.-L. Law and K.-L. Wong, *Chem. Sci.*, 2016, **7**, 2151-2156.
48. H. Li, R. Lan, C.-F. Chan, L. Jiang, L. Dai, D. W. J. Kwong, M. H.-W. Lam and K.-L. Wong, *Chem. Commun.*, 2015, **51**, 14022-14025.
49. D. Parker, J. W. Walton, L. Lamarque and J. M. Zwier, *Eur. J. Inorg. Chem.*, 2010, **2010**, 3961-3966.
50. P. Pitchaimani, K. M. Lo and K. P. Elango, *J. Coord. Chem.*, 2015, **68**, 2167-2180.
51. G. L. Powell, *J. Chem. Phys.*, 1967, **47**, 95-101.
52. S. V. Larionov and Y. A. Bryleva, *Russian J. Coord. Chem.*, 2016, **42**, 293-310.
53. P. Pitchaimani, K. M. Lo and K. P. Elango, *Polyhedron*, 2015, **93**, 8-16.
54. L. Ying, A. Yu, X. Zhao, Q. Li, D. Zhou, C. Huang, S. Umetani and M. Matasai, *J. Phys. Chem.*, 1996, **100**, 18387-18391.
55. J. S. Brinen, F. Halverson and J. R. Leto, *J. Chem. Phys.*, 1965, **42**, 4213-4219.
56. B. N. Bandyopadhyay and A. Harriman, *J. Chem. Soc., Faraday Trans.*, 1977, **73**, 663-674.
57. Y. C. Miranda, L. L. A. L. Pereira, J. H. P. Barbosa, H. F. Brito, M. C. F. C.

Felinto, O. L. Malta, W. M. Faustino and E. E. S. Teotonio, *Eur. J. Inorg. Chem.*, 2015, **2015**, 3019-3027.
58. V. Tsaryuk, V. Zolin, L. Puntus, V. Savchenko, J. Legendziewicz, J. Sokolnicki and R. Szostak, *J. Alloys Compd.*, 2000, **300-301**, 184-192.
59. T.-H. Yang, L. Fu, R. A. S. Ferreira, M. M. Nolasco, J. Rocha, L. D. Carlos and F.-N. Shi, *Eur. J. Inorg. Chem.*, 2015, **2015**, 4861-4868.
60. D. R. Foster, F. S. Richardson, L. M. Vallarino and D. Shillady, *Inorg. Chem.*, 1983, **22**, 4002-4009.
61. M. D. Regulacio, M. H. Pablico, J. A. Vasquez, P. N. Myers, S. Gentry, M. Prushan, S.-W. Tam-Chang and S. L. Stoll, *Inorg. Chem.*, 2008, **47**, 1512-1523.
62. R. T. Moura, A. N. Carneiro Neto, R. L. Longo and O. L. Malta, *J. Lumines.*, 2016, **170**, 420-430.
63. E. R. H. Walter, J. A. G. Williams and D. Parker, *Chem. Commun.*, 2017, **53**, 13344-13347.
64. D. Parker and J. A. G. Williams, *J. Chem. Soc., Perkin Trans. 2*, 1996, 1581-1586.
65. M. S. Henry and M. Z. Hoffman, *J. Phys. Chem.*, 1979, **83**, 618-625.
66. G. M. Badger and I. S. Walker, *J. Chem. Soc.*, 1956, 122-126.
67. S. T. Frey, M. L. Gong and W. D. Horrocks, *Inorg. Chem.*, 1994, **33**, 3229-3234.

Chapter 5 Luminescent enhancement of dye sensitised upconversion nanoparticles

5.1 Introduction

Lanthanide-doped upconversion nanoparticles (UCNPs), capable of converting lower energy near-infrared (NIR) light into the visible light, are highly attractive due to their distinguished advantages such as large anti-Stokes shift, photo-stability, free of background, long lifetime, non-blinking, non-bleaching, biological compatibility, and low cytotoxicity.[1-3] They are considered to be excellent in a broad range of applications including super-resolution microscopy,[4] biomedical imaging,[5] ultrasensitive sensing,[6-9] security ink,[10] drug delivery[11, 12], display,[13] and optogenetics[14].

The small absorption cross-section of the lanthanide ions largely limits the luminescence performance of UCNPs. In typical UCNPs, lanthanide sensitisers (Yb^{3+}) and emitters (such as Er^{3+}, Tm^{3+} or Ho^{3+}) are co-doped in the inert host (typically $NaYF_4$ or $NaGdF_4$).[15] NIR dye has a broad absorption band and 10^3-10^4 times larger absorption cross-section than lanthanide sensitiser Yb^{3+}. Therefore, the introduction of dye sensitisation can directly improve the absorption efficiency of UCNPs with an enhancement of several orders of magnitude. In 2012, Zou et al. first demonstrated IR806-sensitised UCNPs and achieved 1,100 times upconversion enhancement (Figure 5.1).[16] To improve the spectral overlap of the dye and Yb^{3+}, in 2015, Chen et al. designed the core@shell upconversion nanoparticles to facility multistep cascade energy transfer (Dye→Nd^{3+}→Yb^{3+}→Tm^{3+}).[17] Recently, Garfield et al. revealed that increasing Gd^{3+} doping concentration in UCNPs shifted the energy level of the excited dye from singlet to triplet state to better match that of Yb^{3+} acceptors, thereby enhancing the upconversion emission by up to 33,000 times.[18] These studies are all focusing on the design and adjusting of the inorganic particles in the hybrid system, while no effect has been done to improve the performance of the NIR dyes. The

structure skeleton of these employed NIR dyes has alternative chain-like single-double bonds which allow the rotation of bonds and are potential quenching factor (Figure 5.1). The next opportunities are to develop stable NIR dyes with high quantum yield as the sensitiser to improve the performance of the hybrid system.

Here, we design and synthesize a high efficient NIR dye through the steric effect by introducing a bulky moiety tetraphenylethene (TPE) (Figure 5.1). The newly formed TPEO-IR783 exhibits an impressive quantum yield of 22.46%, which is the highest among the reported NIR dyes for UCNP sensitisation. The TPEO-IR783 sensitised UCNPs show more than 200-fold upconversion emission enhancement of the reported IR806 sensitised UCNPs and around 2-fold of the IR783 and IR808.

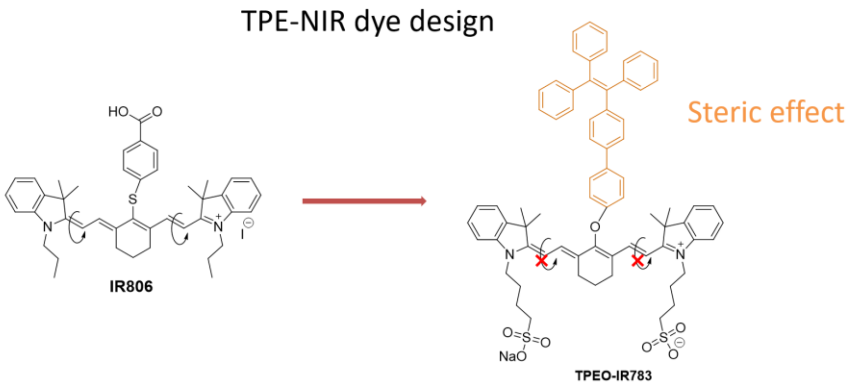

Figure 5.1. The design of TPE-NIR dye by introduction of TPE moiety.

5.2 Results and discussion

5.2.1 Synthesis

TPEO-IR783 was synthesized by nucleophilic substitution of IR783 by TPE-OH (Scheme 5.1) under NaH conditions at room temperature. The TPE-OH was synthesized by substitution and elimination reactions with the starting chemical of diphenylmethane and (4-bromophenyl)(phenyl)methanone, followed by a Suzuki coupling with (4-hydroxyphenyl)boronic acid. For a comparison, we synthesized IR806 and IR808 by substitution of the chlorine on the NIR dyes with 4-mercaptobenzoic acid at room temperature in DMF (Scheme 5.2 and Scheme 5.3). The intermediates and final products were characterized by MS, ^{1}H NMR and ^{13}C NMR.

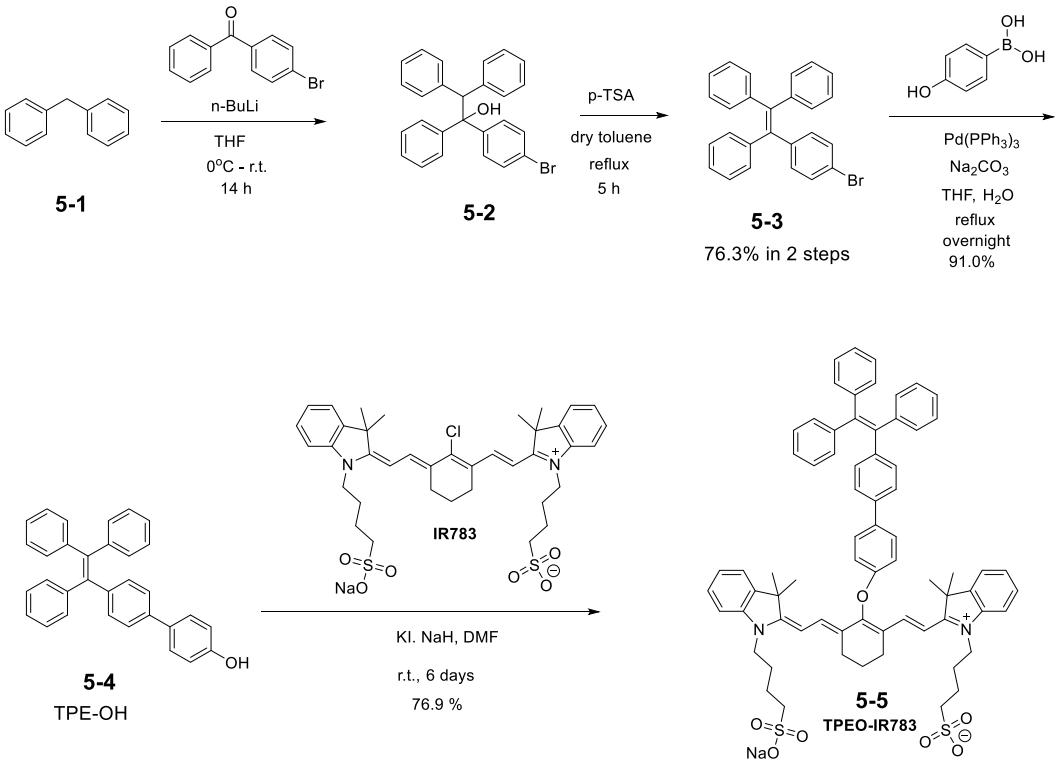

Scheme 5.1. Synthetic scheme of TPEO-IR783.

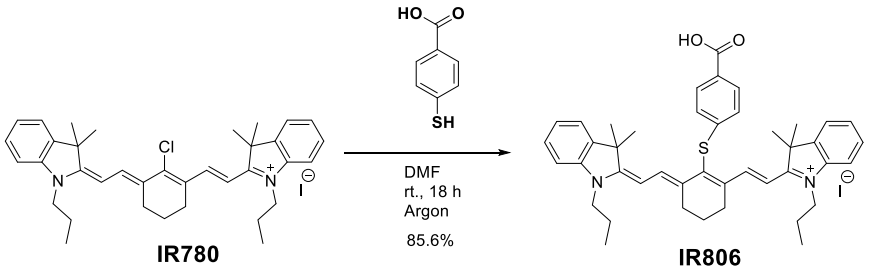

Scheme 5.2. Synthetic scheme of TPE-IR806.

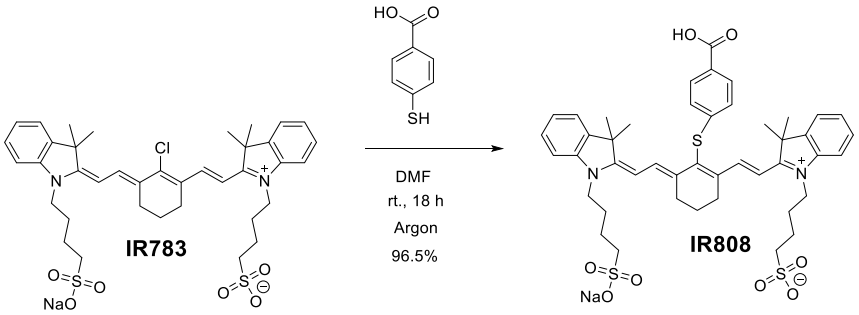

Scheme 5.3. Synthetic scheme of IR808.

5.2.2 Photophysical properties

The TPEO-IR783 exhibits an absorption band peaked at 781 nm with a high absorption coefficiency of 1.85×10^5 M^{-1} cm^{-1}. There is a weak absorption band at

around 300 nm that attributes to TPE moiety. The absorption spectrum of TPEO-IR783 shows almost no absorption in the range between 400 nm and 600 nm, providing a transparent window for the upconversion emission (Figure 5.2). The emission spectrum shows an emission band peaked at 801 nm, resulting in a 20 nm shift from the absorption peak.

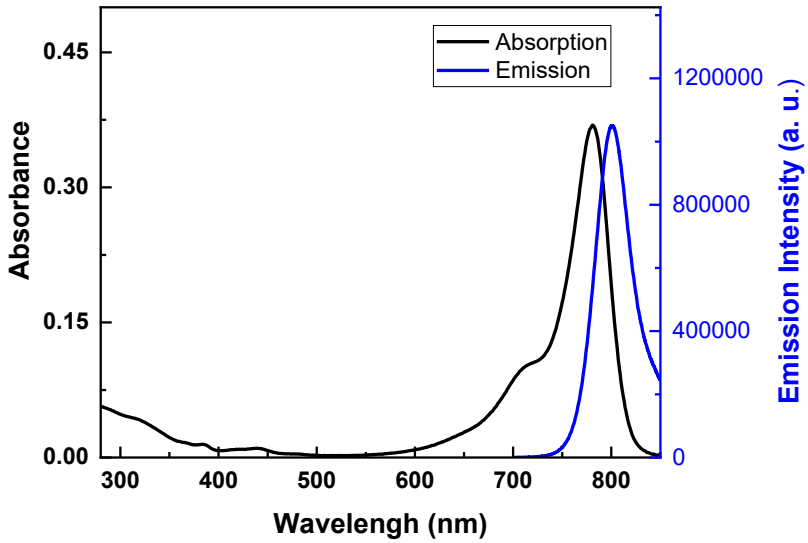

Figure 5.2. The absorption (black) and emission (blue, λ_{exc} = 793 nm) of TPEO-IR783 (2 μM) in DMF.

We next compare the absorption and emission position of the TPEO-IR783 with the conventional NIR sensitisers including IR806, IR808, and IR783 (Figure 5.3). Compared with IR783, the modification of TPEO moiety makes both the absorption and emission bands of TPEO-IR783 undergo blueshift of 12 nm and 14 nm, respectively. While the incorporation of benzoic acid group on the dye skeleton causes the redshift of the IR808 absorption band in comparison with IR783 absorption band. The IR808 has the lowest energy with the absorption and emission bands peaked at 807 nm and 830 nm in DMF, respectively. The IR806, which has the structure different only on its side chains, has similar bands at 804 nm and 828 nm. It is reported that the IR806 triplet state was slightly lower than the absorption of Yb^{3+} and facility the energy transfer between triplet state to Yb^{3+}.[18] Due to the blueshift of the both absorption and emission, we assume that TPEO-IR783 has a triplet higher than that of IR806 and slightly higher than the Yb^{3+} absorption. This slightly higher energy will facility the energy flow from the dye to the Yb^{3+} ions and avoid the back energy

transfer from Yb^{3+} to TPEO-IR783 triplet states, thereby making the energy transfer more efficient. The TPEO-IR783 exhibits expressive quantum yield with a value of 22.46% that is around 3 times of IR806 (7.01%) and IR808 (7.52%) and around 2 times of IR783 (11.59%) (Table 5.1).

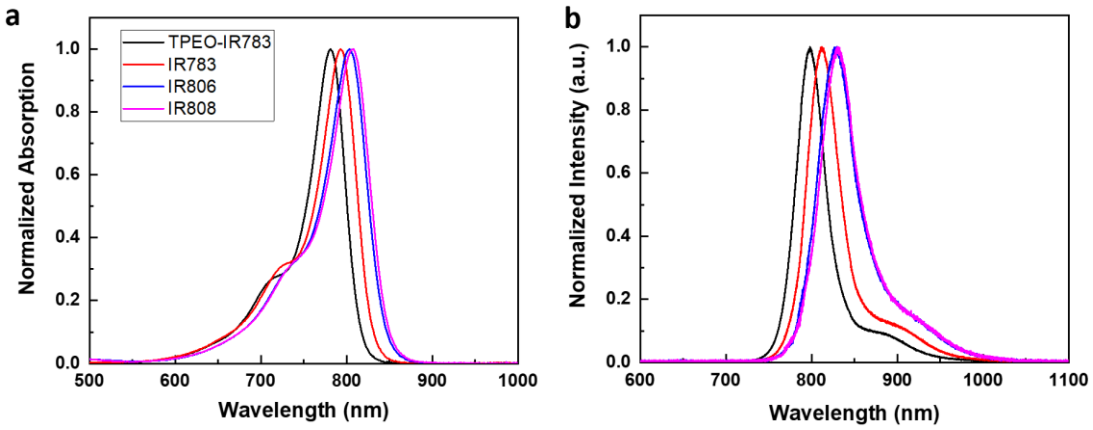

Figure 5.3. (a) The normalized absorption of TPEO-IR783, IR783, IR806 and IR808 in DMF (2 μM). (b) The normalized emission of TPEO-IR783, IR783, IR806 and IR808 in DMF (2 μM).

Table 5.1. The quantum yield of TPEO-IR783, IR783, IR806 and IR808 in DMF.

IR dye	Quantum yield (%)
TPEO-IR783	22.46±0.60
IR783	11.59±0.45
IR806	7.01±0.40
IR808	7.52±0.33

5.2.3 Sensitisation of UCNPs

We use a general oleic acid-free UCNPs ($NaYF_4$: 20% Yb, 2% Er, 22 nm) to investigate the sensitisation by the four NIR dyes (Figure 5.4a). Upon excitation with 793 nm laser excitation, the dye-UCNPs show characteristic upconversion of Er^{3+} with three peaks at 525 nm, 542 nm and 650 nm (Figure 5.4c). The emissions of dye sensitised UCNPs are dependent on the concentration of dyes (Figure 5.4b), with 2.5 or 5 uM as the best concentrations.

The upconversion emission of dye-UCNPs with 2.5 uM dyes are shown in Figure

5.4c,d. TPEO-IR783 sensitised UCNPs have the brightest upconverting emission with 235-fold enhancement in comparison with the popular used IR806. We assume the enhancement attributes to the high quantum yield of TPEO-IR783. The sulfonate side chains on TPEO-IR783 ensure the attachment of the NIR dye to the surface of UCNPs. The IR808 and IR783 also show enhanced emission in comparison with IR806, indicating that these sulfonic acid groups increase the affinity between dye molecules and UCNPs. All the photophysical results indicate the developed TPEO-IR783 is an excellent NIR dye as a sensitiser of upconversion nanoparticles.

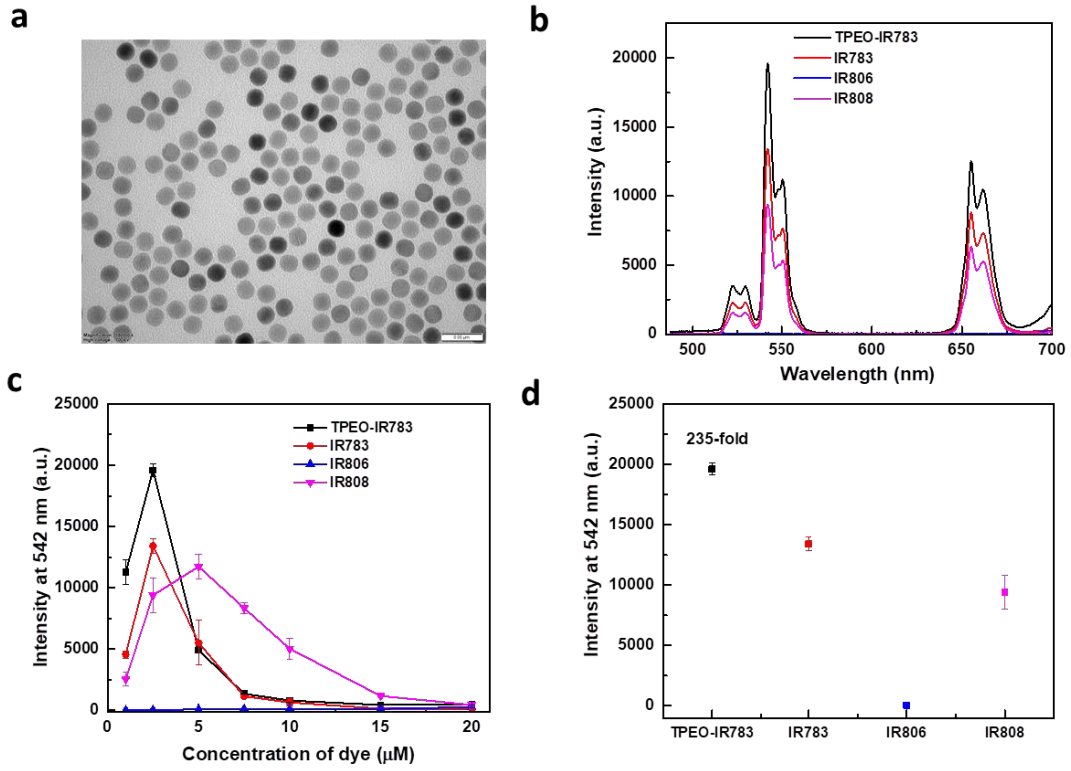

Figure 5.4. (a) TEM image of as-synthesized 22 nm $NaYF_4$:20%Yb, 2%Er UCNPs. (b) The upconversion emission intensity at 542 nm of dye-sensitised UCNPs (1 mg/mL UCNP) as a function of dyes' concentration (λ_{exc} = 793 nm, 2.0 W cm^{-2}). (c) The upconversion emission spectra of dye-sensitised UCNPs (1 mg/mL UCNP) with 2.5 μM NIR dyes). (d) The upconversion emission intensity at 542 nm of dye-sensitised UCNPs.

5.3 Conclusion

In conclusion, we have developed a new NIR dye that has an impressive quantum yield of 22.46%. We find that the TPEO-IR783 has a transparent window in the

visible range to avoid the reabsorption of upconversion emissions. The TPEO-IR783 enhanced the upconversion emission with a factor of 235 in comparison with IR806 and around 2 in comparison with IR808 and IR783. Designing dyes with higher quantum, together with the tuning the electronic transition band to increase the energy transfer may further brighten the dye sensitised UCNPs. Developing dye sensitiser with improved properties such as photostability may result in superior dye-UCNPs performance and boost their applications in a wide range of field.

5.4 References

1. A. Sedlmeier and H. H. Gorris, *Chem. Soc. Rev.*, 2015, **44**, 1526-1560.
2. G. Chen, H. Ågren, T. Y. Ohulchanskyy and P. N. Prasad, *Chem. Soc. Rev.*, 2015, **44**, 1680-1713.
3. G. Chen, H. Qiu, P. N. Prasad and X. Chen, *Chem. Rev.*, 2014, **114**, 5161-5214.
4. Y. Liu, Y. Lu, X. Yang, X. Zheng, S. Wen, F. Wang, X. Vidal, J. Zhao, D. Liu, Z. Zhou, C. Ma, J. Zhou, J. A. Piper, P. Xi and D. Jin, *Nature*, 2017, **543**, 229-233.
5. L. Zhou, R. Wang, C. Yao, X. Li, C. Wang, X. Zhang, C. Xu, A. Zeng, D. Zhao and F. Zhang, *Nat. Commun.*, 2015, **6**, 6938.
6. Y. Zhou, W. Pei, C. Wang, J. Zhu, J. Wu, Q. Yan, L. Huang, W. Huang, C. Yao, J. S. Loo and Q. Zhang, *Small*, 2014, **10**, 3560-3567.
7. X. Zhu, W. Feng, J. Chang, Y. W. Tan, J. Li, M. Chen, Y. Sun and F. Li, *Nat. Commun.*, 2016, **7**, 10437.
8. J. Peng, A. Samanta, X. Zeng, S. Han, L. Wang, D. Su, D. T. Loong, N. Y. Kang, S. J. Park, A. H. All, W. Jiang, L. Yuan, X. Liu and Y. T. Chang, *Angew. Chem. Int. Ed.*, 2017, **56**, 4165.
9. M. Xu, X. Zou, Q. Su, W. Yuan, C. Cao, Q. Wang, X. Zhu, W. Feng and F. Li, *Nat. Commun.*, 2018, **9**, 2698.
10. Y. Lu, J. Zhao, R. Zhang, Y. Liu, D. Liu, E. M. Goldys, X. Yang, P. Xi, A. Sunna, J. Lu, Y. Shi, R. C. Leif, Y. Huo, J. Shen, J. A. Piper, J. P. Robinson and D. Jin, *Nat. Photonics*, 2014, **8**, 32-36.
11. G. Jalani, V. Tam, F. Vetrone and M. Cerruti, *J. Am. Chem. Soc.*, 2018, **140**, 10923-10931.
12. T. Zhao, P. Wang, Q. Li, A. A. Al-Khalaf, W. N. Hozzein, F. Zhang, X. Li and D. Zhao, *Angew. Chem. Int. Ed.*, 2018, **57**, 2611-2615.
13. R. Deng, F. Qin, R. Chen, W. Huang, M. Hong and X. Liu, *Nat. Nanotechnol.*, 2015, **10**, 237.
14. X. Wu, Y. Zhang, K. Takle, O. Bilsel, Z. Li, H. Lee, Z. Zhang, D. Li, W. Fan, C. Duan, E. M. Chan, C. Lois, Y. Xiang and G. Han, *ACS Nano*, 2016, **10**, 1060-1066.

15. S. Wen, J. Zhou, K. Zheng, A. Bednarkiewicz, X. Liu and D. Jin, *Nat. Commun.*, 2018, **9**, 2415.
16. W. Zou, C. Visser, J. A. Maduro, M. S. Pshenichnikov and J. C. Hummelen, *Nat. Photonics*, 2012, **6**, 560-564.
17. G. Chen, J. Damasco, H. Qiu, W. Shao, T. Y. Ohulchanskyy, R. R. Valiev, X. Wu, G. Han, Y. Wang, C. Yang, H. Agren and P. N. Prasad, *Nano Lett.*, 2015, **15**, 7400-7407.
18. D. J. Garfield, N. J. Borys, S. M. Hamed, N. A. Torquato, C. A. Tajon, B. Tian, B. Shevitski, E. S. Barnard, Y. D. Suh, S. Aloni, J. B. Neaton, E. M. Chan, B. E. Cohen and P. J. Schuck, *Nat. Photonics*, 2018, **12**, 402–407.

Chapter 6 Ytterbium nanoparticle-mediated upconversion system

6.1 Introduction

Photon upconversion, in which low energy light are converted to higher energy light, has huge potential in photoredox catalysis[1], organic light-emitting diodes[2], night vision[3], lassing[4], optogenetics[5], bioassays[6], imaging[7], nanomedicine[8], and anti-counterfeiting[9]. Triplet triplet annihilation (TTA) is a well-known photon upconversion strategy due to its excellent light absorption cross section and high energy conversion yield.[10]

In the triplet triplet annihilation system, upon the photoexcitation of singlet of sensitiser by low energy light, the excited singlet states undergo intersystem crossing (ISC) and the energy transforms to excited triplet states. The excited triplet states of sensitiser then populate the triplet states of annihilator. When two excited annihilators in their triplet state diffuse, an excited singlet state on one annihilator is generated by the triplet triplet annihilation process. Consequently, an upconversion emission occurs with higher energy.[11-13] These processes require the sensitiser capable of the intersystem crossing for triplet generation. A narrow singlet-triplet gap is also required to avoid reabsorption of the upconversion emissions by sensitiser.

ISC is a spin forbidden electronic transition process, and specific modification is needed to enhance this process. The heavy atom effect is a common strategy to induce the intersystem crossing by heavy atoms such as iodine, bromine,[14] transition metals[15]. The n, π* groups on the chromophore also help to enhance the generation of triplet excitons.[14, 16] Thus, the sensitisers of triplet triplet annihilation are usually limited to transition metal complexes, bromine and iodine-based chromophores, and n, π* organic dyes, such as metallic porphyrin derivertives[1], iridium complexes[17], and naphthalene and perylene diimides[14]. The strict requirement of triplet generation largely limits the choices of sensitisers for the TTA upconversion process. Especially

in the near-infrared ranges, the modification and functionalization of the sensitiser are more challenging.

Here in this work, we report a new strategy that enables the sensitiser singlet energy transfer to the annihilator triplet states without the requirement of ISC (Figure 6.1). By introducing an intermediate ytterbium energy level in $NaGdF_4$:Yb nanoparticles, the energy can transfer to the ytterbium excited states from the sensitiser singlet states directly. The triplet state of annihilator is populated by ytterbium excited states. The combination of excited triplet state of annihilator and excited state of ytterbium ion further creates singlet excited states on annihilator and consequently give a long-lived singlet emission. This strategy does not require specific modification of sensitiser for intersystem crossing. We choose a general near-infrared dye, IR808, as sensitiser and rubrene acid as annihilator. While no upconversion emission occurs in the mixture of IR808 and rubrene acid, the adding of ytterbium nanoparticles activates the upconversion process between the two molecular pairs. Since the annihilation happens between the ytterbium ion and rubrene, the concentration of acceptor does not have to be at a high level like conventional TTAs does.

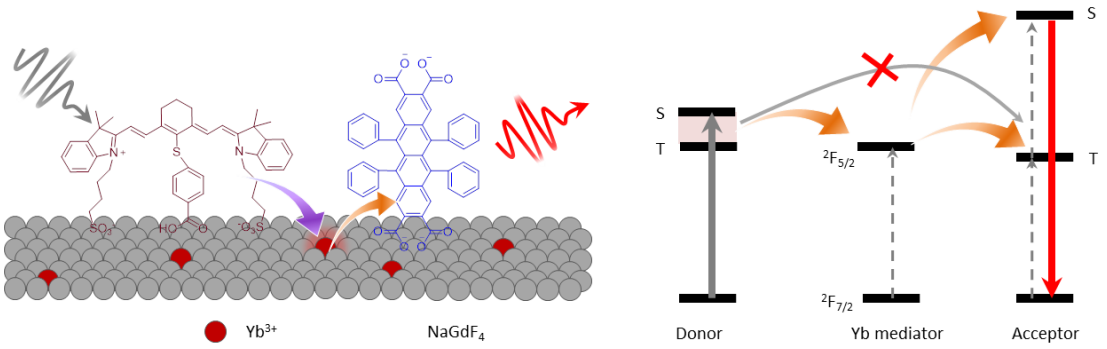

Figure 6.1. Schematic illustration of the ytterbium nanoparticle-mediated upconversion system and its energy transfer process.

6.2 Result and discussion

6.2.1 Synthesis

The synthesis of IR808 was described in the Chapter 7 by a substitution reaction of IR783 with 4-mercaptobenzoic acid. We modified the carboxylic acid groups on

rubrene acid to make the molecule attach on the surface of nanoparticles. The rubrene derivative was synthesized according to a reported paper.[18] Firstly, the rubrene was modified with carboxylate groups by addition reaction with dimethyl acetylenedicarboxylate on 1,4,7,10 carbons. This addition of the two phenyl groups to rubrene produced both cis- and trans-form product (6-2a and 6-2b). Then, the compounds **6-2** were reduced by hydrogen gas catalysed by Pd/C at room temperature to form compound **6-3**. The Ethyl groups on each side of compound **6-3** (cis-and trans-form) were removed by heating the solid at 330-340 °C for 5 min, recovering the rubrene skeleton to form compound **6-4**. The carboxylate groups ester on **6-4** was hydrolyzed and formed the final product **6-5** (Scheme 6.1). All the product and intermediates were characterized by high-resolution mass spectrometry (HRMS). The compounds **6-4** and **6-5** were also confirmed by ^{1}H NMR and ^{13}C NMR.

The ytterbium nanoparticles were synthesized by a reported procedure.[19] Firstly the $GdCl_3$ and $YbCl_3$ mixture in methanol was added to oleic acid and ODE, followed by heating to 150 °C for 30 min to remove the methanol. The reaction mixture was cooled down to 50 °C before adding with 2.5 mmol sodium hydroxide and 4 mmol ammonium fluoride. The content was kept at 50 °C for 30 min and 150 °C for 30 min, then it is heated to 280 °C and kept for 1.5 h. The nanoparticles were characterized by transmission electron microscopy (TEM).

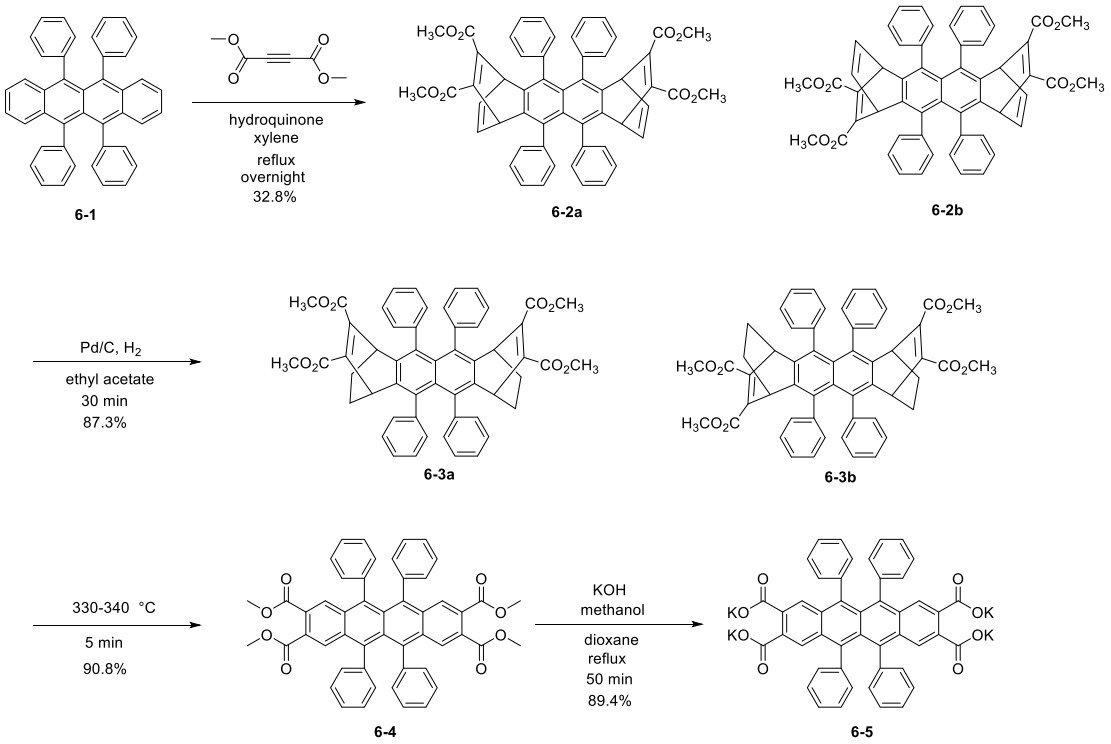

6-1 6-2a 6-2b 6-3a 6-3b 6-4 6-5

Scheme 6.1. The synthesis of potassium 5,6,11,12-tetraphenyltetracene-2,3,8,9-tetracarboxylate (rubrene acid).

6.2.2 Photophysical properties

The rubrene acid shows absorption peaked at 567 nm (2.19 eV) while its emission band ranges from 450 nm to 800 nm, peaking at 600 nm (Figure 6.2). Both the absorption and emission of rubrene acid show slight redshift in comparison with the rubrene (**6-1**) and rubrene ester (**6-4**). We assume the lowest triplet energy level (T_1) of rubrene acid is slightly lower than the rubrene which has a value between 1.04–1.05 eV in solution[20]. This triplet energy level allows the energy transfer from ytterbium (1.27 eV) to it. The combined energy (around 2.3 eV) of annihilation between its dye triplet and ytterbium ion can well match the singlet state of rubrene acid.

We choose a general near-infrared dye, IR808, as a sensitiser to demonstrate our new upconversion strategy. The IR808 shows a broad emission band between 750 – 1050 nm that overlaps with the ytterbium absorption at around 980 nm. The overlap enables the energy transfer from the organic dye to the ytterbium ions. The IR808 has wide absorption centred at 808 nm, providing more than 200 nm gap from the

emission band of rubrene acid (Figure 6.3). We estimate that the IR808 has the triplet energy level lying in the same range with the ytterbium absorption, according to the reported triplet of its derivative, IR806, which has the same chromophore with IR808.[21] This triplet serves as an additional pathway to transfer energy from dye to ytterbium ion.[21]

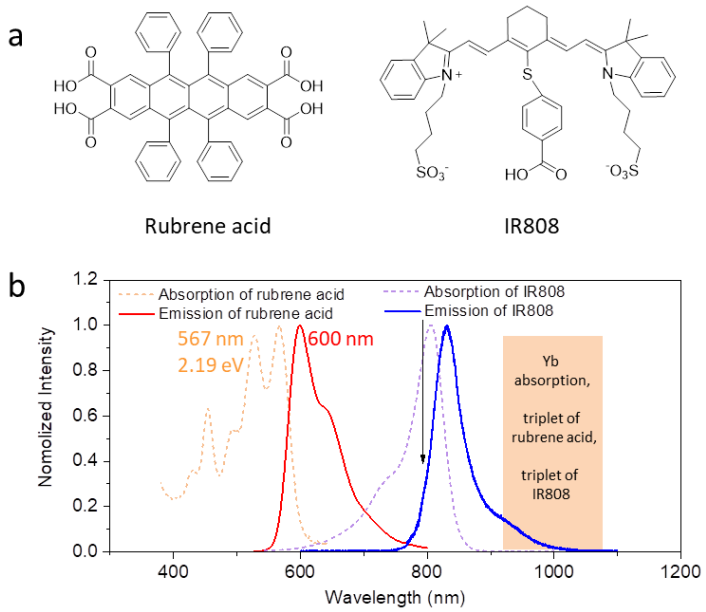

Figure 6.2. The structure, absorption, emission of sensitiser and acceptor. a. The structure of rubrene acid and IR808. b. the absorption and emission spectra of rubrene acid and IR808 in DMF.

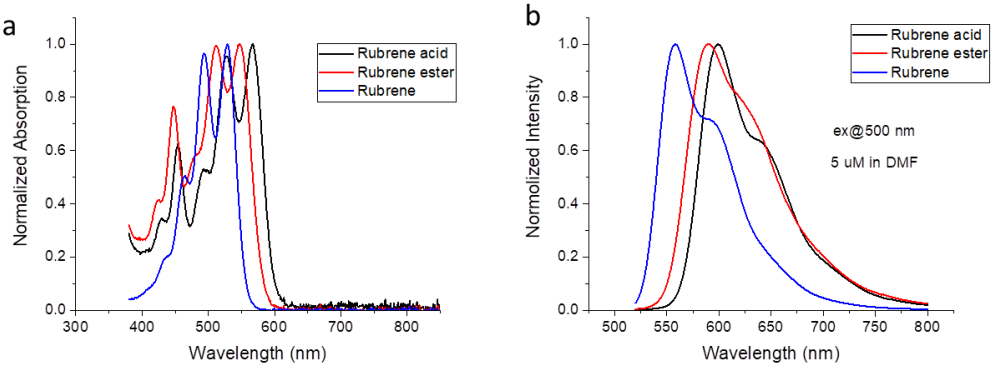

Figure 6.3. The absorption and emission spectra of rubrene and its derivatives in DMF. a. The absorption of rubrene, rubrene ester and rubrene acid. b. The emission of rubrene, rubrene ester and rubrene acid (λ_{ex} = 500 nm).

We choose $NaGdF_4$:50%Yb nanoparticles with 18 nm diameter to demonstrate our design (Figure 6.4). The oleic acid on the surface of as-synthesized ytterbium nanoparticles was removed with $NOBF_4$. As we can see in Figure 6.4, the mixture of

IR808 and rubrene acid showed no upconversion emission under 793 nm excitation, because the energy absorbed by IR808 cannot transfer to the triplet states of rubrene and no triplet triplet annihilation occurs. We then added the ytterbium nanoparticles to the system, and we can see that the nanoparticles activated the upconversion emission of rubrene acid under the same conditions (Figure 6.4a). We illustrate the energy transfer pathways in Figure 6.4b. The energy absorbed by IR808 populates its singlet states. The energy then transfers to ytterbium nanoparticle to populate ytterbium ions which further transfer the energy to triplet states of rubrene acid. The annihilation between annihilator and ytterbium creates singlet excited states on annihilator and consequently give a long-lived singlet emission. In addition to the main pathway, the triplet also has a chance to be populated through the intersystem crossing and transfers its energy to ytterbium. To further verify the role of ytterbium energy levels, we use the 980 nm laser to excite the nanoparticles directly. We can see that the direct excitation of ytterbium can also produce the upconversion emission (Figure 6.5).

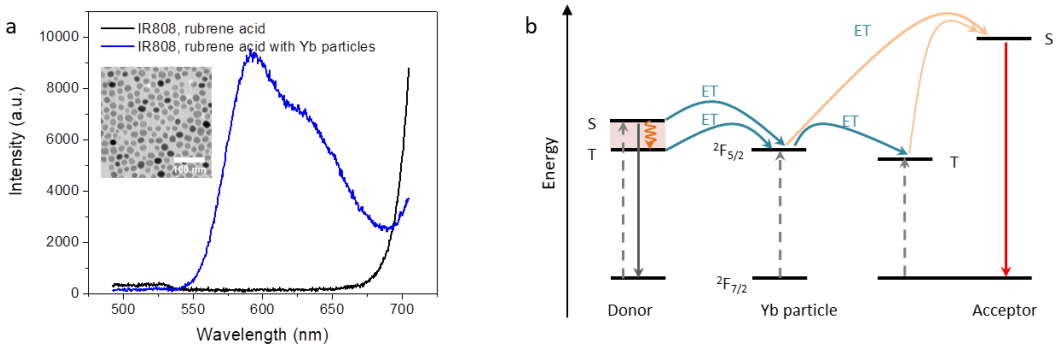

Figure 6.4. The ytterbium mediated upconversion. a. The upconversion emission spectra of IR808 and rubrene acid with and without $NaGdF_4$: 50%Yb nanoparticles (λ_{ex} = 793 nm, 7.5 W cm^{-2}) in DMF. Inset. The TEM image of $NaGdF_4$: 50%Yb nanoparticles. Scale bar, 100 nm. b. The energy transfer process form sensitiser to ytterbium to accepter triplet states and annihilation between ytterbium excited states and rubrene acid triplet.

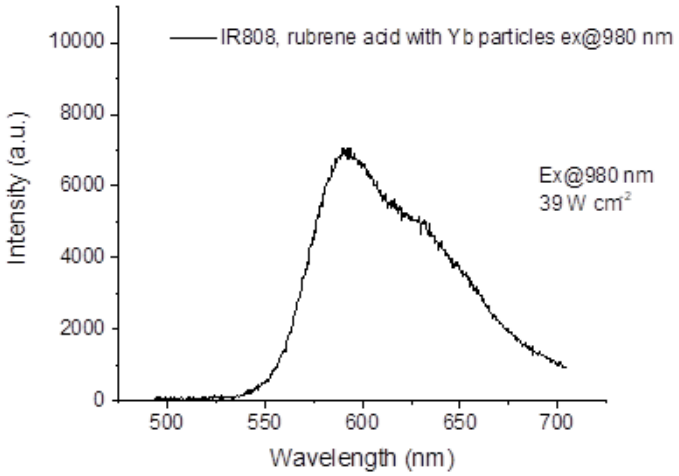

Figure 6.5. The upconversion emission of IR808-Yb-Rub upon 980 nm excitation.

6.3 Conclusion

We have designed an ytterbium nanoparticle-mediated upconversion system that can enable the general near-infrared dyes as sensitisers for the ahinilation upconversion by excited ytterbium and dye triplet annihilation, without structure modification for inducing intersystem crossing. We modified to the rubrene with carboxylic acid groups to make it attach on the surface of the ytterbium nanoparticles. Both the emission and absorption bands show slight redshifts after modification. We found that the addition of ytterbium nanoparticles activated the upconversion process while it remained in dark state without the ytterbium nanoparticles. This novel upconversion system breaks the limitation of the structure of sensitisers in TTA system, providing wide opportunities for deep penetration applications.

6.4 References

1. B. D. Ravetz, A. B. Pun, E. M. Churchill, D. N. Congreve, T. Rovis and L. M. Campos, *Nature*, 2019, **565**, 343-346.
2. R. Ieuji, K. Goushi and C. Adachi, *Nat. Commun.*, 2019, **10**, 5283.
3. Y. Ma, J. Bao, Y. Zhang, Z. Li, X. Zhou, C. Wan, L. Huang, Y. Zhao, G. Han and T. Xue, *Cell*, 2019, **177**, 243-255.e215.
4. A. Fernandez-Bravo, K. Yao, E. S. Barnard, N. J. Borys, E. S. Levy, B. Tian, C. A. Tajon, L. Moretti, M. V. Altoe, S. Aloni, K. Beketayev, F. Scotognella, B. E. Cohen, E. M. Chan and P. J. Schuck, *Nat. Nanotechnol.*, 2018, **13**, 572-577.

5. S. Chen, A. Z. Weitemier, X. Zeng, L. He, X. Wang, Y. Tao, A. J. Y. Huang, Y. Hashimotodani, M. Kano, H. Iwasaki, L. K. Parajuli, S. Okabe, D. B. L. Teh, A. H. All, I. Tsutsui-Kimura, K. F. Tanaka, X. Liu and T. J. McHugh, *Science*, 2018, **359**, 679-684.
6. J. Peng, A. Samanta, X. Zeng, S. Han, L. Wang, D. Su, D. T. Loong, N. Y. Kang, S. J. Park, A. H. All, W. Jiang, L. Yuan, X. Liu and Y. T. Chang, *Angew. Chem. Int. Ed.*, 2017, **56**, 4165. .
7. Y. Liu, Y. Lu, X. Yang, X. Zheng, S. Wen, F. Wang, X. Vidal, J. Zhao, D. Liu, Z. Zhou, C. Ma, J. Zhou, J. A. Piper, P. Xi and D. Jin, *Nature*, 2017, **543**, 229-233.
8. X. Ai, C. J. Ho, J. Aw, A. B. Attia, J. Mu, Y. Wang, X. Wang, Y. Wang, X. Liu, H. Chen, M. Gao, X. Chen, E. K. Yeow, G. Liu, M. Olivo and B. Xing, *Nat. Commun.*, 2016, **7**, 10432.
9. Y. Lu, J. Zhao, R. Zhang, Y. Liu, D. Liu, E. M. Goldys, X. Yang, P. Xi, A. Sunna, J. Lu, Y. Shi, R. C. Leif, Y. Huo, J. Shen, J. A. Piper, J. P. Robinson and D. Jin, *Nat. Photonics*, 2014, **8**, 32-36.
10. L. Huang, E. Kakadiaris, T. Vaneckova, K. Huang, M. Vaculovicova and G. Han, *Biomaterials*, 2019, **201**, 77-86.
11. V. Gray, K. Moth-Poulsen, B. Albinsson and M. Abrahamsson, *Coord. Chem. Rev.*, 2018, **362**, 54-71.
12. D. Yildiz, C. Baumann, A. Mikosch, A. J. C. Kuehne, A. Herrmann and R. Göstl, *Angew. Chem. Int. Ed.*, 2019, **58**, 12919-12923.
13. C. Ye, V. Gray, J. Mårtensson and K. Börjesson, *J. Am. Chem. Soc.*, 2019, **141**, 9578-9584.
14. M. K. Manna, S. Shokri, G. P. Wiederrecht, D. J. Gosztola and A. J.-L. Ayitou, *Chem. Commun.*, 2018, **54**, 5809-5818.
15. N. Yanai, K. Suzuki, T. Ogawa, Y. Sasaki, N. Harada and N. Kimizuka, *J. Phys. Chem. A*, 2019, **123**, 10197-10203.
16. W. Wu, H. Guo, W. Wu, S. Ji and J. Zhao, *J. Org. Chem.*, 2011, **76**, 7056-7064.
17. P. K. A., S. T. M., C. Kepeng, H. Yuqi, Z. Jianzhang, C. S. J., H. P. N., K. S. J., S. E. C., F. I. A., H. A. J., O. K. S. P., B. J. M. and P. S. J. A., *Chem.-Eur. J.*, 2018, **24**, 8577-8588.
18. J. M. Aubry, J. Rigaudy and N. K. Cuong, *Photochem. Photobiol.*, 1981, **33**, 149-153.
19. F. Wang, R. Deng and X. Liu, *Nat. Protoc.*, 2014, **9**, 1634-1644.
20. V. Jankus, E. W. Snedden, D. W. Bright, E. Arac, D. Dai and A. P. Monkman, *Phys. Rev. B*, 2013, **87**, 224202.
21. D. J. Garfield, N. J. Borys, S. M. Hamed, N. A. Torquato, C. A. Tajon, B. Tian, B. Shevitski, E. S. Barnard, Y. D. Suh, S. Aloni, J. B. Neaton, E. M. Chan, B. E. Cohen and P. J. Schuck, *Nat. Photonics*, 2018, **12**, 402–407.

Chapter 7 Experimental Section

7.1 Experimental section of Chapter 2

Materials and characterization

The chemicals purchased were used as received. The mass spectra were measured using a Bruker Autoflex MALDI-TOF or ESI mass spectrometer. The NMR data were recorded on a Bruker400 nuclear magnetic resonance spectrometer.

Photophysical Measurement

The absorption spectra were measured by an Agilent spectrophotometer. The excitation spectra, emission spectra, and lifetime were recorded on a Horiba spectrofluorometer (Fluorolog-3). HEPES buffer (1 mM, pH = 7.4) was used as the medium for the data measurement of visible range and the acetonitrile was used as the solvent for the near-infrared measurement. Quantum yield (Φ), was recorded with $Yb(tta)_3phen$ (Φ_R =1.1%) as a reference by the following formula:

$$\Phi = (A_R/A_Y)(I/I_R)(n/n_R)^2\Phi_R \quad (1)$$

where A is the absorbance value of excitation wavelength, I is the integrated area of the calibrated emission, n is the solvent refractive index, R represents the standard reference.

Binding Constant

The binding constant (K_b) was estimated by analysing absorption intensity versus mercury concentration by nonlinear least-squares fitting with the following formula:[1]

$$Y = Y_0 + \frac{Y_{max}-Y_0}{2c_s}\left[\left(c_s + c_M + \frac{1}{K_b}\right) - \sqrt{\left(c_s + c_M + \frac{1}{K_b}\right)^2 - 4c_s c_M}\right] \quad (2)$$

where Y is the absorbance at peak; Y_0 is concentration value at 0 μM of mercury ion; Y_{max} is the limiting absorbance intensity; c_s and c_M are the sensor and mercury ion concentrations, respectively.

HPLC analysis

An Agilent 1200 HPLC system was used to record the HPLC. The mobile phase was 0.05% trifluoroacetic acid in Milli-Q water and acetonitrile solvent system. The ratio of mobile gradients is listed in Table 7.1.

Table 7.1. The gradient ratio of HPLC

Time/min	0.05% TFA in water/%	CH_3CN/%
0	90	10
5	90	10
15	20	80
25	20	80

In vitro confocal microscopy

The MRC-5 cells were imaged in the presence of the sensor. The cells were incubated with 5 μM sensor for 1 h, then, 0.5, 1, and 2 equivalent of mercury ions were added, incubating for 30 min. Before images were recorded, the MRC-5 cells were washed for three times with PBS. After taking the images, the 2 equivalent mercury incubated cells were added with sodium sulfide (1 mM) and incubated for 1 h for the investigation of the reversibility of the sensor at cellular levels. Leica TCS SP8 confocal laser-scanning microscope was used for the cell imaging measurement. The excitation wavelength was 552 nm and the emission range was taken in 570-670 nm.

MTT cell viability assay

MRC-5 cells ($1x10^5$) were incubated with the sensor (1, 5, 15, 30, 50, 100 μM) for 24 h. The cell monolayers were washed with PBS for one time and treated with MTT solution. The cell viability of the **GBYb001** was examined by incubating the cells with MTT solution for 3 h to allow the formazan generation. The formazan crystals were then dissolved in DMSO. Then the solution absorbance at was 570 nm measured.

Flow cytometry measurements of cellular uptake

The MRC-5 cells ($1x10^5$) were treated with 5 μM of the sensor for 0 h, 0.5 h, 1 h and

2 h before incubating with mercury ion for another 0.5 h. The cells were collected with trypsin and rinsed with PBS twice. BD Accuri C6 flow cytometer was used to analyse the uptake of the probe by living cells. 10000 events were analysed.

DFT calculations

Structures were drawn using Avogadro[4] and Gabedit[5] and preliminary optimizations were made using "optimize geometry" and/or "molecular dynamics". Geometry optimizations and TDDFT calculations were performed using ORCA 4.0.1[6] with BP86 and B3LYP functionals with appropriate basis sets. The optimized geometries did not have any imaginary frequencies. The B3LYP calculation for **py** and **rhodamine** used the libint2 library[7] for the computation of 2-el integrals, the def2-TZVP basis set[8] and the auxiliary basis set def2-XVP/J **(**def2/J).[9] The RIJCOSX approximation, which involves different approximations for the formation of the Coulomb- and exchange-type matrices was applied. The BP86 calculation for **py** and **rhodamine** utilized the def2-SVP basis set[8] and the auxiliary basis set def2/J.[9] The TDDFT calculations in ORCA 4.0.1 were restricted to the first 25 singlet and 25 triplet states, giving energies for both and oscillator strengths for singlet states. The same calculations were performed for the ring-opened and ring-closed structures.

Synthesis procedure and characterization

Synthesis of methyl 4-(2-bromoacetyl)benzoate (2-1). The NBS (5.22 g, 29.48 mmol) was added to a solution of methyl 4-acetylbenzoate (5 g, 28.08 mmol) and p-TsOH•6H_2O (8.0 g, 42.12 mmol) in 100 mL of MeCN. The reaction contents were heated to 85 ^oC and kept for 4 h. 300 mL of water was added after removal of the organic solvent. The residue was extracted with DCM (200 mL × 3), then washed with saturated aqueous $NaHCO_3$ (300 mL). The organic phase was dried over anhydrous Na_2SO_4. After removing the solvent, the residue was purified via chromatography using silica gel with hexane and ethyl acetate (4:1), giving 5.8 g white solid. Yield: 80.3%. ^1H NMR (400 MHz, $CDCl_3$) δ = 8.15 (d, *J* = 8.7 Hz, 2H), 8.04 (d, *J* = 8.7 Hz, 2H), 3.96 (s, 3H), 4.47 (s, 2H). ^{13}C NMR (101 MHz, $CDCl_3$) δ =

30.71,52.57, 128.84, 129.98, 134.58, 137.12, 165.91, 190.78.

Synthesis of methyl 4-(2-((pyrrolidine-1-carbonothioyl)thio)acetyl)benzoate (2-2). Ammonium pyrrolidine-1-carbodithioate (3.824 g, 23.274 mmol) was added to a solution of methyl 4-(2-bromoacetyl)benzoate **2-1** (4.0 g, 15.516 mmol) in acetone (120 mL) and stirred for 8h at r.t. Then the solvent was removed and water (300 mL) was added prior to the extraction with 300 mL of DCM for three times, washing with brine (100 mL) and drying over anhydrous sodium sulfate. Then purification by chromatography was performed on silica gel eluting with hexane and DCM (1:1, v/v) to give a white solid (4.52 g) as product. Yield: 90.1%. ^{1}H NMR (400 MHz, $CDCl_3$) δ = 2.00 (p, *J* = 6.9 Hz, 2H), 2.12 (p, *J* = 6.9 Hz, 2H), 3.76 (t, *J* = 6.9 Hz, 2H), 3.92 (t, *J* = 7.0 Hz, 2H), 3.96 (s, 3H), 4.90 (s, 2H), 8.14 (d, *J* = 1.6 Hz, 4H). ^{13}C NMR (101 MHz, $CDCl_3$) δ = 24.37, 26.16, 44.30, 50.83, 52.50, 55.56, 128.47, 129.87, 134.11, 139.40, 166.15, 190.65, 193.18. MS: calculated $[M + H]^+$ = 324.0723, found: 324.0748.

Synthesis of 2-3. To a solution of **2-2** (1.0 g, 3.1 mmol) in 20 mL of THF was added $LiOH \cdot H_2O$ (651 mg, 15.5 mmol) in 4 mL of water at 0 °C. The reaction mixture was stirred for 4 h at room temperature. The pH value was adjusted to the acidic range by 1 M HCl aqueous solution and the precipitate was filtered, rinsed with water and DCM, and dried to give the white solid (550 mg). Yield: 78.2%. ^{1}H NMR (400 MHz, DMSO-d_6) δ = 1.98 – 1.85 (m, 2H), 2.13 – 2.00 (m, 2H), 3.72 (m, 4H), 4.96 (s, 2H), 8.11 (m, 4H), 13.36 (s, 1H). ^{13}C NMR (101 MHz, DMSO-d_6) δ = 23.84, 25.69, 43.43, 50.76, 55.35, 128.32, 129.58, 139.44, 134.64, 166.56, 189.93, 192.85. MS: calculated $[M + H^+]$ = 310.0566, found: 310.0563.

Synthesis of 2-4. To a mixture of 2-methylpropan-2-amine (12.43mL, 82.72 mmol) in DCM (250 mL) was added K_2CO_3 (37.8 g, 273.50 mmol). Then 2-bromoacetyl bromide (13.1 mL, 150.31 mmol) was added slowly at 0 ^{o}C before stirring the reaction mixture at room temperature for 6 h. The reaction content was quenched with 200 mL of water and extracted with 200 mL of DCM three times. After washing with saturated aqueous NH_4Cl and water, the organic phase was dried with anhydrous Na_2SO_4. A white product (24.251 g) was obtained by removing the solvent.

Yield: 91.3%. ^{1}H NMR (400 MHz, $CDCl_3$) δ = 1.38 (s, 9H), 3.79 (s, 2H), 6.29 (s, 1H). ^{13}C NMR (101 MHz, $CDCl_3$) δ = 28.40, 29.89, 51.92, 164.35.

Synthesis compound 2-5. To a solution of 1,4,7,10-tetraazacyclododecane (4.0 g, 23.22 mmol) in 150 mL of CH_3CN was added 19.5 g of $NaHCO_3$ (232.2 mmol). A solution of **2-4** (13.97 g, 72.5 mmol) in CH_3CN (150 mL) was added slowly at room temperature. The reaction content was stirred for 24 h. The organic phase was collected and the solvent was removed and give light yellow solid. The solid was added with water (250 mL) and we adjusted the pH value to 8 with NaOH aqueous solution (1 M). The water phase was washed with 50 mL of dichloromethane three times. We then adjusted the pH value to 13 with NaOH aqueous solution (1 M). The solution was extracted with dichloromethane (50 mL× 5). The solvent was removed and the resulting solid was recrystallized with water to give the white product (5 g). Yield: 42.3%. ^{1}H NMR (400 MHz, DMSO-d_6) δ = 1.25 (s, 18H), 1.27 (s, 9H), 2.54 (s, 8H), 2.63 (s, 8H), 2.95 (s, 2H), 3.01 (s, 4H), 3.46 (s, 1H), 7.54 (s, 2H), 7.63 (s, 1H). ^{13}C NMR (101 MHz, DMSO-d_6) δ = 28.58, 28.63, 46.08, 49.83, 50.01, 50.46, 51.96, 52.44, 57.19, 58.19, 169.86, 169.94. MS: calculated $[M + H]^+$ = 512.4283, found: 512.4287; calculated $[M + Na]^+$ = 534.4102, found: 534.4048.

Synthesis of compound 2-6. (4-bromopyridin-2-yl)methanol (10 g, 53.12 mmol), and Copper(I) iodide (202 mg, 1.06 mmol) and $Pd(PPh_3)_4$ (614 mg, 0.531 mmol), were added to a 500 mL flask. 250 mL of DCM and 92.54 mL of DIPEA (531.24 mmol) were added and bubbled with nitrogen gas for 0.5 h. Ethynyltrimethylsilane (9 mL, 63.7 mmol) was added dropwise. The solution was reacted at room temperature for 15 h under nitrogen atmosphere. After adding 250 mL of water, extraction by dichloromethane (250 mL × 3) was performed. The organic phase was combined and dried over anhydrous Na_2SO_4. Chromatography on silica gel was used to purify the product using the eluent of hexane and ethyl acetate (1:1 - 1:2, v/v) to give the yellow product (8.0 g). Yield: 73.3%. ^{1}H NMR (400 MHz, DMSO-d_6) δ = 0.25 (s, 9H), 4.54 (d, *J* = 5.9 Hz, 2H), 5.47 (t, *J* = 5.9 Hz, 1H), 7.27 (d, *J* = 5.0 Hz, 1H), 7.43 (s, 1H), 8.48 (d, *J* = 5.0 Hz, 1H). ^{13}C NMR (101 MHz, DMSO-d_6) δ = -0.39, 63.88, 99.13, 102.56, 121.80, 123.37, 130.25, 149.01, 162.57.

Synthesis of compound 2-7. A solution of 14.26 g of TBAF in 250 mL of dichloromethane was added slowly to a mixture of 8.0 g of **2-6** in dichloromethane (250 mL). After 1 h stirring at room temperature, we added water and extracted with dichloromethane. The dichloromethane phase was dried over anhydrous Na_2SO_4. Chromatography was used to purify the product with a mixture of hexane and ethyl acetate (2:1, v/v) as eluents, giving 4.89 g of product. Yield: 94.3%. ^{1}H NMR (400 MHz, $CDCl_3$) δ = 3.30 (s, 1H), 3.65 (t, *J* = 5.2 Hz, 1H), 4.76 (d, *J* = 5.2 Hz, 2H), 7.27 (d, *J* = 5.1 Hz, 1H), 7.34 (s, 1H), 8.54 (d, *J* = 5.1 Hz, 1H). ^{13}C NMR (101 MHz, $CDCl_3$) δ = 64.00, 80.89, 81.96, 122.92, 124.75, 131.00, 148.55, 159.38.

Synthesis of the compound 2-8. 2.88 g of tert-butyl (4-iodophenyl)carbamate, 80 mL of THF, 13.08 mL of DIPEA (75.10 mmol), 173 mg of $Pd(PPh_3)_4$, 57 mg of CuI and 1.00 g of (4-ethynylpyridin-2-yl)methanol (**2-7**) were added to a flask under nitrogen protection. The reaction content was kept at room temperature for 72 h before adding 100 mL of water and extraction with dichloromethane (100 mL) three times. The organic phases was dried over anhydrous Na_2SO_4, and chromatographed on silica gel eluting with hexane and ethyl acetate (2:1 - 1:1, v/v), giving 2.10 g of white solid. Yield 86.2%. ^{1}H NMR (400 MHz, $CDCl_3$) δ = 1.53 (s, 9H), 3.62 (t, *J* = 4.5 Hz, 1H), 4.76 (d, *J* = 4.1 Hz, 2H), 6.61 (s, 1H), 7.28 (d, *J* = 5.1 Hz, 1H), 7.34 (s, 1H), 7.39 (d, *J* = 8.7 Hz, 2H), 7.48 (d, *J* = 8.7 Hz, 2H), 8.53 (d, *J* = 5.1 Hz, 1H). ^{13}C NMR (101 MHz, $CDCl_3$) δ = 28.31, 64.05, 81.14, 86.08, 94.26, 116.14, 118.08, 122.18, 124.15, 132.40, 132.90, 139.43, 148.48, 152.31, 159.14. MS: calculated $[M + H]^+$ = 325.1547, found: 325.1552.

Synthesis of compound 2-9. To a solution of 973 mg of **2-8** and 5.23 mL of DIPEA in 150 mL of dry DCM was added MsCl (0.70 mL) slowly. The reaction content was kept at room temperature for 1 h and then added with 100 mL of water. The mixture was extracted using 100 mL of DCM three times, washed with 50 mL saturated $NaHCO_3$ aqueous solution and dried. After removing the solvent, the solid was immediately purified by chromatography using silica gel eluting with the mixture of dichloromethane and ethyl acetate (1:1, v/v), giving 1.11 g white solid as intermediate. 1.05 g of the intermediate was immediately added to 250 mL of

acetonitrile, followed by adding 2.77 g of K_2CO_3 and 1.03 g of **2-5**. The mixture was heated to 50 ^oC and kept the temperature for 19 h. The K_2CO_3 was filtered off. The product was purified using chromatography on Al_2O_3 (neutral) eluting with methanol and dichloromethane mixture. 1.60 g of yellow solid was obtained. Yield: 90.0% in the two steps. ^1H NMR (400 MHz, DMSO-d_6) δ = 1.21 (s, 18H), 1.29 (s, 9H), 1.48 (s, 9H), 2.46 – 1.82 (br, 10H), 3.19 – 2.56 (br, 12H), 3.97 – 3.44 (br, 2H), 7.36 (d, *J* = 5.1 Hz, 1H), 7.46 (d, *J* = 8.8 Hz, 2H), 7.53 (d, *J* = 8.8 Hz, 2H), 7.56 (s, 1H), 7.65 (s, 1H), 7.83 (s, 2H), 8.36 (d, *J* = 5.1 Hz, 1H), 9.68 (s, 1H).^{13}C NMR (101 MHz, DMSO-d_6) δ = 28.08, 28.13, 28.28, 50.38, 50.42, 54.93, 57.26, 57.96, 58.04, 79.64, 85.88, 94.17, 114.21, 117.91, 123.39, 125.02, 131.21, 132.47, 140.89, 148.94, 152.55, 158.61, 169.90, 170.54. MS: calculated $[M + Na]^+$ = 840.5470, found: 840.5500.

Synthesis of compound 2-10. 30 mL of HCl aqueous solution (6 M) was added to 1.0 g of **2-9** in methanol (30 mL) at 0 ^oC. Room temperature was reached naturally and kept for 6 h. The pH value was adjusted to 9 by 1 M NaOH aqueous solution. Then the content was extracted using 100 mL of dichloromethane three times and dried over anhydrous Na_2SO_4. The organic phase was evaporated under vacuum and the resulting solid was chromatographed on Al_2O_3 (neutral) eluting by a mixture of methanol and dichloromethane (50:1, v/v). 750 mg of yellow solid was obtained. Yield: 85.5%. ^1H NMR (400 MHz, DMSO-d_6) δ = 1.21 (s, 18H), 1.30 (s, 9H), 2.19 (br, 10H), 2.72 (br, 12H), 3.65 (br, 2H), 5.75 (s, 2H), 6.56 (d, *J* = 8.6 Hz, 2H), 7.21 (d, *J* = 8.6 Hz, 2H), 7.28 (dd, *J* = 5.1, 1.4 Hz, 1H), 7.43 (s, 1H), 7.65 (s, 1H), 7.82 (s, 2H), 8.31 (d, *J* = 5.1 Hz, 1H). ^{13}C NMR (101 MHz, DMSO-d_6) δ = 28.13, 28.28, 50.39, 50.43, 54.93, 57.36, 58.03, 84.62, 96.54, 106.68, 113.58, 123.04, 124.53, 132.01, 133.15, 148.86, 150.40, 158.42, 169.93, 170.52. MS: calculated $[M + H^+]$ = 718.5127, found: 718.5089.

Synthesis of compound 2-11. 172 mg of compound **2-3**, 25 mL of dry acetonitrile, 0.24 mL of DIPEA, 160 mg of EDCI and 112 mg of HOBt was added to a flask, followed by stirring for 0.5 h at room temperature. Then 200 mg of **2-10** was added, followed by stirring at the same temperature for another 36 h. Then we removed the solvent, before adding water (30 mL) and extracting using 30 mL of dichloromethane

three times. The dichloromethane was combined and dried over anhydrous Na_2SO_4. The product was purified on neutral Al_2O_3 with the mixture of dichloromethane and methanol (50:1, v/v) as eluent, giving 164 mg of yellow solid. Yield 58.6%. ^{1}H NMR (400 MHz, DMSO-d_6) δ =1.22 (s, 18H) 1.30 (s, 9H), 2.39 – 1.87 (m, 14H), 2.66 (m, 12H), 3.73 (m, 6H), 4.98 (s, 2H), 7.41 (d, *J* = 6.2 Hz, 1H), 7.59 (d, *J* = 8.6 Hz, 2H), 7.63 (d, *J* = 8.3 Hz, 2H), 7.82 (s, 2H), 7.91 (d, *J* = 8.8 Hz, 2H), 8.09 (d, *J* = 8.5 Hz, 2H), 8.19 (d, *J* = 8.5 Hz, 2H), 8.39 (d, *J* = 5.0 Hz, 1H), 10.70 (s, 1H). ^{13}C NMR (101 MHz, DMSO-d_6) δ = 23.88, 25.74, 28.12, 28.27, 43.35, 49.39, 50.35, 50.41, 50.81, 54.93, 55.40, 57.22, 57.90, 58.10, 86.40, 93.83, 113.56, 116.17, 120.22, 123.47, 125.14, 128.24, 131.06, 132.39, 133.14, 138.59, 140.23, 148.97, 158.67, 165.12, 169.89, 170.55, 189.99, 192.84. MS: calculated $[M + Na]^+$ = 1031.5334, found: 1031.5319.

Synthesis of compound 2-12. 230 mg of **2-11**, 0.23 mL of hydrazine hydrate and 0.23 mL of acetic acid were added 12 mL of tetrahydrofuran and 12 mL of ethanol. The mixture was refluxed for 2 h and cooled down. Water (40 mL) and saturated aqueous $NaHCO_3$ solution (3 mL) were added after the removal of most of solvent. The reaction content was extracted with dichloromethane (30 mL) three times, and dried over anhydrous Na_2SO_4. The crude solid was chromatographed using Al_2O_3 (neutral) by dichloromethane and methanol (50:1. v/v), affording 128 mg of yellow solid. Yield: 54.9%. ^{1}H NMR (400 MHz, DMSO-d_6) δ = 1.22 (s, 18H), 1.30 (s, 9H), 2.40 – 1.80 (m, 14H), 2.66 (br, 12H), 3.71 (m, 6H), 4.61 (s, 2H), 7.32 (s, 2H), 7.40 (dd, *J* = 5.1, 1.1 Hz, 1H), 7.56 (d, *J* = 8.7 Hz, 2H), 7.61 (s, 1H), 7.65 (s, 1H), 7.75 (d, *J* = 8.6 Hz, 2H), 7.83 (s, 2H), 7.92 (m, 4H), 8.38 (d, *J* = 5.1 Hz, 1H), 10.46 (s, 1H). ^{13}C NMR (101 MHz, DMSO-d_6) δ23.73, 25.57, 28.11, 28.26, 29.34, 50.34, 50.40, 50.59, 55.56, 57.21, 57.87, 58.07, 86.27, 93.94, 115.76, 120.05, 123.45, 124.25, 125.10, 127.92, 131.10, 132.33, 132.66, 135.79, 140.54, 141.07, 148.96, 158.65, 165.43, 169.88, 189.99, 170.54. MS: calculated $[M + H]^+$ = 1023.5783, found: 1023.5765.

Synthesis of compound 2-13 (GB001). 43 mg of rhodamine B and 0.20 mL of $POCl_3$ were added to 4 mL of 1,2-dichloroethane and the reaction mixture was

refluxed for 5 h before the removal of the solvent. The resulting rhodamine B acid chloride, together with 0.30 mL of trimethylamine, and 50 mg of **2-12** was dissolved in dry dichloromethane (10 mL) before it was stirred for 12 h at room temperature. 10 mL of water was added before extracting the mixture with 10 mL of dichloromethane four times. The dichloromethane phase was dried over anhydrous Na_2SO_4. Chromatography was used to purify the product using silica gel eluting with the mixture of dichloromethane and methanol (100:1-50:1, v/v), giving 50 mg of red solid. Yield: 71.0%. ^{1}H NMR (400 MHz, DMSO-d_6) δ = 1.08 (t, *J* = 6.9 Hz, 12H), 1.21 (s, 18H), 1.30 (s, 9H), 2.00 – 1.77 (br, 6H), 2.33 (br, 8H), 2.71 br, 14H), 3.31 (q, 8H), 3.74 (m, 4H), 4.73 (s, 2H), 6.43 – 6.27 (m, 4H), 6.49 (d, *J* = 8.8 Hz, 2H), 7.20 (d, *J* = 6.8 Hz, 1H), 7.39 (d, *J* = 5.8 Hz, 1H), 7.62 (m, 8H), 7.88 (m, 7H), 8.38 (d, *J* = 5.1 Hz, 1H), 10.51 (s, 1H). ^{13}C NMR (101 MHz, DMSO-d_6) δ = 12.41, 23.65, 25.50, 28.12, 28.26, 30.71, 50.36, 50.41, 54.92, 55.78, 57.24, 57.88, 58.10, 66.97, 86.36, 93.84, 97.24, 105.97, 107.93, 116.04, 120.08, 123.19, 123.47, 124.06, 125.14, 127.17, 127.86, 128.27, 128.93, 129.77, 131.07, 132.38, 133.37, 136.26, 138.02, 140.26, 148.35, 148.97, 150.81, 153.15, 158.68, 160.36, 165.01, 165.51, 169.90, 170.56, 189.43. MS: calculated [M + Na^+] = 1469.7753, found: 1469.7783.

Synthesis of GBYb001 (2-14a). 0.01 mmol of **2-13** in 1mL of methanol**,** 0.0105 mmol of $YbCl_3$ in 1.05 mL of water were mixed and stirred at room temperature for 1 day. After removing the solvent, the resulting residue was re-dissolved in water (2 mL) followed by washing with 2 mL of dichloromethane three times. The solvent was removed under vacuum, affording 15 mg purple product with 83.3% yield. MS: calculated [M –2H^+ – 3Cl^- –H_2O] is 1618.7, found: 1618.9; calculated [M –H^+ – 3Cl^- –H_2O]/2 = 809.9, found: 810.1.

Synthesis of GBLa001 (2-14b). 5 mg of **2-13** (0.0035 mmol) in methanol (0.7 mL), 0.00354 mmol of $LaCl_3$ in pure water (0.71 mL) was mixed and stirred at room temperature for 1 day. The solvent was removed and the resulting crude product was re-dissolved in water (2 mL) which was then washed using 1 mL of dichloromethane three times. The solvent was dried under vacuum, affording 5.8 mg of purple solid. Yield 93.3%. ^{1}H NMR (400 MHz, DMSO-d_6) δ = 1.08 (m, 12H), 1.18 (m, 18H), 1.30

(s, 9H), 1.89 m, 6H), 2.28 (d, *J* = 35.9 Hz, 8H), 2.65 (d, *J* = 14.3 Hz, 14H), 3.31 – 3.29 (m, 8H), 3.74 (s, 4H), 4.72 (s, 2H), 6.42 – 6.27 (m, 4H), 6.49 (d, *J* = 8.9 Hz, 2H), 7.20 (d, *J* = 7.2 Hz, 1H), 7.39 (d, *J* = 5.2 Hz, 1H), 7.74 – 7.52 (m, 8H), 7.95 – 7.76 (m, 7H), 8.38 (d, *J* = 5.2 Hz, 1H), 10.51 (s, 1H).

Synthesis of GBLa002 (2-15). 0.0065 mmol of **2-11** in 1 mL of methanol and 0.0065 mmol of $YbCl_3$ in water (1 mL) was mixed and stirred at room temperature for 1day. After removing the solvent, the residue was re-dissolved in water (2 mL) and washed with 1 mL of dichloromethane three times. The product was dried under vacuum, giving 8.0 mg of yellow solid with 92.0% yield.

7.2 Experimental section of Chapter 3

Materials and method

All the chemicals were used without further purification except indicated. Magnetic resonance spectrometer of Bruker (400 Hz) was used to measure NMR spectra. Quadrupole-time-of-flight mass spectrometer (ABI QSTAR Elite) was used to measure the mass spectrometry. Agilent 1200 series HPLC instrument was used to record HPLC analysis. FT-IR spectrometer (PerkinElmer Paragon 1000 PC) was utilized to record FT-IR data. Emission, excitation, and decay were measured using iHR550 spectrometer, Horiba fluorescence spectrometer, and Edinburgh Mini-tau.

Synthetic procedures

Synthesis of 3-1. K_2CO_3 (5.53 g, 40.96 mmol) was added to a mixture of 1,10-phenanthrolin-5-amine (2.0 g, 10.24 mmol) in 500 mL of DCM. Then 1.3 mL of 2-Bromoacetyl bromide (15.36 mmol) was added dropwise at 0 °C. The reaction content was stirred for 22 h at room temperature. The content was then quenched by 20 mL of water and stirred for 10 min. The yellow precipitate (2.48 g) was obtained by filtration, washing with small amount of DCM, saturated aqueous $NaHCO_3$ and then water, and drying.Yield 78.3%. ^{1}H NMR (400 MHz, DMSO-d_6) δ = 4.29 (s, 2H), 7.76 (dd, *J* = 8.1, 4.3 Hz, 1H), 7.86 (dd, *J* = 8.4, 4.3 Hz, 1H), 8.18 (s, 1H), 8.50 (dd, *J*

= 8.1, 1.6 Hz, 1H), 8.61 (dd, *J* = 8.4, 1.5 Hz, 1H), 9.06 (dd, *J* = 4.3, 1.7 Hz, 1H), 9.15 (dd, *J* = 4.2, 1.6 Hz, 1H), 10.60 (s, 1H). ^{13}C NMR (101 MHz, DMSO-d_6) δ = 30.02, 120.55, 123.02, 123.72, 124.53, 127.97, 131.06, 131.4, 136.10, 136.18, 149.63, 150.05, 166.26. MS: calculated $[M + H]^+$ = 316.0080, found: 316.0078; calculated for $[M + Na]^+$ = 337.9899, found: 337.9902.

Synthesis of 3-2. 2,2',2''-(1,4,7,10-tetraazacyclododecane-1,4,7-triyl)tris(N-(tert-butyl)acetamide) was added to a mixture of **3-1** (1 g, 3.16 mmol) and $NaHCO_3$ (3.24 mmol) in 200 mL of MeCN at room temperature. The reaction content was stirred for 3 days. Then the solid was filtered off and washed with small amount of MeOH. The organic phase was removed. The crude product was washed with MeCN at 60 ^oC in ultrasound condition for 10 min. The yellow product was obtained by filtration and washing with MeCN and drying under vacuum (2.260 g). Yield: 95.8%. ^{1}H NMR (400 MHz, DMSO-d_6) δ = 1.11 (s, 18H), 1.27 (s, 9H), 2.27 (br, 11H), 2.90 (br, 13H), 7.67 (s, 3H), 7.78 – 7.71 (m, 2H), 8.04 (s, 1H), 8.23 (d, *J* = 6.8 Hz, 1H), 8.64 (dd, *J* = 8.4, 1.5 Hz, 1H), 9.02 (dd, *J* = 4.2, 1.6 Hz, 1H), 9.10 (dd, *J* = 4.2, 1.5 Hz, 1H), 10.35 (s, 1H). ^{13}C NMR (101 MHz, DMSO-d_6) δ = 28.19, 28.28, 50.22, 50.33, 56.22, 57.11, 57.61, 120.25, 122.65, 123.54, 124.83, 127.90, 132.29, 135.29, 143.87, 145.76, 149.29, 149.32, 149.80, 170.18, 170.48, 171.43. MS: calculated $[M + H^+]$ = 747.5028, found: 747.5046; calculated $[M + Na^+]^+$ = 769.4848, found: 769.4743; calculated $[M + Na^+ + H^+]^{2+}/2$ = 385.2460, found: 385.2444.

Synthesis of compound cycLa-phen (3-3a). The solution of $LaCl_3$•$6H_2O$ (142 mg, 0.4 mmol) in deionized H_2O (40 mL) was added to a solution of **3-2** (299 mg, 0.4 mmol) in 40 mL of MeOH at room temperature. The reaction content was stirred for 24 h. Then half of the solvent was removed and the remained content was washed with dichloromethane (20 mL × 2). The solvent was removed and the residue was recrystallized with MeOH and Et_2O to give yellow solid as product (400 mg). Yield: 99.0%. ^{1}H NMR (400 MHz, DMSO-d_6) δ = 1.14 (s, 18H), 1.24 (s, 9H), 1.96 - 3.07 (br, 12H), 3.39 - 4.12 (br, 12H), 7.84 (m, 2H), 8.02 (s, 1H), 8.38 (d, *J* = 7.6 Hz, 1H), 8.71 (d, *J* = 8.2 Hz, 1H), 9.11 (m, 5H), 11.82 (s, 1H). MS: calculated $[M - 2H^+ - 3Cl^-]^+$ =

883.3857, found: 883.3858.

Synthesis of compound cycTb-phen (3-3b). The solution of $TbCl_3$•$6H_2O$ (112 mg, 0.3 mmol) in deionized H_2O (30 mL) was added to a mixture of **3-2** (224 mg, 0.3 mmol) in 30 mL of methanol at room temperature. The content was stirred for 24 h. Then half of the solvent was removed and the remained content was washed with dichloromethane (20 mL × 2). After removing the solvent, the residue was recrystallized with MeOH and Et_2O to give the yellow solid as product (299 mg). Yield: 96.8%. MS: calculated $[M - 2H^+ - 3Cl^-]^+$ = 903.8938, found: 903.4052.

Synthesis of compound cycEu-phen (3-3c). A mixture of 146 mg of $EuCl_3$•$6H_2O$ (0.4 mmol) in 40 mL of deionized H_2O was added to a mixture of 299 mg of **3-2** (0.4 mmol) in 40 mL of methanol at room temperature. The reaction was stirred for 24 h. Then half of the solvent was removed and the remained content was washed with dichloromethane (20 mL × 2). The solvent was removed and the residue was recrystallized with MeOH and Et_2O to give the yellow solid as product (400 mg). Yield: 97.8%. MS: calculated $[M - 2H^+ - 3Cl^-]^+$ = 897.4000, found: 897.4065.

Synthesis of compound cycLa-phLa (3-4a). A mixture of **3-3a** (101 mg, 0.10 mmol) and ammonium pyrrolidine-1-carbodithioate (49 mg, 0.30 mmol) in methanol (10 mL) were added to a mixture of $LaCl_3$•$6H_2O$ (35 mg, 0.10 mmol) in 5 mL of methanol dropwise at room temperature. Then the reaction content was stirred for 10 min. After removing around half of the solvent, the left solution was transferred to a 50 mL centrifugal tube. 30 mL of Et_2O was added dropwise and yellow solid was precipitated. The suspension was centrifuged and the solvent was removed. The precipitation and centrifugation were repeated twice. The precipitate was dried under vacuum to give 141 mg of yellow solid. Yield: 88.7%. ^{1}H NMR (400 MHz, DMSO-d_6) δ = 1.15 (s, 18H), 1.24 (s, 9H), 1.96 – 1.71 (m, 12H), 2.20 (br, 5H), 2.61 (br, 8H), 3.45 (br, 8H), 3.64 (t, *J* = 6.8 Hz, 12H), 3.90 (br, 3H), 7.81 (m, 3H), 7.94 (s, 1H), 8.34 (d, *J* = 7.5 Hz, 1H), 8.71 (d, *J* = 8.1 Hz, 1H), 9.09 (m, 5H). MS: calculated $[M - La^{3+} - 3Cl^- - H^+ - 3pdtc^-]^{2+}/2$ = 442.1965, found: 442.1888.

Synthesis of compound cycTb-phEu (3-4b). A mixture of 155 mg of **3-3b** (0.15 mmol) and 74 mg of ammonium pyrrolidine-1-carbodithioate (0.45 mmol) in

methanol (10 mL) were added to a solution of $EuCl_3•6H_2O$ (55 mg, 0.15 mmol) in 5 mL of MeOH dropwise at room temperature. Then the reaction mixture was stirred for 10 min. After removing around half of the solvent, the left solution was transferred to a 50 mL centrifugal tube. Et_2O (50 mL) was added slowly and yellow solid was precipitated. The suspension was centrifuged and the organic phase was removed. The precipitation and centrifugation were repeated twice. The precipitate was dried under vacuum and gave 223 mg of yellow product. Yield: 91.8%. MS: calculated $[M - 3Cl^- - H^+ - Eu^{3+} - 3pdtc^-]^{2+}/2$ = 452.4508, found: 452.2040.

Synthesis of compound cycEu-phTb (3-4c). A mixture of 153 mg of **3-3c** (0.15 mmol) and 74 mg of ammonium pyrrolidine-1-carbodithioate (0.45 mmol) in methanol (10 mL) were added to a solution of $TbCl_3•6H_2O$ (56 mg, 0.15 mmol) in MeOH (5 mL) dropwise at room temperature. The reaction mixture was stirred for 10 min. After removing around half of the solvent, the left solution was transferred to a 50 mL centrifugal tube. Et_2O (50 mL) was added slowly and yellow solid was precipitated. The suspension was centrifuged and the solvent was removed. The precipitation and centrifugation were repeated twice. The precipitate was dried under vacuum to give yellow solid as product (230 mg). Yield: 94.6%. MS: calculated $[M -3Cl^- - Tb^{3+} - 3pdtc^- - 2H^+]^+$ = 897.4065, found: 897.3974.

Synthesis of compound cycLa-phEu (3-4d). A mixture of **3-3a** (151.5 mg, 0.15 mmol) and 74 mg of ammonium pyrrolidine-1-carbodithioate (0.45 mmol) in 10 mL of methanol was added slowly to a mixture of $EuCl_3•6H_2O$ (55 mg, 0.15 mmol) in 5 mL of MeOH at room temperature. Then the reaction was stirred for 10 min. After removing around half of the solvent, the left solution was transferred to a 50 mL centrifugal tube. Et_2O (40 mL) was added slowly and yellow solid was precipitated. The suspension was centrifuged and the solvent was removed. Then the precipitation and centrifugation was repeated twice. The precipitation was dried under vacuum and gave 229 mg of yellow product. Yield: 95.4%. ^1H NMR (400 MHz, DMSO-d_6) δ = 9.10 (d, *J* = 32.0 Hz, 5H), 1.16 (s, 18H), 1.24 (s, 9H), 1.89 (s, 12H), 2.02 - 2.42 (br, 6H), 2.51 - 3.32 (br, 18H), 3.69 (s, 12H), 7.80 (s, 2H), 7.90 (s, 1H), 8.70 (s, 1H), 8.33 (s, 1H).

Synthesis of compound cycEu-phLa (3-4e). A mixture of **3-3c** (153.5 mg, 0.15 mmol) and 74 mg of ammonium pyrrolidine-1-carbodithioate (0.45 mmol) in 10 mL of MeOH was added slowly to a solution of $LaCl_3$•$6H_2O$ (55 mg, 0.15 mmol) in 5 mL of MeOH at room temperature. Then the reaction was stirred for 10 min. After removing around half of the solvent, the left solution was transferred to a 50 mL centrifugal tube. Et_2O (40 mL) was added slowly and yellow solid was precipitated. The suspension was centrifuged and the solvent was removed. The precipitation and centrifugation were repeated twice. The precipitation was dried under vacuum to give yellow solid as product (240 mg). Yield: 99.9%. MS: calculated $[M- 2H^+ - 3pdtc^- - La^{3+}-3Cl^-]^+$ = 897.4006, found: 897.3903.

Table 7.2. Room temperature overall energy transfer rates (s^{-1}) (= forward transfer rate – backward transfer rate) to Eu^{3+} levels from excited ligand singlet states.

(a) Calculation 1: ***cycEu-phTb***

Singlet state energy	Transfer rate to Eu^{3+} *J*-multiplet				
(cm^{-1})	$^5D_4$	$^5G_6$	$^5L_6$	$^5D_1$	$^5D_0$
23084	-1.2E9	-1.5E6	-1.1E4	4.0E-7	2.5E-7
24059	-1.8E7	-2.0E4	-1.3E2	2.2E-7	1.1E-7
25556	-2.4E4	-2.3E1	2.3E-1	7.1E-8	2.5E-8
25921	-1.4E4	-6.4E0	4.9E-1	1.9E-7	6.3E-8
26837	-4.9E2	8.0E-2	8.4E-1	4.7E-7	1.3E-7
27226	-2.0E1	1.1E-1	4.1E-1	5.0E-8	1.2E-8
27434	-5.6E0	1.3E-1	4.3E-1	5.3E-8	1.2E-8
27782	2.9E0	1.2E-1	3.7E-1	3.1E-8	6.7E-9
28550	3.9E0	9.9E-2	2.6E-1	1.0E-8	1.8E-9

(b) Calculation 2: ***cycEu-phTb***

Singlet state energy	Transfer rate to Eu^{3+} *J*-multiplet				
(cm^{-1})	$^5D_4$	$^5G_6$	$^5L_6$	$^5D_1$	$^5D_0$
23084	-1.2E9	-1.5E6	-1.1E4	4.0E-7	2.5E-7
24059	-1.8E7	-2.0E4	-1.3E2	2.2E-7	1.1E-7
25556	-2.4E4	-2.3E1	2.3E-1	7.1E-8	2.5E-8
25921	-1.4E4	-6.4E0	4.9E-1	1.9E-7	6.3E-8
26837	-4.9E2	8.0E-2	8.4E-1	4.7E-7	1.3E-7
27226	-2.0E1	1.1E-1	4.1E-1	5.0E-8	1.2E-8
27434	-5.6E0	1.3E-1	4.3E-1	5.3E-8	1.2E-8

27782	2.9E0	1.2E-1	3.7E-1	3.1E-8	6.7E-9
28550	3.9E0	9.9E-2	2.6E-1	1.0E-8	1.8E-9

(c) Calculation 3: ***cycTb-phEu***

Singlet state energy	Transfer rate to Eu^{3+} *J*-multiplet				
(cm^{-1})	$^5D_4$	$^5G_6$	$^5L_6$	$^5D_1$	$^5D_0$
23059	-1.3E9	-1.6E6	-1.3E4	4.0E-7	2.5E-7
24044	-1.9E7	-2.2E4	-1.4E2	2.2E-7	1.1E-7
25497	-3.1E4	-3.0E1	1.9E-1	7.5E-8	2.7E-8
25889	-1.3E4	-7.5E0	4.8E-1	2.0E-7	6.5E-8
26766	-6.9E2	1.5E-2	8.6E-1	5.1E-7	1.4E-7
27121	-3.5E1	1.0E-1	4.2E-1	5.6E-8	1.4E-8
27186	-1.9E1	9.4E-2	3.6E-1	3.4E-8	8.5E-9
27421	-6.2E0	1.3E-1	4.3E-1	5.4E-8	1.3E-8
27704	2.0E0	1.2E-1	3.8E-1	3.4E-8	7.4E-9
28509	3.9E0	1.0E-1	2.6E-1	1.1E-8	2.0E-9
29396	3.5E0	8.0E-2	1.8E-1	3.6E-9	5.4E-10
29533	4.1E0	8.4E-2	1.8E-1	4.0E-9	5.8E-10

Table 7.3. Room temperature overall energy transfer rates (s^{-1}) (= forward transfer rate – backward transfer rate) to Eu^{3+} levels from excited triplet states.

(a) Calculation 1: ***cycEu-phTb***

Triplet state energy	Transfer rate to Eu^{3+} *J*-multiplet				
(cm^{-1})	$^5D_4$	$^5G_6$	$^5L_6$	$^5D_1$	$^5D_0$
20501	-2.7E14	-1.1E11	-1.4E9	9.6E-5	1.1E-4
23015	-5.2E8	-6.6E5	-5.1E3	4.1E-7	2.6E-7
23981	-4.7E7	-2.3E4	-1.5E2	3.0E-6	1.6E-6
24239	-2.6E7	-9.9E3	-6.1E1	5.7E-6	2.8E-6
25172	-1.1E5	-7.1E1	-1.9E-1	3.8E-7	1.5E-7
25296	-1.8E5	-7.0E1	-4.7E-2	1.7E-6	6.4E-7
25920	-1.5E4	-4.6E0	3.4E-1	1.7E-6	5.5E-7
26451	-1.6E3	-3.3E-1	3.9E-1	1.4E-6	4.2E-7
26536	-2.0E2	-7.6E-2	1.6E-1	1.0E-7	2.9E-8
26823	-3.2E2	3.1E-2	3.9E-1	1.2E-6	3.1E-7
27411	-2.3E0	4.3E-2	1.4E-1	5.5E-8	1.3E-8
27656	4.5E-1	4.1E-2	1.3E-1	3.6E-8	7.9E-9
27864	1.5E0	4.7E-2	1.4E-1	4.4E-8	9.2E-9

28412	1.8E0	4.0E-2	1.1E-1	2.0E-8	3.7E-9

(b) Calculation 2: ***cycEu-phTb***

Triplet state energy	Transfer rate to Eu^{3+} *J*-multiplet (s^{-1})				
(cm^{-1})	$^5D_4$	$^5G_6$	$^5L_6$	$^5D_1$	$^5D_0$
18946	-2.3E17	-9.2E16	-1.5E15	-1.1E-4	3.5E-4
20946	-3.5E15	-1.3E13	-1.5E11	7.7E-6	7.8E-6
21918	-7.1E11	-2.5E11	-2.3E9	5.6E-6	4.6E-6
23324	-3.1E9	-8.8E8	-6.4E6	8.2E-6	4.8E-6
23419	-2.8E9	-7.5E8	-5.4E6	1.7E-5	9.6E-6
23491	-1.8E9	-4.9E8	-3.5E6	1.2E-5	6.7E-6
24326	-6.5E7	-1.5E7	-9.3E4	1.4E-5	6.5E-6
24869	-3.7E6	-8.8E5	-4.3E3	2.7E-6	1.1E-6
25230	-1.0E6	-2.3E5	-4.3E2	4.9E-6	1.9E-6
25485	-1.8E5	-4.2E4	2.4E2	8.3E-7	3.0E-7
25768	-9.2E4	-1.9E4	6.5E2	3.1E-6	1.1E-6
26117	-2.4E4	-4.4E3	8.7E3	4.4E-6	1.4E-6
26507	-2.1E3	-2.9E2	4.9E2	6.1E-7	1.8E-7
26634	-2.3E3	-1.8E2	8.6E2	3.0E-6	8.4E-7
27001	-2.8E2	1.2E2	6.1E2	9.0E-7	2.3E-7
27071	-1.4E2	1.0E2	4.5E2	3.6E-7	9.2E-8
27394	-2.0E1	1.2E2	4.1E2	2.5E-7	5.8E-8
27572	-8.0E-1	1.0E2	3.2E2	1.1E-7	2.6E-8
27944	1.0E1	1.2E2	3.4E2	1.2E-7	2.5E-8
28083	8.2E0	8.6E1	2.4E2	4.5E-8	9.0E-9

(c) Calculation 3: ***cycTb-phEu***

Triplet state energy	Transfer rate to Eu^{3+} *J*-multiplet				
(cm^{-1})	$^5D_4$	$^5G_6$	$^5L_6$	$^5D_1$	$^5D_0$
19597	-7.7E15	-3.6E12	-5.3E10	8.9E-5	1.3E-4
22971	-6.3E8	-8.0E5	-6.2E3	4.2E-7	2.7E-7
23932	-5.8E7	-2.9E4	-1.9E2	3.1E-6	1.6E-6
24127	-4.0E7	-1.6E4	-9.9E1	5.6E-6	2.8E-6
24889	-8.4E5	-3.9E2	-1.9E0	1.5E-6	6.2E-7

25134	-1.3E5	-8.5E1	-2.7E-1	3.9E-7	1.5E-7
25710	-3.3E4	-1.1E1	2.8E-1	1.5E-6	5.2E-7
26273	-4.9E3	-1.0E0	4.6E-1	2.5E-6	7.6E-7
26412	-3.4E2	-1.6E-1	1.5E-1	1.0E-7	3.0E-8
26502	-1.6E2	-7.8E-2	1.3E-1	5.6E-8	1.6E-8
26687	-4.8E2	-3.6E-2	3.5E-1	9.4E-7	2.6E-7
27356	-3.5E0	4.3E-2	1.4E-1	5.8E-8	1.4E-8
27548	-3.4E-1	4.2E-2	1.4E-1	4.5E-8	1.0E-8
27782	3.0E0	7.5E-2	2.2E-1	1.8E-7	3.8E-8
27808	1.4E0	4.7E-2	1.4E-1	4.7E-8	1.0E-8
28263	2.8E0	5.3E-2	1.5E-1	4.7E-8	9.1E-9

7.3 Experimental section of Chapter 4

Materials and method

All the chemicals were used without further purification except indicated. Magnetic resonance spectrometer of Bruker (400 Hz) was used to measure NMR spectra. Quadrupole-time-of-flight mass spectrometer (ABI QSTAR Elite) was used to measure the mass spectrometry. Agilent 1200 series HPLC instrument was used to record HPLC analysis. FT-IR spectrometer (PerkinElmer Paragon 1000 PC) was utilized to record FT-IR data. Emission, excitation, and decay were measured using iHR550 spectrometer, Horiba fluorescence spectrometer, and Edinburgh Mini-tau. The sample was held in an optical cryostat-CS202I-DMX-1SS from Advanced Research Systems Instruments Inc. with a base temperature of ~10 K. Quantum efficiencies were determined using a Horiba Fluorolog with a Horiba integrating sphere, Quanta–φ (λ_{ex} = 370 nm; λ_{em} = 575 – 720 nm).

Synthetic procedure

Synthesis of phLa. To a solution of 177 mg of $LaCl_3$•$6H_2O$ (0.5 mmol) in 5 mL of MeOH was added slowly a mixture of 98 mg of 1,10-phenanthrolin-5-amine (0.5 mmol) and 246 mg of ammonium pyrrolidine-1-carbodithioate (1.5 mmol) in 10 mL of MeOH at room temperature. The yellow precipitate appeared and the reaction content was stirred for 10 min. The yellow solid was collected by filtration and rinsed with a small amount of MeOH and dried under vacuum and gave the 265 mg of

yellow product. Yield:70.0%. ^{1}H NMR (400 MHz, DMSO-d_6) δ = 2.05 – 1.61 (m, 12H), 3.64 (t, *J* = 6.7 Hz, 12H), 6.21 (s, 2H), 6.88 (s, 1H), 7.55 (s, 1H), 7.78 (s, 1H), 8.09 (s, 1H), 8.72 (s, 2H), 9.09 (s, 1H). MS: calculated [M - La^{3+} -3pdtc$^-$ + H^+] = 196.0869, found: 196.0854.

Synthesis of phEu. To a mixture of $EuCl_3 \cdot 6H_2O$ (183 mg, 0.5 mmol) in 5 mL of MeOH was added slowly a mixture of 98 mg of 1,10-phenanthrolin-5-amine (0.5 mmol) and 246 mg of ammonium pyrrolidine-1-carbodithioate (1.5 mmol) in 10 mL of MeOH at room temperature. A yellow precipitate appeared and the mixture was stirred for 10 min. The yellow solid was collected by filtration and rinsed with a small amount of MeOH and dried under vacuum to give 340 mg of yellow product. Yield: 86.5%. ^{1}H NMR (400 MHz, DMSO-d_6) δ = 1.97 (s, 12H), 3.67 (s, 13H), 6.18 (s, 2H), 6.86 (s, 1H), 7.51 (s, 1H), 7.73 (s, 1H), 8.04 (s, 1H), 8.67 (s, 2H), 9.04 (s, 1H). MS: calculated [M - Eu^{3+} -3pdtc$^-$ + H^+] = 196.0869, found: 196.0741.

Intensity and efficiency calculations

Table 7.4. Calculation of radiative lifetimes and quantum efficiencies of the complexes.

	cycEu-phen	**cycEu-phLa**	**cycLa-pEu**	**phEu**	unit	
$A(^5D_0 \rightarrow {}^7F_1)$	60.0064	60.0064	60.0064	60.0064	s^{-1}	$A(^5D_0 \rightarrow {}^7F_1) = 0.01465n^3$ = 0.0600064 $(ms)^{-1}$ = 60.0064 s^{-1}
$A(^5D_0 \rightarrow {}^7F_2)$	101.7709	96.19026	171.4383	90.06961	s^{-1}	$A(^5D_0 \rightarrow {}^7F_2)$ = $[S(^5D_0 \rightarrow {}^7F_2)/S(^5D_0 \rightarrow {}^7F_1)]xA(^5D_0 \rightarrow {}^7F_1)$
$A(^5D_0 \rightarrow {}^7F_4)$	149.7760	152.1762	135.2544	164.0575	s^{-1}	$A(^5D_0 \rightarrow {}^7F_4)$ = $[S(^5D_0 \rightarrow {}^7F_4)/S(^5D_0 \rightarrow {}^7F_1)]xA(^5D_0 \rightarrow {}^7F_1)$
ΣA	311.5533	308.3729	366.6991	314.1335	s^{-1}	$\Sigma A = A(^5D_0 \rightarrow {}^7F_1) + A(^5D_0 \rightarrow {}^7F_2) + A(^5D_0 \rightarrow {}^7F_4)$
τ_R	3.21	3.24	2.73	3.18	ms	$\tau_R = 1/\Sigma A \times 1000$
τ_{obs}	0.55	0.57	0.16	<0.20	ms	
Φ_{int}	17.0	17.6	5.9	<6	%	$\Phi_{int} = \tau_{obs}/\tau_{rad}$
Φ_{ext}	4.4	0.40	0.38	<0.1	%	
Φ_{sens}	25.9	2.3	6.4	-	%	$\Phi_{ext} = \Phi_{sens}\Phi_{int}$
$\bar{\nu}$ $(^5D_0 \rightarrow {}^7F_1)$	1.6863	1.6863	1.6892	1.6892	10^6 m^{-1}	10^9(nm)/ λ (nm)
$\bar{\nu}$ $(^5D_0 \rightarrow {}^7F_2)$	1.6260	1.6260	1.6340	1.6287	10^6 m^{-1}	10^9(nm)/ λ (nm)
$\bar{\nu}$ $(^5D_0 \rightarrow$	1.4286	1.4286	1.4306	1.4286	10^6 m^{-1}	10^9/ λ (nm)

$^7F_4$)						
Ω_2	2.766	2.614	4.591	2.436	10^{-20}cm^2	$A\,(ED)(s^{-1}) = \frac{1}{4\pi\varepsilon_0}\frac{64\pi^4\bar{\nu}^3}{3h(2J+1)}\{\frac{n(n^2+2)^2}{9}D_{ED}\}$ $D_{ED} = e^2S_{ED}$ where S is linestrength $^5D_0 \rightarrow {}^7F_2$, S_{ED} $= \Omega_2 \lvert\langle {}^5D_0 \rvert\rvert U^{(2)} \rvert\rvert {}^7F_2\rangle\rvert^2$ $= \Omega_2 \times 0.0032$ (Ω_2 in m^2) $A(^5D_0 \rightarrow {}^7F_2)$ $= 0.085597321 \times 10^8 \times \bar{\nu}^3 \times \Omega_2$
Ω_4	8.350	8.484	7.509	9.146	10^{-20}cm2	$^5D_0 \rightarrow {}^7F_4$, S_{ED} $= \Omega_4 \lvert\langle {}^5D_0 \rvert\rvert U^{(4)} \rvert\rvert {}^7F_4\rangle\rvert^2$ $= \Omega_4 \times 0.0023$ (Ω_4 in m^2) $A(^5D_0 \rightarrow {}^7F_2)$ $= 0.061523075 \times 10^8 \times \bar{\nu}^3 \times \Omega_4$
Intensity ratio	4626	199	63	1		Ratio by comparing intensity area

*Table 7.5. Relative intensities of $^5D_0 \rightarrow {}^7F_J$ transitions of **cycEu-phen** normalized to that of $^5D_0 \rightarrow {}^7F_1$.*

Complex	Relative intensity				
	$^5D_0 \rightarrow {}^7F_0$	$^5D_0 \rightarrow {}^7F_1$	$^5D_0 \rightarrow {}^7F_2$	$^5D_0 \rightarrow {}^7F_3$	$^5D_0 \rightarrow {}^7F_4$
cycEu-phen	0.122	1	1.696	0.140	2.496

Illustrative example of the Judd-Ofelt treatment of Eu^{3+} emission using cycEu-phen.

$A(^5D_0 \rightarrow {}^7F_1) = 0.01465n^3 = 0.0600064\ (ms)^{-1} = 60.0064\ s^{-1}$

$A(^5D_0 \rightarrow {}^7F_2) = [S(^5D_0\text{-}^7F_2)/S(^5D_0\text{-}^7F_1)] \times A(^5D_0\text{-}^7F_1) = 1.696 \times 60.0064 = 101.771\ s^{-1}$ (=0.101771 ms^{-1})

$A(^5D_0 \rightarrow {}^7F_4) = [S(^5D_0\text{-}^7F_4)/S(^5D_0\text{-}^7F_1)] \times A(^5D_0\text{-}^7F_1) = 2.496 \times 60.0064 = 149.776\ s^{-1}$

Here S is the integrated band area, using photon counts

$\Sigma A = 60.0064+101.771+149.776 = 311.55\ s^{-1}$

Radiative lifetime, $\tau_R = 1/\Sigma A = 0.00321$ s = 3.21 ms (have neglected transitions to $^7F_0$,$^7F_3$)

Measured lifetime 0.55 ms

Internal quantum efficiency = $\Phi_{int} = \tau_{obs}/\tau_{rad} = 0.55/3.21 = 0.17$

$A = A_{ED} + A_{MD}$

For $^5D_0 \rightarrow {}^7F_1$, $A_{MD} = n^3 D_{MD} = 0.01465n^3 = 0.0600064\ (ms)^{-1} = 60.0064\ s^{-1}$

$$A\,(ED)(s^{-1}) = \frac{1}{4\pi\varepsilon_0}\frac{64\pi^4\bar{\nu}^3}{3h(2J+1)}\{\frac{n(n^2+2)^2}{9}D_{ED}\} \qquad \text{Eq 1}$$

In MKS units: $\varepsilon_0 = 8.85419 \times 10^{-12}\ m^{-3}\ kg^{-1}\ s^4\ A^2$

$\bar{\nu}$ in m^{-1}

$h = 6.62607 \times 10^{-34}$ Js (= kg $m^2\ s^{-1}$)

J degeneracy of upper state in emission so for $^5D_0$, $2J+1 = 1$

n = refractive index, if 1.6 then $n(n^2+2)^2/9 = \chi_{ED} = 3.697$

$D_{ED} = e^2 S_{ED}$ where S is linestrength

$e = 1.60217 \times 10^{-19}$ C (1 C = 1 A s)

For $^5D_0 \rightarrow {}^7F_2$, $S_{ED} = \Omega_2|\langle {}^5D_0||U^{(2)}||{}^7F_2\rangle|^2 = \Omega_2 \times 0.0032$ (Ω_2 in m^2)

$^5D_0 \rightarrow {}^7F_4$, $S_{ED} = \Omega_4|\langle {}^5D_0||U^{(4)}||{}^7F_4\rangle|^2 = \Omega_4 \times 0.0023$ (Ω_4 in m^2)

where the reduced square matrix elements for the $^7F_2$ and $^7F_4$ transitions are taken as 0.0032 and 0.0023, respectively.

Check units in Eq 1:

$$s^{-1} = \frac{1}{m^{-3}kg^{-1}s^4A^2}\frac{m^{-3}}{kgm^2s^{-1}}A^2s^2 \times m^2$$

For emission from $^5D_0$: from Eq 1

$$A\,(ED)(s^{-1}) = \frac{1}{4\pi\varepsilon_0}\frac{64\pi^4\bar{\nu}^3}{3h(2J+1)}e^2\{\frac{n(n^2+2)^2}{9}S_{ED}\}$$

$$= 7.23537 \times 10^8 \times \sum \bar{\nu}_i^3\{\frac{n(n^2+2)^2}{9}S_i^{ED}\}$$

Where $\bar{\nu}$ in m^{-1} and sum over *i* transitions

Mean wavelengths are ~593, 615 (16260 cm^{-1}: $1.626 \times 10^6\ m^{-1}$), 700 nm (14286 cm^{-1}: $1.4286 \times 10^6\ m^{-1}$)

$A(^5D_0\text{-}{}^7F_2) = 101.771\ s^{-1} = 7.23537 \times 10^8 \times 3.697 \times (1.6260 \times 10^6)^3 \times \Omega_2 \times 0.0032$

$\Omega_2 = 101.771/7.23537 \times 10^8 \times 3.697 \times 4.2989 \times 10^{18} \times 0.0032 = 1.022 \times 10^{-21}/3.697$

$= 2.7657 \times 10^{-24}\ m^2 = 2.77 \times 10^{-20}\ cm^2$

$A(^5D_0\text{-}{}^7F_4) = 149.776\ s^{-1} = 7.23537 \times 10^8 \times 3.697 \times (1.4286 \times 10^6)^3 \times \Omega_4 \times 0.0023$

and $\Omega_4 = 149.776/(10^{18} \times 1.8486 \times 10^7) = 8.102 \times 10^{-24}\ m^2 = 8.35 \times 10^{-20}\ cm^2$

External quantum yield found by experiment 0.044 = Φ_{ext}

$\Phi_{ext} = \Phi_{sens}\Phi_{int}$

$\Phi_{sens} = 0.044/0.17 = 0.26$

7.4 Experimental section of Chapter 5

Materials and Characterization

The lanthanide chlorides, oleic acid, and 1-octadecene were purchased from Sigma-Aldrich. The absorption was measured with Agilent Cary 60 UV-Vis. The dye emissions were carried out on Shimadzu RF-6000 and Horiba iHR550. The laser peak in the emission spectra was arbitrarily cut off. The upconversion emission spectra were measured on an Andor detector with 793 nm laser excitation. The quantum yields were obtained using IR783 as a standard reference (8.4% in methanol)[2].

Synthesis Procedure of UCNPs

A mixture of 1 mmol of lanthanide chloride in methanol was added to 15 mL of octadecene and 6mL of oleic acid. The reaction mixture was heated to 150 ^{o}C and kept the temperature for 30 min to remove methanol and water molecule and then cooled down to room temperature. 2.5 mmol of sodium hydroxide and 4 mmol of ammonium fluoride in 5 mL of methanol was added to the reaction flask. The reaction mixture was stirred for 0.5 h at room temperature. The mixture was then heated to 150 ^{o}C and kept for 0.5 h, followed by heating to 300 ^{o}C and keeping for 1.5 h to form the upconversion nanoparticles. The upconversion nanoparticles were obtained by centrifugation (9000 r/min) for 5 min and purified by redispersing in cyclohexane and precipitating with ethanol three times. The upconversion nanoparticles were dispersed in cyclohexane. The size and morphology were characterized by TEM.

Synthesis procedure of organic molecules

Synthesis of 5-3. To a solution of diphenylmethane **5-1** (10 mL, 60 mmol) in tetrahydrofuran (150 mL, 37.5 mL), n-BuLi (1.6 M, in hexane, 60 mmol) was added

slowly in ice bath protected by nitrogen gas. The mixture was kept in the ice bath for 1 h, followed by adding slowly with a solution of (4-bromophenyl)(phenyl)methanone (10.4 g, 40 mmol) in 40 mL of tetrahydrofuran. The reaction was stirred at room temperature for 14 h. The solution was added with 200 mL of saturated ammonium chloride aqueous solution, followed by extraction with 200 mL of dichloromethane twice. The dichloromethane phase was dried over anhydrous Na_2SO_4. The solvent was removed and the resulting product was redissolved in toluene (400 mL) and added with p-toluenesulfonic acid (2.5 g). The reaction solution was refluxed for 4 h. The toluene was removed and the residue was added with water (300 mL), then extracted using 200 mL of hexane three times and dried over anhydrous Na_2SO_4. The purification was conducted by chromatography using silica gel with hexane as eluent, giving white product (12.56 g). Yield: 76.3%. ^{1}H NMR (400 MHz, $CDCl_3$) δ = 6.89 (d, *J* = 8.6 Hz, 2H), 7.04 – 6.98 (m, 6H), 7.14 – 7.08 (m, 9H), 7.22 (d, *J* = 8.6 Hz, 2H). ^{13}C NMR (101 MHz, $CDCl_3$) δ = 120.43, 126.59, 126.64, 126.69, 127.67, 127.77, 127.87, 130.84, 131.22, 131.24, 131.29, 132.97, 139.65, 141.59, 142.70, 143.22, 143.32, 143.41.

Synthesis of 5-4. The compound **5-3** (500 mg, 1.215 mmol), tetrahydrofuran (37.5 mL) and sodium carbonate (1.285 g, 12.15 mmol) were added to H_2O (12.5 mL). Then (4-hydroxyphenyl)boronic acid (335 mg, 2.430 mmol) and $Pd(PPh_3)_4$ (140 mg, 0.1215 mmol) were added. The mixture was refluxed under nitrogen protection overnight. The reaction solution was added with water (60 mL), extracted with dichloromethane (50 mL) three times, and dried over anhydrous sodium sulfate. The purification was conducted by chromatography using silica gel with a mixed solution of hexane and ethyl acetate (15:1) as eluent. Yield, 91.0%. ^{1}H NMR (500 MHz, $CDCl_3$) δ = 4.67 (s, 1H), 6.86 (d, *J* = 8.7 Hz, 2H), 7.14 – 7.02 (m, 17H), 7.29 (d, *J* = 8.5 Hz, 2H), 7.44 (d, *J* = 8.7 Hz, 2H). ^{13}C NMR (126 MHz, $CDCl_3$) δ = 115.71, 125.82, 126.51, 126.58, 127.76, 127.80, 127.88, 128.23, 131.48, 131.49, 131.56, 131.88, 133.57, 138.52, 140.72, 141.09, 142.28, 143.91, 143.91, 143.95, 155.15. MS (negative): Calculated $[M-H]^-$ = 423.2, found 423.4.

Synthesis of 5-5 (TPEO-IR783). Sodium hydride (24 mg, 0.6 mmol 60%), compound **5-4** (85 mg, 0.2 mmol) and potassium iodide (18 mg, 0.1 mmol) were added in dry dimethylformamide (5 mL) under argon gas atmosphere. The reaction mixture was stirred for 30 min and injected 60 mg of IR783 (0.08 mmol) in 2 mL of dry dimethylformamide. The solution was kept in argon gas atmosphere for 6 d at room temperature under stirring. The dimethylformamide was removed and the left solid was purified using chromatography by silica gel with a mixture of dichloromethane and methanol (10:1) as eluent. 70 mg of desired product was obtained. Yield: 76.9%. ^{1}H NMR (500 MHz, CD_3OD) δ = 1.35 (s, 12H), 1.99 – 1.86 (m, 8H), 2.09 – 2.02 (m, 2H), 2.78 (t, *J* = 6.0 Hz, 4H), 2.87 (t, *J* = 7.1 Hz, 4H), 4.14 (t, *J* = 7.1 Hz, 4H), 6.20 (d, *J* = 14.2 Hz, 2H), 7.12 – 6.97 (m, 17H), 7.21 – 7.15 (m, 4H), 7.36 (m, 4H), 7.30 (m, 4H), 7.61 (d, *J* = 8.9 Hz, 2H), 8.01 (d, *J* = 14.2 Hz, 2H). ^{13}C NMR (126 MHz, CD_3OD) δ = 23.58, 25.25, 27.21, 28.21, 30.73, 44.86, 50.26, 51.79, 101.16, 112.06, 116.27, 123.35, 123.39, 126.11, 126.80, 127.53, 127.58, 127.65, 128.71, 128.78, 128.86, 129.72, 129.78, 132.32, 132.41, 132.97, 136.28, 139.26, 141.85, 142.44, 142.56, 143.35, 143.54, 143.97, 145.00, 145.04, 160.87, 165.25, 173.59. MS: calculated $[M - Na]^-$ = 1113.5, found: 1113.9.

Synthesis of IR806. IR780 (100 mg, 0.15 mmol) and 4-mercaptobenzoic acid (46 mg, 0.3 mmol) were added to 4 mL of dry dimethylformamide. The reaction content was stirred at room temperature overnight. The solution was filtered and precipitated with 40 mL of diethyl ether. The precipitation was re-dissolved in dimethylformamide. Repeated the precipitation twice, giving 101 mg of product. Yield: 85.6%. ^{1}H NMR (500 MHz, $CDCl_3$) δ = 1.04 (t, *J* = 7.4 Hz, 6H), 1.43 (s, 12H), 1.88 (m, 4H), 2.12 – 2.01 (m, 2H), 2.81 (t, *J* = 5.7 Hz, 4H), 4.13 (t, *J* = 7.3 Hz, 4H), 6.26 (d, *J* = 14.1 Hz, 2H), 7.12 (d, *J* = 8.0 Hz, 2H), 7.19 (t, *J* = 7.5 Hz, 2H), 7.27 (d, *J* = 7.5 Hz, 4H), 7.34 (t, *J* = 7.7 Hz, 2H), 7.96 (d, *J* = 8.3 Hz, 12H), 8.58 (d, *J* = 14.1 Hz, 2H). ^{13}C NMR (126 MHz, $CDCl_3$) δ = 11.82, 20.88, 21.09, 26.96, 28.00, 46.54, 49.35, 102.13, 111.09, 122.31, 125.43 125.60, 126.82, 128.84, 131.22, 134.23, 141.23, 142.37, 144.52, 145.67, 149.01, 169.94, 172.63. MS (positive): calculated $[M]^+$ = 657.3, found: 657.4.

Synthesis of IR808. The IR808 was synthesized by the same procedure of IR806.

Yield: 96.5%. ^{1}H NMR (500 MHz, DMSO-d_6) δ = 1.38 (s, 12H), 1.75 (m, 8H), 1.95 (m, 2H), 2.48-2.54 (m, 4H), 2.80 (t, *J* = 5.9 Hz, 4H), 4.18 (t, *J* = 7.2 Hz, 4H), 6.40 (d, *J* = 14.2 Hz, 2H), 7.22 (t, *J* = 7.7 Hz, 2H), 7.38 (m, 4H), 7.44 (d, *J* = 8.0 Hz, 2H), 7.52 (d, *J* = 7.2 Hz, 2H), 7.86 (d, *J* = 8.6 Hz, 2H), 8.53 (d, *J* = 14.1 Hz, 2H). ^{13}C NMR (126 MHz, DMSO-d_6) δ = 22.51, 25.86, 26.13, 27.14, 34.27, 43.75, 48.74, 50.68, 102.03, 111.57, 122.35, 124.97, 125.31, 127.76, 128.53, 130.43, 133.29, 141.08, 142.04, 142.94, 144.60, 146.97, 166.69, 171.91. MS (negative): calculated $[M\text{-}Na]^-$ = 844.3, found: 643.8; calculated $[M - Na - H]^{2-}/2$=421.6, found:421.5.

7.5 Experimental section of Chapter 6

Materials and Characterization

The lanthanide chlorides, oleic acid, and 1-octadecene were purchased from Sigma-Aldrich. The mass spectra were measured on Agilent 6500 QTOF. The NMR results were carried out by Agilent 500/54 Premium Shields instrument. The absorption was measured with Agilent Cary 60 UV-Vis. The dye emissions were carried out on Shimadzu RF-6000 and Horiba iHR550. The Upconversion emissions were measured on an Andor detector with 793 nm or 980 nm laser excitation.

Synthesis of rubrene acid

The rubrene acid is synthesized according the literature.[3]

Synthesis of tetramethyl 5,6,11,12-tetraphenyl-1,4,7,10-tetrahydro-1,4:7,10-diethenotetracene-2,3,8,9-tetracarboxylate (mixture of trans and cis form). Hydroquinone (40 mg, 0.009 mmol), rubrene (5 g, 9.39 mmol), dimethyl acetylenedicarboxylate (20 mL), were added to 20 mL of xylene. The content was heated to 170 °C and kept overnight. After removing the solvent, the residue was added with acetonitrile (65 mL) and triturated, filtered, and rinsed with acetonitrile, giving 2.51 g of solid with a 32.8% yield. MS: Calculated $[M+1]^+$: 817.2123, found: 817.2883.

Synthesis of tetramethyl 5,6,11,12-tetraphenyl-1,4,7,10-tetrahydro-1,4:7,10-

diethanotetracene-2,3,8,9-tetracarboxylate (mixture of trans and cis form). The tetramethyl 5,6,11,12-tetraphenyl-1,4,7,10-tetrahydro-1,4:7,10-diethenotetracene-2,3,8,9-tetracarboxylate (trans and cis form, 200 mg, 0.24 mmol) was added to 250 mL of ethyl acetate. The reaction content was bubbled with argon gas for 30 min before 200 mg of Pd/C was added. Then the content was bubbled with argon gas for 15 min and hydrogen gas for 0.5 h. The catalyst was filtered off by kieselguhr before removing the solvent under vacuum. The residue was added with methanol (8 mL), sonicated and centrifuged, giving 702 mg solid with an 87.3% yield. MS: calculated $[M+1]^+$ = 820.3036, found: 821.3290.

Synthesis of tetramethyl 5,6,11,12-tetraphenyltetracene-2,3,8,9-tetracarboxylate. The tetramethyl 5,6,11,12-tetraphenyl-1,4,7,10-tetrahydro-1,4:7,10-diethanotetracene-2,3,8,9-tetracarboxylate (trans and cis form, 200 mg, 0.24 mmol) was heated up to 330-340 °C for 5 min. The obtained red solid was collected and purified by chromatography on silica gel eluted with hexane and ethyl acetate (5:1 – 5:2), giving 180 mg of red product with a 90.8% yield. ^{1}H NMR (500 MHz, $CDCl_3$) δ = 3.78 (s, 12H), 6.85 (d, *J* = 7.0 Hz, 8H), 7.09 (m, 8H), 7.16 (m Hz, 4H), 7.86 (s, 4H). ^{13}C NMR (126 MHz, $CDCl_3$) δ = 52.63, 126.92, 127.74, 127.75, 129.91, 130.26, 131.55, 132.13, 139.89, 140.02, 168.07. MS: calculated $[M+1]^+$: 765.2410, found: 765.2452.

Synthesis of potassium 5,6,11,12-tetraphenyltetracene-2,3,8,9-tetracarboxylate (Rubrene acid). The tetramethyl 5,6,11,12-tetraphenyltetracene-2,3,8,9-tetracarboxylate (100 mg, 0.13 mmol) in 2.5 mL of dioxane was added into 15 mL of KOH solution in methanol (1 M). The reaction content was refluxed for 50 min before cooling down to room temperature. The reaction content was filtered. The residue was washed with methanol, giving 101 mg red solid as product. Yield: 89.4%. ^{1}H NMR (500 MHz, D_2O) δ = 6.97 (d, *J* = 7.1 Hz, 8H), 7.21 (m, *J* = 23.0, 7.2 Hz, 12H), 7.55 (s, 4H). ^{13}C NMR (126 MHz, D_2O) δ = 125.43, 126.28, 127.51, 129.18, 129.92, 132.03, 135.60, 137.99, 140.60, 176.78. MS: calculated $[M - 4K^+ + 5H^+]^+$ =709.1784, found 709.2033.

7.5 Characterization data

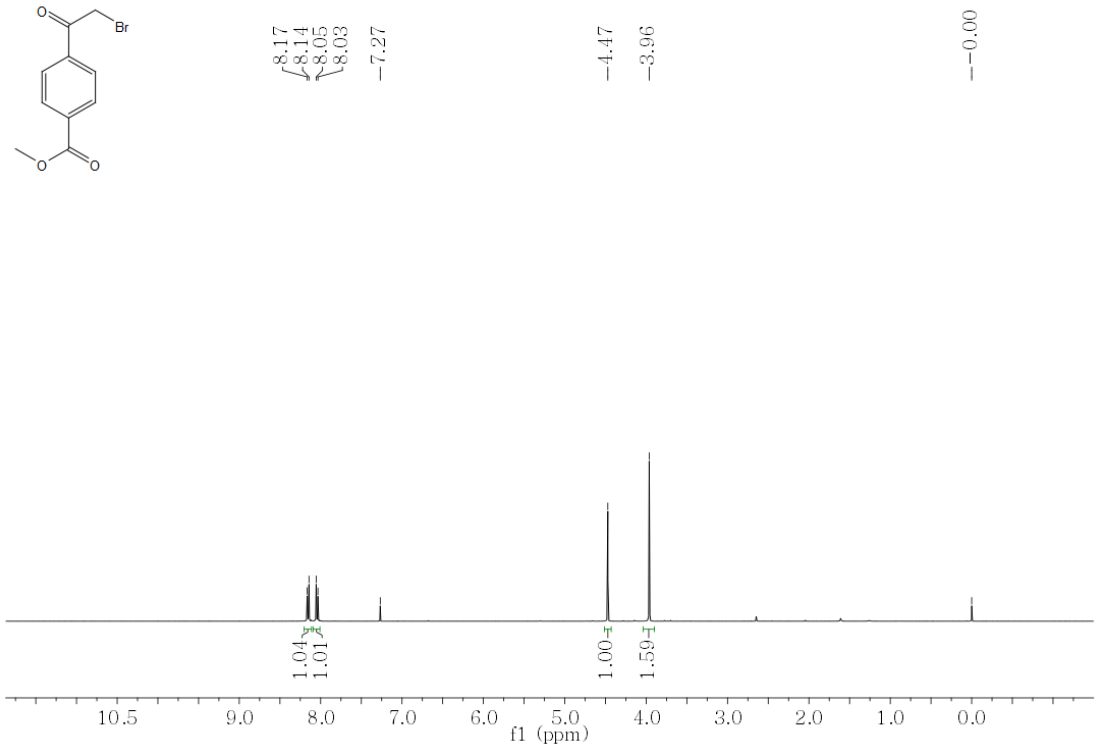

*Figure 7.1. [1]H NMR of compound **2-1**.*

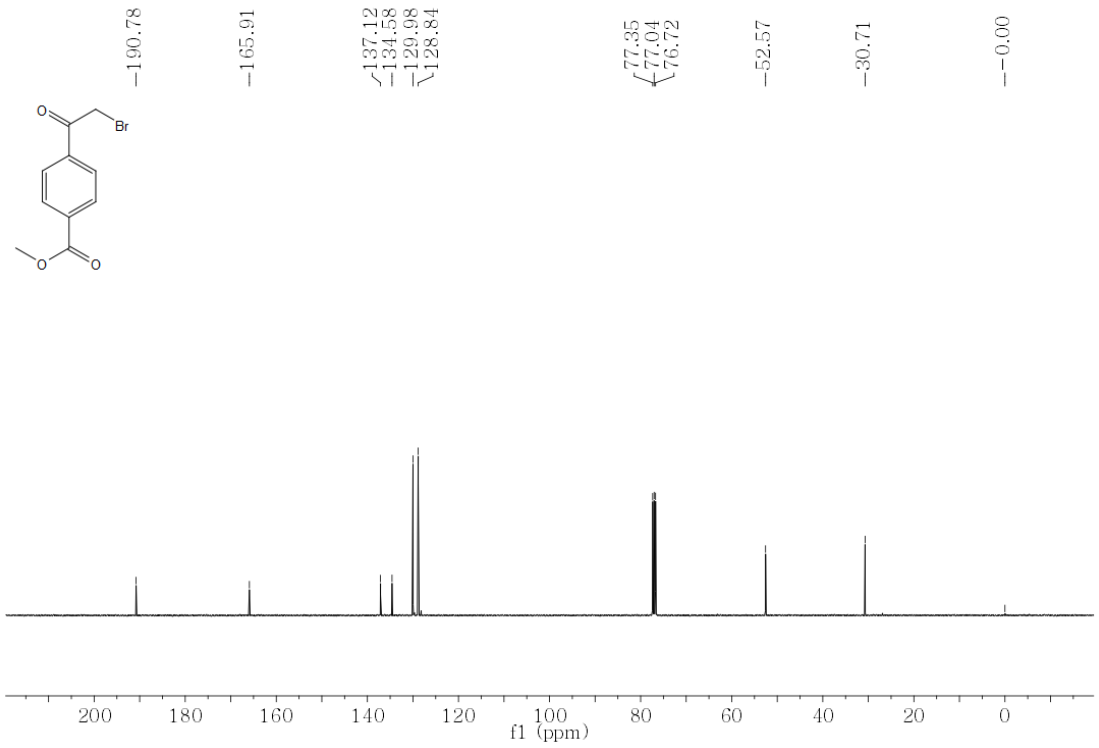

*Figure 7.2. [13]C NMR of compound **2-1**.*

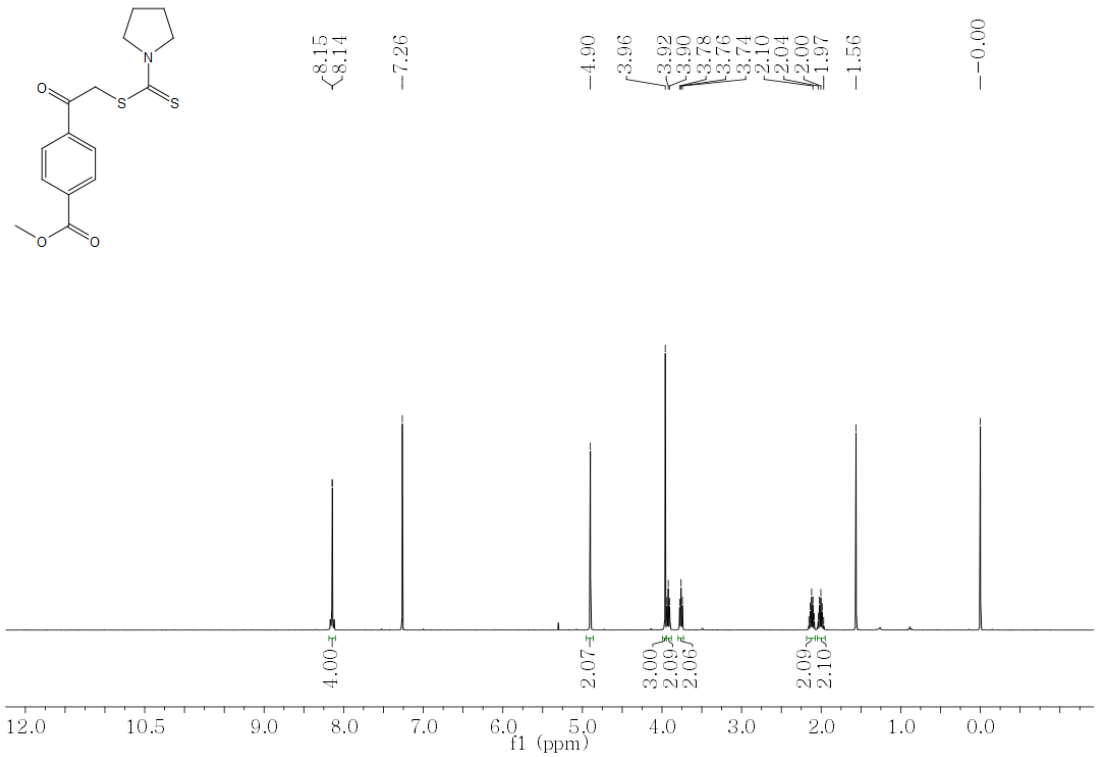

*Figure 7.3. [1]H NMR of compound **2-2**.*

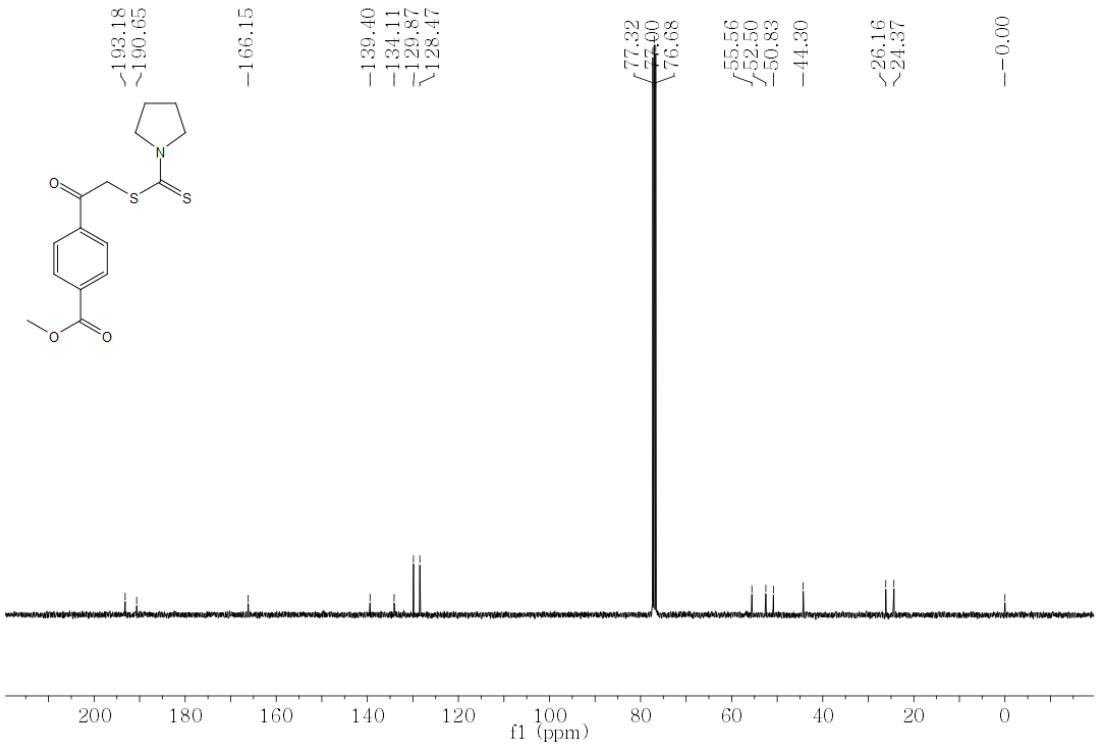

*Figure 7.4. [13]C NMR of compound **2-2**.*

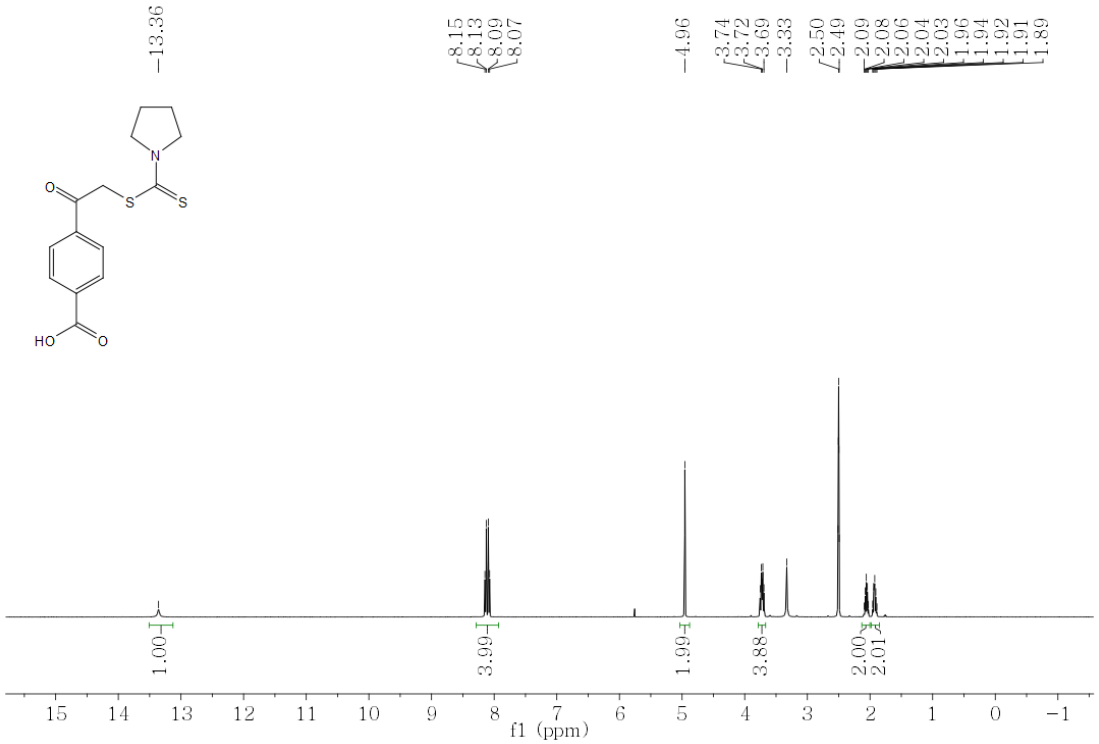

*Figure 7.5. [1]H NMR of compound **2-3**.*

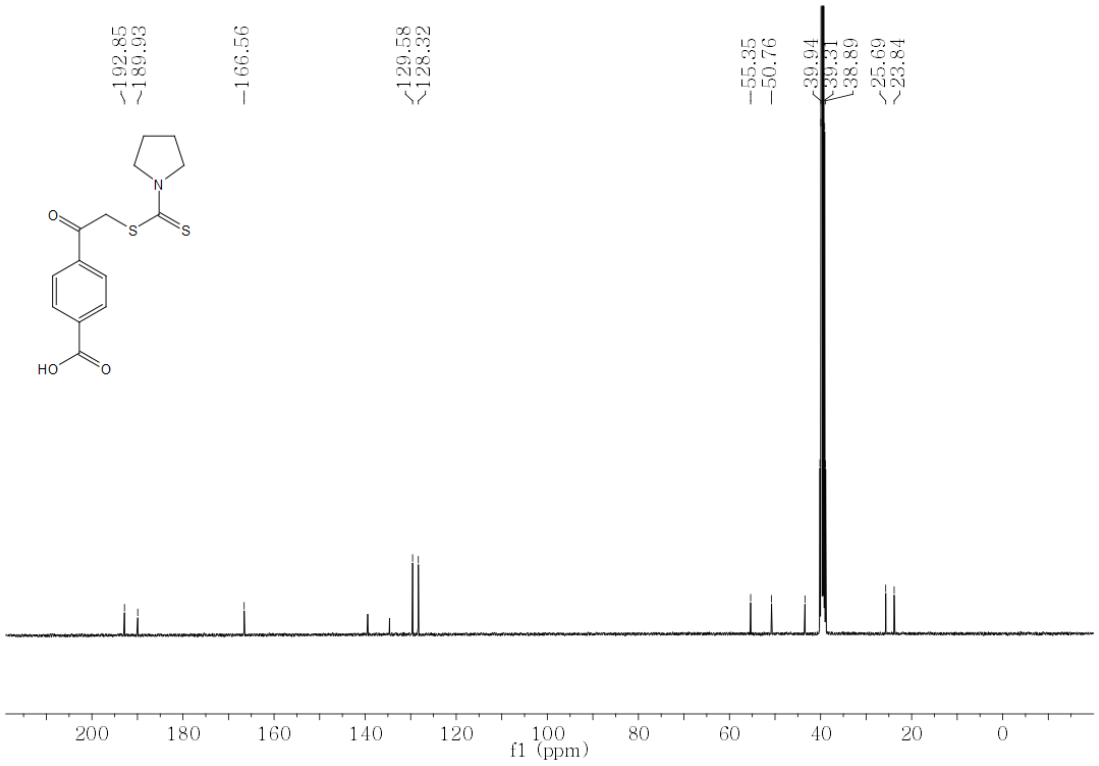

*Figure 7.6. [13]C NMR of compound **2-3**.*

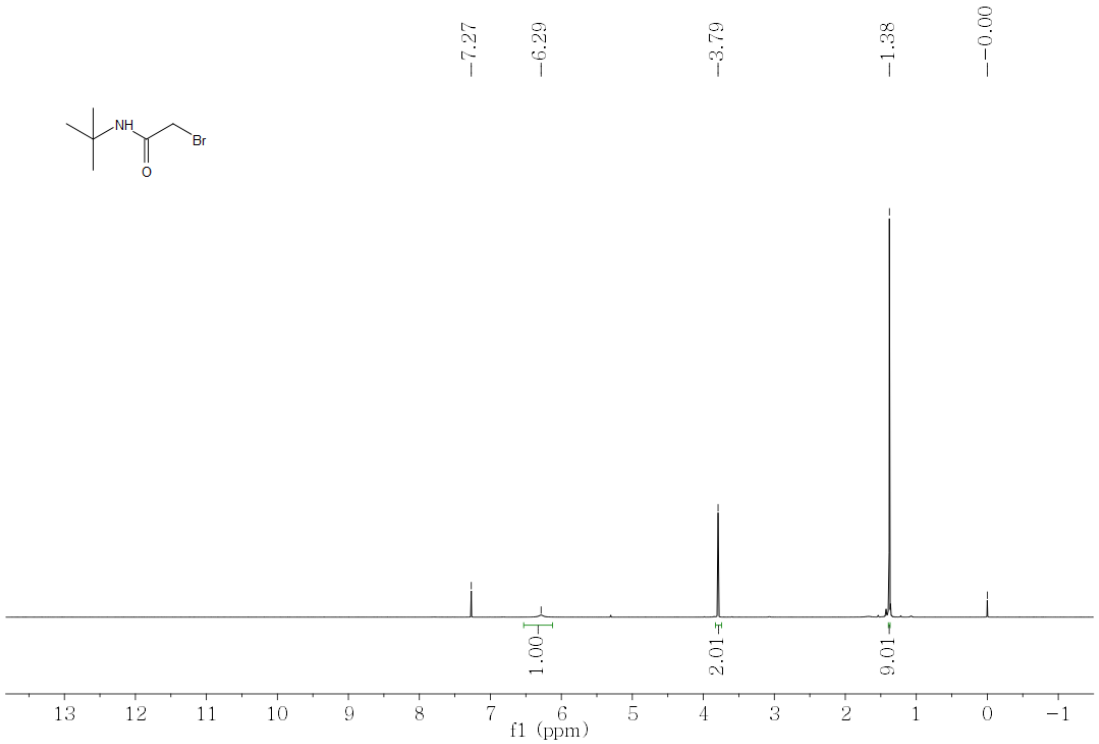

*Figure 7.7. [1]H NMR of compound **2-4**.*

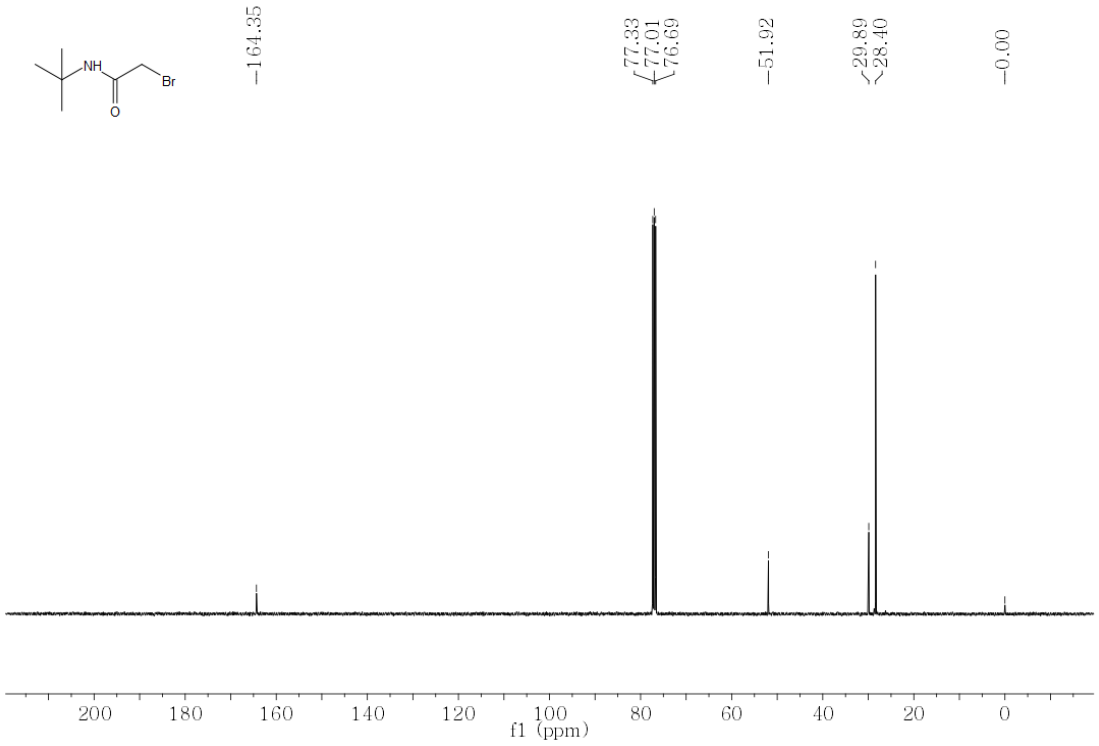

*Figure 7.8. [13]C NMR of compound **2-4**.*

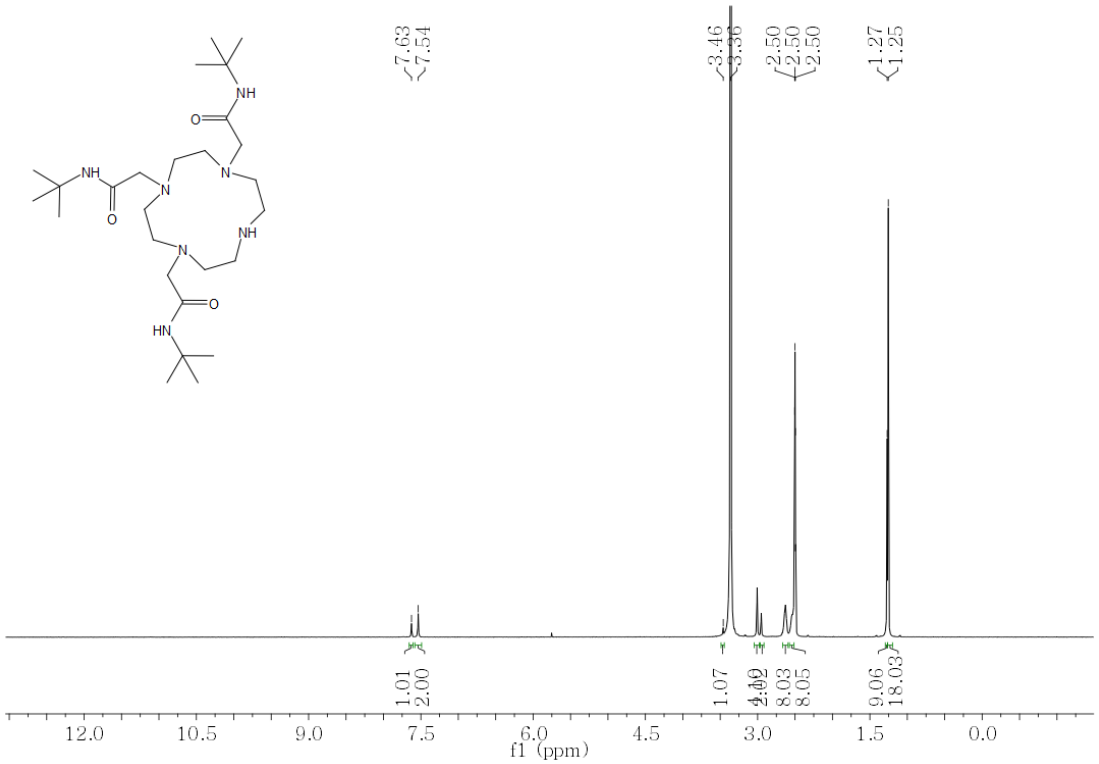

*Figure 7.9. [1]H NMR spectrum of compound **2-5**.*

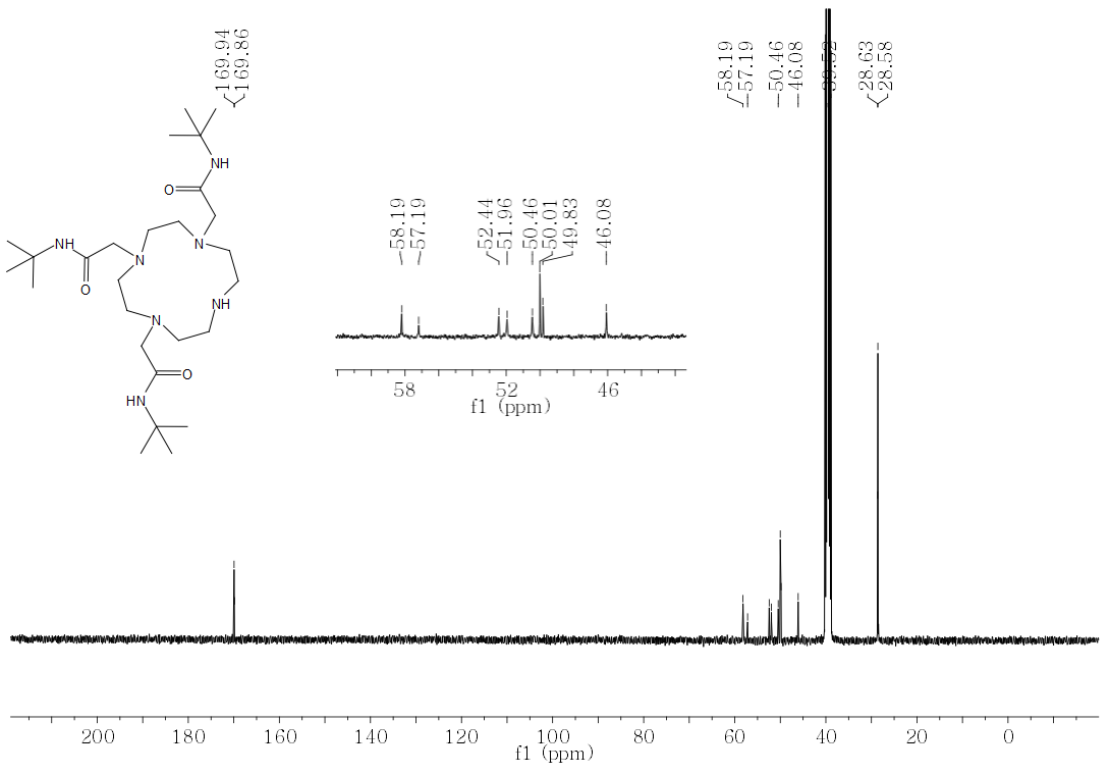

*Figure 7.10. [13]C NMR spectrum of compound **2-5**.*

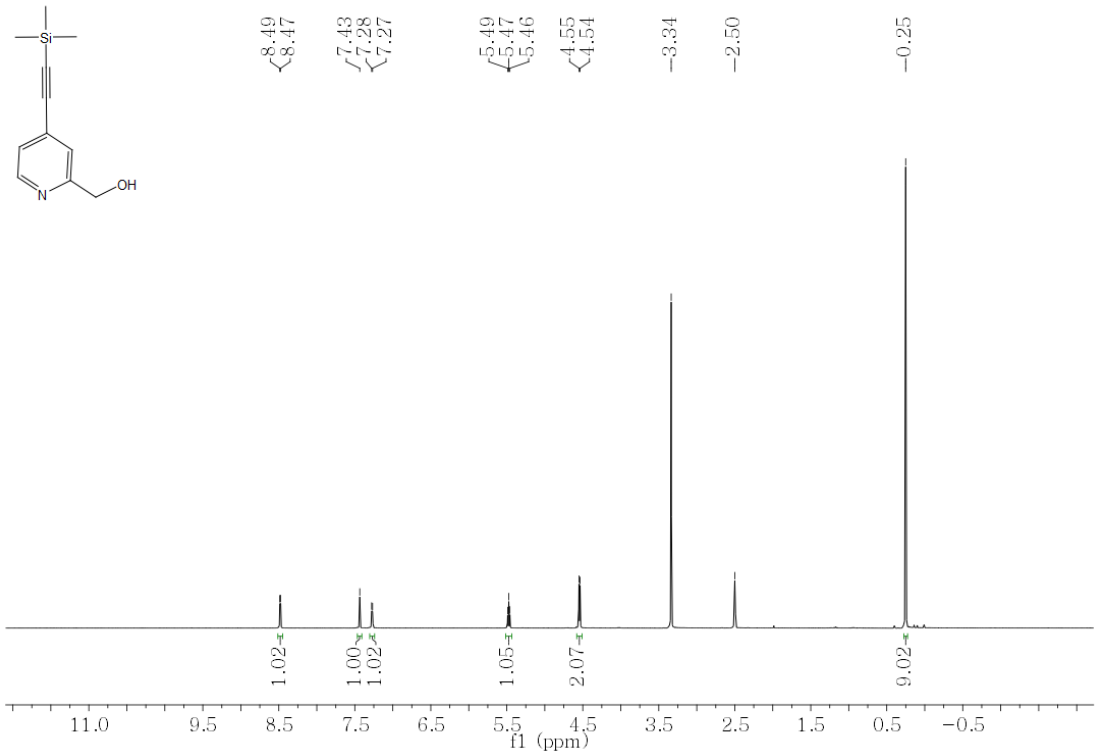

*Figure 7.11. [1]H NMR of compound **2-6.***

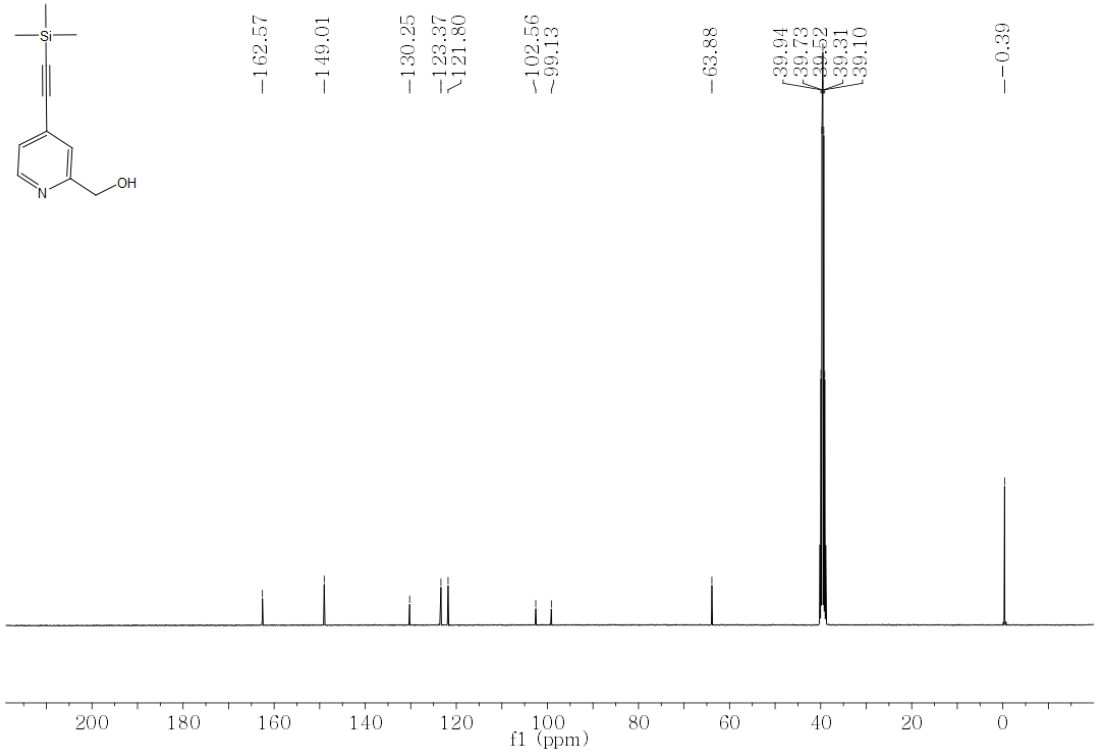

*Figure 7.12. [13]C NMR of compound **2-6.***

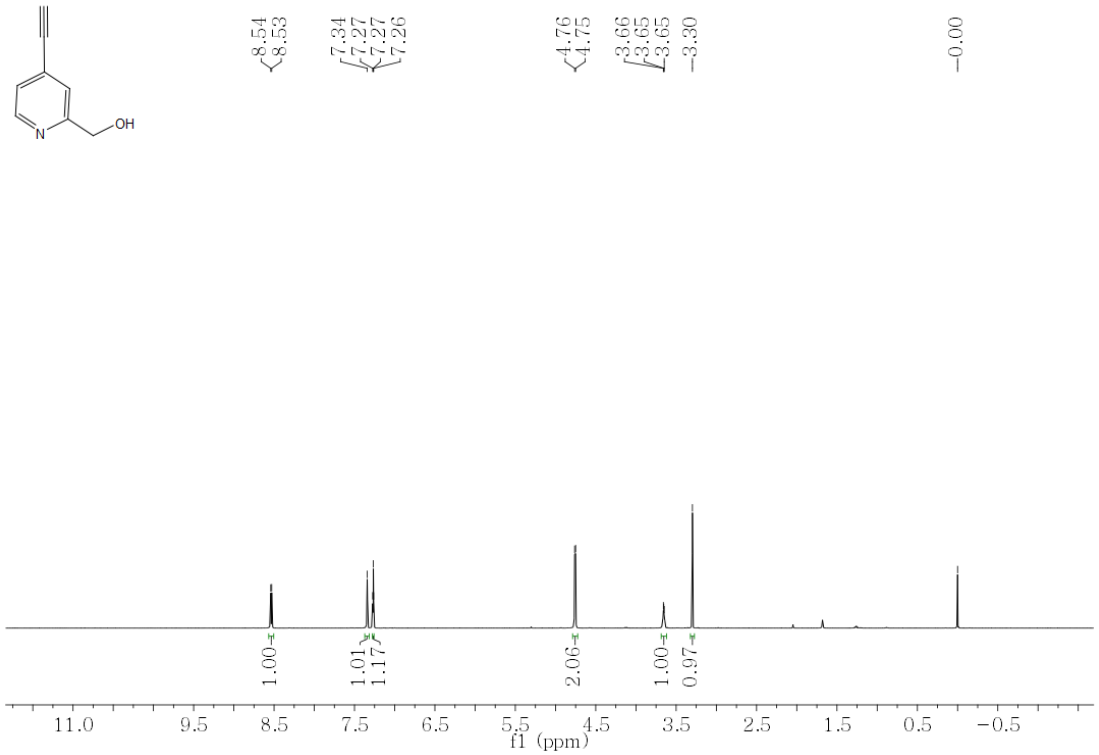

*Figure 7.13. [1]H NMR of compound **2-7**.*

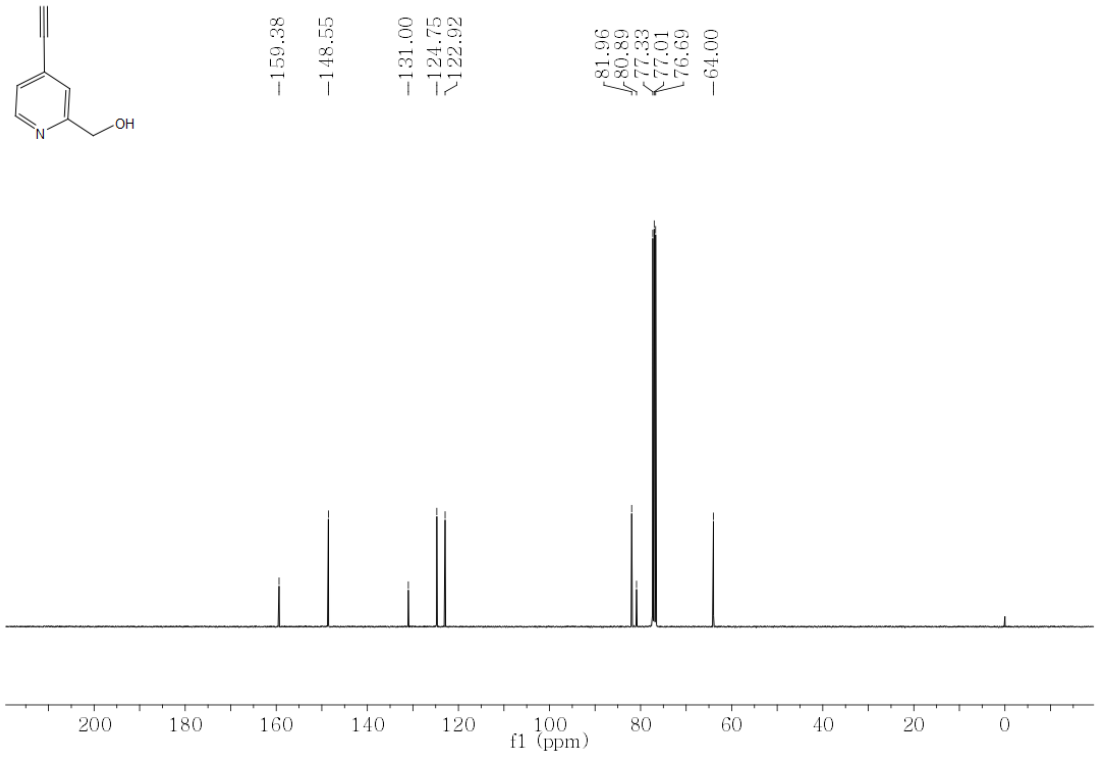

*Figure 7.14. [13]C NMR of compound **2-7**.*

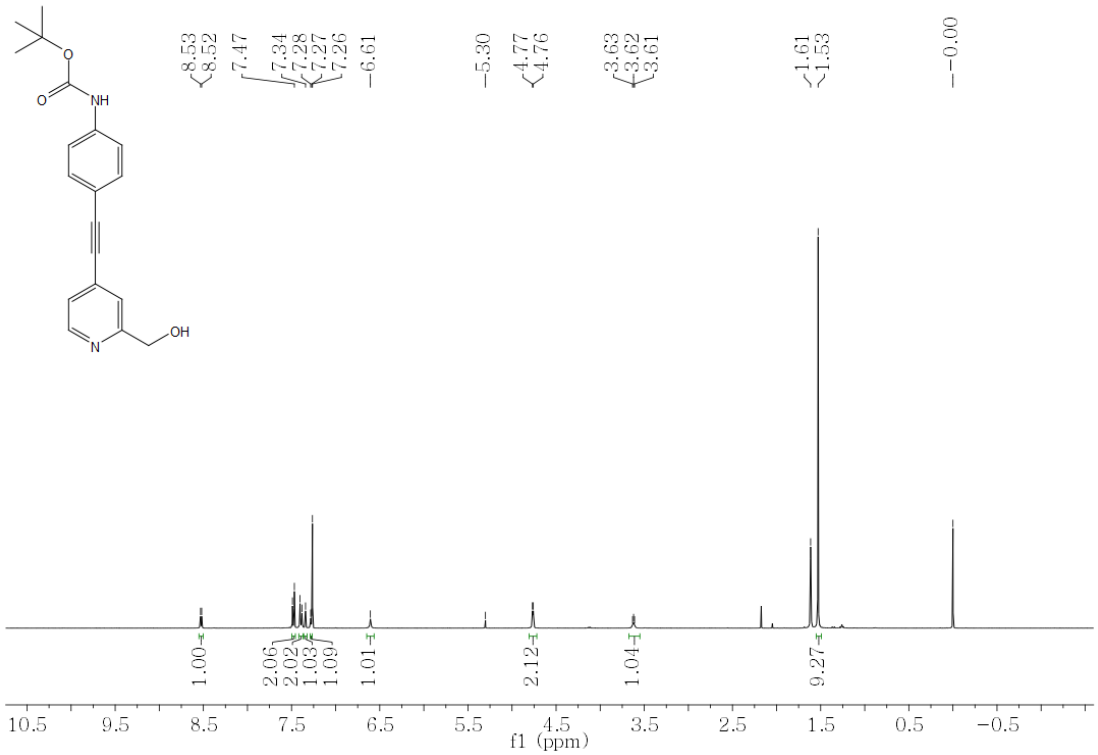

*Figure 7.15. [1]H NMR of compound **2-8**.*

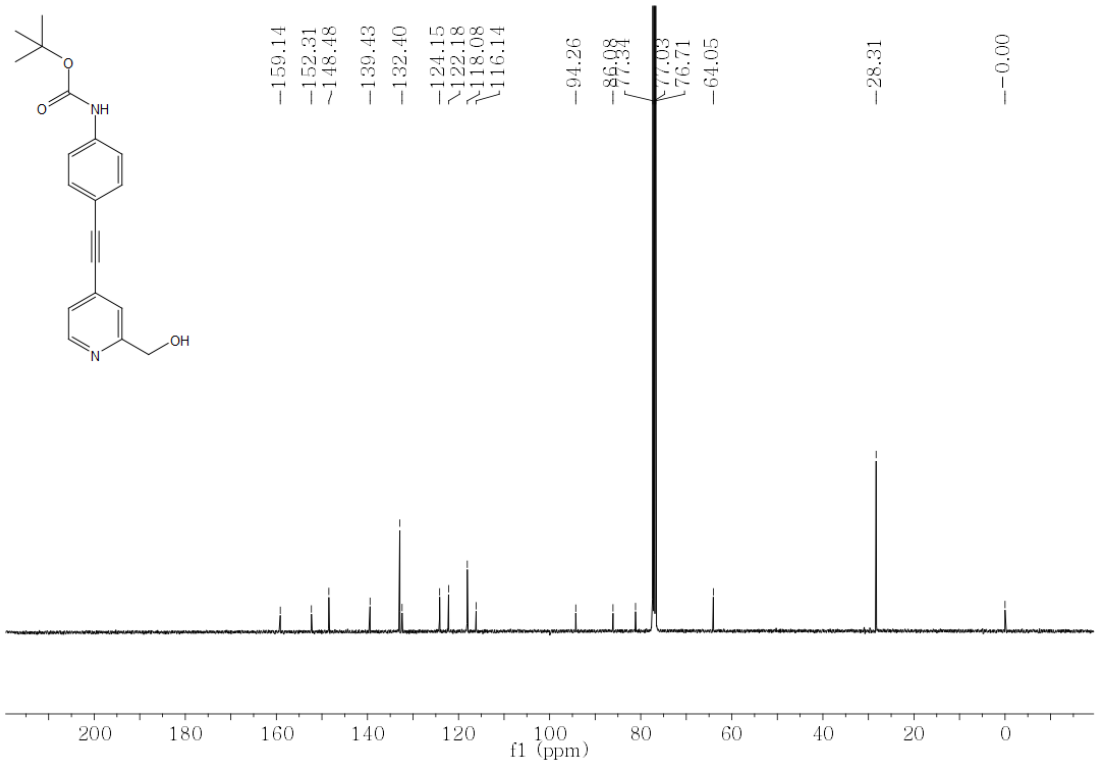

*Figure 7.16. [13]C NMR of compound **2-8**.*

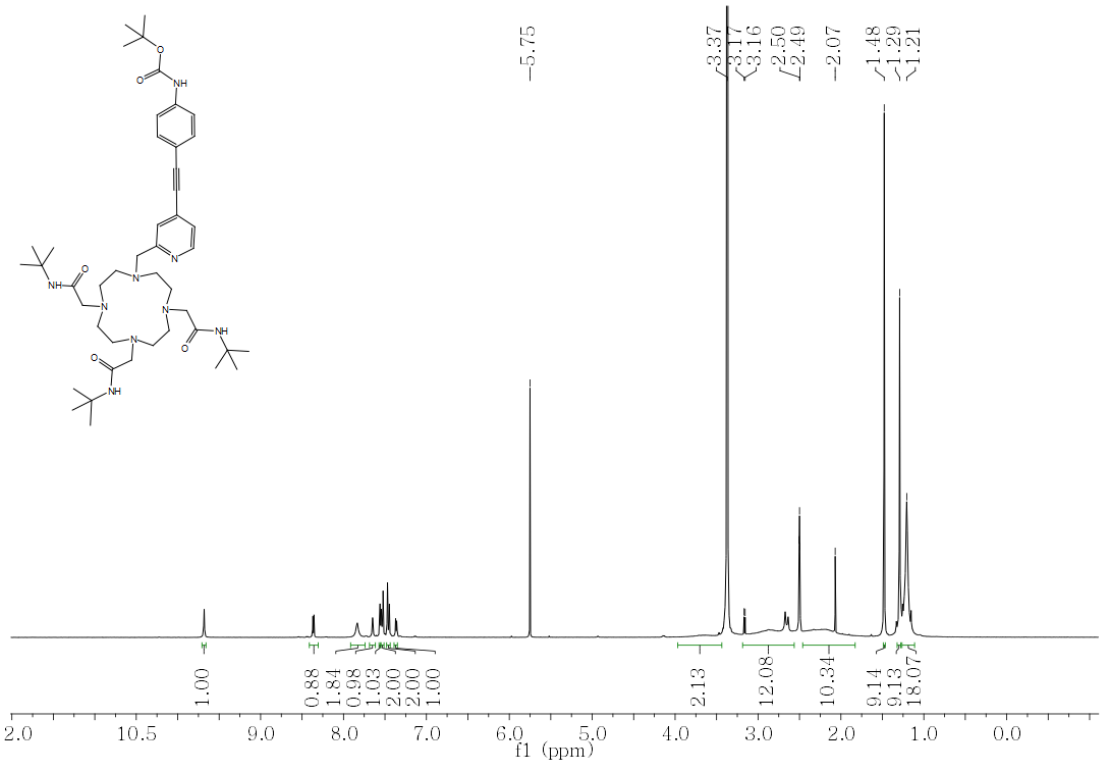

*Figure 7.17. [1]H NMR of compound **2-9**.*

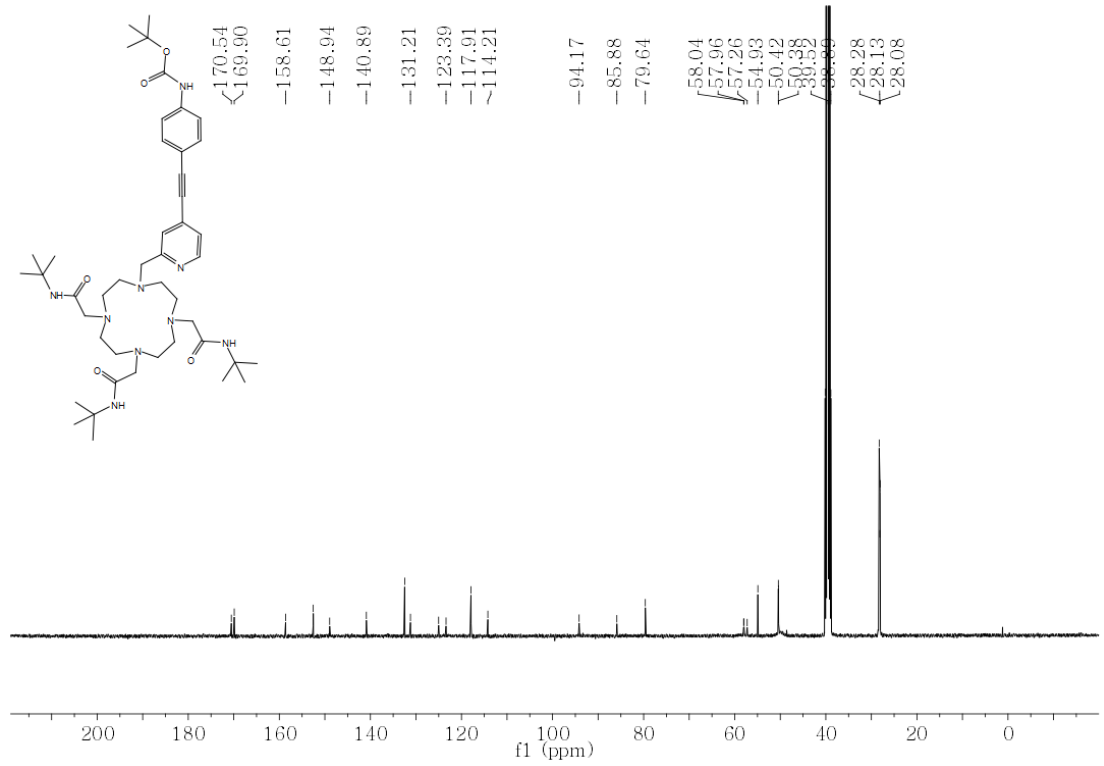

*Figure 7.18. [13]C NMR of compound **2-9**.*

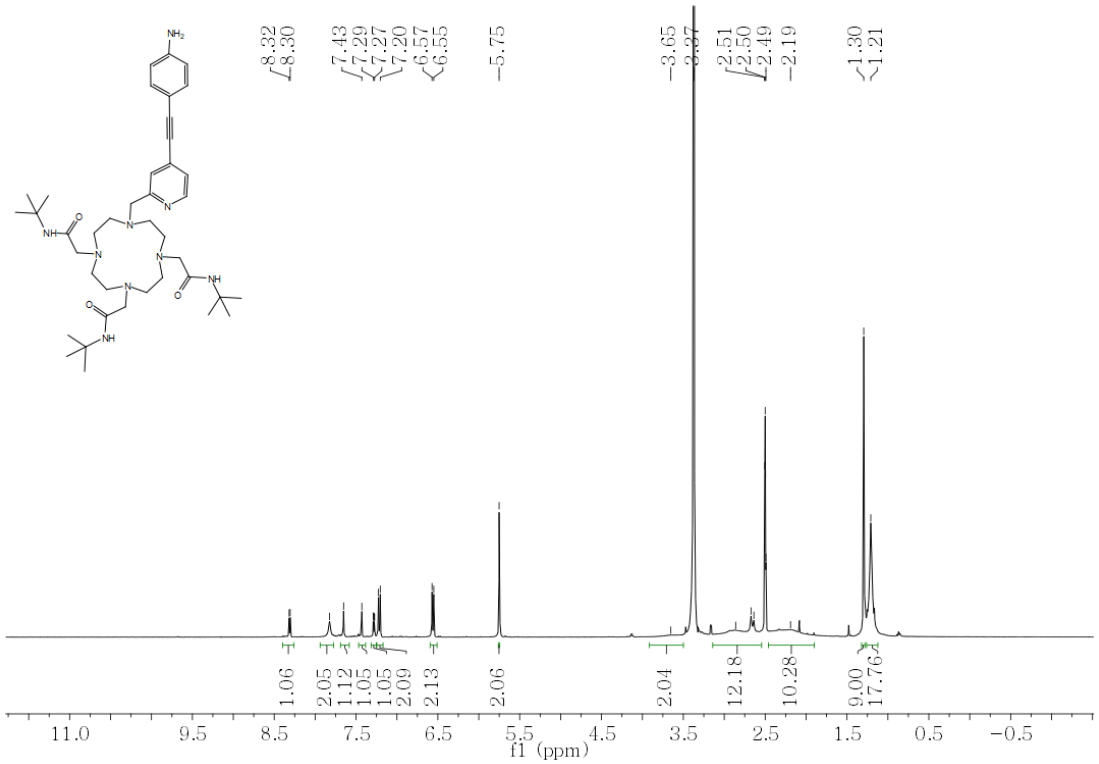

*Figure 7.19. [1]H NMR of compound **2-10**.*

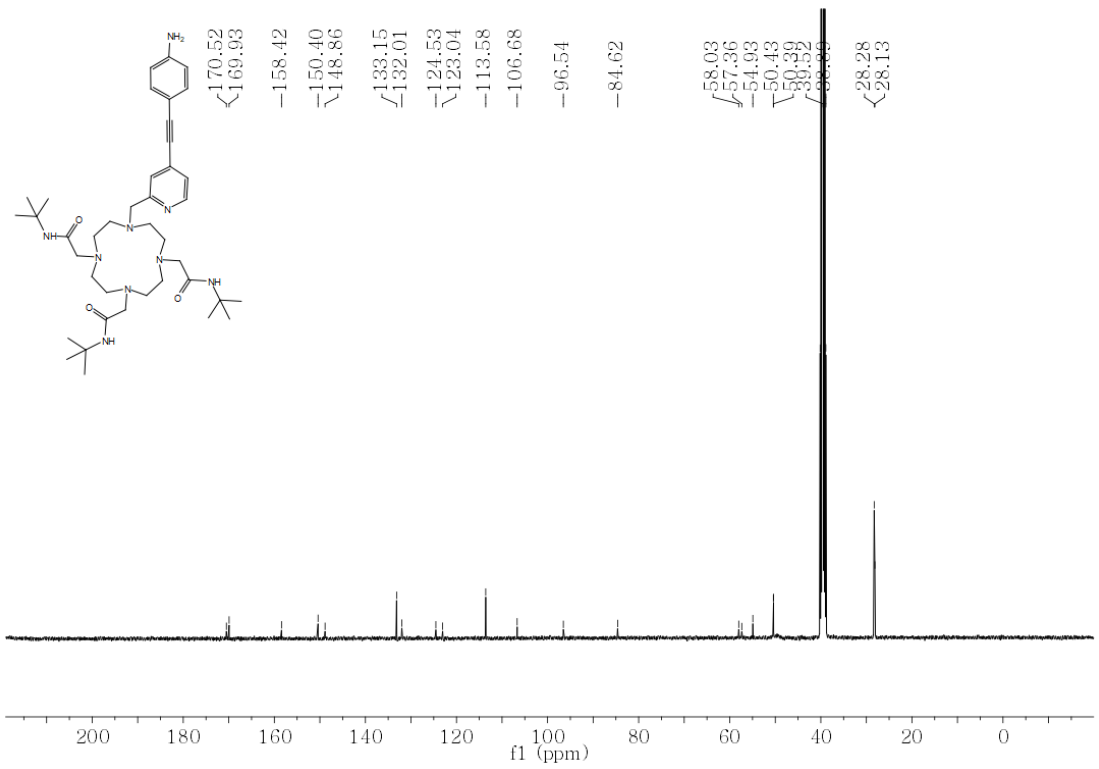

*Figure 7.20. [13]C NMR of compound **2-10**.*

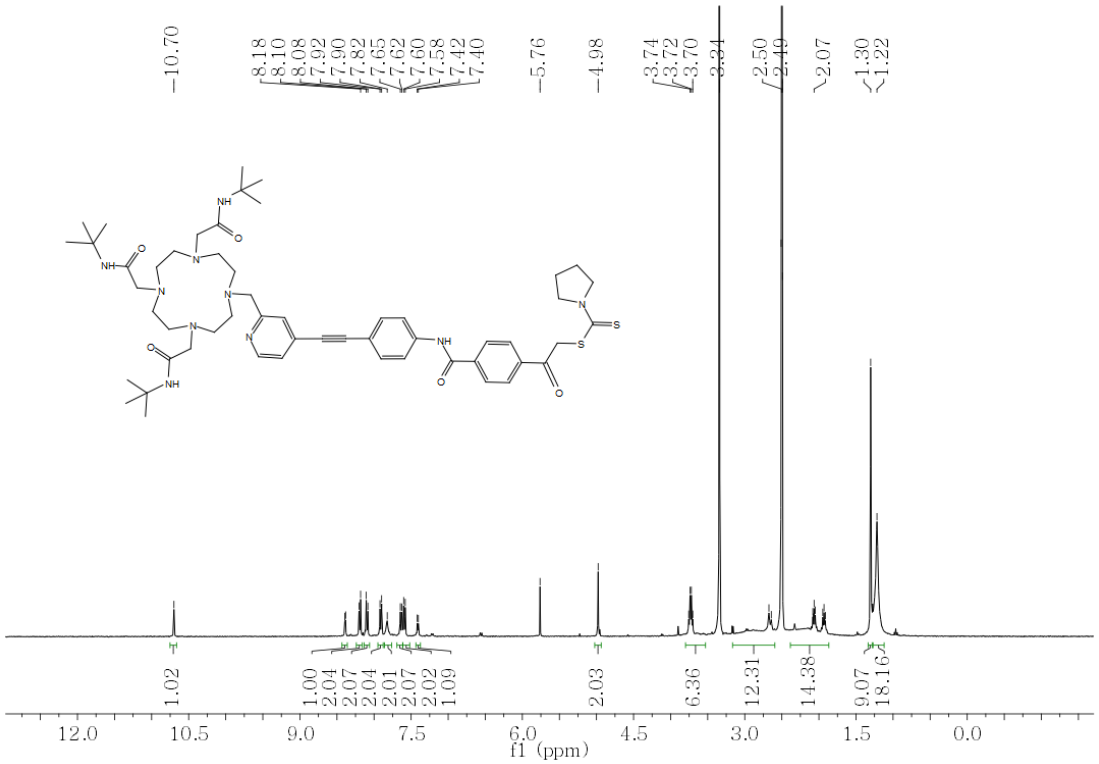

Figure 7.21. ^{1}*H NMR of compound* ***2-11***.

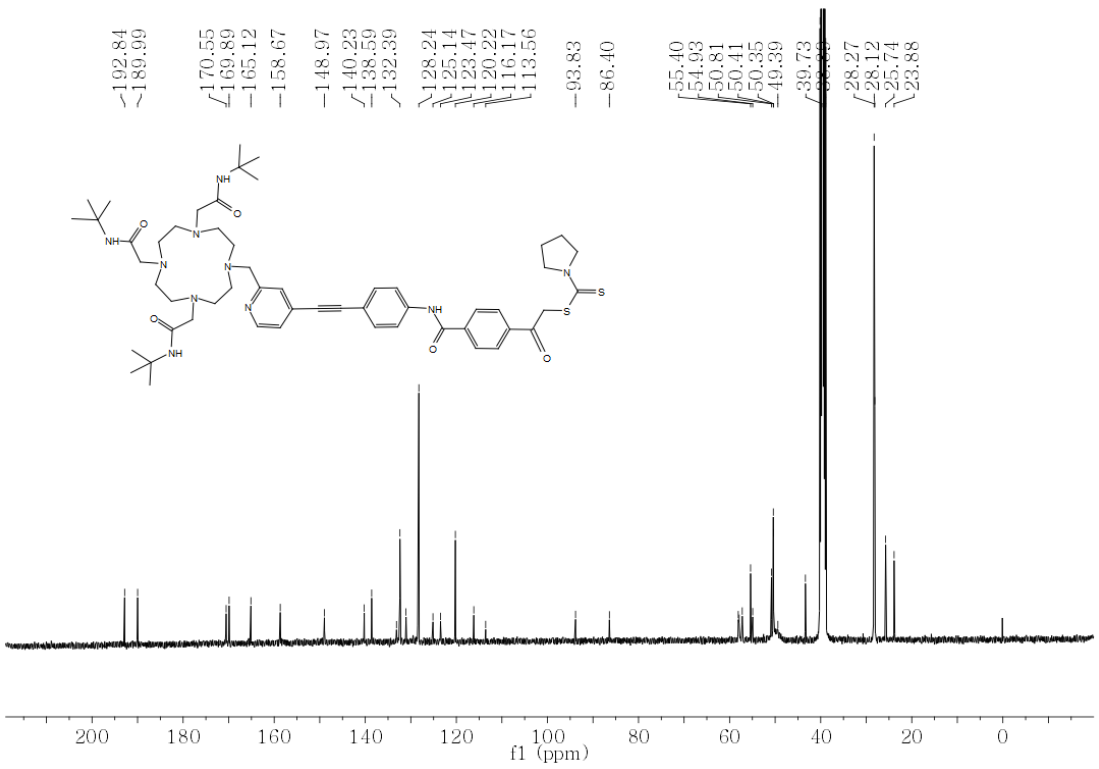

Figure 7.22. ^{13}*C NMR of compound* ***2-11***.

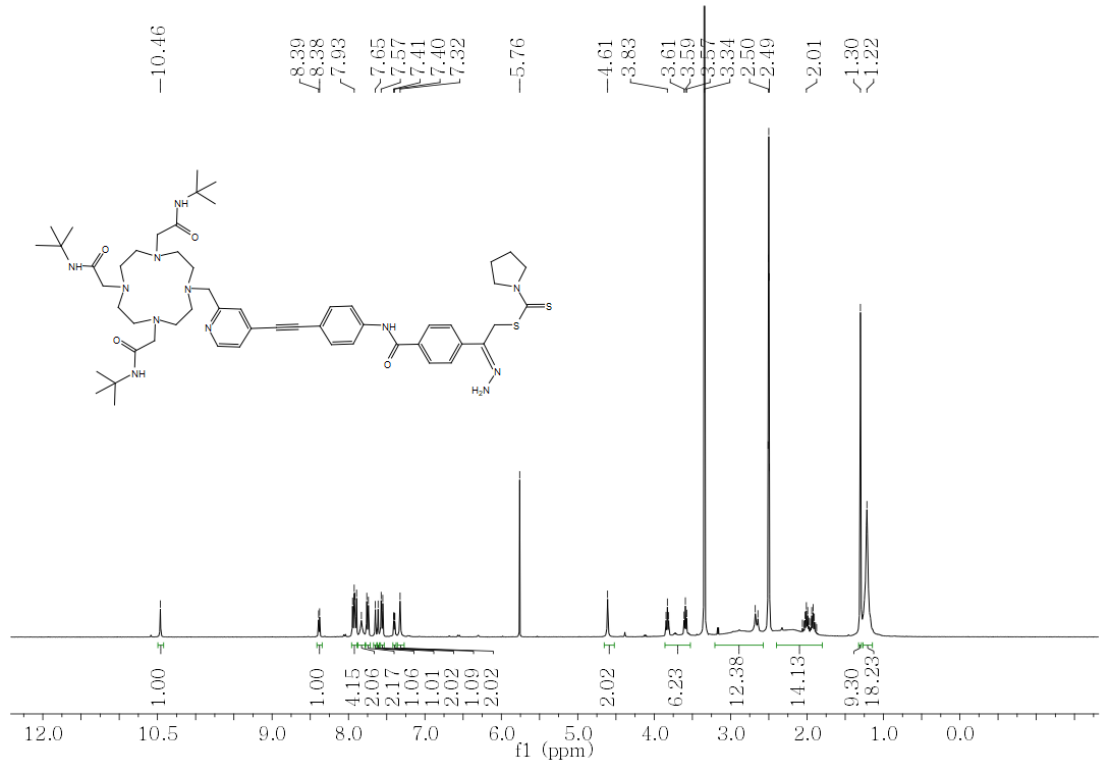

*Figure 7.23. ^{1}H NMR of compound **2-12***

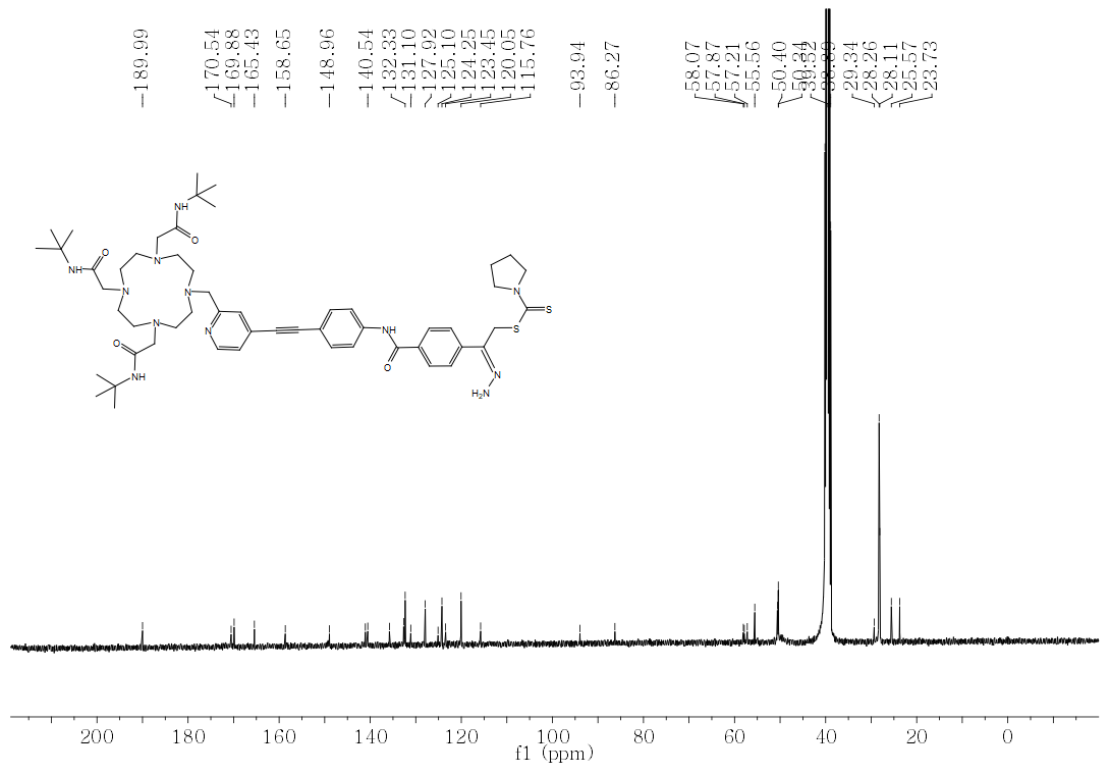

*Figure 7.24. ^{13}C NMR of compound **2-12***

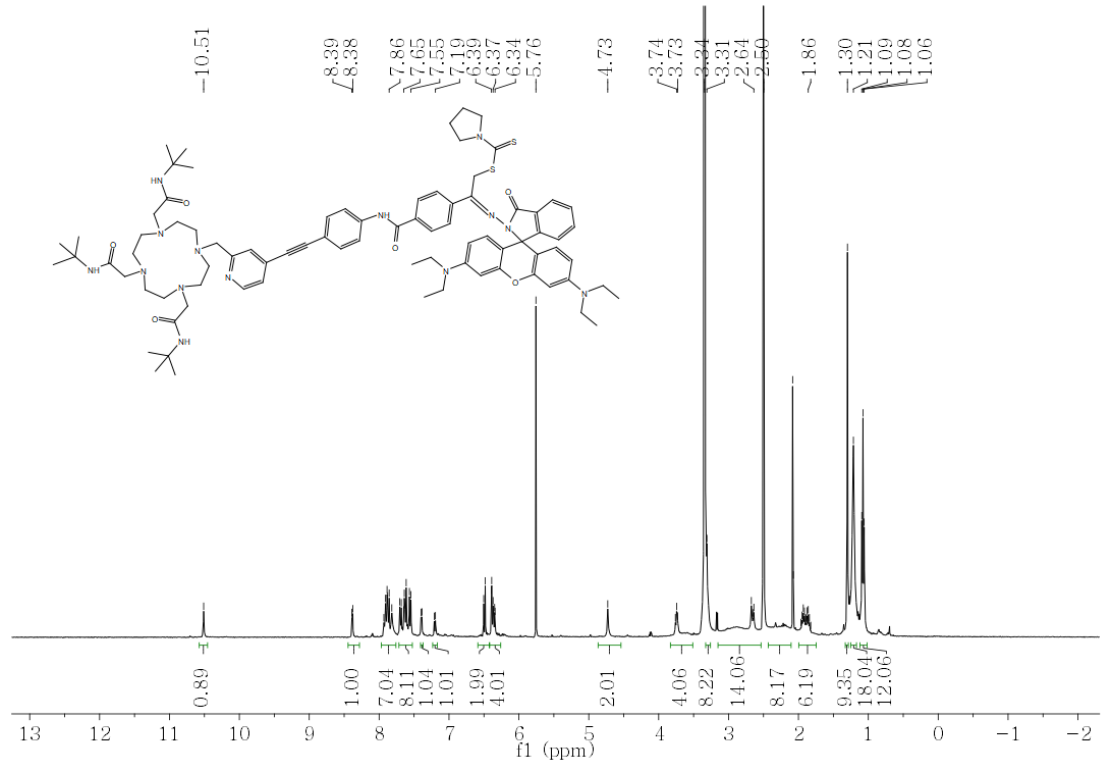

*Figure 7.25. [1]H NMR of **2-13 GB001.***

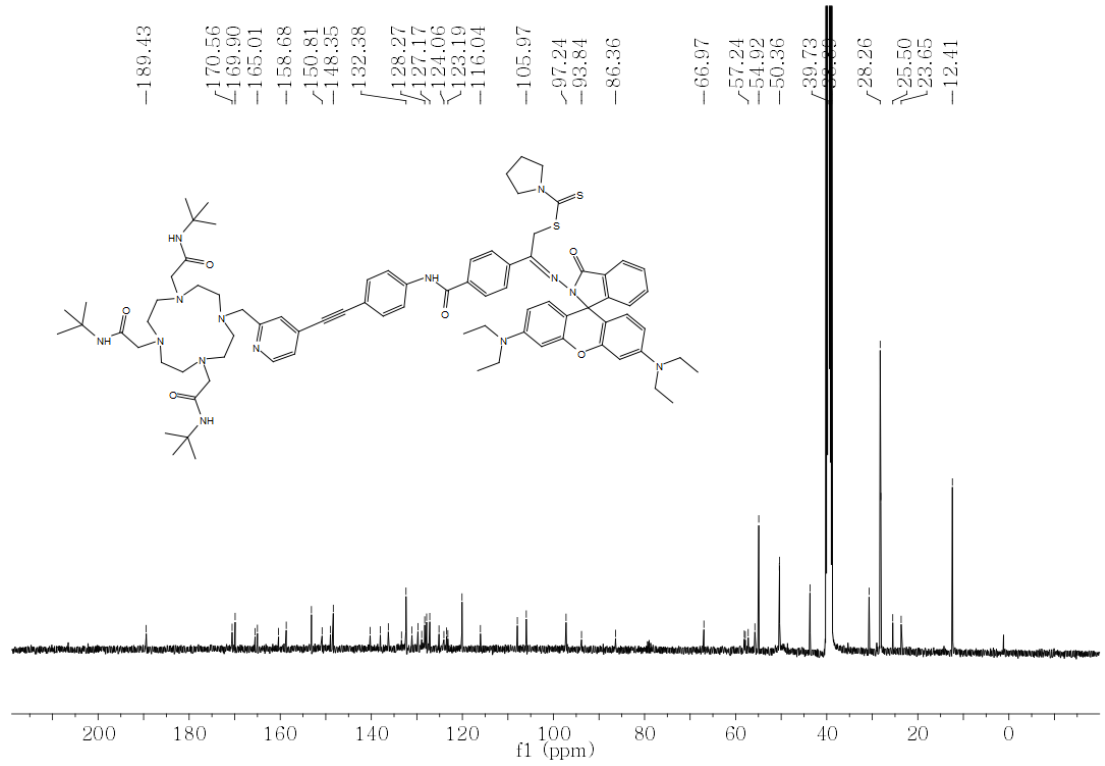

*Figure 7.26. [13]C NMRof **2-13 GB001***

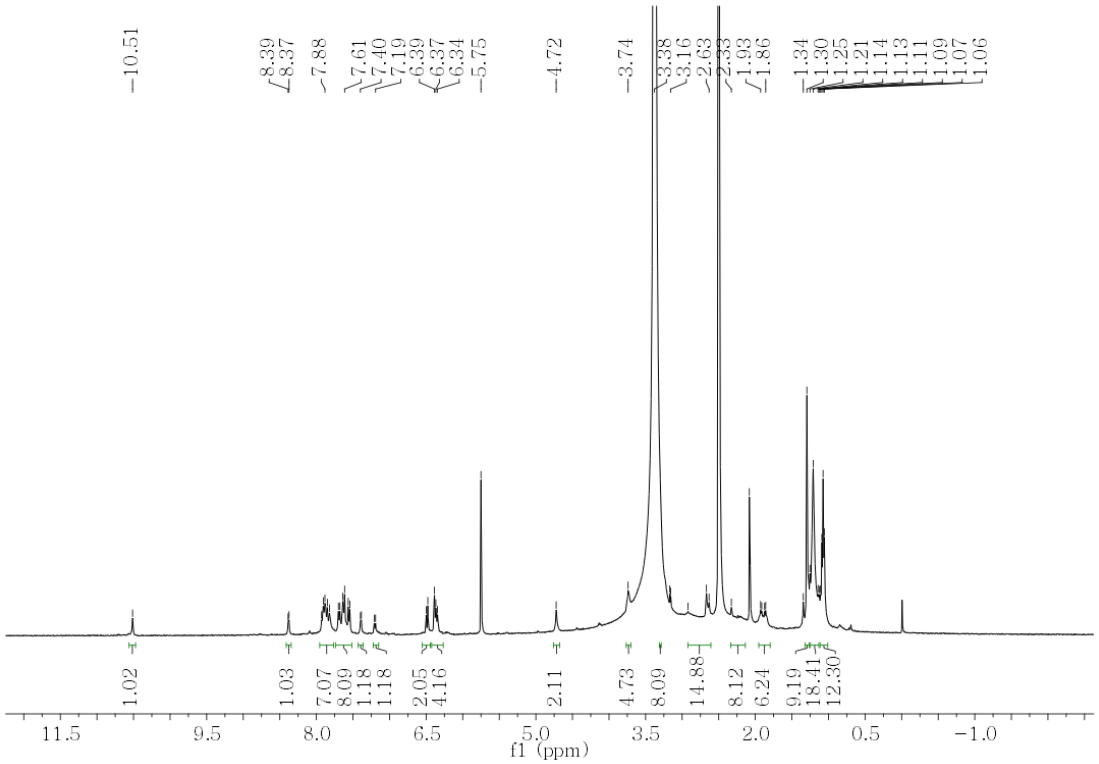

*Figure 7.27. [1]H NMR of compound **2-15**.*

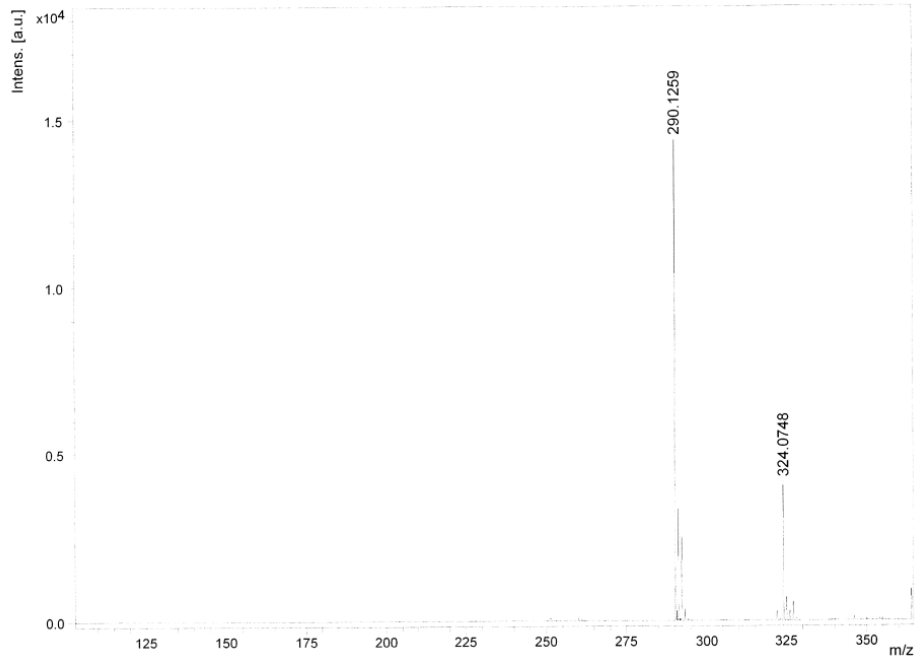

*Figure 7.28. MS of compound **2-2**.*

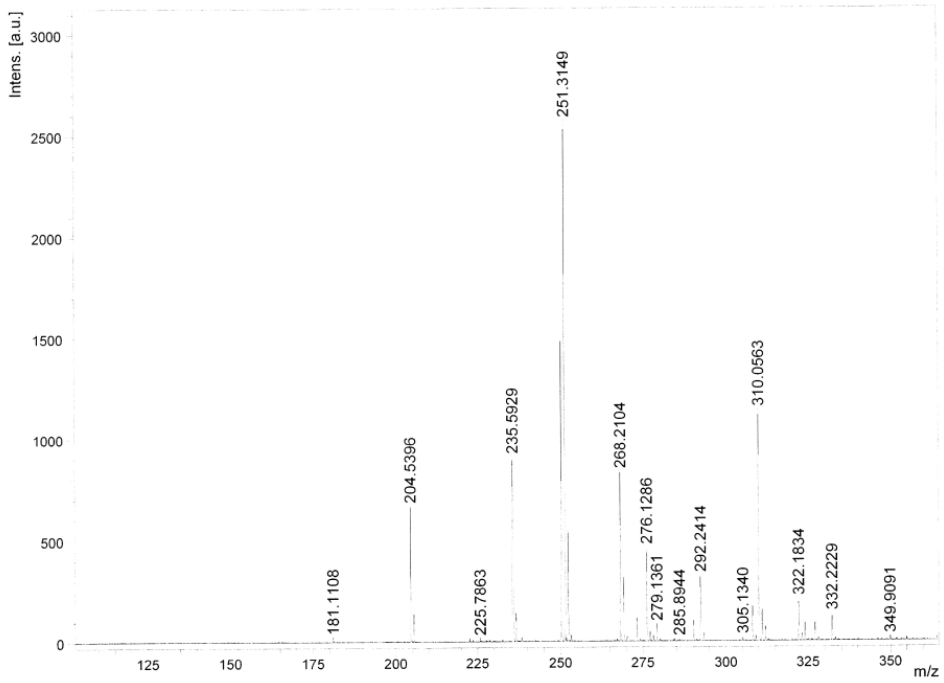

*Figure 7.29. MS of of compound **2-3**.*

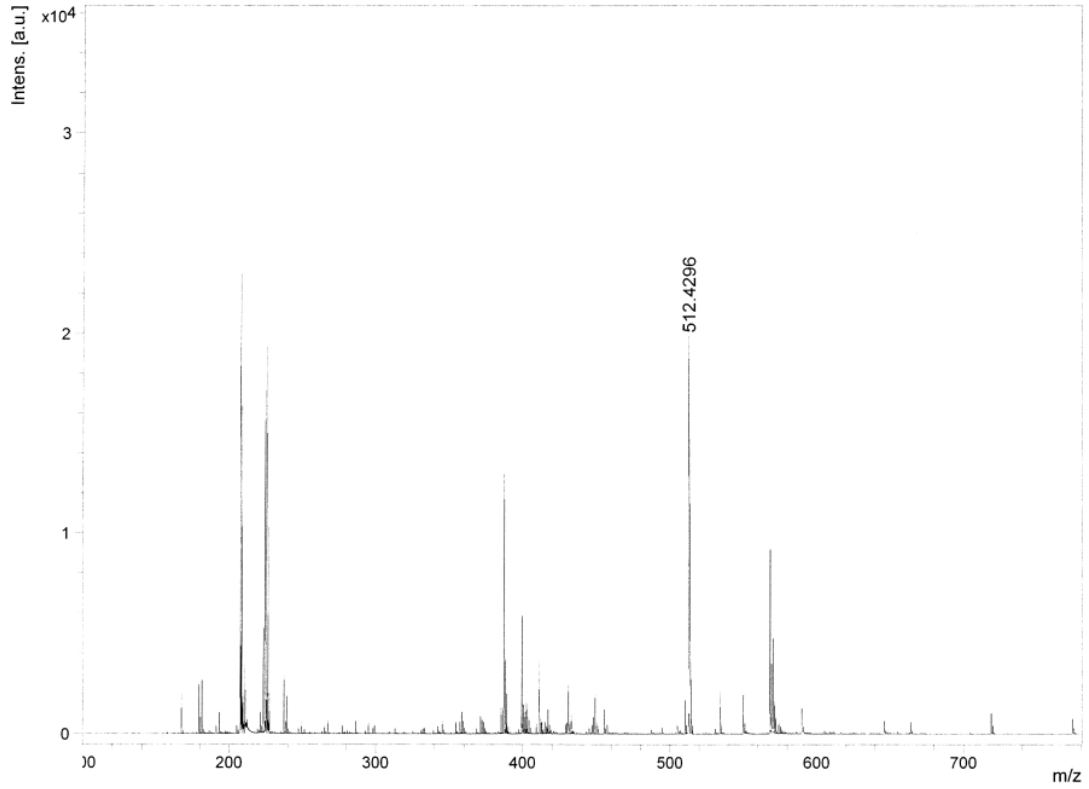

*Figure 7.30. MS of compound **2-5**.*

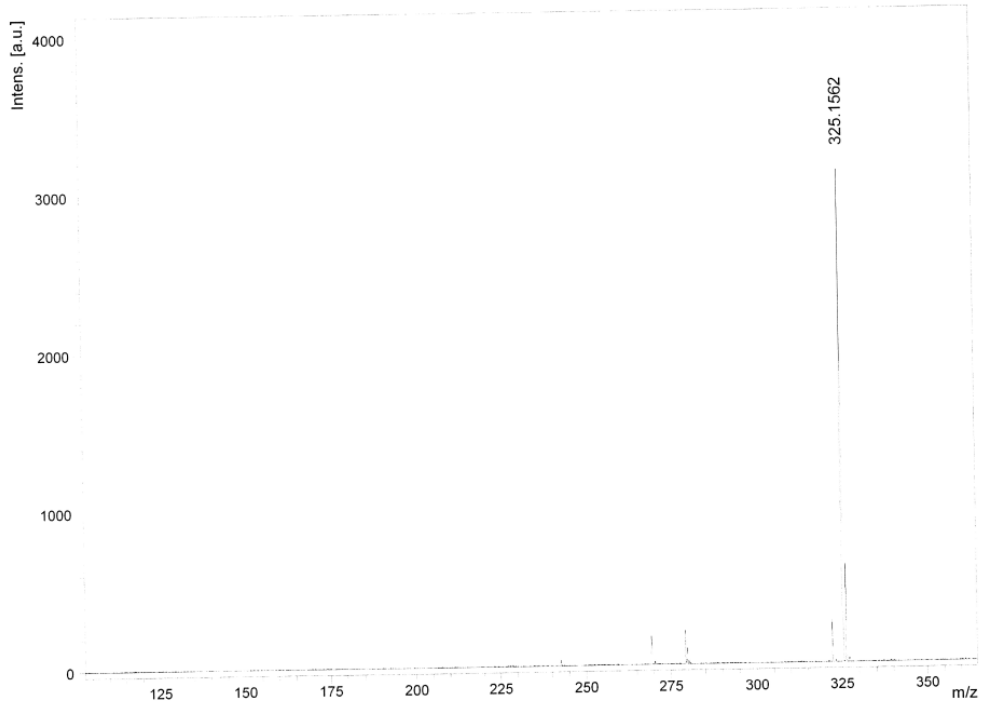

*Figure 7.31. MS of of compound **2-8**.*

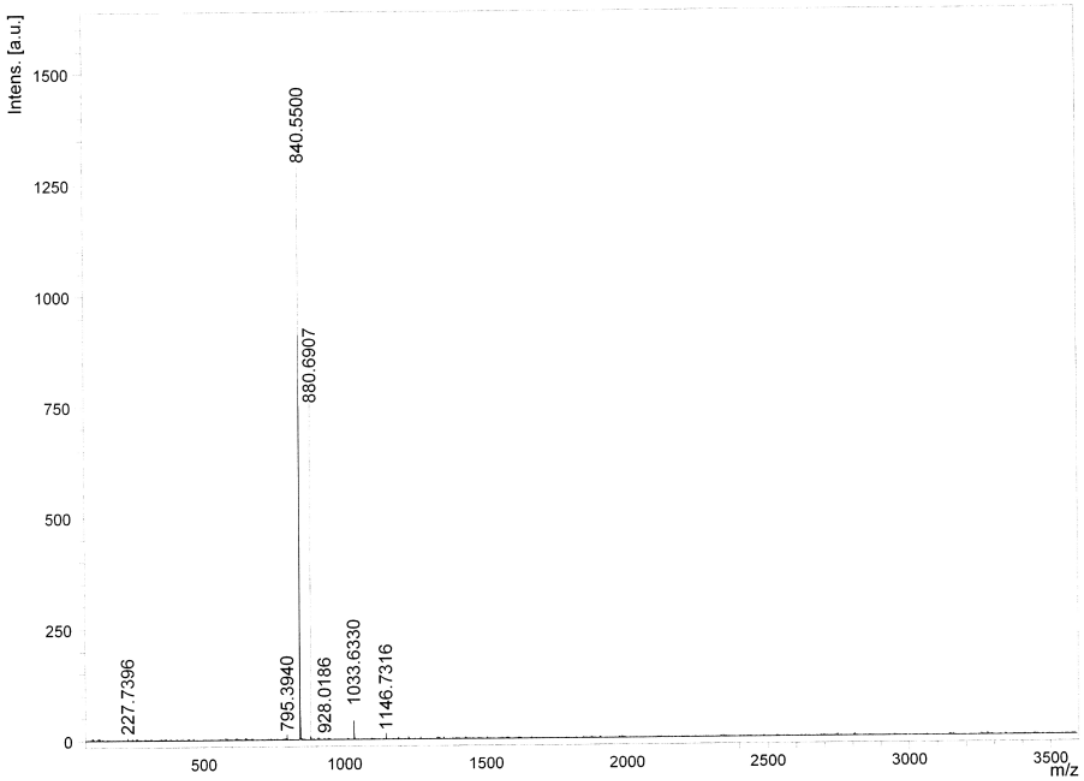

*Figure 7.32. MS of of compound **2-9**.*

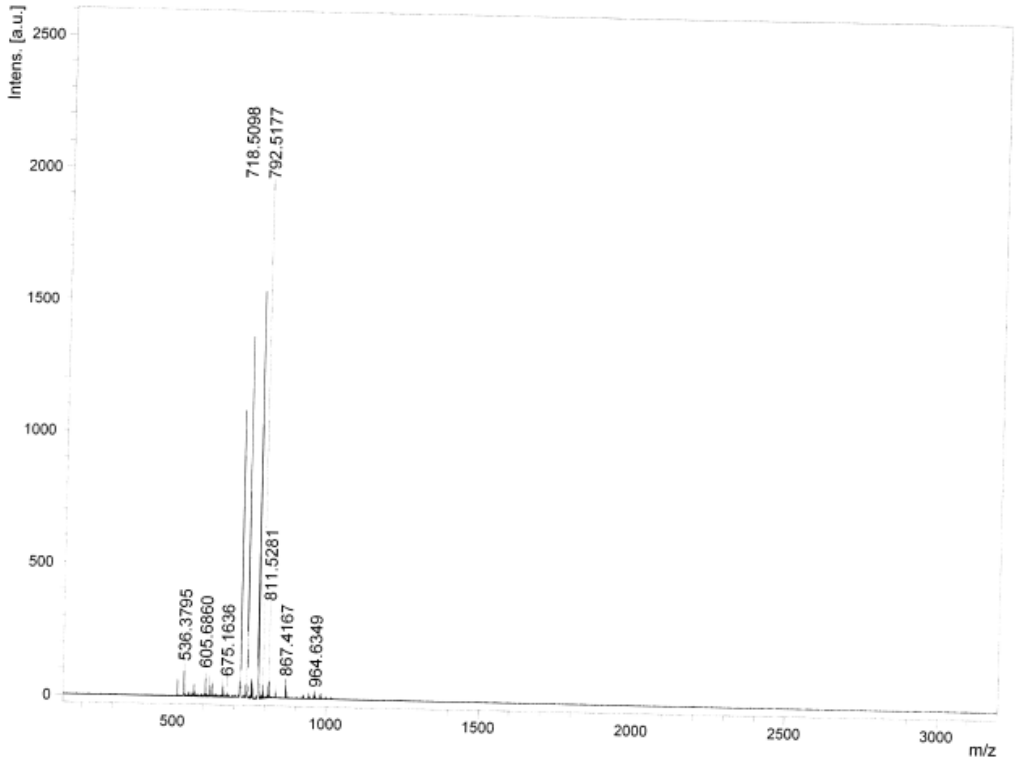

*Figure 7.33. MS of compound **2-10**.*

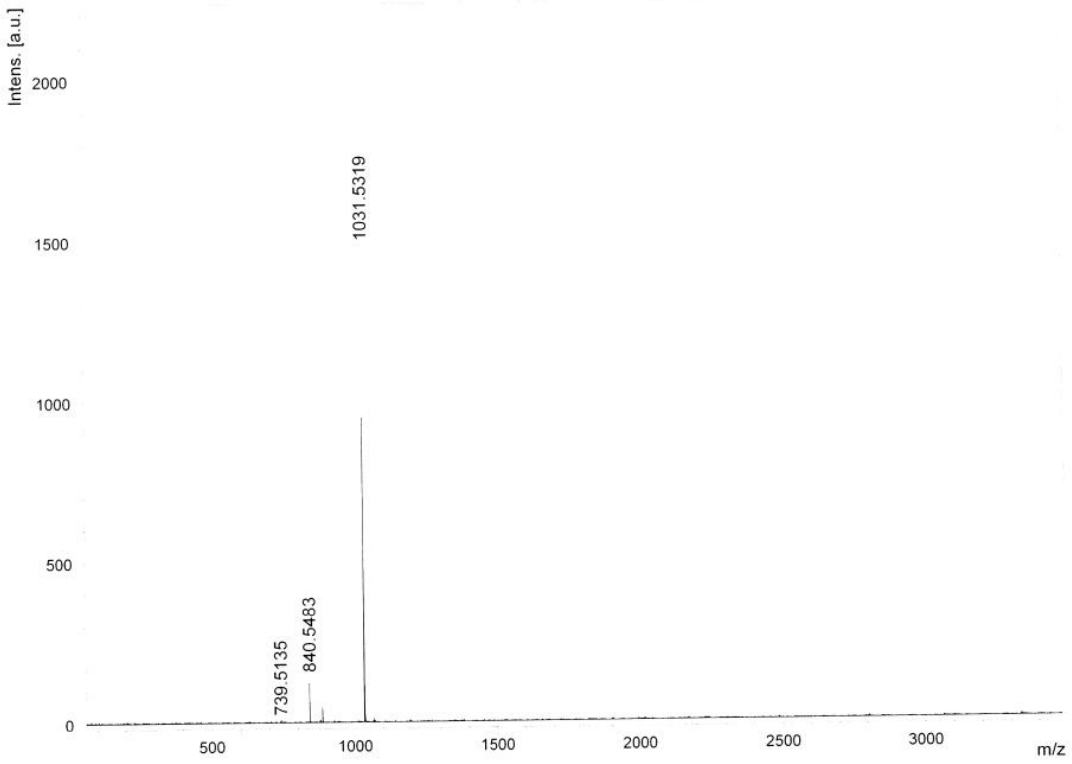

*Figure 7.34. MS of compound **2-11**.*

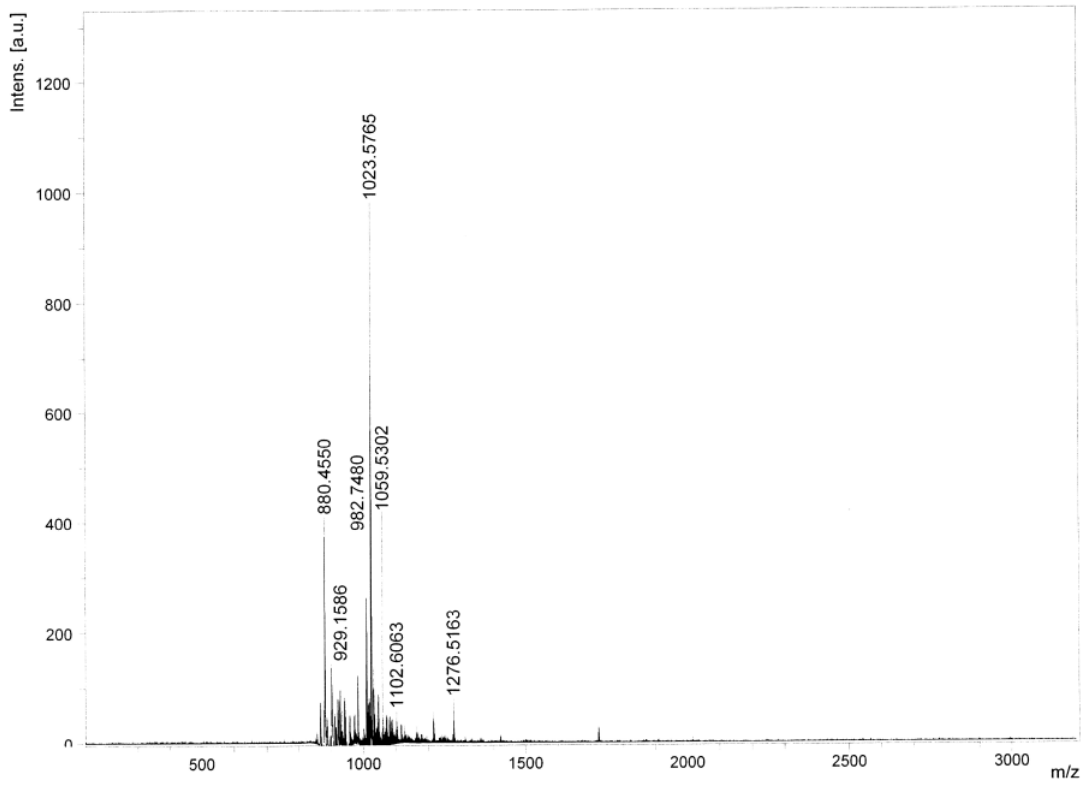

Figure 7.35. MS of compound ***2-12***

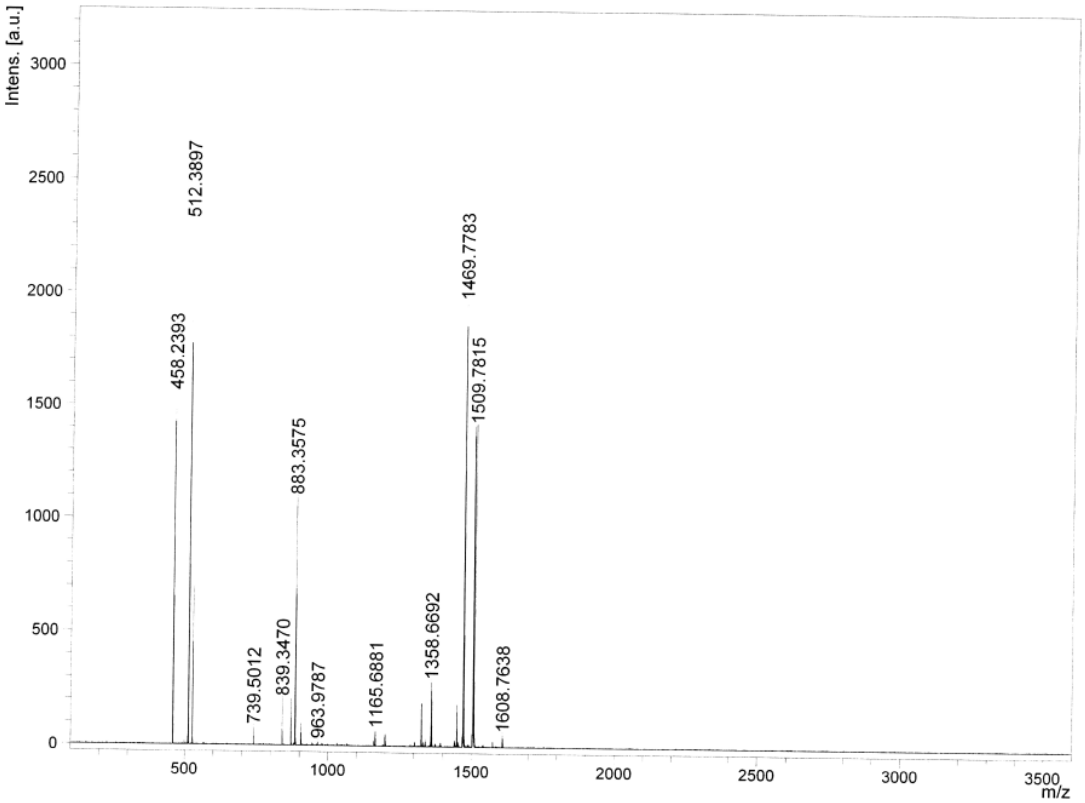

Figure 7.36. MS of ***GB001(2-13).***

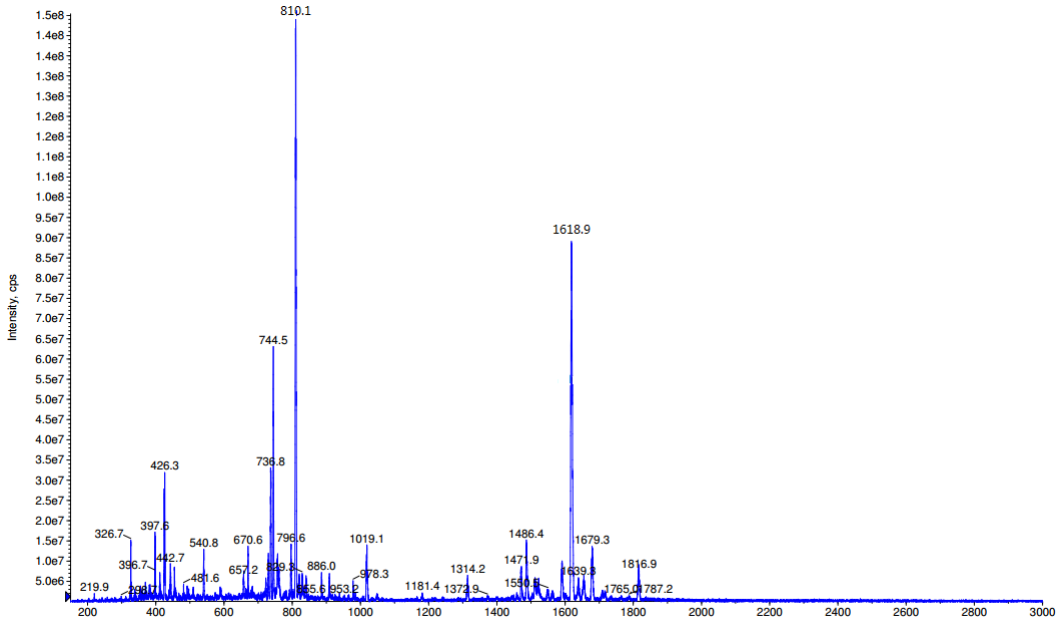

Figure 7.37. MS of complex GBYb001 ***2-14a (GBYb001)****.*

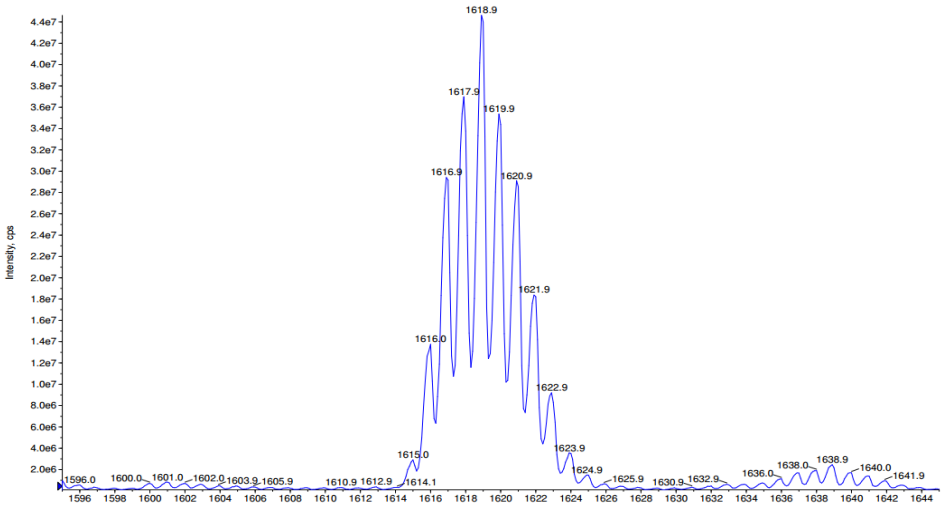

Figure 7.38. Isotope ratio of complex GBYb001 ***2-14a (GBYb001)****.*

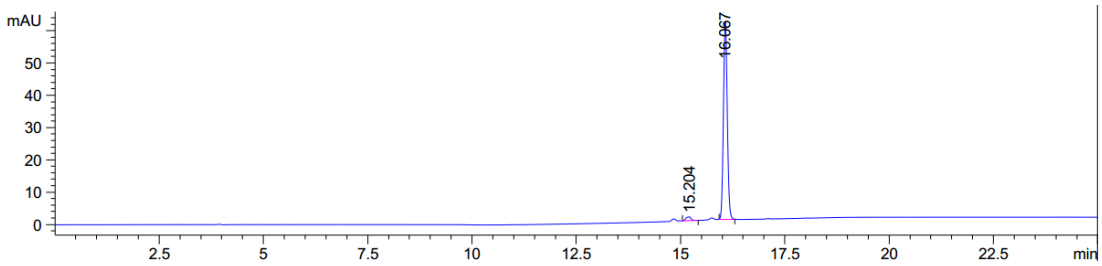

Figure 7.39. HPLC chromatogram of ***GBYb001****.*

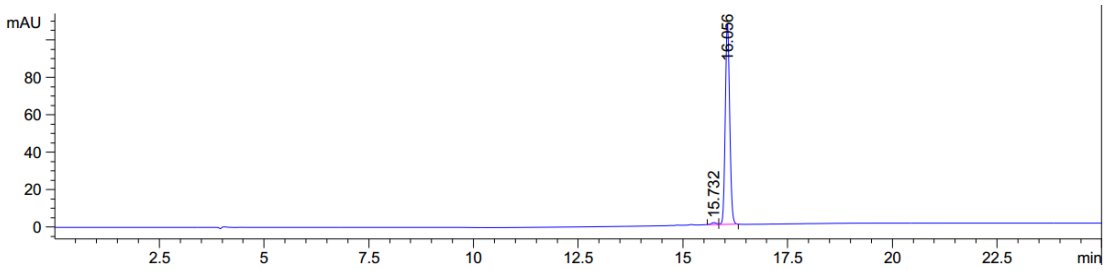

*Figure 7.40. HPLC chromatogram of **GBLa001**.*

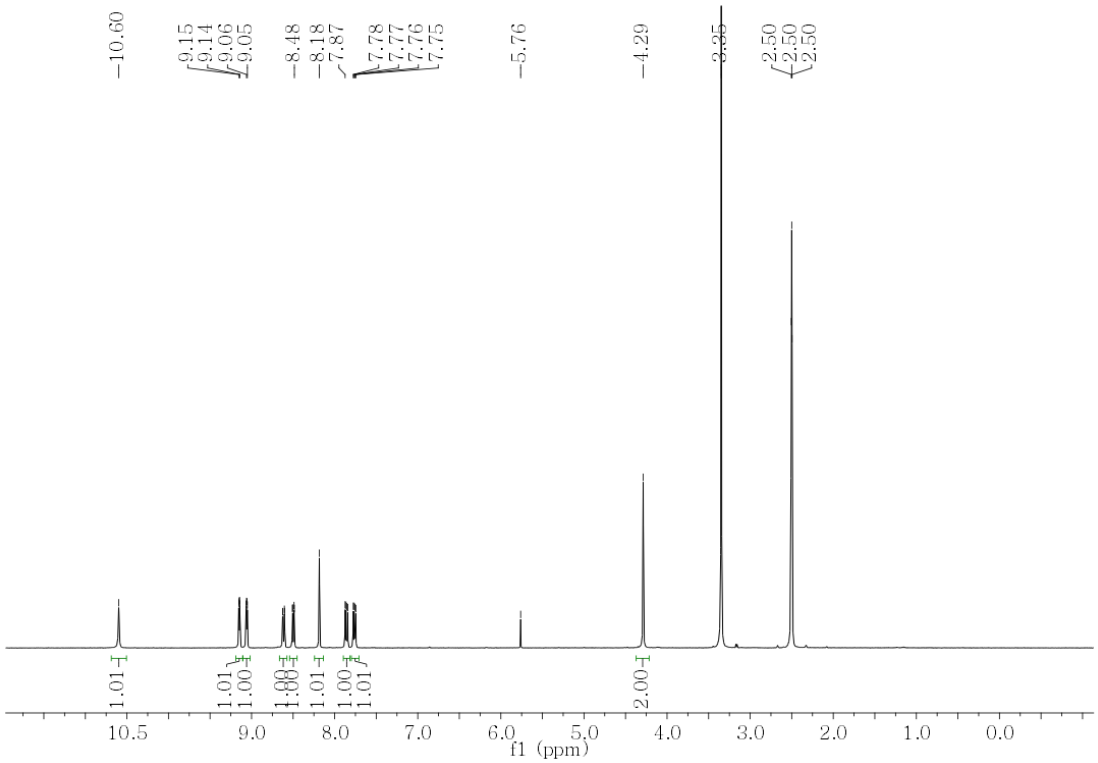

*Figure 7.41. ^{1}H NMR spectrum of compound **3-1.***

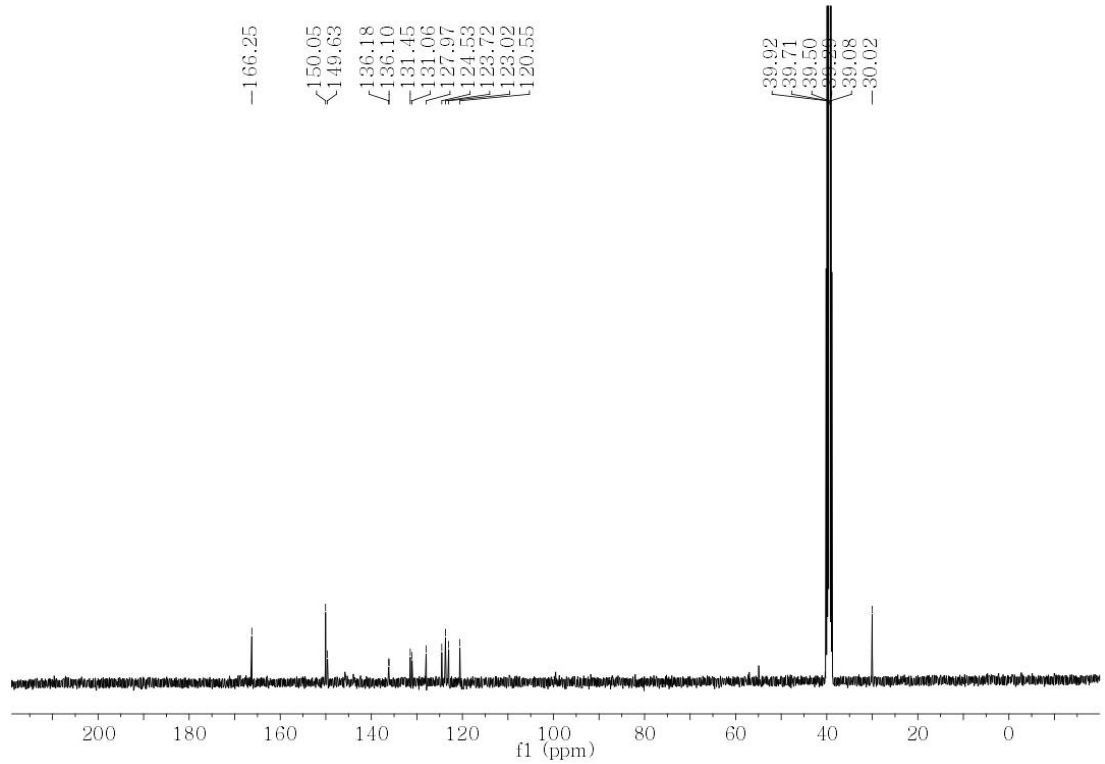

*Figure 7.42. ^{13}C NMR spectrum of compound **3-1**.*

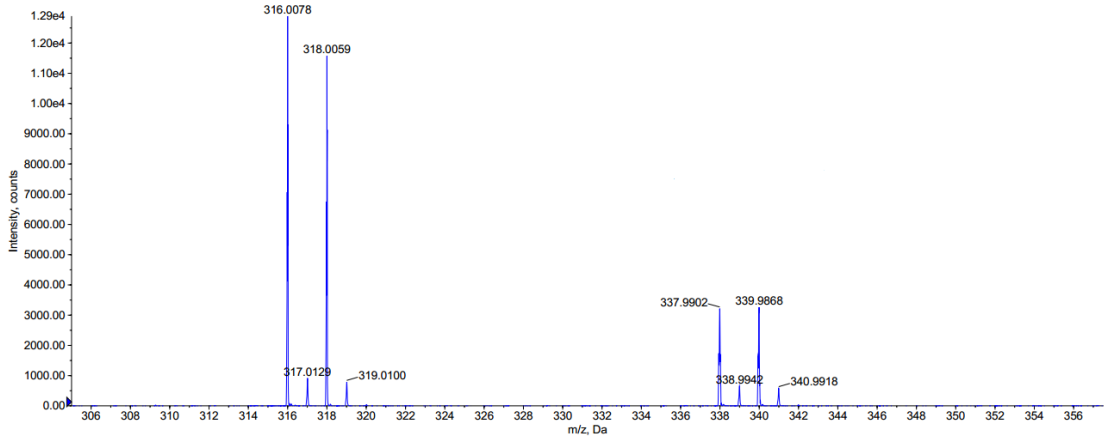

*Figure 7.43. MS of compound **3-1**.*

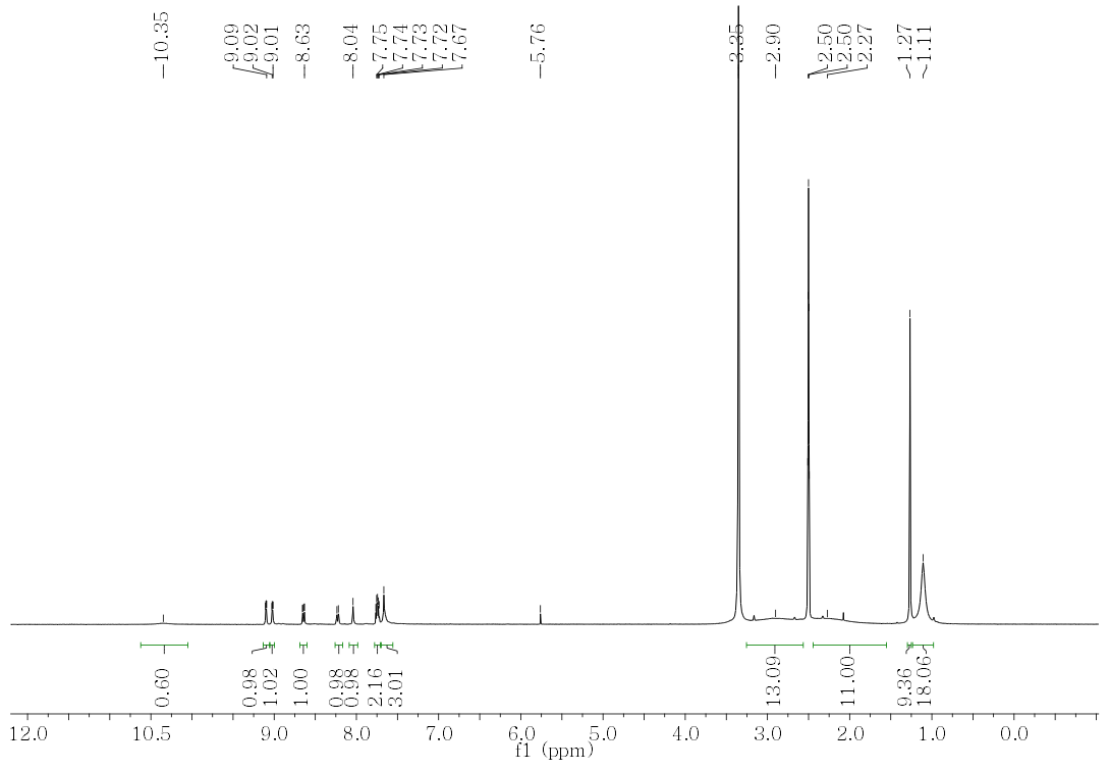

*Figure 7.44. [1]H NMR Spectrum of compound **3-2**.*

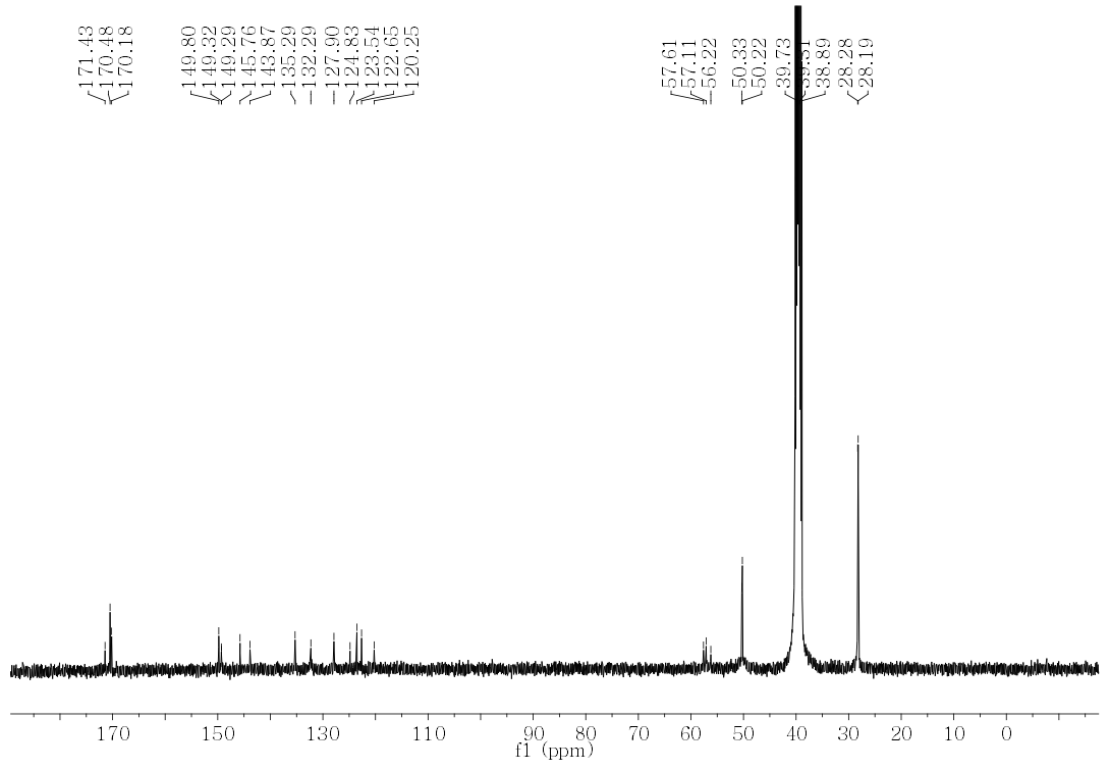

*Figure 7.45. [13]C NMR spectrum of compound **3-2**.*

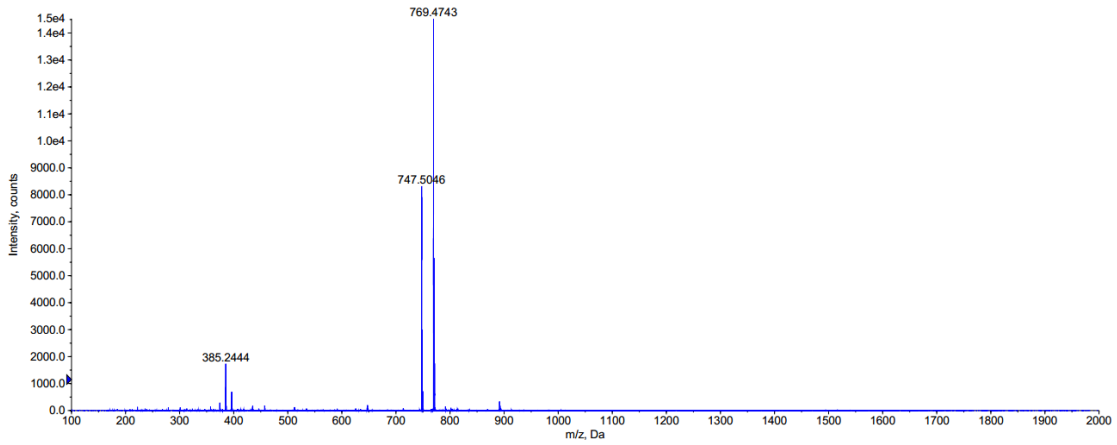

*Figure 7.46. MS of compound **3-2**.*

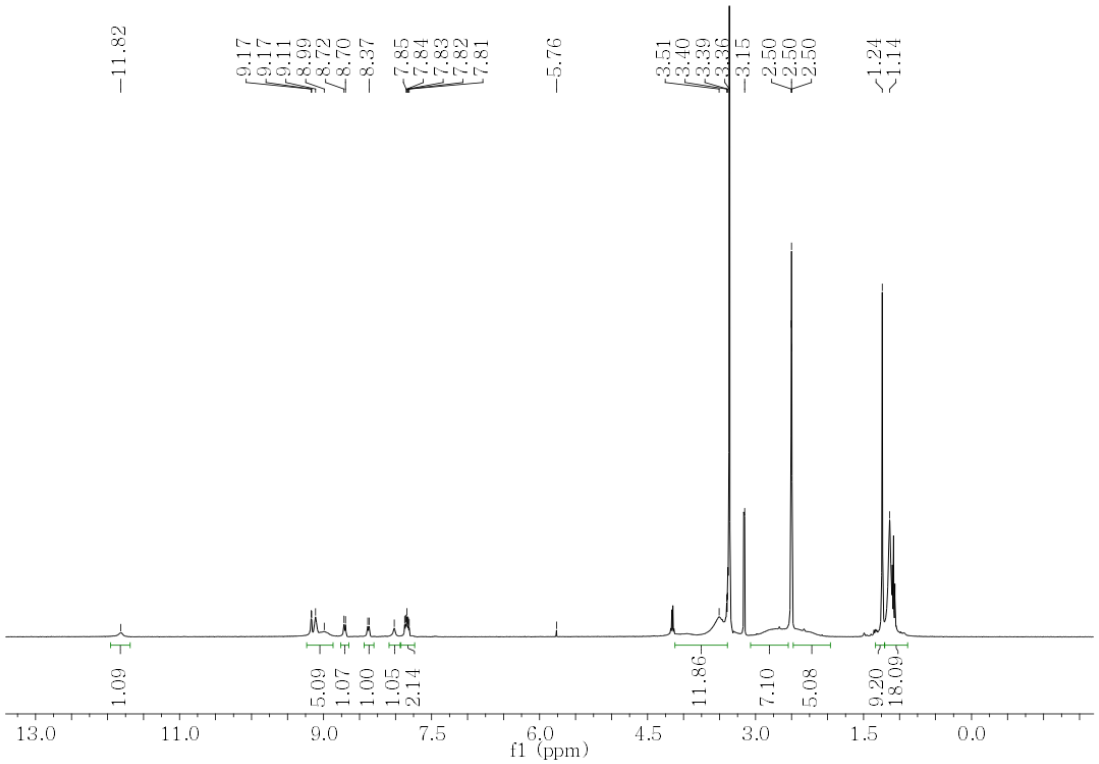

*Figure 7.47. ^{1}H NMR spectrum of **3-3a**.*

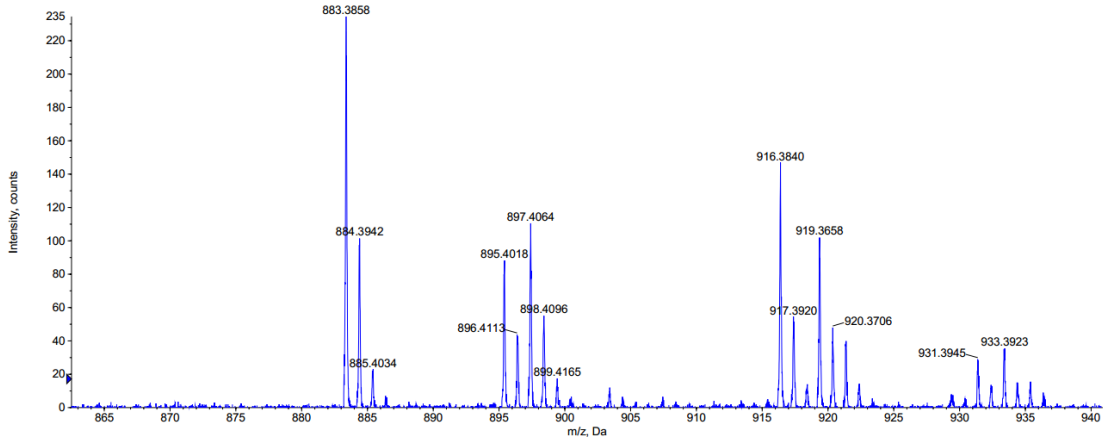

*Figure 7.48. MS of **3-3a***

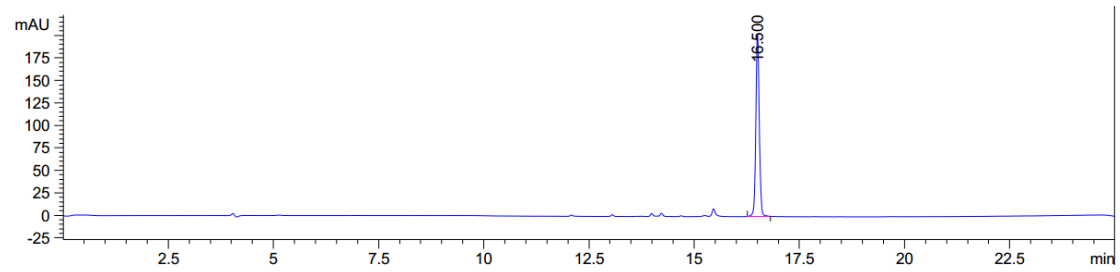

*Figure 7.49. HPLC chromatogram of **3-3a**.*

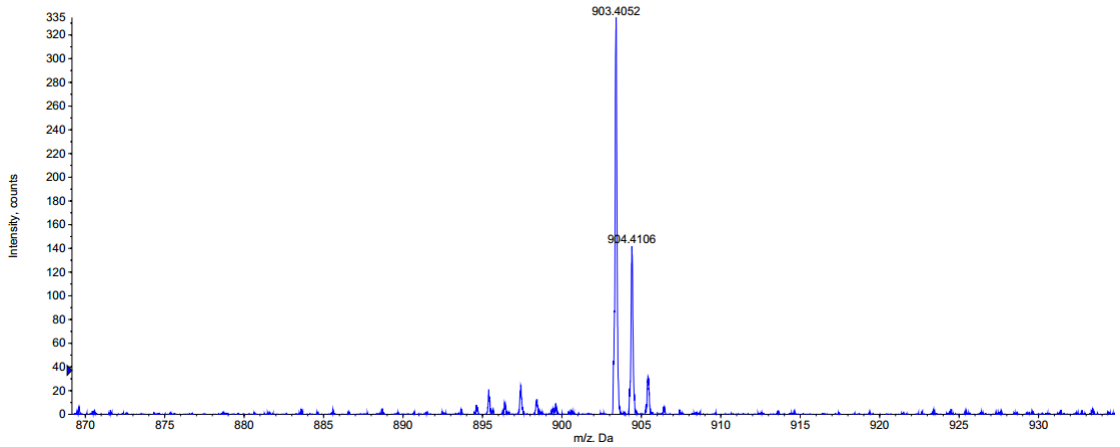

*Figure 7.49. MS of **3-3b**.*

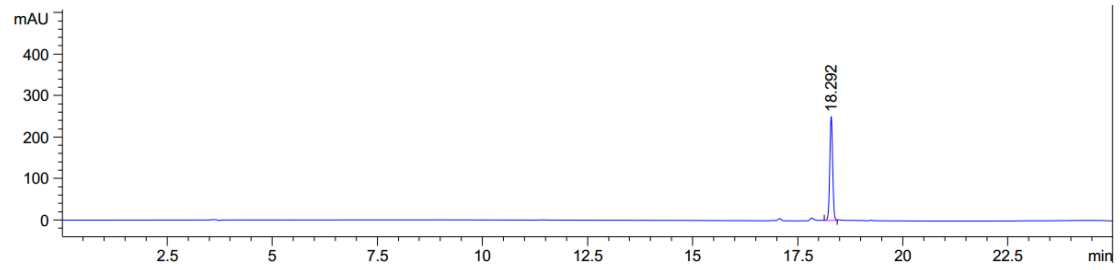

*Figure 7.50. HPLC chromatogram of **3-3b**.*

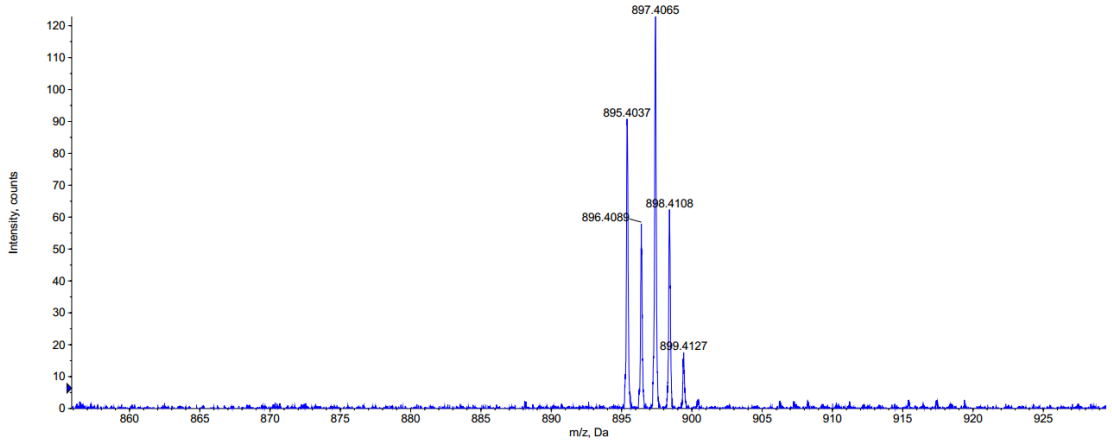

*Figure 7.51. MS of **3-3c**.*

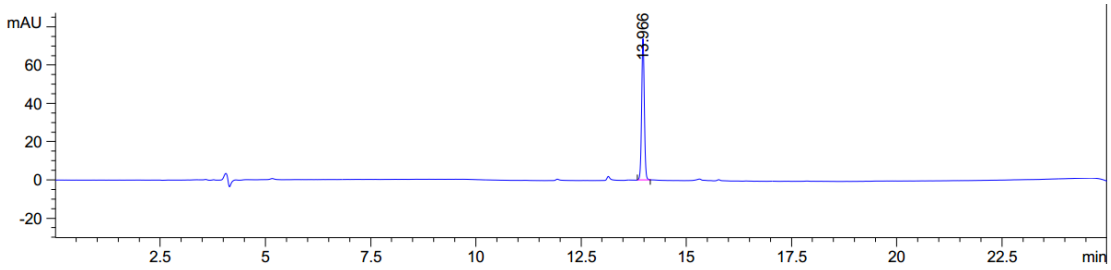

*Figure 7.52. HPLC chromatogram of **3-3c**.*

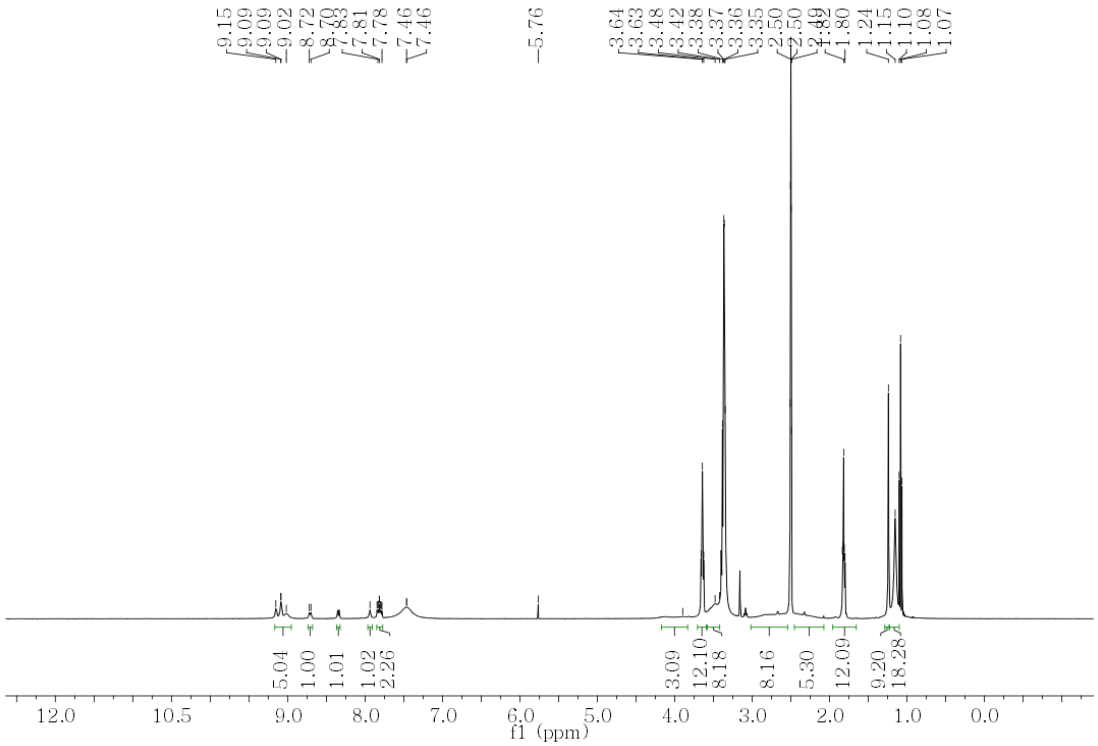

*Figure 7.53. ^{1}H NMR spectrum of **3-4a***

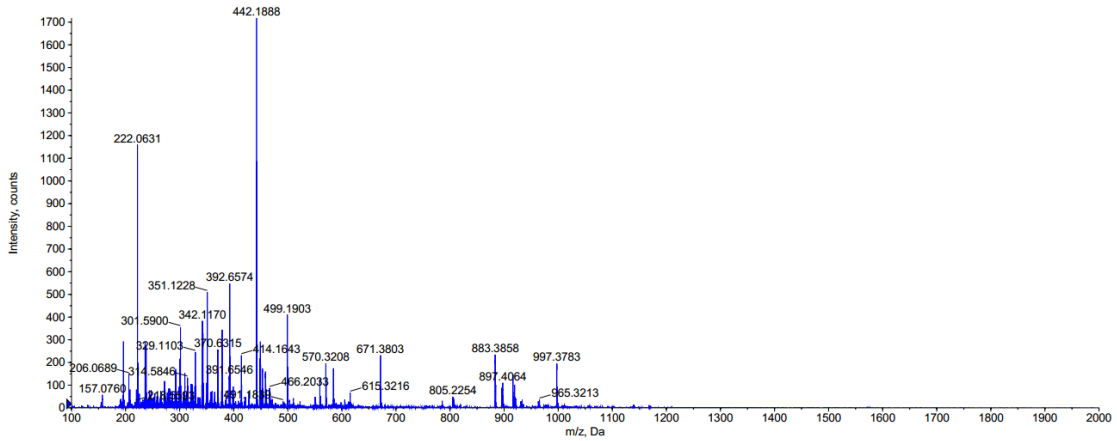

*Figure 7.54. MS of **3-4a**.*

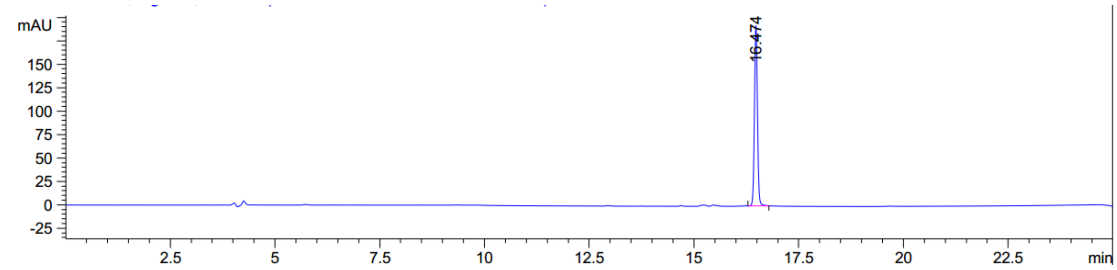

*Figure 7.55. HPLC chromatogram of **3-4a**.*

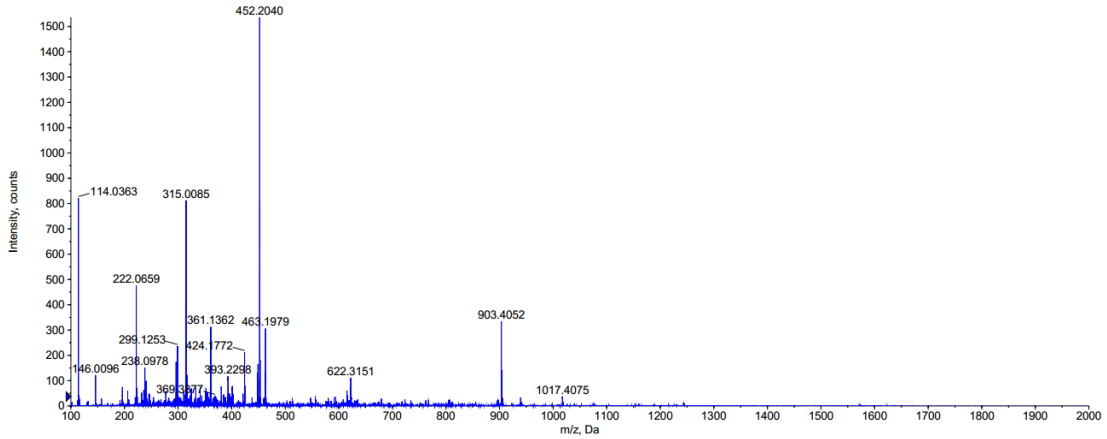

*Figure 7.56. MS of **3-4b**.*

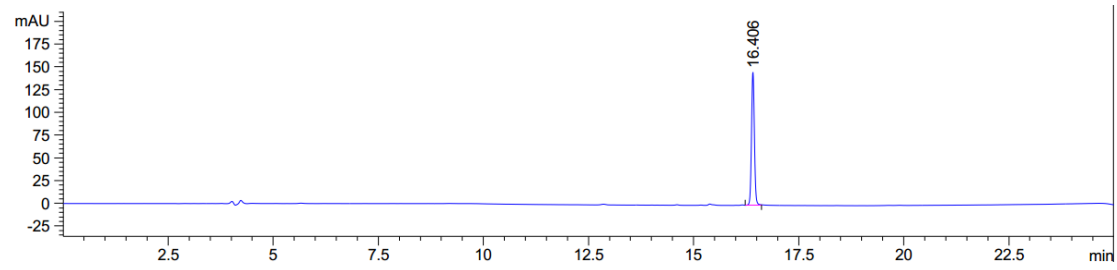

*Figure 7.57. HPLC chromatogram of **3-4b**.*

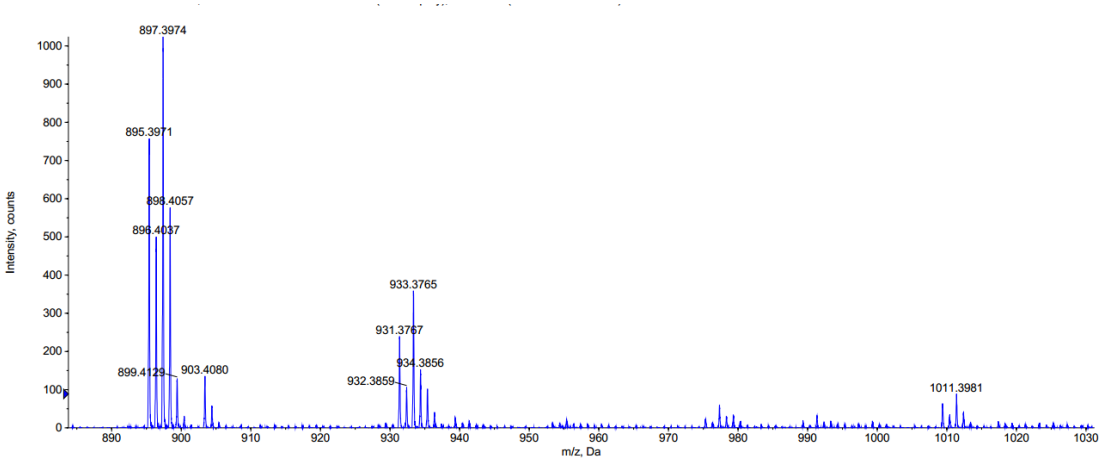

*Figure 7.58. MS of **3-4c**.*

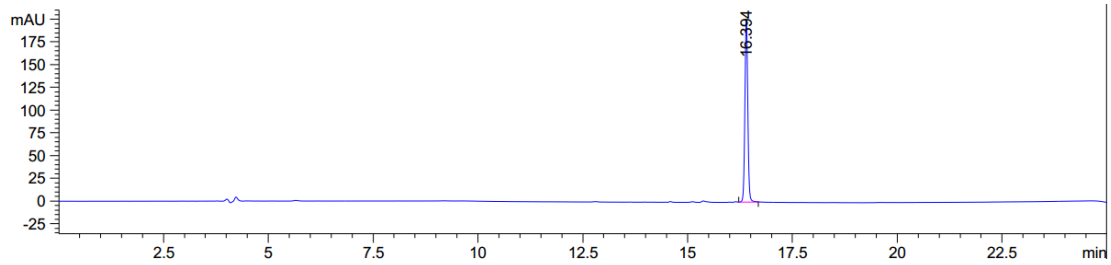

*Figure 7.59. HPLC chromatogram of **3-4c**.*

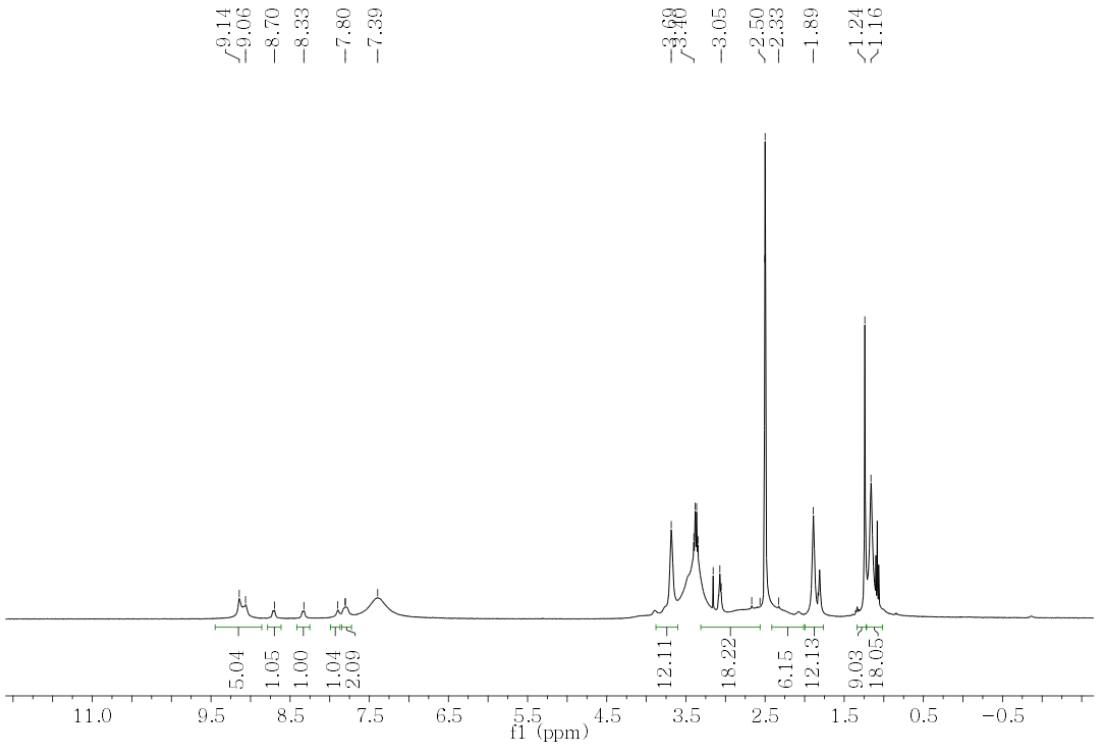

*Figure 7.60. ^{1}H NMR spectrum of **3-4d**.*

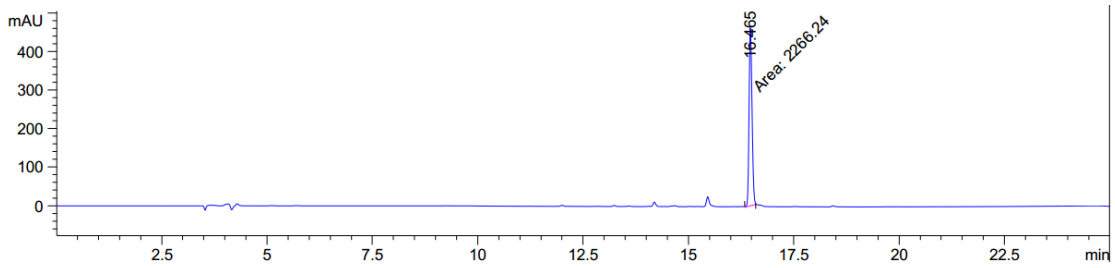

*Figure 7.61. HPLC chromatogram of **3-4d**.*

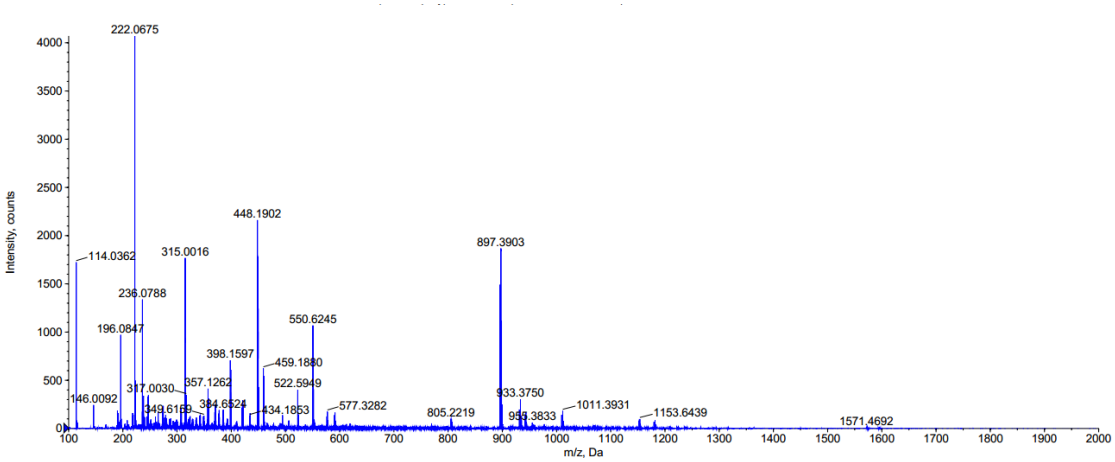

*Figure 7.62. MS of **3-4e**.*

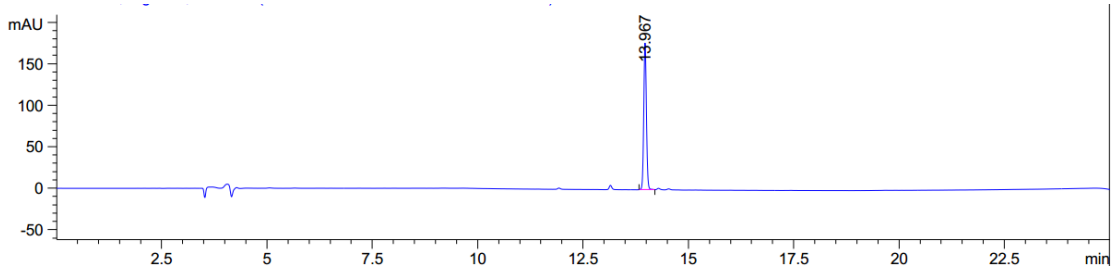

*Figure 7.63. HPLC chromatogram of **3-4e**.*

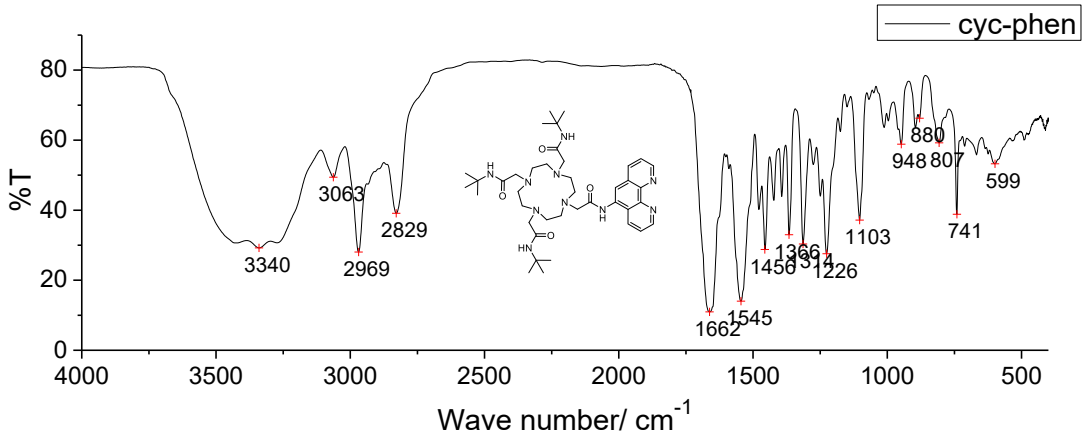

*Figure 7.64. FT-IR spectrum of **cyc-phen**.*

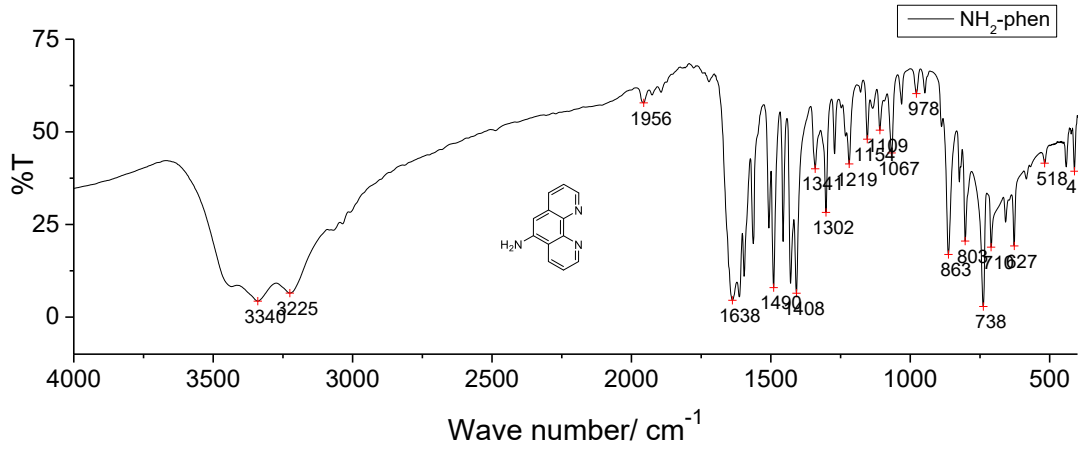

Figure 7.65. FT-IR spectrum of ***phenNH₂****.*

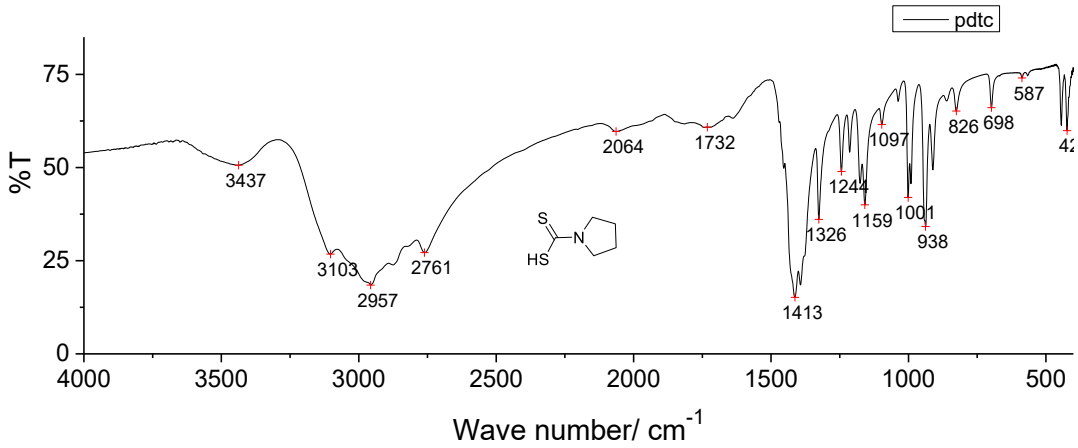

Figure 7.66. FT-IR spectrum of ***pdtc****.*

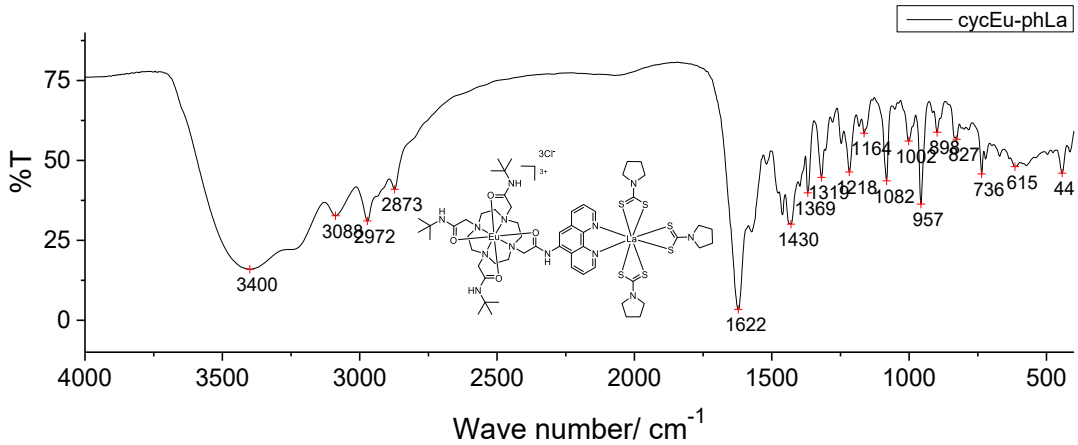

Figure 7.67. FT-IR spectrum of ***cycEu-phLa****.*

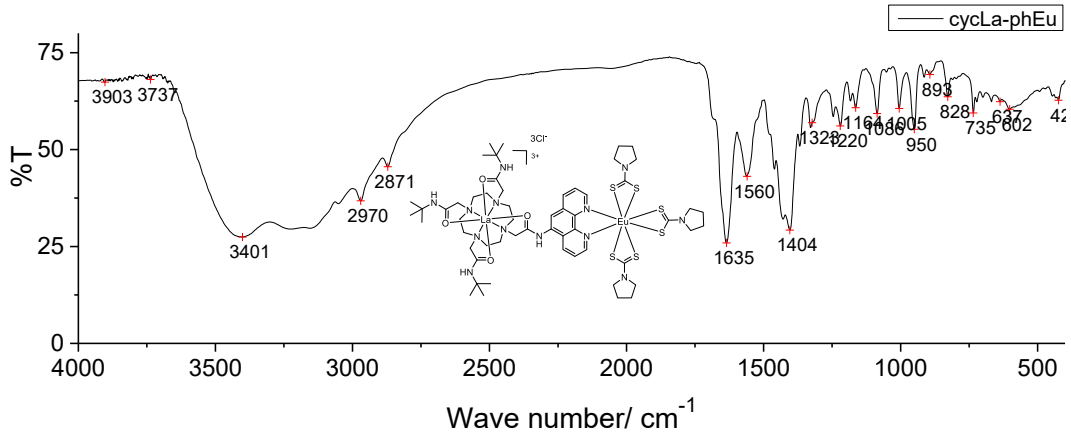

Figure 7.69. FT-IR spectrum of ***cycLa-phEu****.*

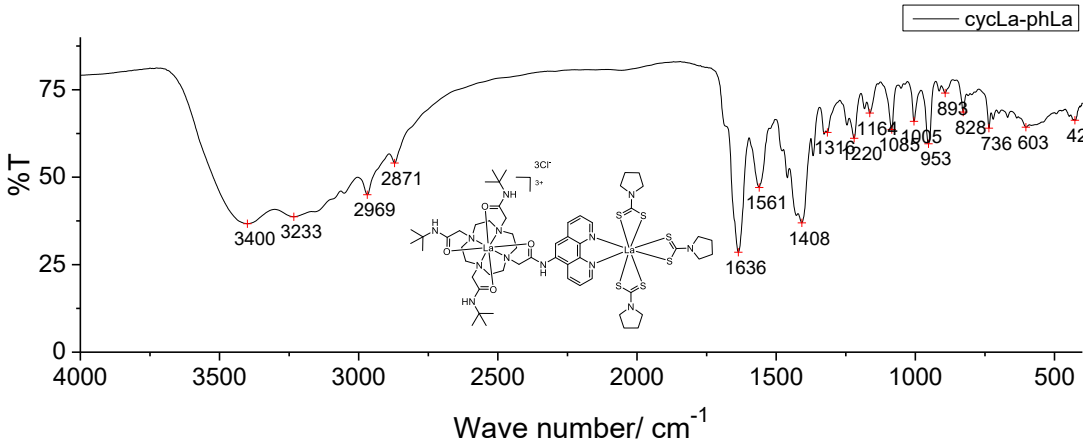

Figure 7.68. FT-IR spectrum of ***cycLa-phLa****.*

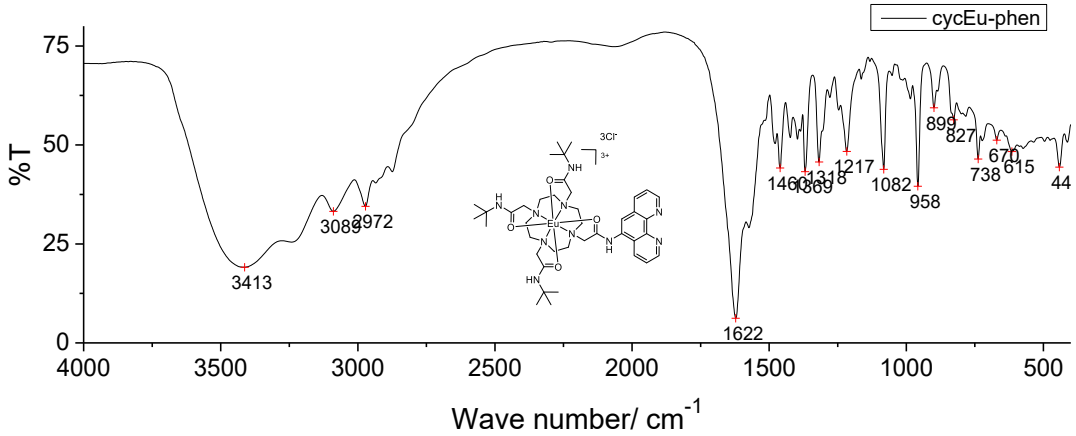

Figure 7.69. FT-IR spectrum of ***cycEu-phen****.*

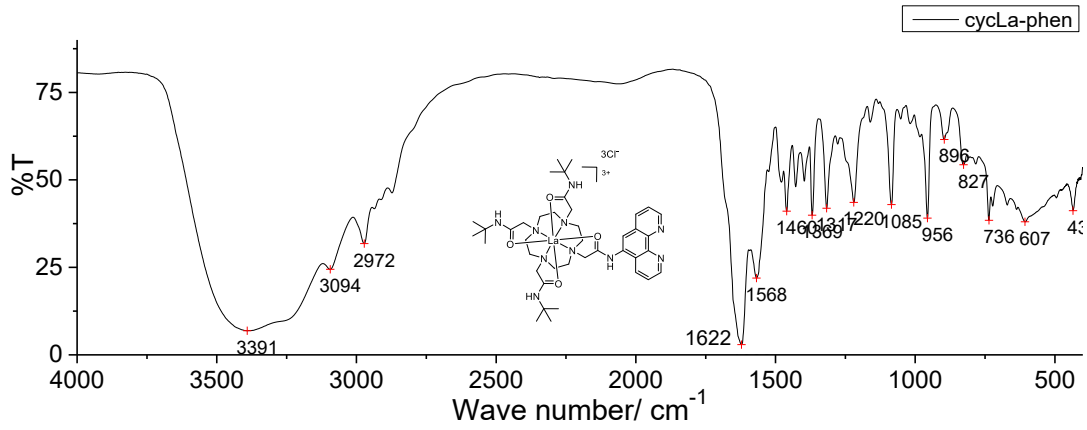

*Figure 7.70. FT-IR spectrum of **cycLa-phen**.*

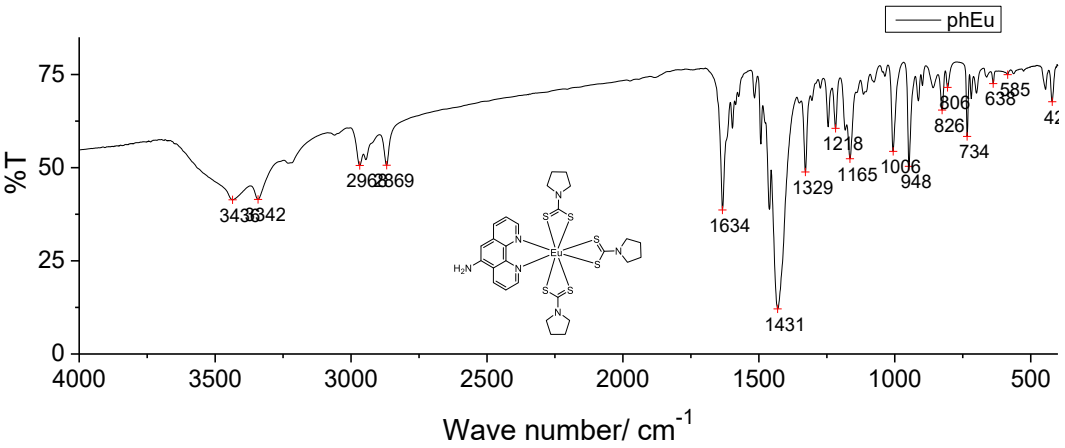

*Figure 7.71. FT-IR spectrum of **phEu**.*

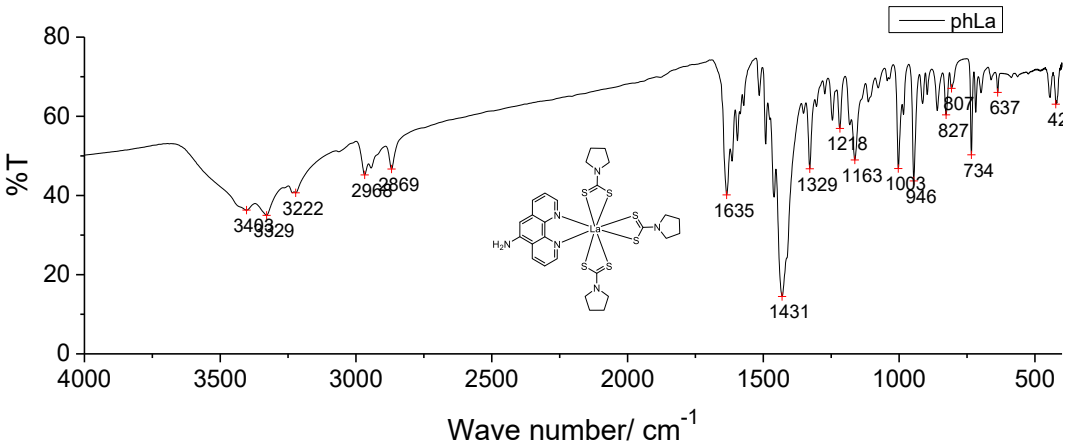

*Figure 7.72. FT-IR spectrum of **phLa**.*

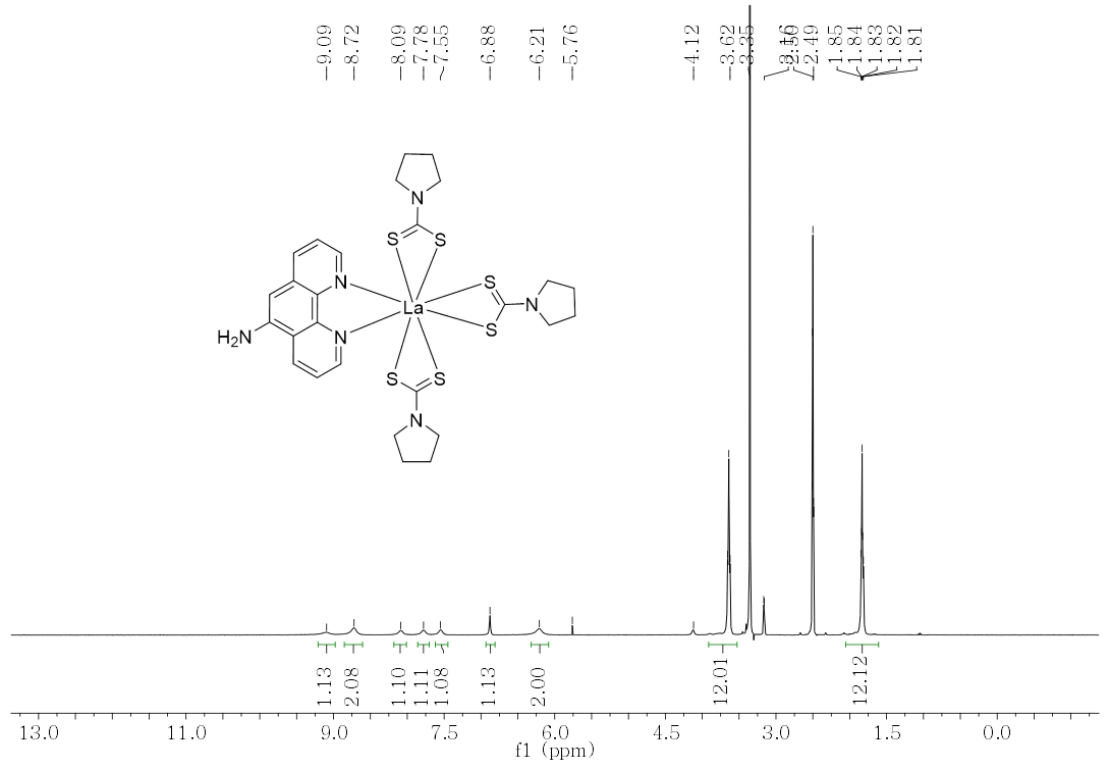

*Figure 7.73. [1]H NMR spectrum of **phLa**.*

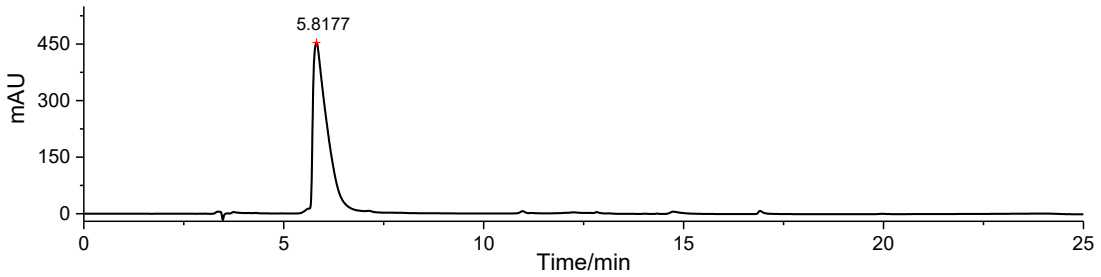

*Figure 7.74. HPLC chromatogram of **phLa**.*

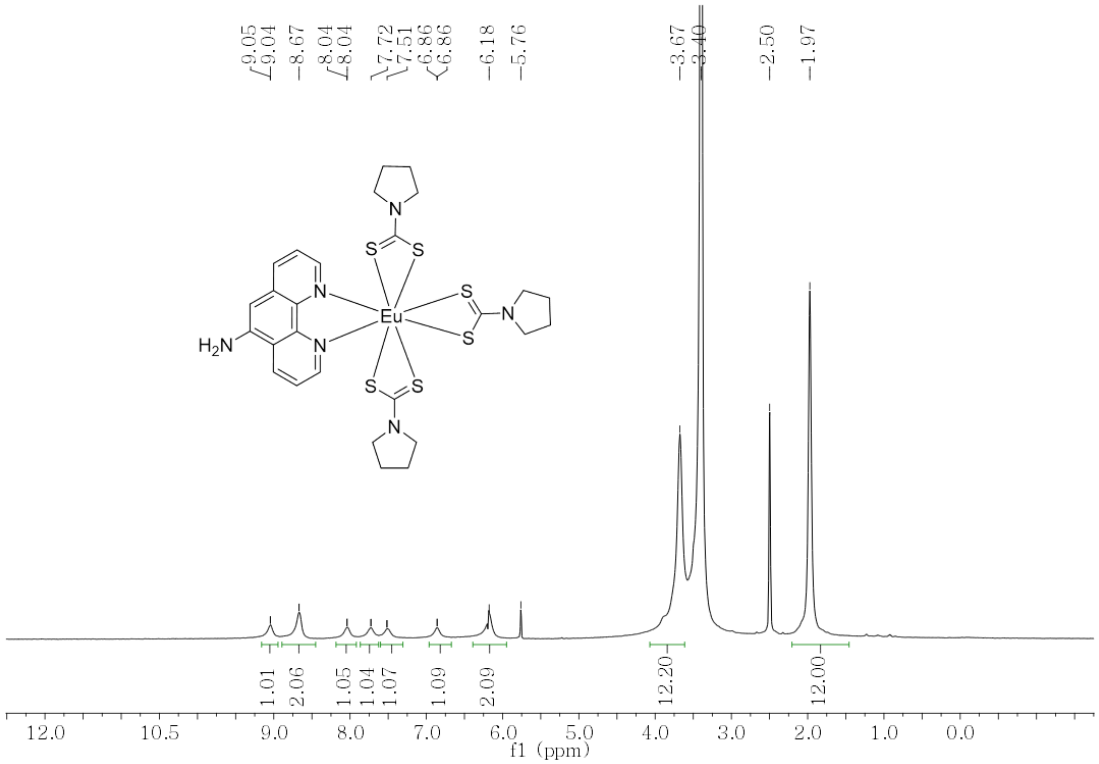

*Figure 7.75. [1]H NMR spectrum of **phEu.***

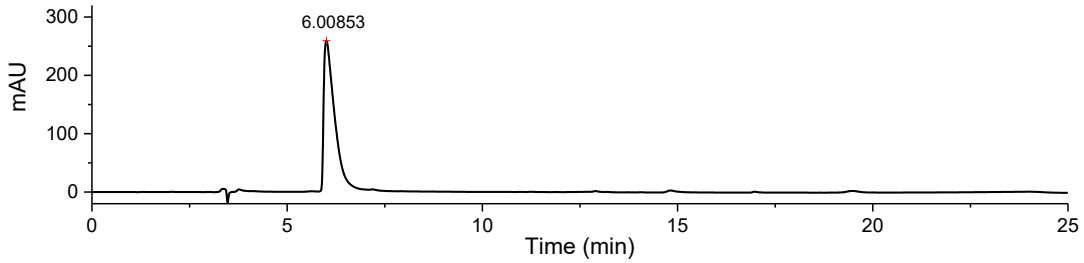

*Figure 7.76. HPLC chromatogram of **phEu.***

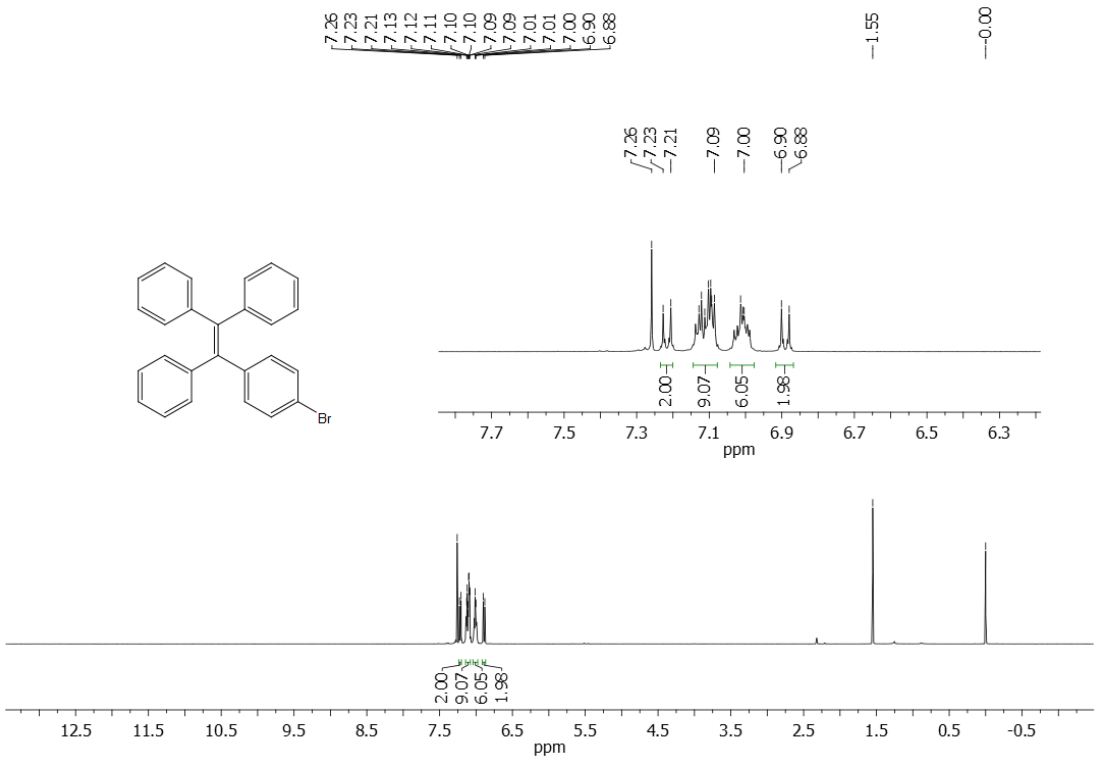

*Figure 7.79. Figure X. [1]H NMR of compound **5-3**.*

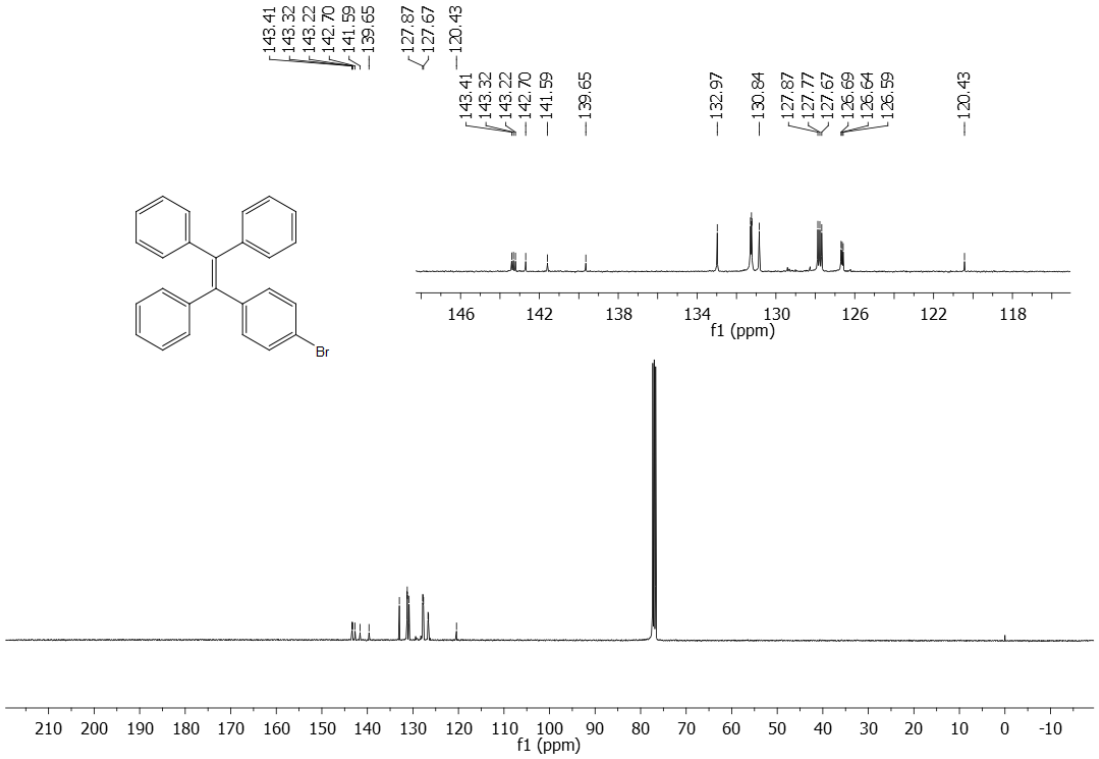

*Figure 7.77. [13]C NMR of compound **5-3**.*

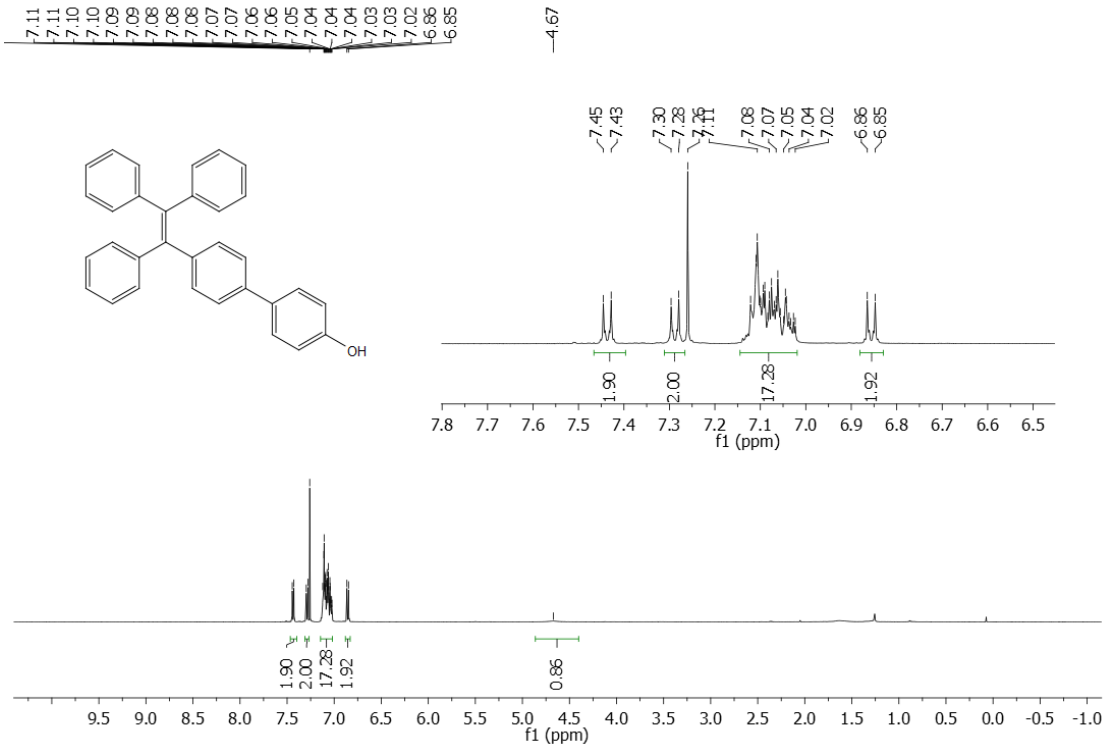

*Figure 7.78. [1]H NMR of compound **5-4**.*

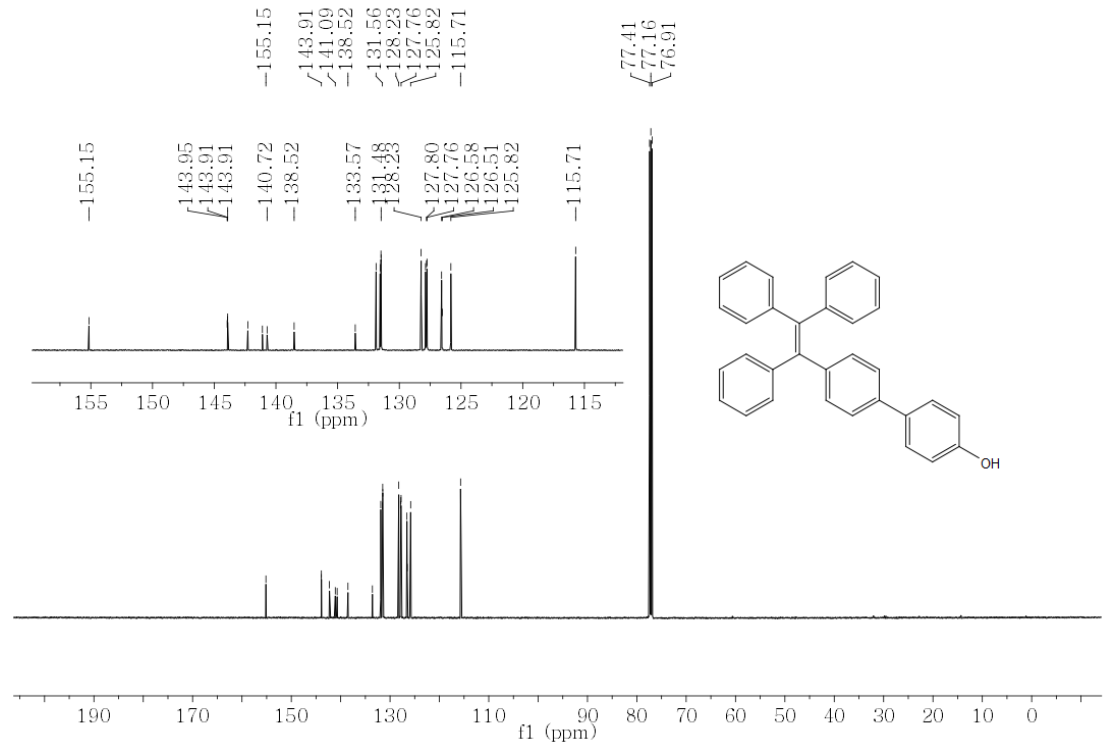

*Figure 7.79. [13]C NMR of compound **5-4**.*

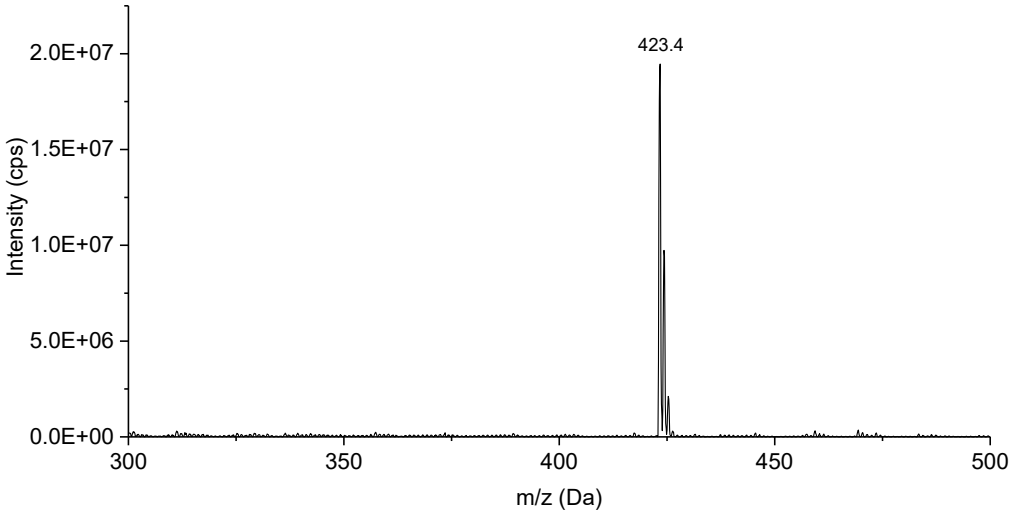

*Figure 7.80. MS of compound 5-**4**.*

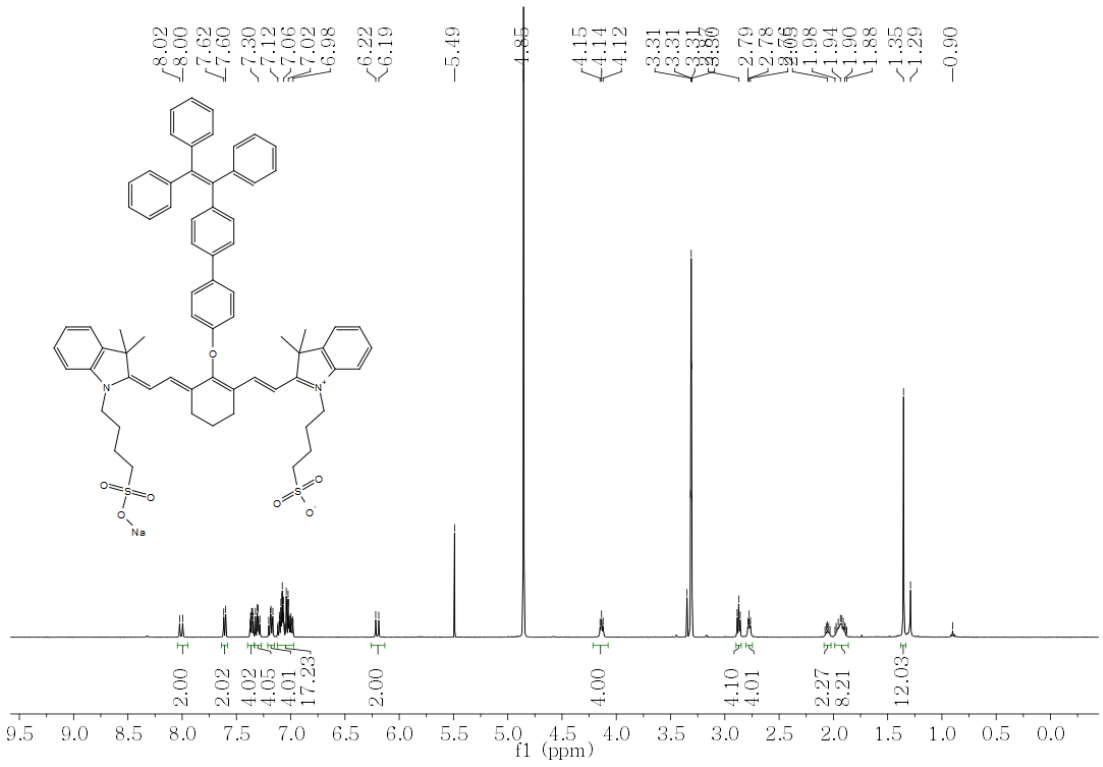

*Figure 7.81. ^{1}H NMR of compound **5-5**.*

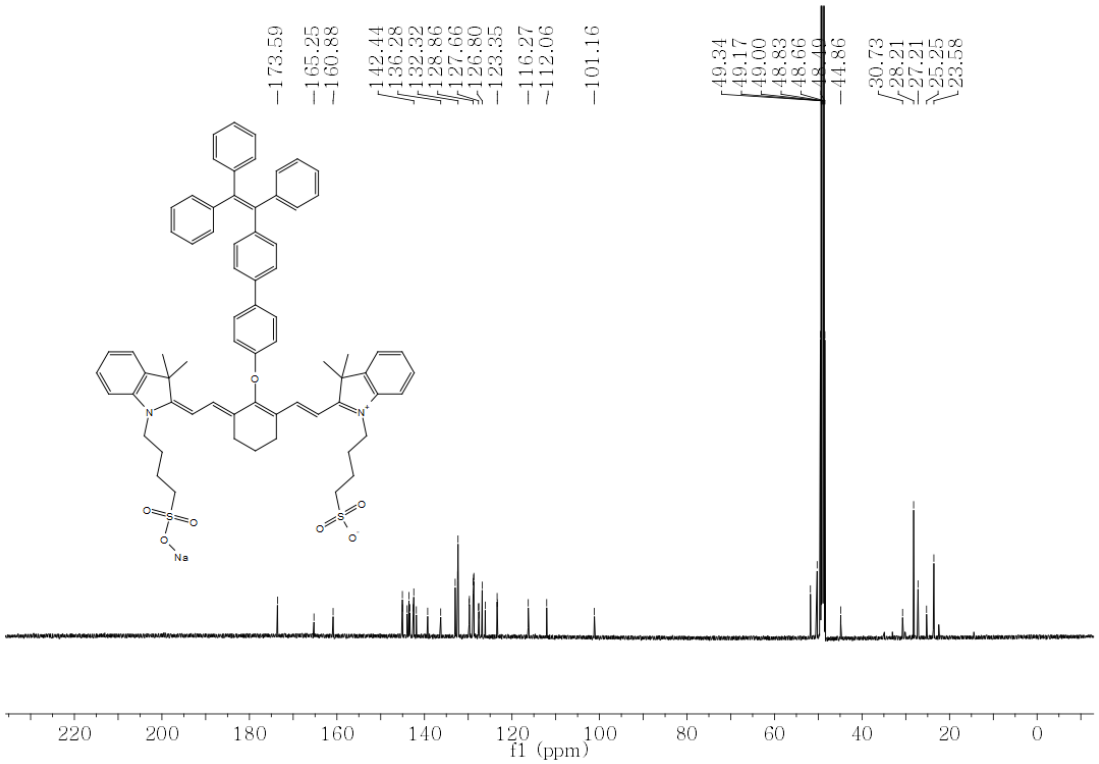

*Figure 7.82. ^{13}C NMR of compound **5-5**.*

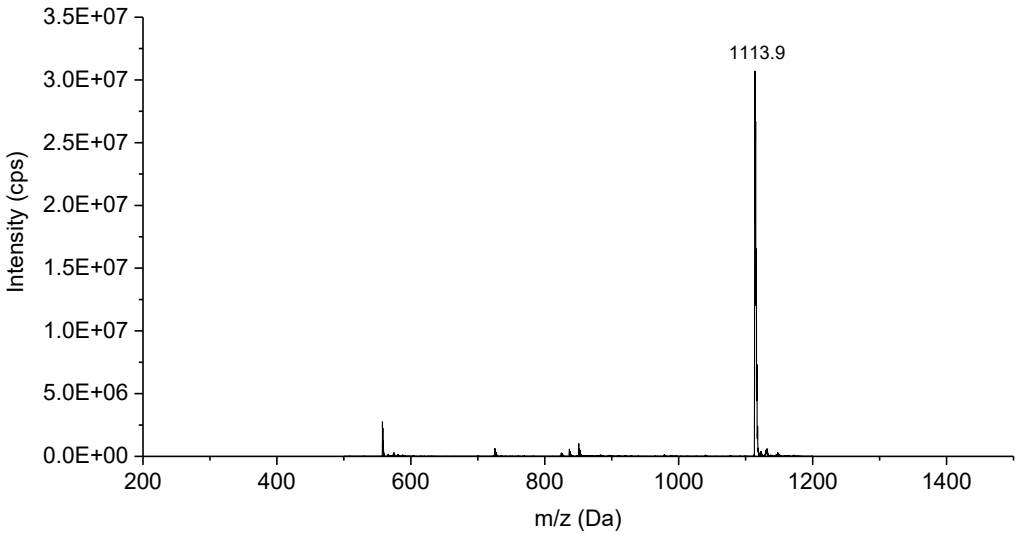

*Figure 7.83. MS of compound **5.5**.*

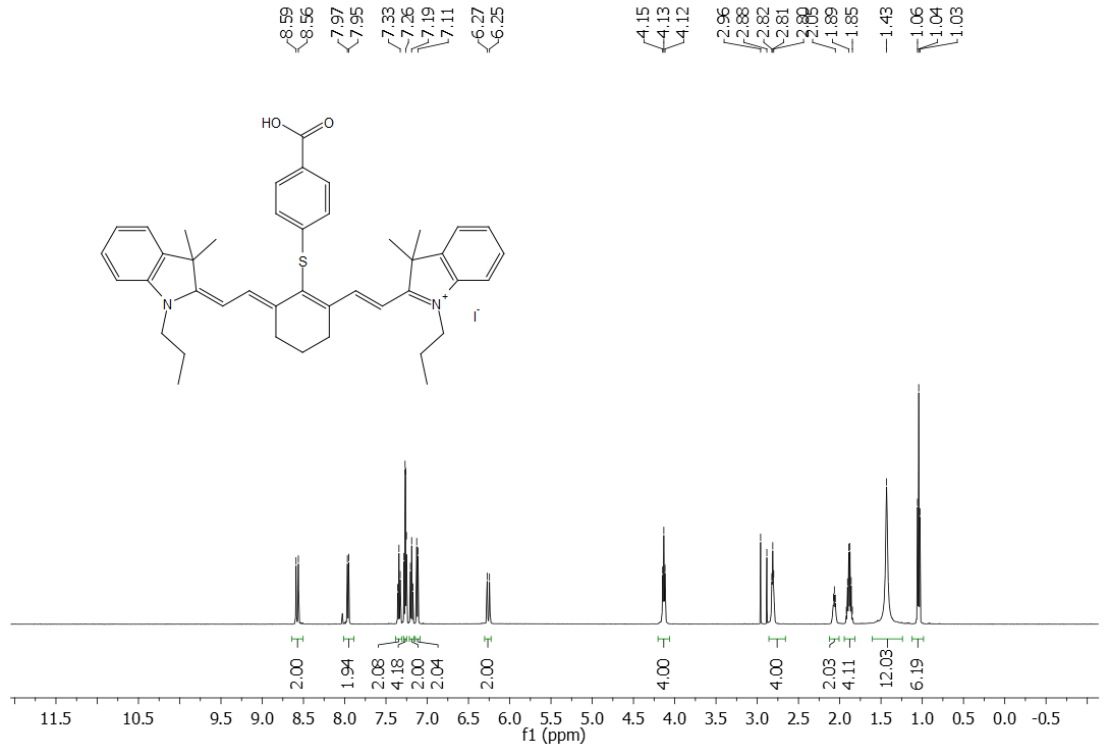

*Figure 7.84. [1]H NMR of compound **IR806**.*

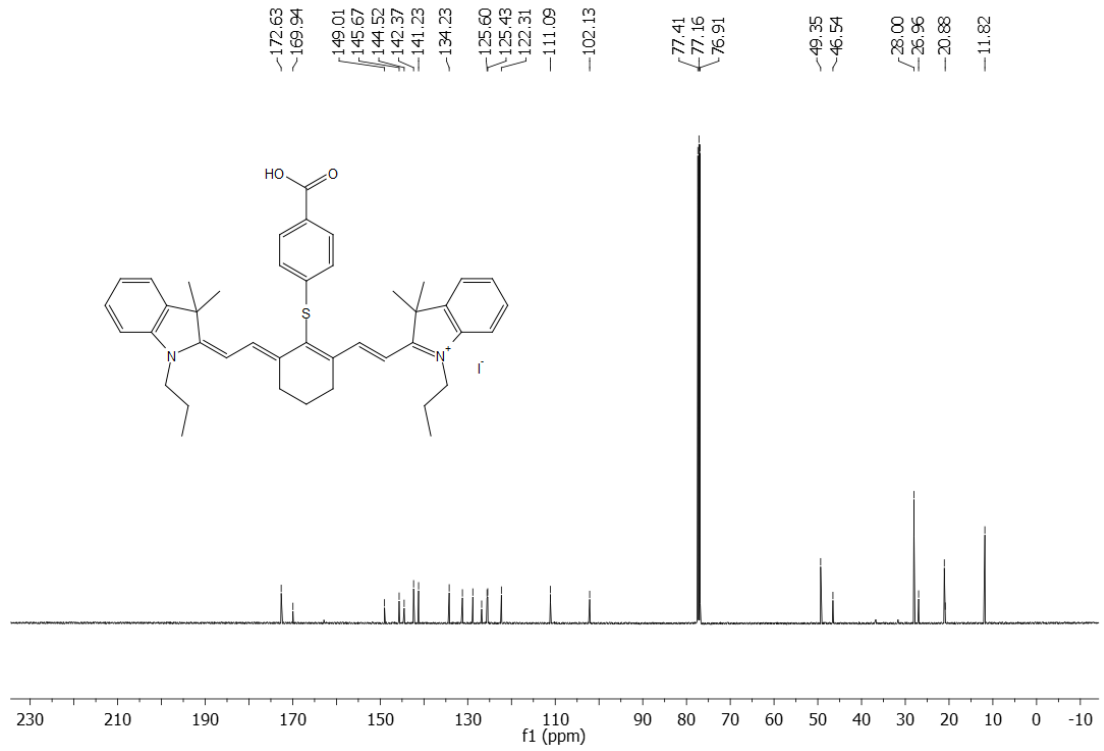

*Figure 7.85. [13]C NMR of compound **IR806**.*

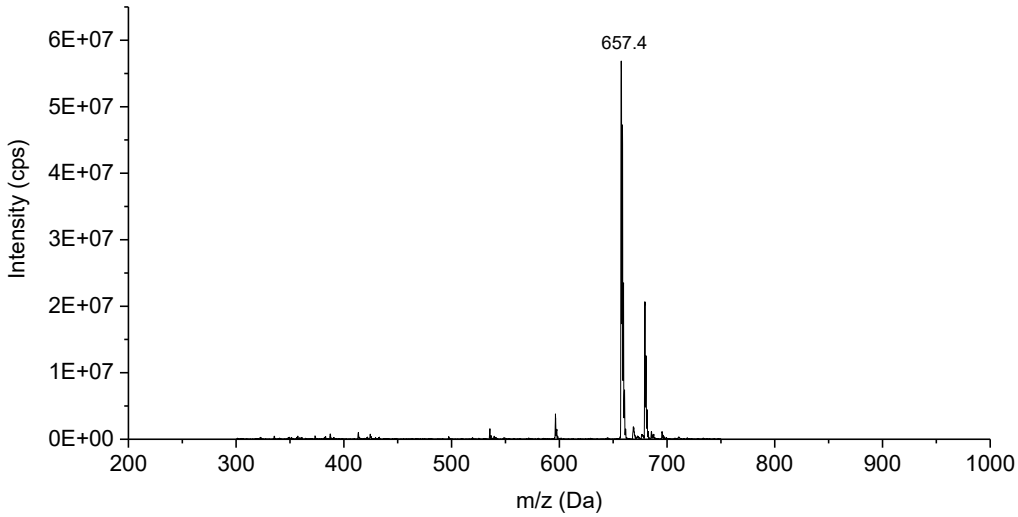

*Figure 7.89. MS of compound **IR806**.*

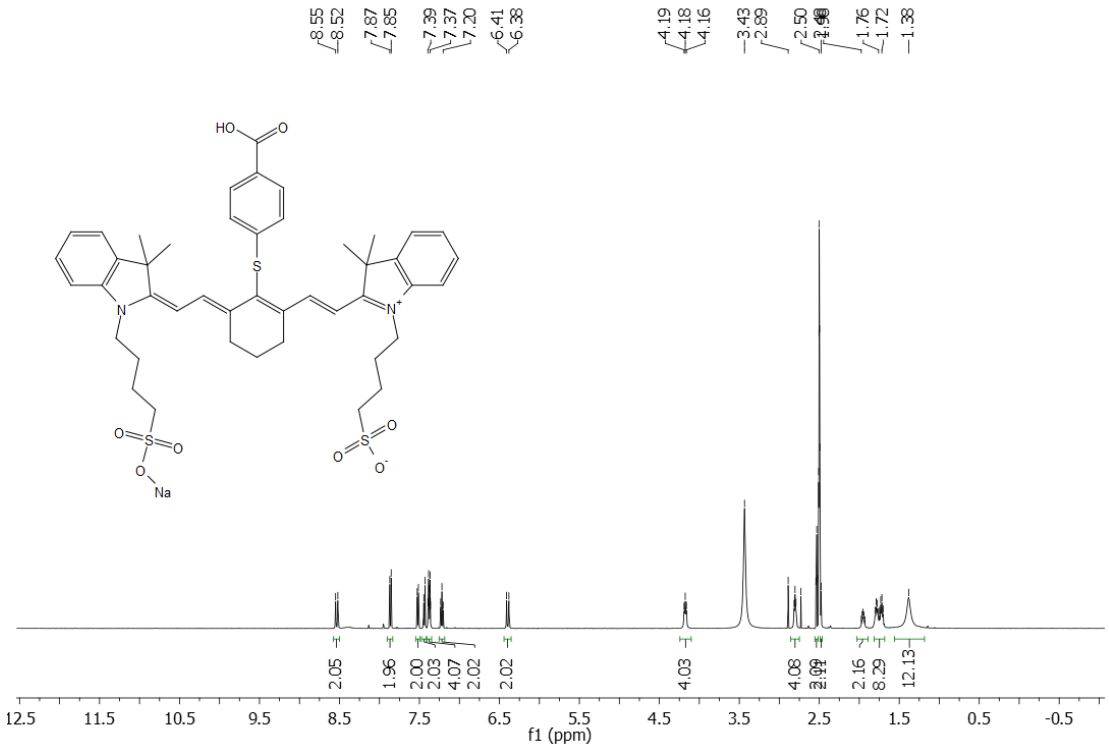

*Figure 7.86. ^{1}H NMR of compound **IR808**.*

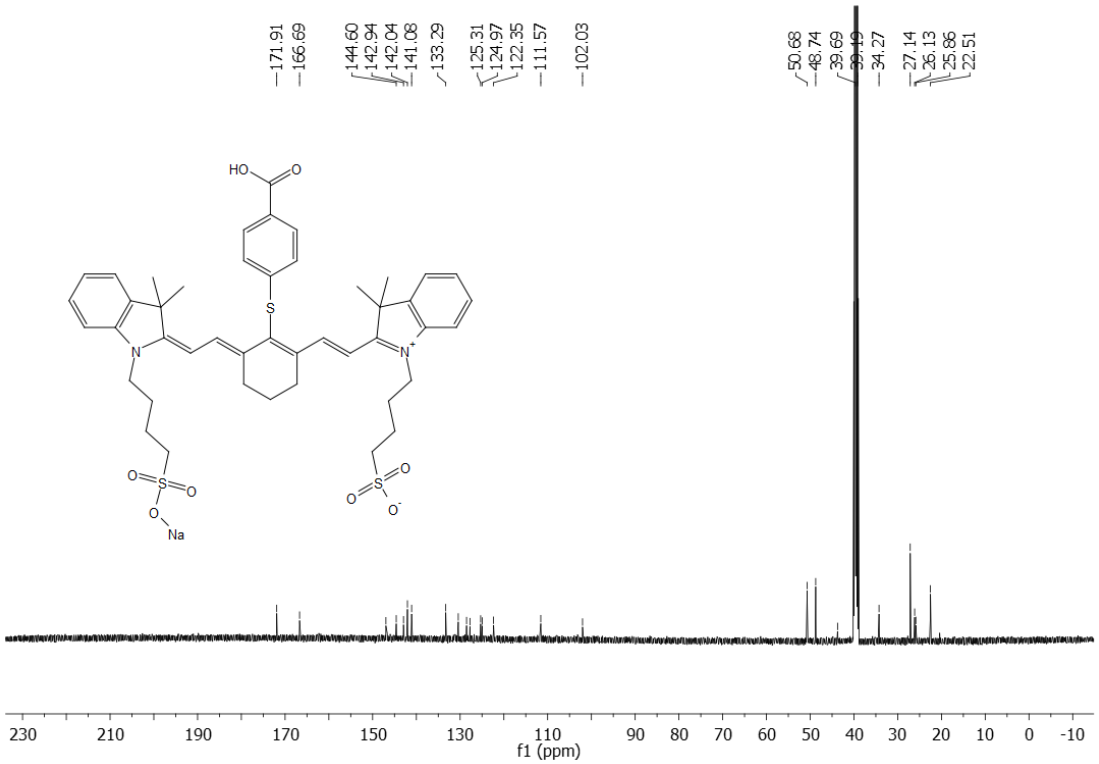

*Figure 7.87. ^{13}C NMR of compound **IR808**.*

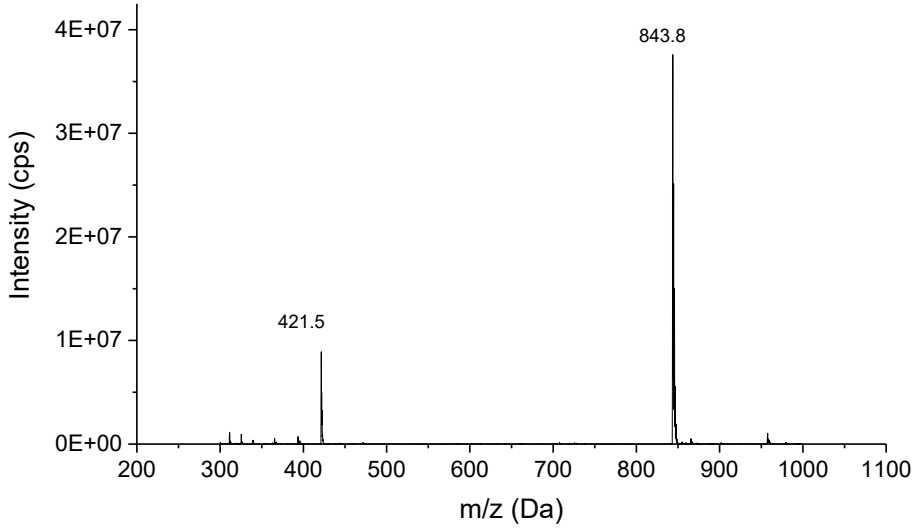

*Figure 7.88. MS of compound **IR808**.*

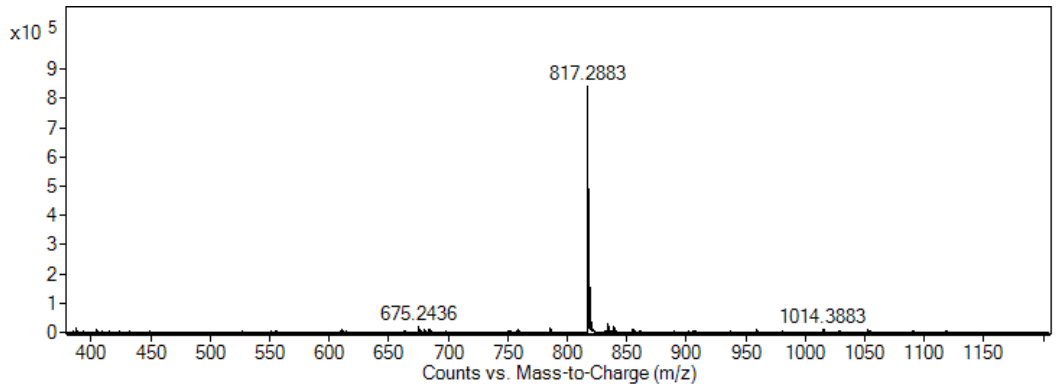

Figure 7.89. The MS of ***6-2****.*

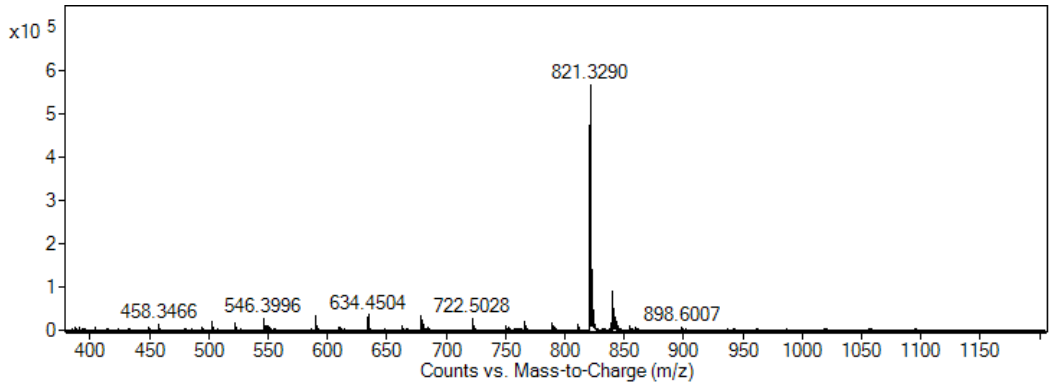

Figure 7.90. The MS of ***6-3****.*

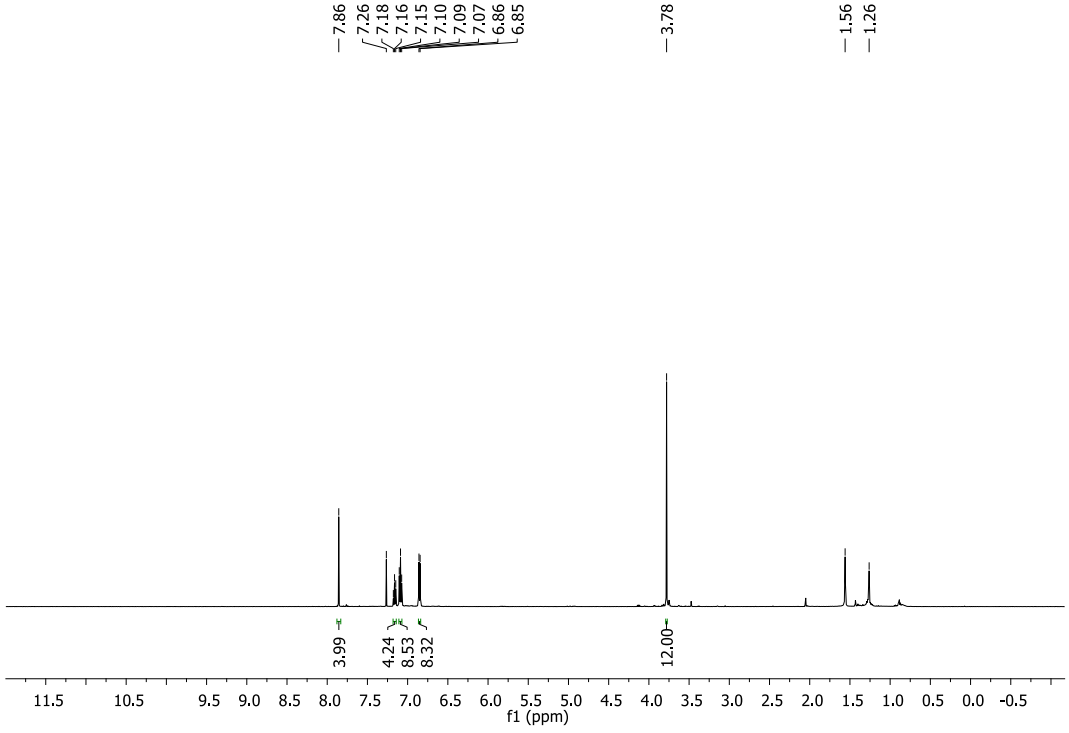

Figure 7.91. The ^{1}H *NMR of* ***6-4****.*

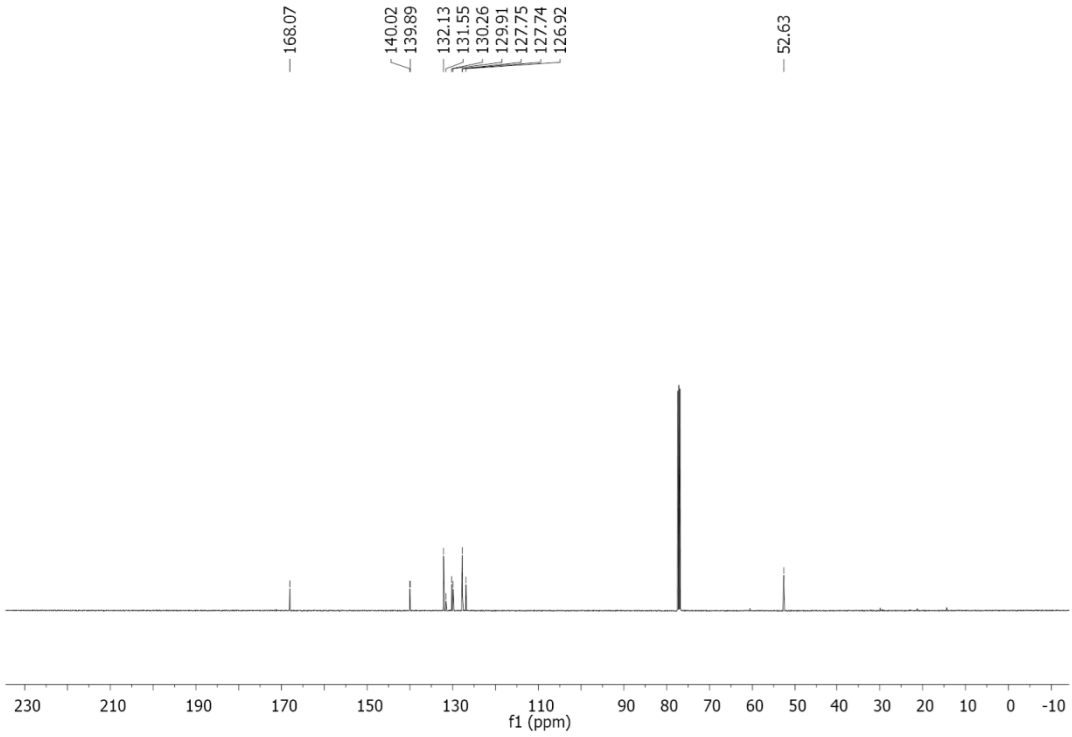

Figure 7.92. The ^{13}C NMR of 6-4.

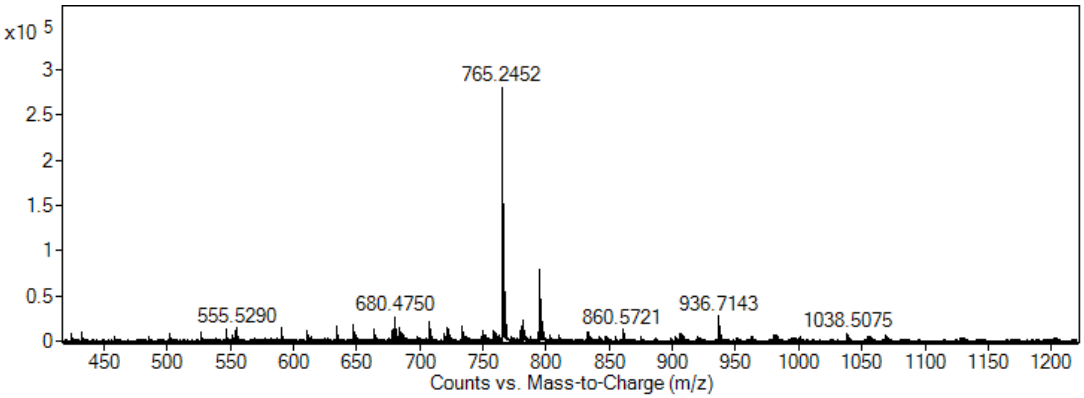

*Figure 7.93. The MS of **6-4**.*

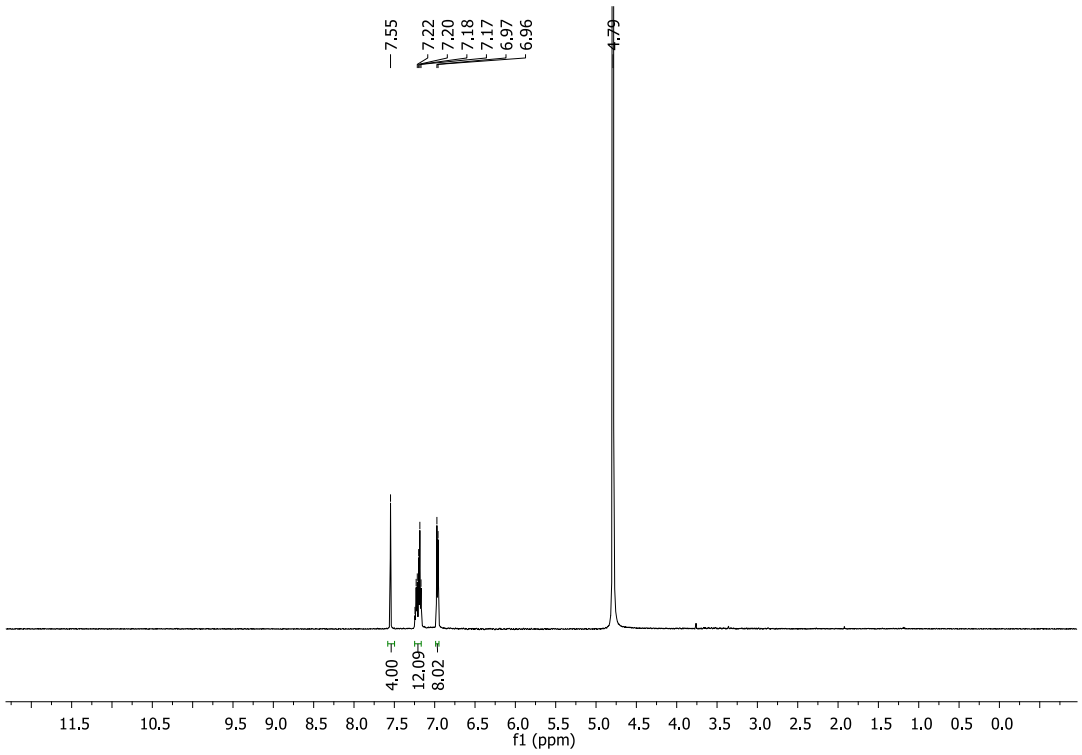

*Figure 7.94. The [1]H NMR of **6-5**.*

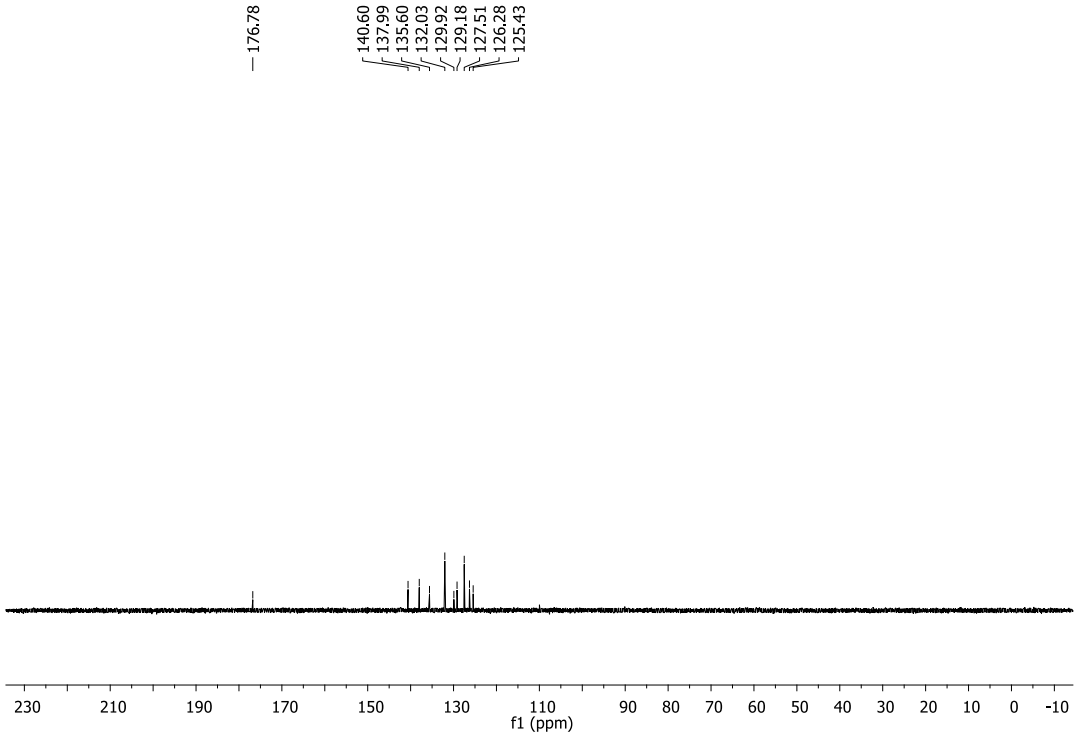

*Figure 7.99. The [13]C NMR of **6-5**.*

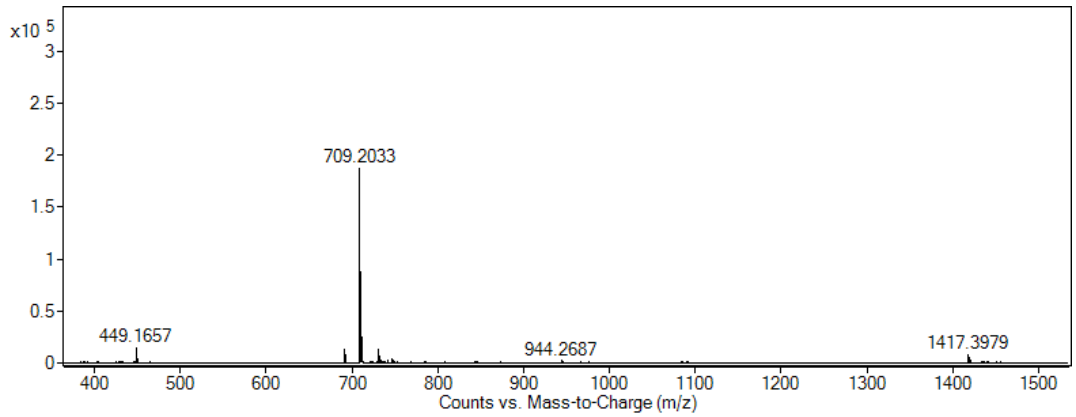

Figure 7.95. The MS of ***6-5****.*

7.6 References

1. J. Bourson, J. Pouget and B. Valeur, *J. Phys. Chem*, 1993, **97**, 4552-4557.
2. N. S. James, Y. Chen, P. Joshi, T. Y. Ohulchanskyy, M. Ethirajan, M. Henary, L. Strekowsk and R. K. Pandey, *Theranostics*, 2013, **3**, 692-702.
3. J. M. Aubry, J. Rigaudy and N. K. Cuong, *Photochem. Photobiol.*, 1981, **33**, 149-153.

Chapter 8 Conclusion and future perspective

8.1 Conclusion

In this thesis, we focus on exploring novel organic-lanthanide hybrid materials and their photophysical properties and applications. To this end, my Ph.D study was designed to have two main themes. One was to develop new probes based on lanthanide complexes for energy transfer study and sensing applications (Chapter 2, 3, &4). Learning from lanthanide complexes, the other theme was to develop brighter dye-nanoparticle upconversion systems including dye-sensitised UCNPs (Chapter 5) and ytterbium nanoparticle-mediated upconversion hybrid (Chapter 6).

The main research achievements and outcomes of this thesis are summarised below:

1) The comprehensive literature review in Chapter 1 on five types of organic-lanthanide hybrid materials, including lanthanide complex, dye-sensitised downshifting nanoparticles (DSNPs), dye-sensitised downconversion nanoparticles (DCNPs), dye-sensitised upconversion nanoparticles (UCNPs), and UCNPs-dye energy transfer systems, together with their optical properties and applications have been thoroughly discussed.
2) In Chapter 2, in the format of a published paper, an ytterbium complex-based Hg^{2+} sensor was designed and synthesized. The water-soluble ytterbium complex exhibits reversible off−on visible and NIR emission upon the binding with mercury ion. The fast response and 150 nM sensitivity of Hg^{2+} detection are based upon FRET and the lanthanide antenna effect. The reversible Hg^{2+} detection can be performed *in vitro*, and the binding mechanism has been proved by NMR employing the motif structure in a La complex and by DFT calculations. This lanthanide complex-based sensor offers potential applications for deep tissue mercury ion sensing.
3) In Chapter 3, also as a published paper, I report a pair of stoichiometric terbium-europium dyads as molecular thermometers and study their energy

transfer properties. A strategy for synthesizing hetero-dinuclear complexes that contain chemically similar lanthanides was developed. By this strategy, a pair of thermosensitive dinuclear complexes, **cycTb-phEu** and **cycEu-phTb,** was synthesized. Their structures were geometrically optimized with an internuclear distance of approximately 10.6 Å. The dinuclear complexes have sensitive temperature-dependent luminescent intensity ratios of europium and terbium emissions, and temporal dimension responses over a wide temperature range (50 - 298 K and 10 - 200 K, respectively). This indicates that both dinuclear complexes can form excellent self-referencing thermometers.

4) In Chapter 4, published as a peer-reviewed paper, I investigated the spectral structure and intensity changes of a pair of dinuclear complexes with a europium ion on cyclen site and a lanthanum ion on phen site or vice verses (**cycEu-phLa** and **cycLa-phEu)**. Though they have the same components and the same energy levels, they present different photophysical properties due to the different coordination environment. The band positions are different in the emission spectra. The emission of **cycEu-phLa** showed a stronger relative intensity of $^5D_0 \rightarrow {}^7F_2$ transition whereas the relative intensity of $^5D_0 \rightarrow {}^7F_4$ transition was weaker in comparison with **cycLa-phEu**. We found the **cycEu-phLa** have higher internal quantum efficiency while the **cycEu-phLa** have higher sensitising efficiency, though they have similar external quantum yield. We determined the singlet-triplet intersystem crossing rate with values as $\sim 10^8$ s^{-1}. This study offers a new insight into energy transfer from ligand to lanthanide ions, especially, in terms of the binding sites.
5) In Chapter 5, I report a dye sensitised upconversion nanoparticle with highly enhanced upconversion emission. I designed and synthesized a new dye by connecting tetraphenylethene (TPE) with a cyanide NIR dye, IR783. The resultant compound (TPEO-IR783) has a quantum yield of 22.46% which is 3 times higher than that of reported UCNP sensitiser (IR806). The TPEO-IR783 exhibits a transparent window in a range of 400 nm to 600 nm, making it suitable sensitiser for upconversion nanoparticles by avoiding reabsorption.

The TPEO-IR783 sensitised UCNPs show more than 200-fold upconversion emission than the reported IR806 sensitised UCNPs under the same condition. This study offers a strategy to increase the quantum yields of organic dyes to improve dye-UCNPs performance.

6) In Chapter 6, I report an ytterbium nanoparticle-mediated upconversion system. The system enables the singlet energy transfer from sensitisers to acceptor triplet states without the requirement of intersystem crossing. I evaluate the hybrid upconversion design by IR808 and rubrene acid. While the mix of IR808 and rubrene acid does not show any upconversion emission, the introduction of an intermediate ytterbium energy level in $NaGdF_4$:Yb nanoparticles displays strongly enhanced upconversion emissions. This design bypasses the specific requirement of traditional sensitisers in TTA system, providing a wide range of opportunities in deep tissue applications.

8.2 Perspective

By exploring the dye-lanthanide hybrid materials for sensing, energy transfer study and improving the luminescence brightness of upconversion nanoparticles, this Ph.D thesis suggests a new field in high-quality luminescent materials with many future opportunities in the photophysical study and their applications.

8.2.1 Lanthanide complex

The lanthanide complexes have shown huge advantages in a wide range of bio-applications due to their small size, clear structure, good reproducibility, and cell permeability. However, the excitation wavelength of the current lanthanide complexes lies in the UV and visible range with poor tissue penetration and cytotoxicity concerns. Though two-photon technique shifts the excitation to NIR ranges, the damage to living tissue remains concerned by high-power density required in two-photon technique. Developing lanthanide complexes with both absorption and emission through biological transparent windows will benefit biological applications.

Hetero-dinuclear lanthanide complex allows doping different lanthanide ions in

one complex. This provides opportunities to develop multiple functional probes. For instance, when Gd^{3+} and Yb^{3+} ions are coordinated in one complex, the probe will have both MRI and NIR signals. The multiple signals will provide more precise localization by overcoming tissue penetration issues.

The hetero-lanthanide complex also provides a platform for photon upconversion,[1, 2] offering a new direction for background-free probes at the molecular level, though it remains challenging to achieve high quantum efficiency. Exploring and engineering lanthanide complex-based upconverters will bring in many opportunities in biology-compatible probes for various background-free applications

8.2.2 Organic-lanthanide nanoparticle hybrid materials

Dye-UCNPs hybrid system tremendously enhances the light harvesting capacity of the lanthanide materials. However, the current reported NIR dyes are limited to the cyanine derivatives or their similar species. More dyes with improved quantum yield and stability are expected to be further exploited from organic chemistry community. These dyes should possess no significant UV or visible absorption to prevent quenching effects on the upconversion emissions.

The triplet state of NIR dye was shown as a critical pathway to increase the energy transfer from the surface dye to UCNPs.[3] To ensure this energy transfer efficient, the match of triplet energy level and absorption of UCNPs is critical. The shorter distances between the organic dye and lanthanide nanoparticles are preferred, which can be achieved by direct attachment of conjugated skeleton of dye to lanthanide ion on the surface of nanoparticles. The back energy transfer from UCNPs to triplet state of the dyes needs to be thoroughly investigated in hybrid materials. One could set an appropriate energy gap between the triplet state of dye and Yb excited states to prevent the back energy transfer.

Concentration quenching of the dye sensitisers limits the brightness enhancement of dye-nanoparticle hybrids. The concentration of the dyes used in the current system is usually at the level of micromolar.[4] When the dye loading is beyond this range, the luminescence decreases dramatically due to the self-quenching of dyes.[5] To overcome

this limitation, the concept of aggregation-induced emission (AIE) can be introduced for dye-sensitised nanoparticles. AIE dyes do not suffer from concentration quenching; instead, they provide enhanced luminescence at aggregated state. The surface of nanoparticles can be fully covered with a high density of AIE dyes, maximizing the light harvest. This strategy has been demonstrated to be effective for dye-sensitised downconversion nanoparticles.[6] The implementation of this design concept in upconversion system yet to be tested.

Although translating the laboratory findings to clinical practices remains challenging. The FDA approved lanthanide MRI agents and radiation therapeutic agents show promise for the future use of dye-lanthanide materials in clinical practices. The recent advances in super-resolution microscopy,[7, 8] deep learning techniques,[9] smart point-of-care platforms[10, 11] offer many interdisciplinary opportunities for boosting the discovery and improvements of these versatile materials and enriching their applications.

8.3 References

1. N. Souri, P. Tian, C. Platas-Iglesias, K. L. Wong, A. Nonat and L. J. Charbonniere, *J. Am. Chem. Soc.*, 2017, **139**, 1456-1459.
2. A. Nonat, C. F. Chan, T. Liu, C. Platas-Iglesias, Z. Liu, W. T. Wong, W. K. Wong, K. L. Wong and L. J. Charbonniere, *Nat. Commun.*, 2016, **7**, 11978.
3. D. J. Garfield, N. J. Borys, S. M. Hamed, N. A. Torquato, C. A. Tajon, B. Tian, B. Shevitski, E. S. Barnard, Y. D. Suh, S. Aloni, J. B. Neaton, E. M. Chan, B. E. Cohen and P. J. Schuck, *Nat. Photonics*, 2018, **12**, 402-407.
4. Z. Wang and A. Meijerink, *J. Phys. Chem. Lett.*, 2018, **9**, 1522-1526.
5. W. Shao, G. Chen, A. Kuzmin, H. L. Kutscher, A. Pliss, T. Y. Ohulchanskyy and P. N. Prasad, *J. Am. Chem. Soc.*, 2016, **138**, 16192-16195.
6. W. Shao, C. K. Lim, Q. Li, M. T. Swihart and P. N. Prasad, *Nano Lett.*, 2018, **18**, 4922-4926.
7. C. Chen, F. Wang, S. Wen, Q. P. Su, M. C. L. Wu, Y. Liu, B. Wang, D. Li, X. Shan, M. Kianinia, I. Aharonovich, M. Toth, S. P. Jackson, P. Xi and D. Jin, *Nat. Commun.*, 2018, **9**, 3290.
8. Y. Liu, Y. Lu, X. Yang, X. Zheng, S. Wen, F. Wang, X. Vidal, J. Zhao, D. Liu, Z. Zhou, C. Ma, J. Zhou, J. A. Piper, P. Xi and D. Jin, *Nature*, 2017, **543**, 229-233.
9. H. Wang, Y. Rivenson, Y. Jin, Z. Wei, R. Gao, H. Gunaydin, L. A. Bentolila, C. Kural and A. Ozcan, *Nat. Methods*, 2019, **16**, 103-110.

10. H. He, B. Liu, S. Wen, J. Liao, G. Lin, J. Zhou and D. Jin, *Anal. Chem.*, 2018, **90**, 12356-12360.
11. Z. Grcs, M. Tamamitsu, V. Bianco, P. Wolf, S. Roy, K. Shindo, K. Yanny, Y. Wu, H. C. Koydemir, Y. Rivenson and A. Ozcan, *Light Sci. Appl.*, 2018, **7**, 66.